UNIVERSIDAD COMPLUTENSE DE MADRID
FACULTAD DE CIENCIAS FÍSICAS
DEPARTAMENTO DE FÍSICA DE MATERIALES

TESIS DOCTORAL

Pulsed Laser Deposited Silver Nanoestructures For Molecular Sensing And Photovoltaic Applications

Nanoestructuras de plata producidas por depósito por láser pulsado para aplicaciones de detección molecular y fotovoltaicas

MEMORIA PARA OPTAR AL GRADO DE DOCTOR

PRESENTADA POR

Giorgio Baraldi

Director

José Gonzalo de los Reyes

Madrid, 2015

Pulsed Laser Deposited Silver Nanostructures for Molecular Sensing and Photovoltaic Applications

Nanoestructuras de Plata Producidas por Depósito por Láser Pulsado para Aplicaciones de Detección Molecular y Fotovoltaicas

Giorgio Baraldi

Memoria de tesis dirigida por

Dr. Jose Gonzalo de los Reyes

Presentada en el

Departamento de Física de Materiales,
Facultad de Ciencias Físicas de la Universidad Complutense de Madrid

Para optar al grado de

Doctor en Física

Consejo Superior de Investigaciones Científicas

Laser Processing Group
Instituto de Óptica

Universidad Complutense de Madrid

Madrid, Octubre de 2014

Contents

Chapter 1

Introduction

Stain-resistant and anti-bacterial clothes, scratch-resistant glasses, fast-recharging batteries and electrically conductive displays are just a few examples of consumer products making use of nanotechnologies.[1] Nanotechnology is usually defined as the applied science and technology that aims at manipulating and manufacturing matter at the atomic or molecular scale, usually in the 1-100 nm range.[1,2] The term was coined by Prof. Taniguchi in 1974,[3] who originally defined it in a more strict way as the "*processing of, separation, consolidation, and deformation of materials by one atom or one molecule*". However, it is worth mentioning that Feynman was the first who, during his talk "*There's Plenty of Room at the Bottom*" at the meeting of the American Physical Society at the California Institute of Technology in 1959,[1,4] exposed the idea that manipulation and control of matter at small (nanometer) scale was a scarcely explored field that could led to the discovery of new phenomena that would have an enormous number of technical applications.

The interest in studying materials having typical dimensions in the nanometer scale resides in the fact that they possess properties that can differ considerably from that of bulk. The properties of massive materials are determined by the atoms in the volume that experience similar bounding forces in all directions due to the surrounding neighbouring atoms, rather than by the atoms at the surface that experience anisotropic bounding forces.[5, 6] However, in the case of nm-sized materials the surface-to-volume ratio increases considerably, thus the contribution of surface atoms to the determination of material properties increases too. This can lead to a discretization of electronic states which, in turn, leads to the appearance of optical, thermal, mechanical, magnetic and electric properties that are completely different from that of the bulk.[1,5]

Nanotechnology tremendously attracted the interest of the scientific community because it opened new exciting challenges, since new and more sophisticated fabrication and characterization techniques were needed in order to explore the nano-world and to manipulate matter at the nanoscale. The development starting from 1980s of scanning tunneling microscope[7] (STM) and of high-resolution transmission and scanning electron microscopes[8] (TEM and SEM) represented a breakthrough for the development of modern nanotechnology. In addition, the capability of working at the nanoscale allowed confirming the validity of theoretical approaches used for describing confined systems and to develop more complex and complete models for the interpretation and prediction of behaviour of matter at the nanoscale.

In the last three decades much has been done and the research in nanotechnology has advanced considerably such that many concepts related to it have been already applied to many sectors of technology, from electronics to information technologies and from energy to medicine.[1] In all these cases, it is generally accepted that the most relevant benefits of applying nanotechnology are to make things smaller, safer, lighter but more robust and more efficient. In addition, this implies less use of raw materials and lower energy consumption, two fundamental goals to make the development of modern societies more sustainable.

The basic products of nanotechnology can be classified on the basis of their spatial confinement. Thin film identifies the products in which only one dimension is reduced to the nanometre scale. Typical examples are antireflection and scratch-resistant coatings.[1] Nanowire and nanotube refer to objects in which two dimensions are reduced to the nanometre scale. Molecular sensors, electrical components and materials with specific mechanical properties can include these types of nanostructures.[1] Finally, a nanoparticle is an object which is confined in the three dimensions. In this thesis, we focus our research in this type of nanoobjects, since they show many properties that make them suitable for a wide range of applications. Nanoparticles have a third order non-linear optical response that is considered a fundamental property for information technology, for developing, for example, efficient optical switches,[6] while their high surface-to-volume ratio that enhances their chemical reactivity makes them feasible as catalysts.[6] In addition metal nanoparticles have attracted in the last decades a renewed interest for their linear optical properties, mainly because of their capability of absorbing and scatter light selectively around specific wavelengths,[9] which make them suitable for applications in photonics and medicine.[9] Among them, noble metals (Au, Ag, Cu) is of great interest since they absorb light in the visible range.

Many centuries ago, the optical properties of metal nanoparticles were already used for decorative purposes. The Lycurgus cup[10] (Figure 1.1a) is considered the oldest example found (4^{th} century AD) of coloured glass obtained by incorporating nm-sized Au and Ag nanoparticles in a transparent glass matrix.[11,12] Its main characteristic is that the colour of the glass "changes" when illuminated in reflection or transmission. More recent examples in which nanoparticles have been used for decorative applications are the rich-in-colour stained glass windows of many middle age cathedrals (Figure 1.1b).[12,13] We can compare them with the example of Figure 1.1c that corresponds to a glass substrate (1×2 cm^2) on which we

deposited a film containing Ag nanoparticles with size in the 60-130 nm using pulsed laser deposition (PLD). Similarly to the previous examples, the glass shows different colours.

Figure 1.1: (a) The Lycurgus cup in (left) reflected and (right) transmitted light. Adapted from Freestone and co-workers.[11] Due to the incorporation of nm-sized Ag and Au nanoparticles, the colour of the cup changes upon different illumination conditions. (b) Image of several fragments of a stained glass window of York Minster.[13] The yellow and ruby colours are associated to the dispersion in the glass matrix of nm-sized Ag and Au nanoparticles, respectively. (b) Glass substrate coated with a nanostructured film containing Ag nanoparticles with size in the 50-130 nm range embedded in an amorphous aluminium oxide matrix. The film was fabricated using PLD. Due to the absorption band characteristic of Ag nanoparticles, the light diffused by the film show different colour, yellow, from the transmitted one (light purple).

The yellow observed on the dark side of the image relates to the light diffused by nanoparticles, while the light purple colour on the white side corresponds to the light transmitted trough the sample.

As previously mentioned, it is now well known that the observed colour relates to the incorporated metal nanoparticles that absorb and scatter light selectively around specific wavelengths in the visible range.[9] This effect was empirically demonstrated by Faraday only in 1857 who studied in a systematic way the optical response of several colloidal metal nanoparticles (Ag, Pt, Cu, Fe, Zn, Hg, ...) synthesized in solution,[14] while the first attempt of theoretical interpretation of the interaction of light with small metal objects was made by Mie, half a century later, in 1908.[15] In his work, Mie solved Maxwell's equations in the case of a spherical metal nanoparticle excited by a sinusoidal plane wave, whose wavelength in the surrounding dielectric medium is longer or comparable to the nanoparticle diameter.[9] Mie obtained two different solutions that mainly depend on the nanoparticle diameter-to-excitation wavelength ratio (D/λ). For $D/\lambda \ll 1$, the nanoparticle shows a strong optical absorption band and enhancement of the electric field in the vicinity of nanoparticle surface (near-field), while scattering is negligable. This result relates to the electric field of the incident light that can induce a coherent oscillation of the conduction electrons of the metal relative to the fixed

positive ions in the nanoparticle. This leads to a redistribution of the surface charges at the poles of the nanoparticle (Figure 1.2), which can be then considered as an oscillating dipole, whose polarizability (and thus absorption and near-field) presents a resonant behaviour.[9] This phenomenon is known today as surface plasmon resonance (SPR), where plasmon refers to the coherent and collective oscillation of conduction electrons of the nanoparticle. On the contrary, if the size of the nanoparticles is large enough such as the condition $D/\lambda<<1$ is not accomplished anymore (i.e., D > 50 nm), scattering starts to be the dominant process and the excitation of several multipole plasmon resonance modes, apart from the dipolar, start to appear.[9,16]

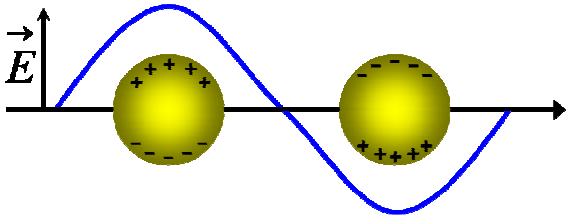

Figure 1.2: Schematic representation of redistribution of the surface charges at the poles of the nanoparticle due to the coherent oscillation of conduction electrons in a nanoparticle due to the electric field of the incident light.

The spectral position at which the SPR is excited can vary from the near-ultraviolet (N-UV) to the near-infrared (N-IR) depending on the dielectric function of the metal.[9] In addition, the SPR spectral position, width and intensity strongly depend on the size, shape and on the medium surrounding nanoparticles.[17] Finally, the spatial arrangement also influences the feature of the SPR, since the optical response of isolated or separated by very small gaps nanoparticles can differ considerably as a result of electromagnetic interaction between nanoparticles.[17,18,19]

Since Mie published his work, many theoretical approaches have been proposed and used to model the optical response of isolated or assemblies of metal nanoparticles. This thesis is mainly an experimental work, however we consider important to make a brief overview of the most representative and commonly used theoretical methods. For a more detailed discussion we refer to the review of Toudert.[9] The quasi-static approximation is probably the most common theoretical classical approach used to model the optical response of a nanoparticle.[9] This approach is valid when the condition $D<<\lambda$ is accomplished and the electric field of the incident light can be considered homogeneous over the whole volume of the nanoparticle. Under these conditions, the laws of electrostatics are verified and the field

outside the nanoparticle is taken equal to that of an electric point dipole immersed in a dielectric medium, superimposed to an external homogeneous electric field (i.e. the incident light).[9] The quasi-static approximation allows calculating accurately the absorption and scattering cross-section, as well as the near-field enhancement[9] (the intensity ratio between total electric field in a specific point outside the nanoparticle volume and the incident field) of isolated, small (D < 50 nm) nanoparticles in a transparent medium. This approach can be applied to the cases of nanoparticles with spherical, (prolate and oblate) spheroidal and ellipsoidal shapes, while it is not adequate to describe the optical behaviour of more complex structures, like the assemblies of interacting nanoparticles or the case of nanoparticles supported on a dielectric substrate (non-homogeneous surrounding medium).[9]

In these cases, the macroscopic optical response is determined by many parameters, as a nanoparticle may experience electromagnetic interactions with neighbouring nanoparticles and with the substrate too.[9] Thus, the optical response is typically determined not only by nanoparticle size and shape distributions but also by their organization and orientation on the surface. If the quasi-static approximation is valid ($D \ll \lambda$), the optical response of a complex nanostructured material can be approximated by considering it, from a macroscopic point of view, as a homogeneous effective medium.[9] The optical response is thus described by an effective dielectric tensor that has to be linked to the nanoparticle size and shape distribution, to their orientation and spatial arrangement. The most representative examples of theoretical approaches based on effective medium modelling are those of Maxwell-Garnet[20] and Yamaguchi,[21] and the related respective extensions.[9] The first is feasible for modelling assemblies of identical nanoparticles dispersed homogeneously in the volume of a dielectric matrix or diluted in a solution, while the second is more appropriate for modelling single-layers of weakly interacting spherical or spheroidal nanoparticles supported or embedded in a dielectric matrix. The main limit of these approaches relates to the point dipole approximation used to model the interaction of a small nanoparticle with neighbouring nanoparticles that does not hold in some cases, for example, when the distance between nanoparticles is reduced such that they are almost in contact.[9]

When the size of nanoparticle is increased such that $D \ll \lambda$ is not accomplished anymore, the quasi-static approximation is no longer valid.[9] In this case, the electric field of the incident light is not homogeneous over the volume of the irradiated nanoparticle and multipolar contributions to the SPR can appear. In addition, the optical response can be also affected by retardation effects that arise from the non-instantaneous interaction between the

polarization charges of the nanoparticle.[9] Under these conditions, the optical response of metal nanoparticles can be studied using approaches based on electrodynamics. Analytical solutions to Maxwell's equation in the electrodynamic regime have been proposed by Mie and, later on, by other authors for nanoparticles with simple shapes, i.e. spheres and spheroids.[9] Nonetheless, when one needs to analyze the optical behaviour of more complex nanostructures, numerical methods are required. Here, we just mention, without enter in more details, those that are commonly used, namely the discrete dipole approximation (DDA), the finite element method (FEM) and the finite difference time domain (FDTD), which are based on the discretization of the nanoparticle volume and to consider it as an assembly of coupled point dipoles.[9]

Nowadays, the interest in the optical response of metal nanoparticles goes well beyond its original application related to decorative purposes. The high chemical reactivity of nanoparticles and the sensitivity of the SPR to the environment surrounding nanoparticles is used, for example, to develop gas detectors[22] or to measure the range of plasmonic interaction.[23] Moreover, the near-field generated at the nanoparticle surface at the SPR allowed developing, approximately 40 years ago, the technique of Surface Enhanced Raman Spectroscopy (SERS).[24] This is a powerful technique for chemical and structural characterization of molecules at very low concentrations, i.e. down to the single-molecule detection limit.[25,26] SERS is commonly used for contaminant and drug detection, as well as for biophysic applications.[25] Instead, the far-field scattering observed at the SPR in the case of large nanoparticles (typical size in the 100-200 nm range) is of great interest for improving the response of photodetectors[27] and, more recently, the efficiency of thin film solar cells.[28] In both cases, the improvement of device characteristics is achieved by incorporating these nanoparticles that can provide additional light absorption by promoting light trapping processes.[28] In Chapter 6, we discuss in detail the role of metal nanoparticles in SERS and photovoltaic applications. Furthermore, metal nanoparticles can provide controlled and localized drug delivery in medicine,[1,29] and, in a next future, they will probably represent an alternative and less-invasive approach for diagnosis and treatment of several diseases,[1,30] like cancer: metal nanoparticles can selectively attach to a specific (diseased) cell and may induce its destruction by photothermal effect activated by laser irradiation. Finally, due to the tunability of the spectral position of the resonances, nanoparticles may also benefit optical filtering and data storage.[31]

We earlier mentioned that the optical response of nanoparticles depend on many morphological parameters. As a consequence, experimental techniques that allow achieving a precise control over nanoparticle morphology are required to fabricate nanostructures with a specific optical response. Nowadays, there is a wide range of techniques based on chemical and physical approaches that aim at controlling the largest number of parameters. However, none of them is able to control simultaneously all parameters. In this introduction, we will briefly describe those generally considered more suitable for nanoparticle fabrication.

Probably, the most common chemical route used to synthesize metal nanoparticles in solution (i.e. colloidal nanoparticles) are redox,[32,33] which are chemical reactions in which atoms have their oxidation state changed. Basically, a solution of a compound containing the metal of interest (i.e., AuCl or $AgNO_3$) is added to a solution containing the reducing agent (i.e., sodium citrate, hydroxylamine hydrochloride). The morphology (size and shape) of the synthesized colloidal nanoparticle is mainly determined by the concentration and nature of the reducing agent. This chemical approach is very flexible and nanoparticles with different sizes and shapes, from nanospheres to nanorods (Figures 1.3a and b), as well as from nanocubes to nanostars (Figures 1.3c and d) can be easily obtained. In addition, Figures 1.3e shows how the prepared solution containing colloidal nanorods looks like when their aspect ratio is increased, while Figure 1.3f shows the colour evolution of the solution containing nanospheres when the concentration of the metal, Au, is increased, which demonstrate the strong relation between the optical responses of (in this case) solutions and nanoparticle size, shape and spatial distribution.

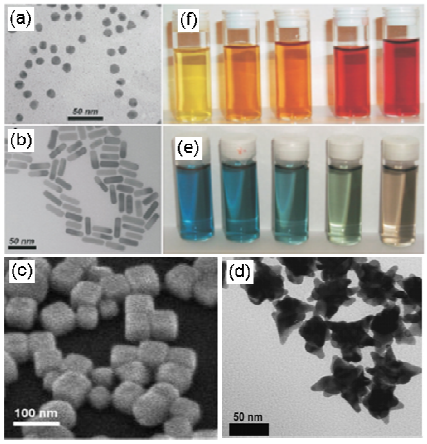

Figure 1.3: Examples of colloidal nanoparticles: (a) nanospheres,[34] (b) nanorods,[34] (c) nanocubes[35] and (d) nanostars.[36] Solutions containing colloidal (e) nanorods and (f) nanospheres with increasing aspect ratio and Au concentration, respectively.[34]

The main drawback of colloidal nanoparticles is that they are synthesized in solution, thus they need to be immobilized to work on solid substrates. Unfortunately, a standard and reliable immobilization method does not exist at all.[25] Generally, nanoparticles are immobilized by submerging a substrate in a solution containing nanoparticles or by pouring a drop of the solution on it, which usually results in a layer of weakly adsorbed and randomly distributed or agglomerated nanoparticles that make them unsuitable for practical applications. This is why, fabrication techniques based on physical methods are usually preferred since they allow fabricating nanoparticles directly supported on a substrate or embedded in a matrix, while maintaining good control over nanoparticle morphology.

Electron beam lithography, which sometimes is considered a mixed technique since it involves a chemical bath step in the nanoparticle fabrication process, is based on projecting an electron beam on a substrate coated with a resin sensitive to the electrons, i.e. Poly(methyl methacrylate) (PMMA).[37] The electron beam modifies the properties of the resin according to a predetermined pattern. Then, the substrate undergoes a chemical bath that removes selectively the resin that was (or, alternatively, not) exposed to the electron beam. Subsequently, the metal is deposited on the patterned substrate to cover the whole surface. Finally, the remaining resin (overcoated by the metal) is removed using a specific solvent. This last step leaves on the substrate only the metal deposited through the patterned resin, resulting in metal nanoparticles with determined size and shape.

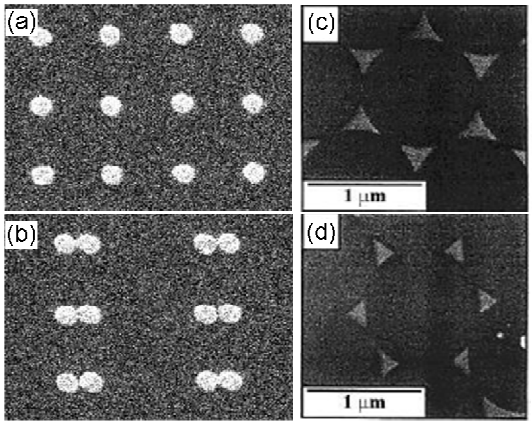

Figure 1.4: (a) and (b) SEM images of Au nanoparticle patterns produced using electron beam lithography. The in-plane nanoparticle diameter is 150 nm, while the interparticle center-to-center distance is (a) 450 nm and (b) 150 nm. Adapted from Rechberger and co-workers.[19] (c) and (d) Field emission scanning electron micrographs of nanoparticle patterns obtained by angle-resolved nanosphere lithography. Adapted from Haynes and co-workers.[38]

Electron beam lithography allows excellent control (of the order of few nm) over nanoparticle size, shape and spatial arrangement (Figures 1.4a and b), but it is a relatively high time-expensive technique and not suitable for working on large areas.[19,37]

A well established alternative technique is nanosphere lithography that allows the deposition of periodic arrays of metal nanoparticles without using electron beams.[38,39] It is based on the deposition of a self-assembled layer of polymer nanospheres with a typical diameter in the 200-600 nm range that acts as a mask. After metal deposition, nanospheres are removed using a solvent such that only the metal deposited on the substrate through the interstices between nanospheres is left on the substrate (Figures 1.4c and d). The characteristics of the final nanoparticle layer are mainly determined by the diameter of the nanospheres and the experimental geometric configuration.[39] This technique leads to the formation of well organized nanoparticles arrays, but the size of the smallest nanoparticles that can be obtained is > 70 nm, such that smaller nanoparticles can be only fabricated by combining nanosphere lithography with, for example, thermal annealing.[39] Finally, techniques based on vapour deposition have shown high versatility for fabrication of nanostructured thin films containing or supporting metal nanoparticles. Thermal evaporation,[39,40] sputtering[41,42,43] and pulsed laser deposition[44,45,46,47] (PLD) are probably the most representative examples of these techniques. The way material vaporization is obtained differs: in the first case an electron beam heats up the material,[48] in the second an ion beam bombards the target promoting material ejection[49] and, finally, in the third case a high power pulsed laser focused on a target leads to ablation and subsequent material ejection.[50,51] However, the way nanoparticles are formed is similar in the three cases. Basically, since a metal on a dielectric surface generally grows following the Volmer-Weber growth mode,[52] nanoparticles are spontaneously formed on the substrate. Nanoparticle size and shape are determined by the amount of deposited material and the structural properties of the substrate, such that arrays of nanoparticles with typical size in the range from a few nm (~ 2 nm) to tens of nm (~ 40 nm) and with typical in-plane circular or elongated shapes can be obtained. In addition, physical vapour deposition techniques are advantageous since they allow working on large areas, in the presence of controlled (vacuum or gas) atmosphere and because they allow depositing both the matrix supporting or embedding nanoparticles and metal nanoparticles in the same environment during the same sequential growth process. Finally, since the dielectric layers can be deposited with very high precision, the position of the nanoparticle layer in a

nanostructured film can be selected arbitrarily according to the specific application of the nanostructure.

Among them, PLD offers a higher versatility[51,53] that is related to its special characteristics, which are described in details in Chapter 2. The basic PLD experimental setup consists of a high power pulsed laser ($\geq 10^7$ W cm^{-2}), a target and a substrate which are usually held in vacuum. Target ablation occurs when the material efficiently absorbs laser light and the laser fluence (the deposited energy per square centimetre) is higher than its ablation threshold. Thus, short laser wavelengths in the ultraviolet spectral region can promote ablation of almost any material. During PLD, congruent ablation of the target can occur, hence even a complex stoichiometry of a multi-component target can be properly transferred to the thin film. If this does not occur the growth can be still performed in a controlled reactive atmosphere (with typical pressure ranging from 10^{-2} mbar to 10 mbar) to compensate the deficiency of a determined element. For example, O_2 can be introduced during deposition of oxide films. Similarly, the introduction of an inert gas (He, Ar) in the chamber can be used to improve the quality of film thickness homogeneity. In addition, the characteristics of the deposit can be controlled through a high number of parameters parameters, like laser fluence, number of pulses on the target and substrate-to-target configuration. Thus, films made of the same materials can show different characteristics depending on the growth conditions. Finally, the high kinetic energy (> 200 eV) of the species produced during target ablation and the large instantaneous flux (~ 10^{16} atoms cm^{-2} s^{-1}) related to the pulsed nature of deposition can promote the growth of films with specific properties showing metastable phases, which are not seen when using conventional techniques. Despite these advantages, PLD also suffer from some drawbacks, the most important is the high directionality of the expanding plasma that, in standard PLD setup configuration, can lead to low homogeneity of the deposit and low control over nanoparticle shape and spatial arrangement.[54]

1.1 Aim and methodology

The *Laser Processing Group* (LPG) of the *Instituto de Óptica* has a large and well established experience in fabricating nanostructured films containing nanoparticles using PLD. They successfully fabricated Au,[46,55,56,57] Fe,[58,59] Bi,[60,61] Ag,[44,47] Cu,[62,63] Co[64] metal nanoparticles as well as semiconductor (Si[65]) nanoparticles generally supported or embedded in amorphous aluminium oxide matrix (a-Al_2O_3). In addition, they also explored the

fabrication of nanostructures containing bi-metallic nanoparticles[66] or made multi-layers containing nanoparticles of different metals.[67,68] Finally, they also showed that a precise control of growth parameters allowed the fabrication of Ag nanocolumns of different aspect ratio oriented perpendicular to the substrate surface.[47,69]

The research carried on by the LPG is mainly addressed to study the effect that the laser and experimental setup parameters (number of laser pulse, laser fluence, target and substrate geometrical configuration) have on the final morphology of nanoparticles and to investigate the relation between the nanoparticle morphology and their optical, vibrational and thermal response. On the one side, they have demonstrated that nanoparticle size increases with the number of laser pulses used to ablate a target, that too high laser fluences can lead to the formation of plasmas containing ions with very high kinetic energies (> 200 eV) that can promote material sputtering from or implantation in the substrate and that the homogeneity of the deposit can be improved by adjusting the position of the substrate with respect to that of the target. On the other side, they have observed that the optical response of nanostructures depend on the nature, size, shape and arrangement of nanoparticles. For example, non-spherical nanoparticles (prolate and oblate spheroids) show an optical response characterized by a longitudinal and transverse mode whose spectral positions depend on the aspect ratio of the nanoobject. Finally, the dependence of vibrational properties on the size and shape of nanoparticles was analyzed as well and, in addition, the interaction between surface plasmons and acoustic vibration was demonstrated.

These findings support that a precise control over nanoparticle morphology is crucial for the fabrication of nanostructured films with specific optical response that are suitable for technological applications. In this thesis we consider the case of nanostructures containing Ag nanoparticles supported on or embedded in a-Al_2O_3 matrix. In particular, we use PLD to fabricate films with different content of Ag and we explore the feasibility of thermal annealing and laser irradiation to improve the control over nanoparticle size, shape and orientation in the substrate plane. In addition, since solid substrates can guarantee more reliable and reproducible SERS spectra and the near-field enhancement and far-field scattering occurring at the SPR can improve the performance of thin film solar cells by promoting light trapping processes, we also studiy the application of the fabricated nanostructures to SERS and as light trapping elements in chalcopyrite solar cells. Finally, we selected Ag among other noble metals mainly because its SPR is well separated from interband transitions and because of its larger scattering cross-section that can play a key role

in applications such as photovoltaics,[9] whereas we selected a-Al_2O_3 matrix since it is a very robust and transparent dielectric that guarantees the proper deposition of metal nanoparticles and because it has been commonly used as host matrix by the LPG, which eases the comparison of our results with those reported in previous works.

Since, in many applications such as SERS, Ag nanoparticles are required to be exposed to the external environment, we initially investigate the evolution of the morphology and optical response of nanoparticles deposited on a thin a-Al_2O_3 layer with the amount of Ag in the films. In particular, we explore in detail three very different but representative cases of nanostructured films containing: small (~ 5 nm) and very dense Ag nanoparticles with almost circular in-plane projected shape; relatively large (~ 20 nm) and dense Ag nanoparticles with circular or elongated in-plane projected shapes; and an almost continuous Ag film, i.e. percolated film. The study of this type of nanostructure configuration allows us to observe that films deteriorate with time. We thus investigate the evolution of their optical response and chemical composition with time and we compare the obtained results with that of nanostructured films in which nanoparticles are covered with a thin layer of a-Al_2O_3. We demonstrate that covered nanostructures show improved stability even for ultrathin covering layers (< 1 nm).

Simultaneously, the comparison of TEM images of uncovered and covered films shows that the deposition of the a-Al_2O_3 covering layer strongly affects nanoparticle morphology. Similar effect was previously observed by Resta and co-workers[46] for Au nanoparticles and associated to the species in the plasma generated upon ablation of ceramic Al_2O_3 target that arrive on the substrates with kinetic energy high enough to promote Au sputtering. We thus verified the observed result by measuring the Ag content in nanostructured films before and after deposition of the covering layer and by modelling sputtering using an approach based on SRIM 2008 software.[46] In order to use in the model an ion kinetic energy distribution resembling that of the ions impinging on Ag nanoparticles, we study the dynamics of the plasma generated upon ablation of ceramic Al_2O_3 target using a Langmuir probe under experimental conditions similar to those used for nanostructured film fabrication.

We then explore the effect of thermal annealing on percolated Ag film to verify its potential to improve our control over nanoparticle size. We performed annealing of percolated Ag films in different environments (air and vacuum) and we observe that, effectively, the dewetting process promoted by the temperature increase leads to the formation of Ag nanoparticles with size well above the one obtained spontaneously as a result of nanoparticle

nucleation and coalescence. In addition, we also demonstrate that, contrary to relatively small nanoparticles (< 50 nm), large nanoparticles (> 100 nm) shows an enhanced contribution of light scattering. Finally, due to Ag tarnishing, we deposit an a-Al_2O_3 layer on annealed films and we observe that conformal growth is achieved. This result goes along with the reduction of Ag sputtering due to the increased nanoparticle size and reduced surface coverage.

In order to achieve better control over nanoparticle shape and orientation, we performed laser irradiation experiments on covered nanostructured films containing coalesced nanoparticles with circular or elongated shapes, the long axis being randomly oriented. In particular, we investigate the effect that irradiation with nanosecond pulses at 800 nm and femtosecond pulses at 400 and 800 nm has on nanoparticle morphology and nanostructure optical response. We observe that nanoparticles are efficiently reshaped by both types of laser pulses with the difference that nanosecond pulses lead to the formation of nanoparticles with in-plane circular shape, while femtosecond pulses lead to in-plane elongated and aligned nanoparticles, which is attributed to the different mechanisms leading to morphology modification.

Finally, we report the results obtained using the fabricated nanostructures as SERS substrates and those related to the first attempts to incorporate our nanostructures in chalcopyrite thin film solar cells to achieve improvement of their performance in terms of plasmonic light trapping processes. First, we describe and discussed the SERS activity as a function of nanoparticle morphology, molecule concentration and molecule-to-nanoparticle surface distance and we conclude the study by verifying if the fabricated films can act as support for creation of nanoparticles superstructures. Second, we report the result obtained by incorporating nanostructured films containing small and large nanoparticles in two different types of chalcopyrite solar cells based on the CuInGaSe and CuInSe compounds. We demonstrate that the incorporation of nanostructured films allows the proper deposition of devices, but without any significant improvement of their characteristics. In this sense, it is important to underline that the performed experiments were the very first attempts and that the incorporation of nanoparticles in chalcopyrite based solar cell can be considered a pioneering work since most of reported works in literature deal with incorporation of nanoparticles in amorphous Si based solar cells.

1.2 Structure

This thesis is structured in seven chapters including this introduction (Chapter 1). Then, Chapter 2 briefly describes the basic principles of pulsed laser deposition and of the technique used to study the kinetic energy distribution of the ions in the laser generated plasma (Langmuir probe, LP) and the corresponding setups. In the case of LP we also report the procedure followed for LP data analysis. We then introduce the characteristics of the substrates and targets used and those of the fabricated nanostructured Ag films. In addition, we also describe the instrumentation used for thermal annealing and the laser irradiation setup. Finally, we introduce the operation mode of the techniques used for compositional, morphological and optical characterization of nanostructures.

Chapter 3 reports on the results obtained in the study of the dynamics of the plasmas generated upon ablation of Ag and ceramic Al_2O_3 targets as a function of laser fluence. We discuss the obtained results in terms of ion current density transient, ion yield, ion kinetic energy distributions and amount of energetic ions.

Chapter 4 deals with the experimental results concerning the morphological and optical characterization of fabricated nanostructured Ag films. We evidence the enhanced chemical reactivity of Ag nanoparticles upon exposure to air and how this affects the optical response of the nanostructures, and we discuss the role of the a-Al_2O_3 covering layer to improve their stability. Subsequently, we analyze the effect the deposition of the covering layer has on nanoparticle morphology and we describe the approach used to model Ag sputtering.

Chapter 5 reports the main results obtained upon thermal annealing of percolated films and irradiation of covered nanostructured Ag films with short and ultrashort laser pulses. We prove that different annealing environments can lead to the formation of nanoparticle with different morphology. In addition, we verify that large nanoparticles obtained by dewetting show improved light scattering compared to the case of small nanoparticles obtained spontaneously as a result of Ag nucleation and coalescence. Concerning laser irradiation experiments, we demonstrate that nanoparticles are efficiently reshaped with both nano and femtosecond laser pulses. The mechanisms responsible for reshaping are also discussed.

Chapter 6 focuses on the SERS activity of fabricated nanostructured Ag films and on their incorporation in chalcopyrite solar cells. We analyze the dependence of SERS activity on nanoparticle size and distribution, on molecule concentration and on the molecule-to-nanoaparticle surface distance. We also discuss the possibility of producing nanoparticles superstructures by combining the fabricated nanostructured films with colloidal Ag

nanoparticles. Finally, we report the very first results obtained by incorporating Ag nanoparticles produced by PLD in chalcopyrite solar cells. We study the effects that the incorporation of nanostructured films containing nanoparticles with different sizes have on the deposition of the absorber layer morphology and on the performance of the devices.

Finally, we summarize the main results obtained and present the main conclusions achieved in this thesis in Chapter 7.

References

(1) http://www.nano.gov/

(2) http://global.britannica.com/

(3) N. Taniguchi, On the Basic Concept of Nanotechnology. in *Proc. Intl. Conf. Prod. Eng.*, Japan Society of Precision Engineering: Tokio, 1974

(4) R. P. Feynman, Journal of Microelectromechanical Systems **1**, 60-66 (1992)

(5) J. M. Albella, In *Laminas Delagads y Recubrimientos.* Edited by J. M. Albella (CSIC, Madrid 2003). Introduction.

(6) S. Link, M. A. El-Sayed, International Reviews in Physical Chemistry **19**, 409-453 (2000) and references therein

(7) G. Binnig, H. Rohrer, IBM Journal of Research and Development **30**, 355-369 (1985)

(8) R. F. Egerton, *Physical Principles of Electron Microscopy*. (Springer US, 2005)

(9) J. Toudert, In *UV-VIS and Photoluminescence Spectroscopy for Nanomaterials characterization*. Edited by Challa S. S. R. Kumar (Springer-Verlag, Berlin, 2013) and references therein

(10) http://www.britishmuseum.org/

(11) I. Freestone, N. Meeks, M. Sax, C. Higgitt, Gold Bulletin **40**, 270-277 (2007)

(12) W. Caseri, Macromolecular Rapid Communications **21**, 705-722 (2000)

(13) http://www.yorkminster.org/home.html

(14) M. Faraday, Phil. Trans. Roy. Soc. Lon. **147**, 145-181 (1857)

(15) G. Mie, Annalen der Physik **330**, 377-455 (1908)

(16) U. Kreibig, M. Volmer, In *Optical Properties of Metal Clusters*. (Springer-Verlag, Berlin, 1995)

(17) K. L. Kelly, E. Coronado, L. L. Zhao, G. C. Schatz, J. Phys. Chem. B **107**, 668-677 (2003)

(18) T. Jensen, L. Kelly, A. Lazarides, G. C. Schatz, Journal of Cluster Science **10**, 295-317 (1999)

(19) W. Rechberger, A. Hohenau, A. Leitner, J. R. Krenn, B. Lamprecht, F. R. Aussenegg, Optics Communications **220**, 137-141 (2003)

(20) J. C. Maxwell-Garnett, Phil. Trans. R. Soc. London A **203**, 385-420 (1904)

(21) T. Yamaguchi, S. Yoshida, A. Kinbara, Thin solid films **21**, 173-187 (1974)

(22) R. Strobel, S. E. Pratsinis, J. Mater. Chem. **17**, 4743-4756 (2007)

(23) M. Kiel, M. Klötzer, S. Mitzscherling, M. Bargheer, Langmuir **28**, 4800-4804 (2012)

(24) M. Fleischmann, P. J. Hendra, A. J. McQuillan, Chem. Phys. Lett **26**, 163-166 (1974)

(25) L. Guerrini, D. Graham, Chem. Soc. Rev. **41**, 7085-7107 (2012) and references therein

(26) M. Moskovits, J. Raman Spectrosc. **36**, 485-496 (2005)

(27) H. R. Stuart, D. G. Hall, Applied Physics Letters **69**, 2327-2329 (1996)

(28) H. A. Atwater, A. Polman, Nature Materials **9**, 205-213 (2010)

(29) J. Qin, Y. S. Jo, J. E. Ihm, D. K. Kim, M. Muhammed, Langmuir **21**, 9346-9351 (2005)

(30) X. Huang, I. H. El-Sayed, W. Qian, M. A. El-sayed, J. Am. Chem. Soc. **128**, 2115-2120 (2006)

(31) P. Zijlstra, J. W. M. Chon, M. Gu, Nature **459**, 410-413 (2009)

(32) J. Turkevich, P. C. Stevenson and J. Hillier, Discuss. Faraday Soc. **11**, 55-75 (1951)

(33) M. V. Cañamares, J. V. Garcia-Ramos, J. D. Gómez-Varga, C. Domingo, S. Sanchez-Cortes, Langmuir **21**, 8546-8553 (2005)

(34) L. M. Liz-Marzán, Materials Today **7**, 26-31 (2004)

(35) P. R. Edwards, D. Sleith, A. W. Wark, R. W. Martin, J. Phys. Chem. C **115**, 14031-14035 (2011)

(36) P. Senthil Kumar, I. Pastoriza-Santos, B. Rodríguez-González, F. Javier García De Abajo, L. M. Liz-Marzán, Nanotechnology **19**, 015606 (2008)

(37) W. Gotschy, K. Vonmetz, A. Leitner, F. R. Aussenegg, App. Phys. B **63**, 381-384 (1996)

(38) C. L. Haynes, A. D. McFarland, M. T. Smith, J. C. Hulteen and R. P. Van Duyne, J. Phys. Chem. B **106**, 1898-1902 (2002)

(39) C. M. Müller, F. C. F. Mornaghini, R. Spolenak, Nanotechnology **19**, 480356 (2008)

(40) I. Tanyeli, H. Nasser, F. Es, A. Bek, R. Turan, Optics Express **21**, A798-A807 (2013)

(41) J. Toudert, D. Babonneau, L. Simonot, S. Camelio and T. Girardeau, Nanotechnology **19**, 125709 (2008)

(42) S. Morawiec, M. J. Mendes, S. Mirabella, F. Simone, F. Priolo, I. Crupi, Nanotechnology **24**, 265601 (2013)

(43) A. Nicolas Filippin, A. Borras, V. J. Rico, F. Frutos, A. R. González-Elipe, Nanotechnology **24**, 045301 (2013)

(44) E. Vogel, W. Kiefer, V. Deckert, D. Zeisel, J. Raman Spectrosc. **29**, 693-702 (1998)

(45) J. P. Barnes, A. K. Petford-Long, R. C. Doole, R. Serna, J. Gonzalo, A. Suárez-García, C. N. Afonso, D. Hole, Nanotechnology **13**, 465-470 (2002)

(46) V. Resta, J. Gonzalo, C. N. Afonso, E. Piscopiello, J. Garca López, J. Appl.Phys.**109**, 094302 (2011)

(47) J. Margueritat, J. Gonzalo, C. N. Afonso, G. Bachelier, A. Mlayah, A. S. Laarakker, D. B. Murray, L. Saviot, Appl. Phys. A **89**, 369-372 (2007)

(48) J. M. Albella, In *Laminas Delagads y Recubrimientos.* Edited by J. M. Albella (CSIC, Madrid 2003). Chapter 4.

(49) J. M. Albella, In *Laminas Delagads y Recubrimientos.* Edited by J. M. Albella (CSIC, Madrid 2003). Chapter 5.

(50) C.N. Afonso, J. Gonzalo, In *Laminas Delagads y Recubrimientos*. Edited by J. M. Albella (CSIC, Madrid 2003). Chapter 8

(51) J. T. Cheung In *Pulsed Laser Deposition of Thin Films*. Edited by D. B. Chrisey, G. K. Hubler (Wiley, New York 1994). Chapter 1

(52) J. S. Horwitz, J. A. Sprague In *Pulsed Laser Deposition of Thin Films*. Edited by D. B. Chrisey, G. K. Hubler (Wiley, New York 1994). Chapter 8

(53) J. Schou, Applied Surface Science **255**, 5191–5198 (2009)

(54) K. L. Saenger In *Pulsed Laser Deposition of Thin Films*. Edited by D. B. Chrisey, G. K. Hubler (Wiley, New York 1994). Chapter 7

(55) J. Gonzalo, A. Perea, D. Babonneau, C. N. Afonso, N. Beer, J. P. Barnes, A. K. Petford-Long, D. E. Hole, P. D. Townsend, Physical Review B **71**, 125420 (2005)

(56) J. P. Barnes, N. Beer, A. K. Petford-Long, A. Suárez-García, R. Serna, D. Hole, M. Weyland, P. A. Midgley, Nanotechnology **16**, 718-723 (2005)

(57) V. Resta, R. J. Peláez, C. N. Afonso, J. Appl. Phys. **115**, 124303 (2014)

(58) N. M. Dempsey, L. Ranno, D. Givord, J. Gonzalo, R. Serna, G. T. Fei, A. K. Petford-Long, R. C. Doole, D. E. Hole, J. Appl. Phys **90**, 6268-6274 (2001)

(59) G. T. Fei, J. P. Barnes, A. K. Petford-Long, R. C. Doole, R. Serna, J. Gonzalo, J. Phys. D: Appl. Phys. **35**, 916-922 (2002)

(60) R. Serna, J. C. G. de Sande, J. M. Ballesteros, C. N. Afonso, J. Appl. Phys. **84**, 4509-4516 (1998)

(61) R. Serna, M. Jiménez De Castro, J. Toudert, E. Haro-Poniatowski, J. García López, Appl. Phys. A **110**, 863-867 (2013)

(62) R. Serna, C. N. Afonso, J. M. Ballesteros, A. Naudon, D. Babonneau, A. K. Petford-Long, Applied Surface Science **138-139**, 1-5 (1999)

(63) R. Del Coso, J. Requejo-Isidro, J. Solis, J. Gonzalo, C. N. Afonso, J. Appl. Phys. **95**, 2755-2762 (2004)

(64) A. N. Dobrynin, D. N. Ievlev, K. Temst, P. Lievens, J. Margueritat, J. Gonzalo, C. N. Afonso, S. Q. Zhou, A. Vantomme, E. Piscopiello, G. Van Tendeloo, Appl. Phys. Lett. **87**, 012501 (2005)

(65) S. Núñez-Sánchez, P. M. Roque, R. Serna, J. G. López, Thin Solid Films **518**, 4644-4647 (2010)

(66) J. Gonzalo, D. Babonneau, C. N. Afonso, J. P. Barnes, J. Appl. Phys. **96**, 5163-5168 (2004)

(67) J. Gonzalo, R. Serna, J. Solís, D. Babonneau, C. N. Afonso, J. Phys.: Condens. Matter **15**, S3001-S3010 (2003)

(68) J. Margueritat, J. Gonzalo, C. N. Afonso, U. Hörmann, G. Van Tendeloo, A. Mlayah, D. B. Murray, L. Saviot, Y. Zhou, M. H. Hong, B. S. Luk'yanchuk, Nanotechnology **19**, 375701 (2008)

(69) J. Margueritat, J. Gonzalo, C. N. Afonso, M. I. Ortiz and C. Ballesteros, Appl. Phys. Lett. **88,** 093107 (2006)

Chapter 2
Experimental Techniques

In this chapter we describe the fabrication and characterization experimental techniques used in this thesis. We first introduce the pulsed laser deposition technique, its working principles, advantages and drawbacks and we describe the pulsed laser deposition experimental setup used. Then, we introduce the Langmuir probe technique, which has been used to study the dynamics of the laser generated plasmas. The chapter continues with the description of the basic characteristics of the fabricated films and with the introduction to the post-growth techniques used to modify film structure and optical properties. Finally, we briefly summarize the compositional, morphological and optical characterization techniques considered.

2.1 PULSED LASER DEPOSITION

2.1.1 Basic principles

Pulsed laser deposition (PLD) is a physical deposition technique based on the interaction of light with matter. Typically, the beam of a high power pulsed laser is focussed on the surface of a material we want to produce in a thin-film configuration (the target) with enough power density to promote its ablation (10^6 - 10^9 W cm^{-2}). The ablated material that expands from the target surface is then condensed on a substrate properly placed in the vicinity of the target site to promote material deposition and, thus, thin film growth.[1] Figure 2.1 shows a schematic view of the PLD process.

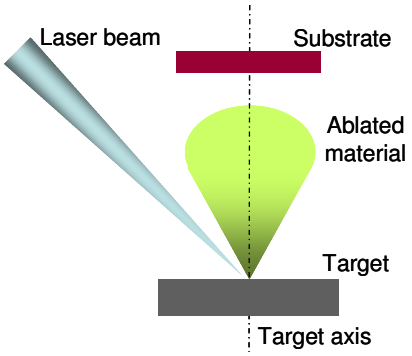

Figure 2.1: Scheme of PLD process.

The experimental setup needed for PLD is thus quite simple since, apart from the laser, it basically requires a target and a substrate and, most of the times, a vacuum chamber to guarantee the deposition of high quality films. Despite this experimental simplicity, the processes that lead to material ablation are very complex and involve different physical and chemical mechanisms. In addition, the efficiency of material ablation strongly depends on the laser parameters (wavelength, pulse duration and power density) and the target optical and thermal properties (reflectivity, absorption coefficient, specific heat and thermal conductivity).

The basic condition that must be satisfied for material ablation is that the heat absorbed per unit volume by the material has to be larger than the latent heat of vaporization of the solid.[2] In the case of laser with a pulse duration of tens of nanoseconds, as the one used in this thesis, the power density of the laser is generally fixed in the range from 10^7 to 10^9 W cm^{-2} to achieve material ablation. Under these conditions, the light absorption mechanisms that lead to material ablation and ejection can be thermal or based on dielectric breakdown.[1,2] The first

mechanism comes into play when moderate power densities are used ($\leq 10^7$ W cm^{-2}). The energy of the laser is absorbed by electrons, which get excited (through linear excitation processes) and, after few picoseconds, relax by efficiently transferring the excitation to the lattice of the irradiated material via electron-phonon coupling. This transfer process leads to an increase of temperature that may be high enough to promote material melting and subsequent evaporation. In this condition the material ejected usually consist of molecules and neutrals.[2]

The way the excitation induced by the laser pulse is transferred to the material lattice is thus determined by heat conduction and thermal diffusion processes[2] and can be classified in terms of the optical absorption depth and the thermal diffusion length.[1,2] The first parameter is defined as $1/\alpha$, where $\alpha = 4\pi k/\lambda$ is the optical absorption coefficient, λ is the wavelength of the laser and k is the extinction coefficient of the target, whereas the second is defined as $L_t = 2\sqrt{D \cdot \tau}$, where D is the thermal diffusion constant and τ the laser-target interaction time (i.e., pulse duration).[1,2,3] The optical absorption depth represents how much the radiation can penetrate in a material before being absorbed completely, while L_t corresponds to the thickness of material affected by thermal heating. If $L_t << 1/\alpha$, the thickness of the target that experiences the temperature increase promoted by the laser pulse is determined by $1/\alpha$, irrespective of pulse duration and thermal conductivity. This situation occurs, for example, in polymers and dielectrics for which D and α are small.[2] Under these conditions, congruent ablation is achieved and target stoichiometry is preserved during mass transfer from the target to the thin film.[1,3]

Instead, if $L_t >> 1/\alpha$. the thickness of irradiated material affected by the temperature increase is determined by the laser pulse duration. For example, this generally occurs in the case of metals for which $1/\alpha \sim 10$ nm, while $L_t \sim 1$ μm.[2] Under this condition material ablation resembles that of thermal evaporation and the stoichiometry of the target is not preserved in the gas phase.[4,5]

When large power densities ($> 10^7$ W cm^{-2}) are used, dielectric breakdown starts to be relevant in the light absorption process.[2] The high electric field ($\sim 10^5$ V cm^{-1}) associated to these power densities can promote electronic excitation via non-linear absorption processes even in transparent dielectric materials. Then, light absorption further increases via electron avalanche process. When electrons relax, the energy transferred to the lattice of the irradiated material leads to a drastic increase of the material surface temperature, which turns the lattice into an unstable phase that leads to congruent ablation of material.[2] This ejection mechanism

is the one that allows to ablate insulating materials with energy band gap higher than photon energy, such as Al_2O_3.[2] In this case, the ablation process is independent on the $1/\alpha$ and D parameters and the ejected material includes neutrals, excited atoms, ions and electrons.[2]

Apart from the power density, the laser wavelength plays an important role in the ablation mechanism. Since high energy photons are efficiently absorbed by most of materials, N-UV lasers are usually preferred since they can promote efficient coupling of the laser light into the surface region (i.e. small $1/\alpha$ values). In addition, short wavelengths favour congruent evaporation and, simultaneously, reduce subsurface boiling effects (see 2.1.2).[1,3,6]

Besides the mechanisms that induce material ablation, it is important to spend few words on the expansion dynamic of the ejected species, since it basically determines the structural properties of the deposit. After ablation, the ejected species forms a very dense gas cloud just above the target surface in correspondence with the laser impact region that progressively expands from the target surface as a result of pressure gradient between the ablated material and the environment.[3,4] Simultaneously, since the laser pulse lasts longer than the time needed for material ejection, the ejected species can interact with laser photons by absorbing them, which leads to molecule dissociation and neutral ionization.[3,4] In general, ions are considered to be generated via multiphoton ionization processes.[7] Subsequently, the increase of the number of free electrons is expected to further increase light absorption and ionization via electron-ion inverse Bremsstrahlung.[7] The progressive increase of the degree of ionization promoted by the mentioned processes converts the initially poorly ionized ablated material in a hot and dense plasma,[7,8,9,10] consisting of neutrals, ions, electrons and atoms in excited states. The degree of ionization, as well as its expansion dynamic, depends on the laser parameters and electronic properties of the ejected species (ionization potential, energy of the atomic/ionic excited states).[8,7,11] In addition, as a result of gas-dynamics collisions, pressure gradient and plasma potential acceleration, the plasma expands perpendicular to the target surface[8,7] with an angular distribution that can be described in terms of a $cos^n\theta$ distribution, where θ is the angle measured from the target normal and n is in the 4-30 range for the laser fluences typically used in PLD.[12,13,14,15] The exact value of n, which determines the degree of narrowing of the angular distribution, depends on the experimental parameters as, for example, the laser fluence and spot size and shape.[13,14]

This brief introduction evidences that efficient material ablation is achieved whenever the laser parameters are properly adjusted to the target properties. Since laser parameters can

be easily modified, one of the most outstanding features of PLD relates to its intrinsic flexibility that warrants working with almost no restriction on the material to be ablated. Despite the fact that laser ablation was a quite well established method for material processing already in the 1960s,[1] it was only in the late 1980s that its suitability for fabrication of thin film was demonstrated by Dijkkamp and co-workers,[16] when they successfully deposited high Tc superconducting thin films with complex stoichiometry. From that moment, PLD has been extended to the deposition of a wide range of materials like oxides[17], nitrides[18,19] and metallic films.[20] More recently, the precise control of film growth parameters (i.e., deposition rate in the 10^{-3} nm pulse^{-1} range) and the development of complex deposition strategies have led to the fabrication of artificially designed nanostructures like multilayers,[21,22] rare-earth doped nanostructures,[23] film containing metal NPs[24] or more complex structures as nanocolumns[25] and nanowires.[26]

Apart from its flexibility, a feature that distinguishes PLD from conventional physical deposition techniques is the kinetic energy of the species involved in the plasma. Since laser ablation is, basically, an explosive process, the generated species can acquire very high kinetic energy values, which strongly depends on the laser parameters (fluence and wavelength) and the electronic properties of the ejected species.[7,11,20,27] In the case of metals, the kinetic energy distribution of neutrals generally peaks around very low values, $\leq$ 10 eV, while that of ions usually peaks at higher values, close to 100 eV.[7,27] In addition, the distribution for ions is typically broader than that of neutrals, with a tail that can extend to energies as high as 1000 eV and a fraction of energetic ions (kinetic energy, $E_k \geq 200$ eV) that increases with the laser fluence.[7,11,27] This will be discussed in more detail in Chapter 3 where we study the dynamics of the plasma upon ablation of Ag and ceramic aluminium oxide (from now on Al_2O_3) targets in terms of their ion kinetic energy distribution.

The high kinetic energy of the species together with the large instantaneous flux related to the pulsed nature of deposition are considered essential to achieve the growth of films with specific properties (high density) or showing metastable phases, that are generally not achievable with conventional techniques.[2,3,4,22] In addition, energetic species can promote the appearance of additional effects at the substrate level such as mixing or alloying at the interface,[20,28] subsurface implantation[27,29,30] or sputtering of deposited species.[29,31,32,33] The first effect occurs when the arriving species have enough energy to penetrate a few nm's in the already deposited material, which leads to alloying with the previously deposited material (Figure 2.2a). Implantation is similar, but the impinging atoms form an additional subsurface

layer without mixing with the host (Figure 2.2b) whose in-depth position and characteristics depend on both the kinetic energy of the arriving species and the amount of deposited material. Finally, sputtering takes place when the energy of the arriving species is high enough to promote material removal (Figure 2.2c). The effect of sputtering will be evidenced and discussed in Chapter 4 in the case of the deposition of a thin amorphous aluminium oxide (a-Al_2O_3) layer on a single-layer of Ag nanoparticles.[34]

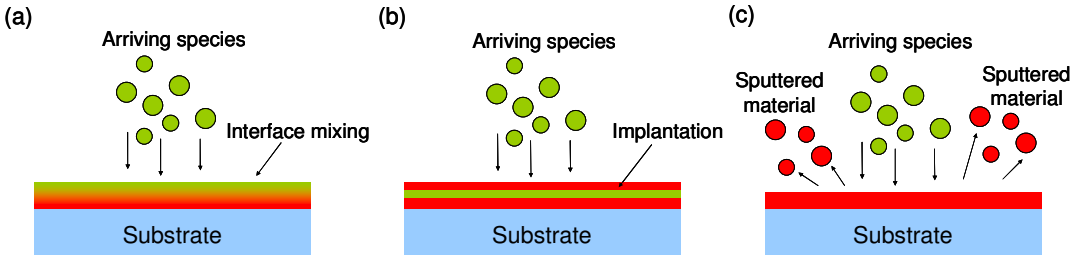

Figure 2.2: Schematic representation of (a) interface mixing, (b) implantation and (c) sputtering processes.

Finally, an additional characteristic of PLD that remarks its versatility is its compatibility with a controlled atmosphere, since the energy source (the laser) is outside the deposition chamber.[3,4,35] The introduction of a background gas in the vacuum chamber is used to regulate the energy of the ablated species and allows improving the quality of the films grown by PLD. The presence of a gas in the growth environment changes completely the expansion dynamics of the plasma making it more complex. Basically, the collision/interaction between the ejected atoms and ions and the molecules of the introduced gas has two main effects: it slows down the plasma and broadens its angular distribution.[4,12,35] In particular, the presence of an inert background gas (He or Ar) introduced during film growth at a proper pressure, that can range from 10^{-2} mbar to 10 mbar, can be beneficial to better control mixing, implantation and sputtering effect and, in addition, to improve deposit homogeneity,[14,29] while of a reactive gas (O_2, N_2) is introduced in the chamber, the species in the plasma can react with the gas molecules. This approach allows to achieve proper replication of target stoichiometry in a film and/or to promote compounds formation in the case of complex nitrides[19,36] and oxides.[26,37,39] However, one has to be careful with the gas pressure, since too high values can drastically slow down the plasma with detrimental consequences on the material deposition process,[4] i.e. it reduces the deposition rate and worsen the adhesion of the species on the substrate. In this thesis we did not work with a background gas, since Ag is deposited successfully in vacuum with no evidence of subsurface

implantation (see Chapter 4), whereas the stoichiometry of the Al_2O_3 target is properly transferred to the film in vacuum, which is likely due to the similar atomic masses of the elements constituting the target and to the used power density ($\approx 10^8$ W cm^{-2}) and short laser wavelength (193 nm) that promotes congruent ablation.

2.1.2 Practical strategies to overcome PLD drawbacks

Pulsed laser deposition suffers from technical drawbacks that may affect film quality, especially in its basic configuration. The small laser spot size (~ 1-2 mm^{-2}) at the target surface and the narrow plasma angular distribution leads to deposition of films with reduced surface coverage and low thickness homogeneity. In general, the area covered is of few cm^2 while the thickness profile follows typically a $\cos^{n+3}(\theta)$ distribution.[12]

Moreover, PLD promotes the production of particulates with macroscopic size (~1 μm) that are ejected during ablation process.[1,3] The mechanisms that can lead to droplet formation and ejection are mainly three, namely: subsurface boiling, recoil ejection, and exfoliation.[1,3] The first two are related to the thermal properties of the material. Subsurface boiling occurs when the time required to transform laser energy into heat is shorter than the one that is needed to evaporate a surface layer with a thickness of the order of optical absorption depth. The subsurface layer is thus superheated before the surface itself has reached the vapour phase. This mechanism is more likely to take place in materials with low melting temperatures and high thermal conductivities.[1,3] Recoil ejection is similar to subsurface boiling but, in this case, the force that promotes expulsion of liquid droplets comes from above the melted layer in a form of recoil pressure exerted by the shock-wave of the expanding plasma.[1,3] Finally, exfoliation is related to an increase of surface roughening promoted by repeated melt-freeze cycles of the irradiated material. This mechanism is common upon ablation of sintered ceramics targets.[1,3] In the present work, particulates have been observed only in the case of deposition of almost continuous Ag films (Figure 2.3), whereas no evidence of exfoliation effect upon ablation of Al_2O_3 target was detected.

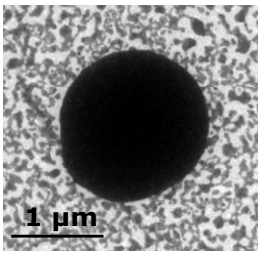

Figure 2.3: Plan-view TEM image of an Ag particulate observed on the surface of an Ag film deposited by PLD.

Many practical strategies have been proposed to overcome these drawbacks of PLD. The use of a background gas, low laser fluences and short laser wavelengths can improve the film homogeneity/quality while reducing the appearance of particulates.[1,3,13,14] In addition, some strategies related to the configuration of the experimental setup and some practical precautions can be beneficial as well. Here we describe briefly some of the most common used strategies. The use of rotating targets allows exploiting a larger surface of the target, while limiting the formation of a deep ablation crater that would deviate the plasma from its expansion trajectory (parallel to the target normal) and lead to the ejection of droplets as a result of exfoliation. In this sense, it is also wise to periodically recondition the target surface to prevent roughness increase. Moreover, the film thickness homogeneity as well as the area covered by the deposit can be improved by rotating the substrate and modifying the PLD geometric configuration. Instead of placing the substrate in front of the target (Figure 2.1), alternative geometries are shifting the axis of the substrate holder with respect to that of the target, off-axis configuration (Figure 2.4a), or tilting the substrate to lie perpendicular to the target surface, tilted configuration (Figure 2.4b). Both of them allow increasing the area covered by the deposit with a better homogeneity.[37,38,39]

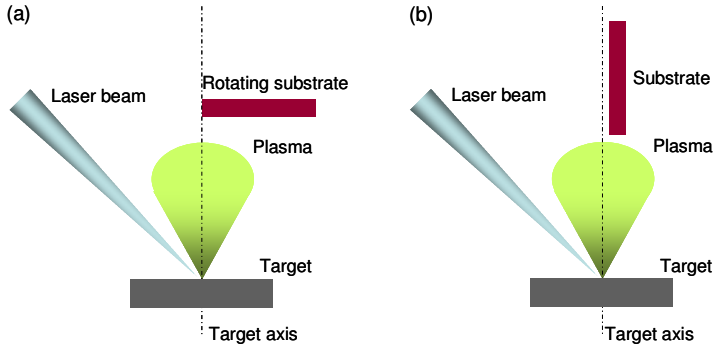

Figure 2.4: Sketch of PLD alternative geometry configurations. In (a) a rotating substrate is placed with its axis shifted from that of the target. In (b) the substrate is placed perpendicular to the target surface.

Off-axis configuration decreases as well the number of particulates arriving to the substrate as their angular spread is smaller than that of the atomic or molecular species inside the plasma. Finally, a larger target to substrate distance leads to larger surface coverage as the lateral extension of the plasma increases with the target to substrate distance.[12] However, the amount of species arriving per pulse to the substrate follows, approximately, an inverse square relationship with the distance ($\sim 1/d^2$), thus a too high distance leads to a substantial

decrease of deposition rate and, possibly, to a film with compositional properties different from the expected ones.

We can thus conclude that the intrinsic flexibility and versatility of PLD together with the introduction of these experimental approaches allow proper deposition of thin films, particularly on small areas. In this sense, one of the major challenges still open within PLD community is its up-scaling. Many efforts have been made in the past years to overcome this limitation as it is evidenced by experimental approaches based on dual-beam laser ablation, plasma and ion beam-assisted deposition,[35] laser beam shaping, homogenization and steering,[22,40] as well as on the incorporation of novel high-power, high repetition rate lasers for record-speed target ablation and target and substrate manipulation.[22,40] Recently, the combination of these strategies led to proper deposition of several complex thin-films like piezoelectrics and transparent conductors[22] and of SiC films[40] on areas in the 24-300 cm^2 range.

2.1.3 Experimental setup

The experimental PLD setup used in the present work is based on an ArF excimer laser (Lambda Physik LPX 200) operating at 193 nm with a pulse duration of 20 ns. Briefly, the operation mode of the laser is based on an electrical discharge that promotes the formation of excimer (acronym for "Excited Dimer") molecules in an unstable excited state.[41] This molecule can dissociate rapidly to a ground repulsive state through the emission of a photon. The pulse duration is determined by the characteristics of the laser discharge design,[41] while the wavelength is determined by the energy gap between the ground and excited state of the excimer molecule. Different inert gas halides (F_2, ArF, KrCl, KrF, XeCl, XeF) lead to different output wavelengths (157, 193, 222, 248, 308, 351).[41]

The laser beam shape is rectangular (25 × 10 mm^2) and its energy distribution corresponds to a *top-hat* distribution along the horizontal (long) axis and near-Gaussian along the vertical (short) one. The beam is focussed, through a convex lens, on the target surface with an angle of incidence of 45º with respect the target normal. As a result the shape of the laser spot at the target surface is not rectangular but it consists of a main central spot, with almost elliptical shape, and of two secondary asymmetric spots at the sides (Figure 2.5), i.e. the 0^{th} and 1^{st} orders of a diffraction pattern of a rectangular aperture.

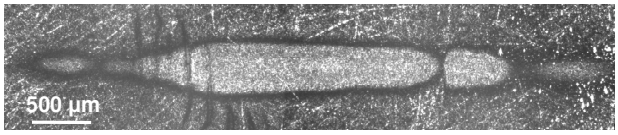

Figure 2.5: Footprint left by 20 laser pulses on the Ag target placed on the target holder. The beam is focussed on the target surface with an angle of incidence of 45º with respect the target normal. Both the main and the secondary spots are observed.

The observed asymmetry in Figure 2.5 is most likely related to the angle of incidence of the laser beam (45º with respect the target normal). The ablation tracks, i.e. the crater, left by a few laser pulses (15-20) on the Ag target has been used to estimate the spot area at the target site, resulting in 0.015 ± 0.002 cm^2, the error being related to the uncertainty in define the ablation track edges, i.e. dark contrast around the footprint in Figure 2.5. The energy of the laser was adjusted before each film deposition experiment to keep the laser fluence in the 2-2.5 J cm^{-2} range inside the chamber at the target surface position. This working fluence was found to minimize the generation of energetic species while keeping the deposition rate at reasonable values.

The scheme of the experimental setup used is shown in Figure 2.6. Samples are grown in a stainless steel vacuum chamber that is evacuated down to a pressure of 2×10^{-7} mbar before each growth experiment by a vacuum system consisting of a turbo molecular pump coupled to a rotary one.

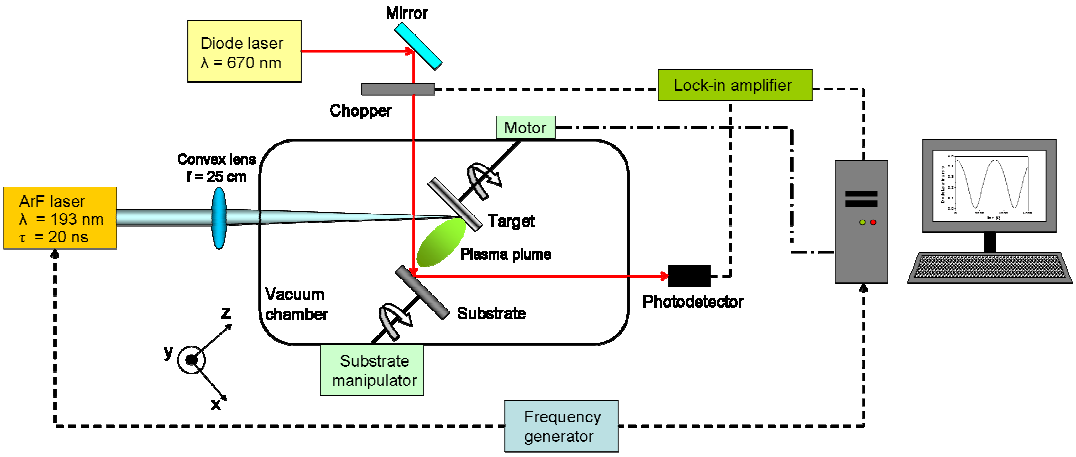

Figure 2.6: Scheme of PLD setup used in the present work.

The target holder, placed inside the chamber, allows hosting up to four targets simultaneously, which allows the fabrication of multilayered films. A software, designed

within the LPG, allows controlling the stepper motor for target switching and the frequency generator that is necessary to synchronize laser shooting with target change. This makes possible to remote-control the growth sequence. The target holder keeps the targets rotating during film growth to prevent fast formation of a deep ablation crater. The substrate holder is placed opposite to the target holder. It consists of a vacuum positioning device (Thermionics, EC series) coupled to a sample heater (Thermionics, SHQ-2D), which allows moving the substrate along the *x*, *y* and *z* directions and performing annealing in vacuum. In addition, it is also motorized to keep the substrate rotating during the growth to improve film thickness homogeneity.

The *x* and *y* cross-roller guides move the substrate laterally with respect its on-axis position ($x = y = 0$) up to ±12.7 mm, while the *z* guide rod moves the substrate in forward (backward) direction from 0 up to 50.8 mm. The substrate was moved 10 mm away from its central position (off-axis configuration, Figure 2.4a) and the target to substrate surface distance was kept at z = 38 mm for film growth, which allowed the fabrication of homogeneous samples with a typical size of 20×20 mm^2. Figure 2.7a shows two dielectric thin films grown on Si rotating substrates either in off- and on-axis PLD configurations. The film on the left shows a nice homogenous colour over its entire surface, while the film on the right shows typical rings related to the thickness variation of the deposit along the surface.

The sample heater (Figure 2.7b) consists of an infrared quartz bulb protected by a quartz glass that can operate at a maximum current of 7.5 A at a voltage of 120 V, in vacuum. The maximum nominal temperature in these conditions is 1000ºC.

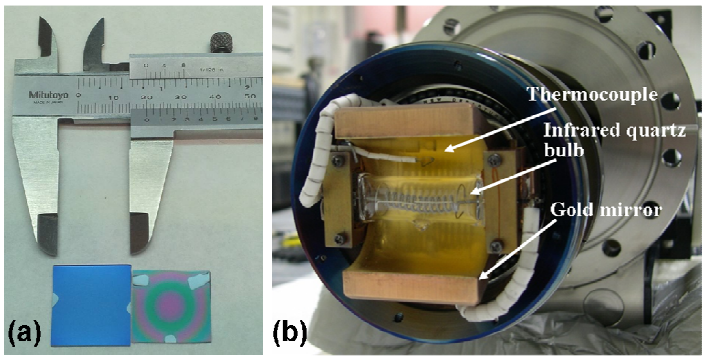

Figure 2.7: (a) Dielectric thin films grown on Si using (left) off- and (right) on-axis PLD configurations. (b) Image of the sample heater that is placed inside the substrate positioning device.

The unit is mounted in front of a parabolic gold mirror to reduce heat losses while a thermocouple placed close to the filament allows *in-situ* control of the temperature. The sample heater has been used to perform thermal treatments in vacuum in the 200-400ºC range with the aim to *in-situ* anneal percolated films.

In order to control the growth process, the PLD system includes an *in-situ* reflectometry setup that allows monitoring the film deposition. It consists of a diode laser (λ=670 nm, s-polarized) that is focussed on the substrate surface (Si is preferred due to the better reflectivity contrast) at an angle of incidence of 45º with respect the substrate normal. The reflected beam is then focussed on a photodetector whose signal is recorded by the computer. The variation of reflectivity signal is related to the interference process between the light wave reflected at the film surface/vacuum interface and the multiple waves rising from partial reflection of the transmitted waves at the film interface(s), i.e. film/Si interface. The degree of constructive or destructive interference depends on the phase difference between the reflected beams which, in turns, depend on the optical properties (refractive index and extinction coefficient) and the thickness of the layers that compose the film.[42,43] Figure 2.8 shows the reflectivity variation during growth of (a) amorphous aluminium oxide (a-Al_2O_3) and (b) Ag calibration films* on Si substrate as a function of the number of pulses used to ablate the targets. Reflectivity curves obtained by modelling the reflectivity of Ag and a-Al_2O_3 films as a function of film thickness with the VASE software (see 2.6.1) are included in the figure.[44]

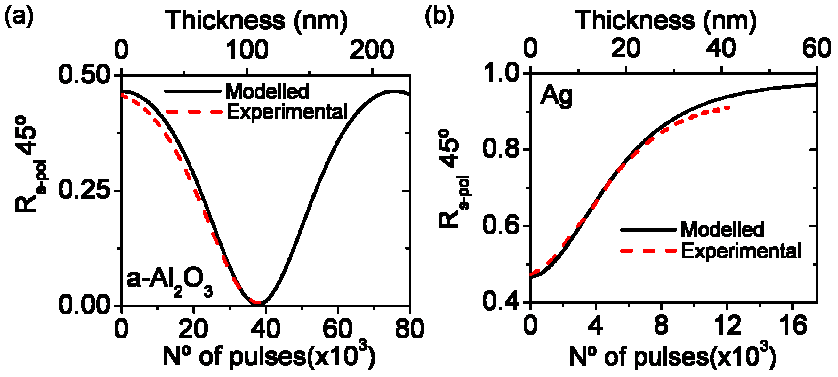

Figure 2.8: Experimental reflectivity signal (red dashed curves) obtained during growth of (a) a-Al_2O_3 and (b) Ag calibration films on Si substrate as a function of the number of pulses used to ablate the targets. The superimposed solid black curves are obtained by modelling with the VASE software (see 2.6.1) the reflectivity of the same films as a function of film thickness, obtained with the beam impinging at 45º with respect the substrate surface.

* With the term *calibration film* we refer to the samples grown before any experiment of this thesis to verify the reliability of the growth conditions.

In the first case (Figure 2.8a) the reflected intensity decreases until it reaches zero and then increase again to recover the original value. This optical behaviour, consisting of a series of consecutive maxima and minima, is typical of transparent materials grown on absorbing substrates.[43] On the contrary, in the case of Ag (Figure 2.8b) the signal increases up to saturation value showing no maxima and minima sequence. Ag efficiently absorbs laser light so interference only occurs while the film thickness is smaller than the optical absorption depth. For larger thicknesses, reflectivity saturation is reached and its value only depends on the optical properties of the Ag.[43] The direct correlation between reflectivity and the number of pulses/film thickness makes reflectometry a very powerful technique to estimate the material deposition rate.

2.1.4 Targets, substrates and fabricated nanostructures

This section briefly describes the main characteristics of the used targets and substrates, as well as of the nanostructured films fabricated in this thesis by PLD. The targets used to produce the nanostructured films investigated in this thesis were high purity silver (≥99.99%) and sintered ceramic aluminium oxide. The laser repetition rates used for target ablation were 5 and 20 Hz for Ag and Al_2O_3, respectively. Under these conditions and using the PLD setup described earlier, the deposition rates were in the 3×10^{-3}-4×10^{-3} nm pulse^{-1} range for both targets, which hints at the high precision we could achieve during film growth. The exposure of the targets to repeated laser ablation processes leads the formation of ring-shaped tracks on their surfaces, whose depth progressively increases. Thus, we periodically polished targets surfaces with sandpaper to preserve their smoothness and to prevent plasma deviation from the normal to the target surface. After polishing and before each growth, we took care of removing any contaminant from the surface of the targets by performing a pre-ablation cleaning cycle consisting of tens of laser pulses.

Samples were grown on different substrates. Commercial [100] monocrystalline Silicon ~0.7 mm thick was mainly used for morphological characterization of films, which included transmission (TEM) and scanning (SEM) electron microscopy. In the case of TEM analysis, samples grown on Si underwent mechanical polishing and ion milling reduction process to make them suitable for plan-view and cross section images. Carbon-coated mica (C-mica) substrates were only used for TEM analysis. In this case the samples were prepared by floating off the film on C from the mica substrate in deionised water and picking it up on Cu grids. Glass, from microscope slides with 1.2 mm thick, and UV grade fused silica 0.5 mm

thick were used for optical characterization of the samples, namely transmission and reflection measurements. Finally, Mo-coated soda lime glass substrates were used for incorporation of the grown nanostructured films in solar cells. These substrates were prepared in the Helmholtz-Zentrum Berlin via sputtering, the Mo being ~1 μm thick.

The above described PLD setup and growth conditions have been used to fabricate nanostructured films consisting of a layer of Ag nanoparticles deposited on or embedded in an a-Al_2O_3 layer at room temperature. Most of the produced films were obtained in a single step process by alternate ablation of the two targets. As it will be described in more detail in Chapter 4, the aluminium oxide grows following the Frank-van-der-Merwe mode, forming layers with amorphous structure.[45] Instead, Ag follows the Volmer-Weber mode.[45] Polycrystalline nanoparticles are thus formed spontaneously until the percolation limit is reached. Once percolation threshold is passed, a continuous Ag film is progressively formed. Below percolation, nanoparticle shape and spatial distribution can not be arbitrarily controlled. The formed nanoparticles usually show circular or elongated in-plane projected shapes with the long axis randomly orientated. The amount of deposited Ag, which determines both the nanoparticle size and distribution, and the thickness of the a-Al_2O_3 layers are controlled by the number of pulses used to ablate the targets. Thus, this number is modified according to the purpose of each experiment.

2.2 LANGMUIR PROBE

2.2.1 Basic principles

The extended use of PLD for fabrication of thin films with specific characteristics and the strong correlation between plasma properties and film quality has led to the application of different plasma diagnostic techniques to study the plasma features that may affect the film growth process and its final properties.[46] In this work we use Langmuir Probe (LP) to study the plasma dynamics. LP is an electrical probe widely used for plasma diagnostic that is based on a small biased metallic electrode placed inside the plasma whose signal can be recorded, for example, by an oscilloscope.[47,48,49] The probe is biased with respect to a second electrode, usually the vacuum chamber at ground potential. Depending on the applied bias, positive or negative, LP collects electrons or positively charged ions, respectively. This allows obtaining information regarding the electron and ion dynamics within the plasma.[7,11]

Despite this apparently simplicity, the theory needed to explain the current-voltage (I-V) curve of the probe inside the plasma is complex.[47,49] Qualitatively, the I-V curve can be

separated in three main regions according to the voltage applied to the probe. The *ion saturation region* corresponds to the case when the probe is biased negatively with respect to the plasma potential and only positive ions are collected on its surface. The opposite situation is the *electron saturation region*. This condition is reached when the LP is positively biased and only electrons are collected. Finally, the intermediate region, known as *electron retarding region*, occurs when the probe is biased at a voltage slightly smaller than the plasma potential and only particles with enough energy to overcome the potential barrier are collected.[47,49]

In this thesis, we have worked in the *ion saturation regime* to study the dynamics of positive ions, since they represent the mot energetic species in the plasmas produced by laser ablation. They can have enough energy to promote sputtering, implantation and mixing effects at the substrate level during film growth,[27,33,34] particularly when working at fluences well above ablation threshold.

2.2.2 Experimental setup

The experimental LP setup used is shown in Figure 2.9a. As in the case of PLD, ablation of the target takes place in a stainless steel vacuum chamber that is evacuated down to a pressure of 1×10^{-5} mbar during the experiments. No substrate is present in this case and the LP is placed in front of the target at a distance of 40 mm from its surface. This position was chosen in order to intercept the central region of the plasma where most energetic species are expected to be present.

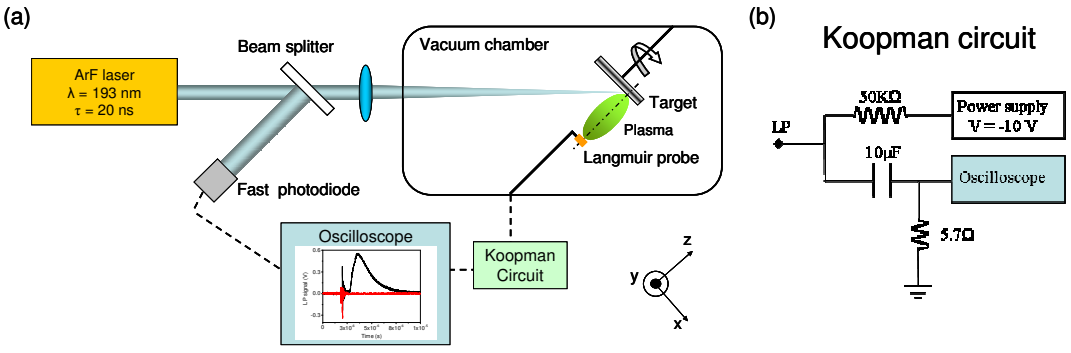

Figure 2.9: (a) Scheme of the LP experimental setup. (b) Electronic elements and connections of the Koopman circuit.

We used as LP a square planar Cu sheet with an area of ≈ 1.07 mm^2 that was located perpendicular to the plasma flow. Its rear side and the circuit connections inside the vacuum

chamber were electrically insulated to ensure that the signal collected comes only from the Cu sheet side exposed to the plasma species flux. The probe was biased at -10 V with respect to the grounded vacuum chamber that was reported to be high enough to guarantee that only positively charged ions are collected at the probe surface.[49] It is important to bear in mind that the voltage generated by the probe does not affect the ion dynamics as the outer electrons of the plasma redistribute and efficiently shield the plasma from any external or internal applied potential, an effect which is known as Debye shielding.[46,49] The detected LP signal is injected into a Koopman circuit (Figure 2.9b) consisting of a high pass filter with R = 5.7 Ω and C = 10 μF to reduce the signal-to-noise ratio[47] and it is finally recorded by a digital oscilloscope triggered by a fast photodiode that collects a small fraction of the laser pulse.

The laser used to ablate the targets is an ArF excimer laser operating at 193 nm with pulse duration of 20 ns. The laser beam is focussed with a convex lens on the target surface with an angle of incidence of 45º with respect to the target normal. Before each experiment, a fresh region of the target is exposed to tens of laser pulses in order to remove surface contaminants. Since contaminants result in an additional and faster peak, its disappearance proves the surface is clean. Figure 2.10a shows the LP signal obtained upon ablation of a fresh region of a metallic target (Cu) after 3, 5, 10 and 19 pulses. The peak observed at very short times (< 1 μs) is the one corresponding to contaminant. Its intensity decreases along with the number of pulses due to the progressive removal of the contaminant. Figure 2.10b shows the typical LP transient signal obtained upon ablation of Ag at 9 J cm^{-2} and the trigger signal coming from the fast photodiode. We use this signal to define the temporal origin of the transients.[48]

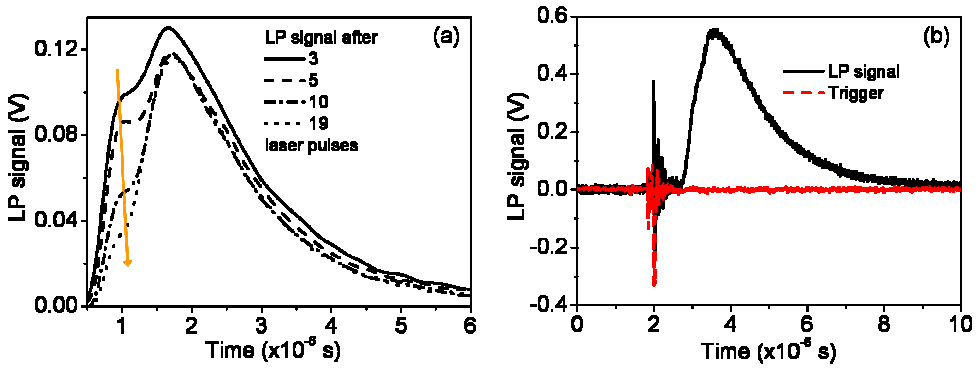

Figure 2.10: (a) LP transient signal obtained upon ablation of a fresh region of a metallic target (Cu) after 3, 5, 10 and 19 pulses. The peak at times < 1 μs is associated to contaminants; its trends with the number of pulses is highlighted by the arrow. (b) LP transient and trigger signal upon ablation of Ag target at 9 J cm^{-2}, once contaminants have been removed.

2.2.3 Data processing

We have used LP to analyse the dynamics of the plasma generated upon ablation of Ag and Al_2O_3, which are the targets used for film growth. In particular, we studied the effect of laser fluence from plasma threshold (< 1 J cm^{-2}) up to 15 J cm^{-2} on the ion yield and ion kinetic energy distribution, to evidence any relevant feature that may affect film growth.

The ion yield, that is the total number of ions arriving to the probe per cm^2 per pulse, is determined by introducing the approximation that the ions that reach the probe are single-ionized.[11,27,49] With this approximation, the ion current density transient plot in Figure 2.11a is calculated as:[11]

$$J(t) = \frac{LP(t)}{R \cdot S \cdot e} \tag{2.1}$$

where *LP(t)* is the recorded transient in volts (Figure 2.10), *R* the circuit resistance, *S* the probe surface and *e* the elemental charge 1.6×10^{-19} C.[27] The ion yield is finally obtained by time integrating *J(t)*.[11]

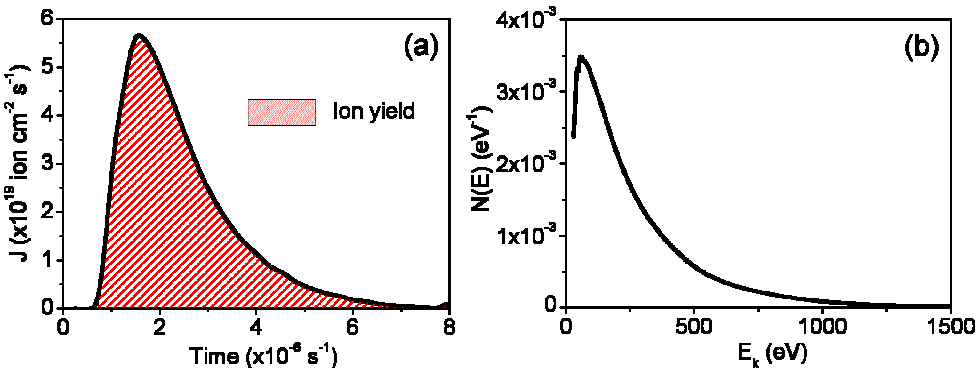

Figure 2.11: (a) Ion current density transient, J(t), and (b) Normalized ion kinetic energy distribution (N(E)) obtained upon ablation of Ag target at 9 J cm^{-2}. The area below the curve in (a) corresponds to the ion yield.

Finally, the ion kinetic energy distribution, N(E), is obtained by introducing a second approximation that consists in considering the laser plasma as an instantaneous point source of ions.[50] This approximation is valid since the target to probe distance is longer than the ion source size (i.e., of the order of the laser spot at the target site) and the transient lasts much longer than the characteristic ion ejection time (i.e., the pulse duration).[50] Under this assumption, the zero time of the transient (i.e. the laser pulse that triggers the oscilloscope) is common to all the ions arriving to the probe and we can approximate their velocity as:[27]

$$v = \frac{d}{t} \tag{2.2}$$

where d is the target to probe distance (d= 40 mm) and t is the time needed by each ion to reach the probe. If we now consider the kinetic energy, E_k:

$$E_k = \frac{1}{2} m \cdot v^2 = \frac{1}{2} m \cdot \left(\frac{d}{t} \right)^2 \tag{2.3}$$

the ion current density, $J(t)$, can be converted into the ion kinetic energy distribution, $N(E)$, by multiplying it for the Jacobian of the transformation:[11,27,31]

$$Jacobian(E) = \frac{t^3}{m \cdot d^2} \tag{2.4}$$

where the energy is expressed in eV and m is the atomic weight of the involved ion in kg. Finally, $N(E)$ has to accomplish the condition:

$$\int N(E) dE = 1 \tag{2.5}$$

Figure 2.11b shows the normalized ion kinetic energy distribution corresponding to the transient shown in Figure 2.10b.

2.3 POST-GROWTH SAMPLE PROCESSING

Besides the fabrication of nanostructured films, we have considered two experimental post-growth approaches based on thermal annealing and laser irradiation to improve our control over nanoparticle shape and distribution and to promote the formation of large Ag nanoparticles from almost Ag continuous films. In the next sections, we describe the process used for thermal annealing and the experimental setup used for laser irradiation experiments.

2.3.1 Thermal annealing

As previously mentioned, Ag forms a continuous film and no more separated nanoparticles can be observed once percolation limit is passed. In the case of PLD at room temperature this fact limits the maximum size of metal nanoparticles that can be formed spontaneously on the substrate. Thermal annealing of metallic films at relatively low

temperature is a strategy widely used to overcome this limitation and to induce the rearrangement of the metal film in separated islands. This process, known as *dewetting* of thin films,[51] is based on the minimization of the surface energy of the metal film. Briefly, since thin films are usually metastable or unstable in their as-grown configuration, a temperature increase, even below the bulk melting temperature, can be high enough to promote atoms to diffuse to a more stable configuration, i.e. spheroidal shape. The characteristics of the nanoparticles formed through dewetting depend on the initial film thickness, the annealing temperature and environment as well as on the substrate properties (structure and surface roughness).[52,53,54] In this thesis, we have studied the effect that dewetting has on percolated Ag films having thickness in the 10-12 nm range in two different environments: air and vacuum.

In the first case we used a commercial furnace (Mestra model R-080148, Figure 2.12). The temperature controller allows programming the heating ramp to reach automatically the pre-set annealing temperature. This can be increased up to 1100ºC via temperature steps in the 1-15 ºC min^{-1} range. Once the pre-set temperature is reached its value is maintained constant within an error of ±10ºC. We usually programmed a single heating ramp to heat up the sample from room to pre-set temperature, typically in the 300-400ºC range, the step being usually fixed at 10ºC min^{-1}. After annealing, the oven was switched off, the temperature freely decreased down to 100ºC and then the oven was open to allow a faster sample cooling.

Figure 2.12: Oven used for annealing in air.

Annealing in vacuum was performed *in-situ*, in the vacuum chamber after film growth. The base pressure was 10^{-6} mbar and the sample was heated using the substrate heater described in 2.1.3 and shown in Figure 2.7b. In all experiments performed in vacuum, we re-calibrated the heater using a thermocouple placed at the substrate site (k-type, cromel-alumel) to get a more precise sample temperature values with respect to those measured by the

temperature controller that are provided by the thermocouple placed near the heating bulb. During the experiments, the temperature was increased manually in steps of 5ºC min^{-1} to avoid filament breakdown and to allow restoring the pressure in the case of any outgasing. Once the pre-set temperature was reached, its value was maintained constant with a proportional-integral-derivative controller (PID) with an error of ±15ºC. After annealing, the temperature was gradually decreased down to room temperature in steps of 5ºC min^{-1}. Using this procedure, we have investigated the effects of annealing time (in the 30-120 minutes range) and temperature (in the 200-450 ºC range) on percolated films. The most relevant results are presented and discussed in Chapter 4.

2.3.2 Laser irradiation

Most techniques used to produce nanostructured films containing metal nanoparticles based on bottom-up approaches (PLD included) provide only a limited control over nanoparticle shape, orientation and spatial arrangement. This represents the main limitation to use these techniques for the design of nanostructured films with specific morphology and controlled optical response. Many approaches have been proposed to overcome this limitation, such as the use of nanostructured substrates to obtain a controlled deposition of regular arrays of nanoparticles[55] or template-free techniques based on specific geometries, like glancing angle deposition, to obtain directly nanoparticle shape control.[56] Besides these techniques, post-growth laser irradiation of nanoparticles is an established technique to achieve effective nanoparticle shaping and reorganization.[57] Here, we have used this method to modify the properties of nanostructured films produced using PLD. In particular, we studied the effect that the wavelength and the pulse duration have on the morphology and distribution of a single layer of coalesced nanoparticles embedded in an a-Al_2O_3 matrix and how the changes induced upon irradiation affect the optical response of the nanostructured films.

Figure 2.13 shows a simplified scheme of the experimental setup used.[58] The sample is mounted on a three-axis motorized sample stage and irradiated by a focused pulsed amplified Ti:Sa laser amplifier working at 800 nm (standard mode) or, alternatively, at 400 nm. The laser provides pulses with a duration of 100 fs, at both wavelengths. Moreover, pulses with 8 ns duration at 800 nm could be obtained by blocking the seed laser of the amplifier. In all cases, the laser arrives at the sample surface with an angle of incidence of 53º with respect the

normal to the substrate surface and its polarization is chosen to be s-polarized (along the y-axis of Figure 2.13) in order to set the polarization vector to lie within the surface plane.

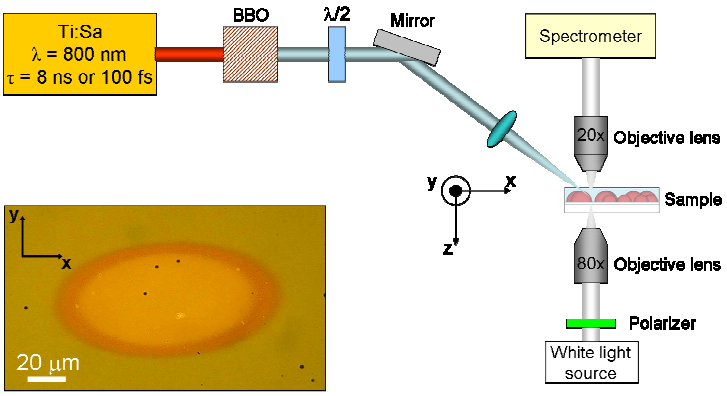

Figure 2.13: Scheme of the laser irradiation setup including the white light transmission micro-spectroscope system. BBO and λ/2 are a frequency doubling crystal and a half-wave plate, respectively. The inset is a colour optical transmittance micrograph of the area of a nanostructured film irradiated with a single pulse of 8 ns at 800 nm. The laser polarization is oriented along the y-axis.

The intensity distribution at the sample plane was measured to be Gaussian. The spot size for irradiation at 400 nm was 98.4 × 59.2 μm^2, and 106.6 × 58.9 μm^2 at 800 nm ($1/e^2$ diameters). The Gaussian nature of the intensity distribution allowed us to determine precisely the local fluence at each position of the spot according to the procedure described by Liu.[59]

The irradiation setup includes an in-situ high-resolution transmission micro-spectroscopy system. A white light source was collimated and imaged onto the front surface of the sample by means of at 80x objective lens, yielding to a spot size of 4 μm^2. A linear polarizer was used to set and align the polarization either along x- or y-axis (i.e. perpendicular and parallel to the laser polarization, respectively). The aperture at the sample plane was adjusted with the help of an in situ microscope (not shown in the Figure), which also enabled positioning the white light probe spot onto the desired location of the irradiated area. The light transmitted through the sample was collimated by a 20x objective and finally coupled into an optical fiber connected to a spectrometer. The high-resolution transmission spectrometer allowed us to measure the optical response of the nanostructured films in different regions of the irradiated area, and thus to study its dependence on laser fluence.

The inset of Figure 2.13 shows a colour optical transmittance micrograph of the laser-irradiated area of a nanostructured film irradiated using a single pulse of 8 ns at 800 nm with the laser polarization oriented along the y axis. The irradiated area corresponds to the

elliptical area. The colour fringes of the film evidence the change in the optical response that are related to changes of nanoparticle morphology, as it will be discussed in Chapter 5.

2.4 COMPOSITIONAL CHARACTERIZATION

The chemical composition of the nanostructured films produced in this thesis has been analyzed by X-ray Photoelectron Spectroscopy (XPS) and Rutherford Backscattering Spectrometry (RBS). The first technique was used to evidence the metallic nature of embedded nanoparticles, as well as to confirm their oxidation when exposed to air. In addition, XPS measurements were also used to verify the stoichiometry of the a-Al_2O_3 layers, while RBS was mainly used to quantitatively estimate the metal content in the films.

2.4.1 X-ray photoelectron spectroscopy

In XPS a monochromatic X-ray beam irradiates the surface of the sample to be analyzed promoting photoelectron emission from the atomic core levels or the valence bands of the atoms in the solid.[60] The emitted electrons are collected and analyzed by an electron detector and analyzer (Figure 2.14a). In a first approximation, the difference between the photon energy and the photoelectron kinetic energy corresponds to the electron binding energy whose value is strongly related to the electronic band structure of a specific element.[60,61] A typical XPS spectrum (Figure 2.14b) plots the number of detected electrons as a function of their binding energy. This results in a series of peaks whose position corresponds to a particular element, while their intensity relate to the relative amount of the element within the XPS sampling volume that, in general, is restricted to a depth $\leq$ 10 nm. In addition, a detailed analysis of the spectrum provides information about the elemental chemical state and the valence band structure.

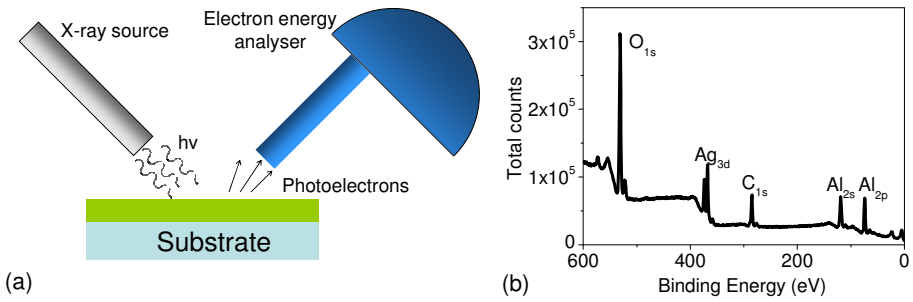

Figure 2.14: (a) Scheme of XPS experimental configuration. (b) Experimental XPS spectrum of a sample containing Ag nanoparticles embedded in a-Al_2O_3 matrix. The main energy peaks observed are identified.

In our case, XPS was useful for elemental and chemical state identification, relative composition quantification and electronic band structure determination. XPS measurements have been performed at the Surface Analysis Service of the Institute of Materials Science of Sevilla of the CSIC using an ESCALAB 210 spectrometer working in the pass energy constant mode at a value of 50 eV and using a Mg Kα (hν = 1253.6 eV) X-ray source. During acquisition the base pressure of the analysis chamber was maintained below 3×10^{-9} mbar. The obtained binding energies were referenced to the Al 2p line at a binding energy of 73.8 eV.[34]

2.4.2 Rutherford backscattering spectrometry

In RBS the material to be analyzed is bombarded with light ions having energy typically in the range of 0.5-4 MeV. These ions interact with the nuclei and electrons of the target and are partially backscattered over a wide range of energies and angles depending on the elements constituting the material and the depth at which they are located. The energy of the backscattered ions is recorded by an energy sensitive detector, placed at specific angle with respect the normal to the target surface.[62] Figure 2.15a shows a scheme of the RBS geometry.

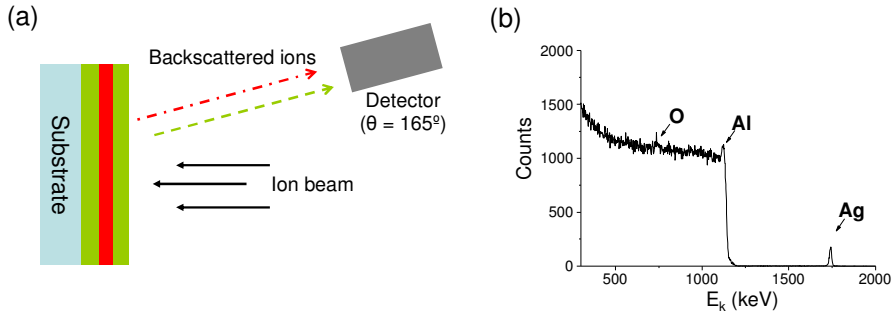

Figure 2.15: (a) Scheme of RBS experimental geometry. (b) RBS spectrum of a sample containing Ag nanoparticles embedded in a-Al_2O_3 matrix deposited on a Si substrate.

The energy lost by the incident ions when they are scattered by the atoms of the sample depends on the scattering cross-section of the sample atom and it is related to their atomic mass and number. In addition, ions scattered by different atoms at different positions with respect the sample surface will reach the detector with different energies, which makes the technique sensitive to the target composition as well as to the in-depth distribution of elements. An experimental RBS spectrum (Figure 2.15b) shows one or more energy peaks according to the number of elements contained in the sample. The height of the energy peak

provides information on the relative concentration of the considered species while its width allows determining the depth profiles of the corresponding element in the target, the wider the peak the broader the element distribution within the sample. This characteristic together with the sampling depth that can reach values in the 1-2 μm range make RBS suitable for the analysis of multilayered films such as those produced in this work. The main limitation of RBS is that it does not give any information about elemental chemical state.

In this thesis we used RBS to study the Ag atomic content ([Ag]) in the nanostructured films, expressed in atoms cm^{-2}. They were obtained by comparing the RBS spectra of the sample with that of a reference target having a known [Ag], or by simulating the experimental spectra with the appropriate software. The measurements have been performed at the *Centro Nacional de Aceleradores* (CNA) in Sevilla using a 2.0 MeV $^4He^{2+}$ ion beam and a surface barrier Si detector, placed at 165°. The obtained spectra were analyzed with the SIMRNA 6.0 code, being the error in the determination of [Ag] close to 2% in all cases.[63]

2.5 MORPHOLOGICAL CHARACTERIZATION

Morphological characterization of nanostructured films having dimensions in the range from a few to 100 nm requires the use of very sophisticated and precise microscopy techniques. In this work we used TEM and SEM to characterize the size, shape and distribution of Ag nanoparticles and the thickness of the a-Al_2O_3 layers.

2.5.1 Transmission electron microscopy

In the case of TEM, an electron beam generated by an electron gun is condensed, through electromagnetic lenses, into a parallel beam at the sample site (Figure 2.16a). The electrons transmitted through the sample are then collected and focused by the objective lenses and a magnified real image of the sample is projected by the projection lenses on an imaging device (fluorescent screen and CCD camera).[64,65] The thickness of the sample must be lower than 0.5 μm to allow electrons to be successfully transmitted through the film, which implies the need of time consuming sample preparation procedures (mechanical polishing, ion milling).[64]

TEM image results from the interactions of the electrons with the sample. Electrons are partially absorbed as a function of sample thickness and composition and scattered over small or well defined angles according to the composition and structure (crystalline or not) of the

sample. These interactions give rise to the so called amplitude, phase and diffraction contrasts that finally leads to the TEM image.[34,64,65]

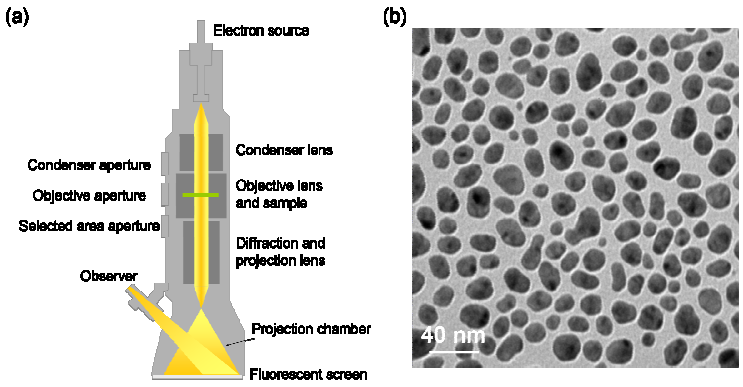

Figure 2.16: (a) TEM scheme showing the main microscope components. (b) Plan-view TEM image of Ag nanoparticles embedded in a-Al_2O_3 layer.

Because of the TEM high resolution (~atomic scale), we used this technique to characterize films containing small nanoparticles with typical sizes in the range from 10 nm to 30 nm. We have performed TEM analysis at the *Centre d'Elaboración de Matériaux et d'Etudes Structurales* (CEMES) in Toulouse (France) and at the *Instituto de Ciencias Agrarias* (ICA) of the CSIC in Madrid. Different types of microscopes have been used. In the first case we used a FEI Tecnai F20 equipped with a spherical aberration corrector and a TEM-FEG CM20, both operating at 200 kV, whereas in the second case we used a LEO 910 operating at 120 kV. Figure 2.16b shows a plan-view TEM image of a sample consisting of a monolayer of Ag nanoparticles embedded in a-Al_2O_3 matrix. The dark areas correspond to Ag nanoparticles, whereas lighter regions correspond to a-Al_2O_3.

2.5.2 Scanning electron microscopy

The schematic operation mode of a SEM is similar to that of a TEM microscope. An electron gun is used to generate an electron beam that is focussed through electromagnetic lenses in a small spot on the sample surface, where the beam is scanned in a rectangular raster.[64,65] In this case, electrons arriving to the detector are not the transmitted ones but those coming from the sample surface, resulting from the interaction between beam electrons and material atoms (Figure 2.17a).

The recorded signal is mapped as a variation of brightness on the image display. In most cases, the recorded signals are secondary (SE) and backscattered (BSE) electrons.[64,65] SE are emitted by the sample itself and come from an interaction volume close to the sample surface.

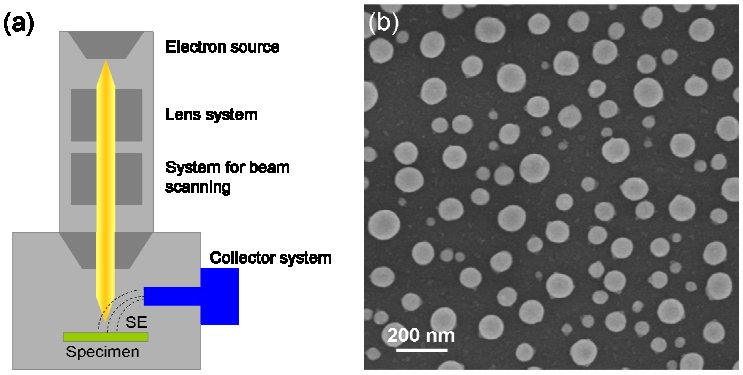

Figure 2.17: (a) SEM scheme showing the main microscope components. (b) Plan-view SEM image of Ag nanoparticles deposited on a a-Al_2O_3 layer.

In general, SE signal gives images with high spatial resolution and strong topographic contrast. BSE are primary electrons that are backscattered by the sample atoms and come from larger interaction volume. BSE signal is usually preferred in SEM because it strongly depends on elemental atomic number. Unlike the case of TEM, SEM sample does not require any specific preparation method. However SEM resolution is lower, of the order of few nanometers depending on the instrument characteristics.

Taking into account the characteristics of SEM, we used it for imaging films containing Ag nanoparticles with typical sizes in the range from 50 nm to 120 nm. Measurements have been carried on at the *Instituto de Ciencia y Tecnología de Polímeros* (ICTP) of the CSIC in Madrid using a Hitachi SU8000. Figure 2.17b show a plan-view SEM image of a sample containing Ag nanoparticles obtained after dewetting of a percolated film. Unlike the case of TEM image (Figure 2.16b), Ag corresponds to the elements showing lighter contrast, while the darker background corresponds to the a-Al_2O_3 layer.

2.5.3 Image processing

Image processing is fundamental to extract useful information from TEM and SEM images. In the case of nanostructured films containing metal nanoparticles, processing is mainly required to perform statistics over nanoparticles and obtain information like nanoparticle density, average size and surface coverage.

TEM and SEM images of the samples fabricated in this thesis have been processed with ImageJ.[66] This software has been used for improving the visual quality of the images, to determine the thickness of the layers constituting the nanostructures and, fundamentally, to perform statistics over nanoparticles. To this purpose, we used the *analyze particles* option that allows performing statistics over nanoparticle size and circularity ranges specified by the user.[66] In addition, this option automatically display the other important parameters earlier mentioned. Figure 2.18 shows (a) a plan-view TEM image of a sample containing Ag nanoparticles, (b) a *mask* of the image in (a) and (c) the in-plane nanoparticle long axis length distribution. The *mask* shows the nanoparticles on which statistics is performed. In the example below, we excluded all nanoparticles whose area is smaller than 300 nm^2. As a result, the mask only shows a few nanoparticles compared to the original TEM image (Figure 2.18a). Then, Figure 2.18c shows the corresponding in-plane long axis length distribution for the nanoparticles selected that is automatically displayed by the software.

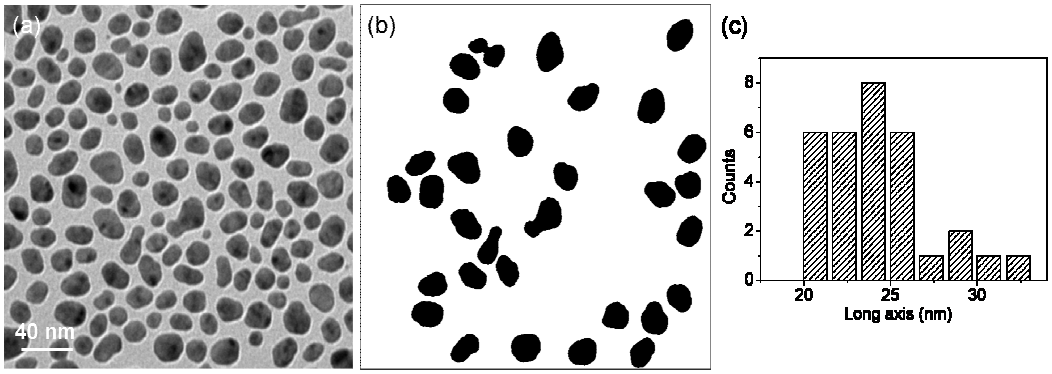

Figure 2.18: (a) Plan-view TEM image of a sample containing Ag nanoparticles. (b) *Mask* of the TEM image in (a) obtained by excluding nanoparticles having an area smaller than 300 nm^2. (c) Distribution of the in-plane long axis length of nanoparticles obtained from the analysis procedure.

2.6 OPTICAL MEASUREMENTS

The optical response of nanostructured films containing metal nanoparticles is characterized by an absorption band peaking at the spectral position corresponding to the excitation of the surface plasmon resonance (SPR) supported by the nanoparticles. The intensity, width and spectral position of the absorption band depend on the nature of the metal and of the medium surrounding the nanoparticles, on nanoparticle size and shape and on their spatial arrangement. It is thus clear that the study of the optical response of nanostructured films allows obtaining important information about nanoparticle morphology.

In this work the optical response of the fabricated nanostructured films has been studied by spectroscopic ellipsometry and spectrophotometry. The first type of measurements are mainly used to determine the optical constant of the matrix used to embed nanoparticles (a-Al_2O_3), while the second is used to characterize the absorption band associated to the SPR.

2.6.1 Spectroscopic ellipsometry

Ellipsometry is based on the change of light polarization that occurs when a beam of polarized light is reflected by the interface of two materials. This change is related to the optical properties and the structure of the media forming the interface, and therefore it can be exploited to determine them. The operation mode of an ellipsometer can be described as follows (Figure 2.19a): an unpolarized white light source enters first a monochromator that selects a specified wavelength and then a polarizer that extracts linearly polarized light (p- or s-polarized).

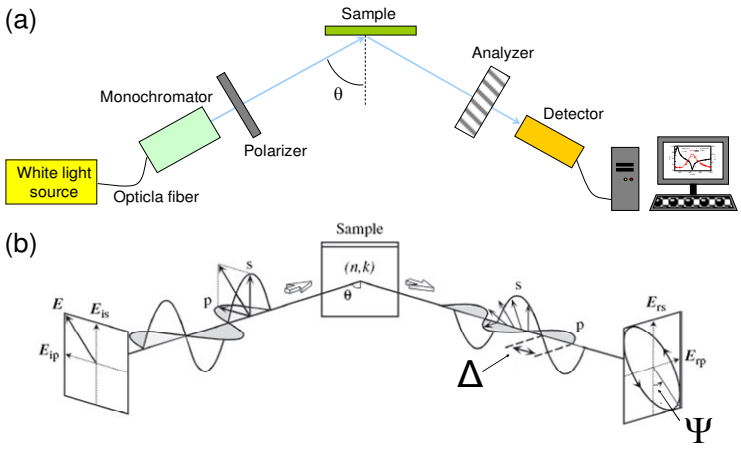

Figure 2.19: (a) Scheme of an ellipsometry setup. (b) Measurement principle of Ellipsometry, adapted from Fujiwara.[42]

Then the polarized light impinges on the sample surface and the reflected light enters a rotating analyzer before reaching the photodetector. The state of polarization is determined from the intensity of light transmitted through the analyzer. Figure 2.19b schematically represents the measurement principle of ellipsometry.

The experimental values measured are Ψ and Δ. They represent the amplitude ratio and phase difference between the reflected p- and s-polarized beams, respectively. Ψ relates to the refractive index while Δ represents light absorption described by the extinction coefficient. The measured Ψ and Δ values are defined by:[42]

$$\rho \equiv \tan\Psi e^{(i\Delta)} \equiv \frac{r_p}{r_s} \tag{2.6}$$

where

$$r_p = \frac{E_{rp}}{E_{ip}} = \frac{n_t \cos\theta_i - n_i \cos\theta_t}{n_t \cos\theta_i + n_i \cos\theta_t} \tag{2.7}$$

$$r_s = \frac{E_{rs}}{E_{is}} = \frac{n_i \cos\theta_i - n_t \cos\theta_t}{n_i \cos\theta_i + n_t \cos\theta_t} \tag{2.8}$$

represent the ratio of the amplitude reflection coefficients for p- and s-polarizations defined by the Fresnel equations.[42] In the equations, the subscripts p and s refer to the two possible polarizations, while the subscripts *i*, *r* and *t* stay for the incident, reflected and transmitted light beams, respectively. It follows that n_i and n_t are the refractive indexes of the materials in which the incident and transmitted beams propagate, and θ_i and θ_t refer to the angle that the incidence and transmitted beams form with the normal to the film surface. In polar coordinates the parameters Ψ and Δ can be expressed as:[42]

$$\tan\Psi = \frac{|r_p|}{|r_s|} \tag{2.9}$$

$$\Delta = \delta_{rp} - \delta_{rs} \tag{2.10}$$

where $|r|$ represent the absolute value of *r* and δ represent the phase change for p- and s-polarizations. In most cases, the values of the optical constant of the sample and its thickness are obtained through numerical analysis of the experimental data with optical models.

In this work we used a variable angle spectroscopic ellipsometry (WVASE-J.A. Woolman Co., Inc.) that allows performing ellipsometry as a function of the wavelength and the angle of incidence. In particular, ellipsometry was used to characterize the a-Al_2O_3 and Ag calibration films grown on Si. In the first case, we determined the optical constants of the grown films to check the reliability of the growth conditions and the film thickness to precisely calculate the a-Al_2O_3 deposition rate. In the case of Ag, since the optical constants were expected to be similar to that of the bulk,[67] we were mainly interested in obtaining the film thickness to estimate its deposition rate. In order to obtain the optical constants of a-Al_2O_3 films, the experimental data were adjusted using an optical model based on a Cauchy

function, according to what it has already been reported in literature for a-Al_2O_3 films grown under similar conditions.[44] In this model, the refractive index *n* is approximated by:[44]

$$n(\lambda) = A + \frac{B}{\lambda^2} + \frac{C}{\lambda^4} \qquad (2.11)$$

while *k* is assumed to be negligible, i.e. transparent film. A, B and C are adjustable parameters, together with the film thickness, and λ is the wavelength of the light probe. Figure 2.20a shows representative measured and generated Ψ and Δ values obtained by measuring an a-Al_2O_3 film ≈115 nm thick grown on Si at an angle of incidence of 65º. The experimental and fitted curves nicely overlap, which confirms the validity of the applied model and, thus, the high transparency of the grown film. Figure 2.20b shows the optical constants values obtained from the fitting procedure as a function of wavelength.

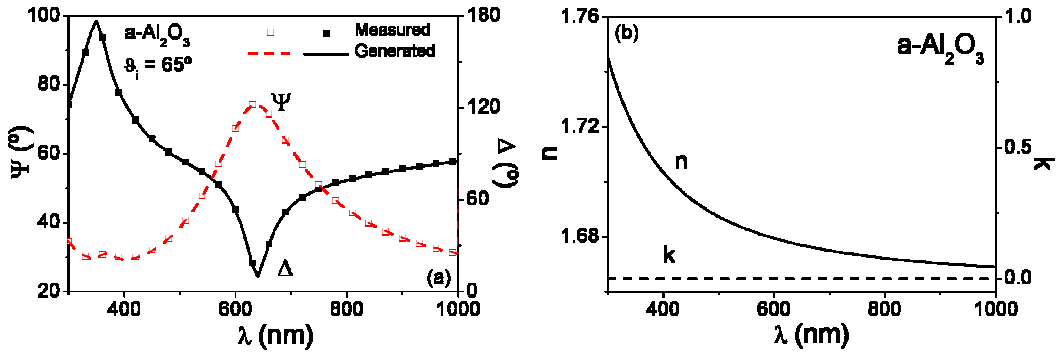

Figure 2.20: (a) Ψ and Δ measured and generated values for a a-Al_2O_3 calibration film. (b) n and k values extracted from the experimental Ψ and Δ values plotted in (a).

Finally, Figure 2.21 shows representative measured and generated Ψ and Δ values obtained for a Ag film ≈30 nm thick grown on Si measured at an angle of incidence of 70º. As in the case of a-Al_2O_3, the curves nicely overlap, thus confirming that the optical constants of a thin Ag film can be reasonably approximated with those of bulk Ag.

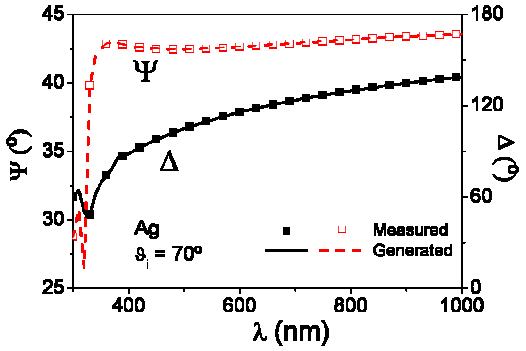

Figure 2.21: Ψ and Δ measured and generated values for a Ag calibration film.

2.6.2 Spectrophotometry

When a light beam impinges on the surface of a sample, it can undergo three different processes: transmission, absorption and reflection.[68] Transmission is a process in which a fraction of incident radiation leaves the surface of the sample from the opposite side of the incident one. Apart from the beam transmitted in a direction determined by the Snell's Law (i.e. specular transmission),[42] a fraction of transmitted light can also be scattered at different angles. The sum of these two components is the total transmission. Absorption is when part of incident light is converted in another form of energy (usually heat). Finally, reflection is when part of incident radiation is returned into the same hemisphere whose base is the surface of the sample. Reflection is usually a combination of specular (in the mirror direction) and diffuse (scattered into the entire hemisphere) components. The sum of these two components is the total reflection. Figure 2.22 schematically represents a light beam impinging on a sample surface and the relative transmitted and reflected beams.

The most common way to measure the fraction of light reflected, transmitted and absorbed by a sample is spectrophotometry. The operation mode of a conventional spectrophotometer is based on a double-beam configuration. The beam coming from the light sources (usually a deuterium lamp for UV generation and mercury/halogen lamps for VIS-NIR) is split into two beams that are directed to the sample and to a reference port.

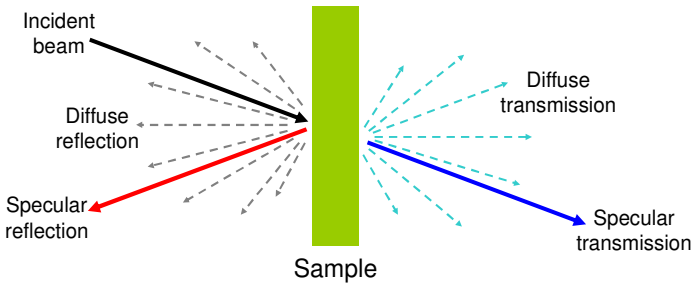

Figure 2.22: Scheme of the processes to which a light beam undergoes once it impinges on the surface of a sample. Adapted from Palmer.[68]

The output is given by the ratio of the signal in the sample beam to the signal in the reference beam plotted as a function of wavelength. A spectrophotometer can be used in transmission mode or in reflection mode. In the first case, the specular transmittance[†] (T) and absorbance can be measured. The absorbance is inferred from transmittance measurements,

[†] We will use the terms ending with -ance since we are dealing with specific samples and no pure materials.[68]

i.e. absorbance = $\log_{10}(1/T)$).[68] For this reason, this approach is particularly adequate for samples for which light scattering (i.e. light diffusion) is negligible. In the reflection mode, an integrating sphere is usually mounted in the optical path of the light beams to measure the total and diffuse reflectance and transmittance. The integrating sphere is an optical element whose internal walls are coated with a material (i.e. polytetrafluoroethylene) that efficiently scatters light in the 250-2500 nm range. Figure 2.23 shows schematically the operation mode of the integrating sphere in (a) reflectance and (b) transmittance configurations. In the first case, total or diffuse reflectance can be measured by leaving the slit close or open, respectively. Specular reflectance is then obtained by subtracting the diffuse component to the total one.

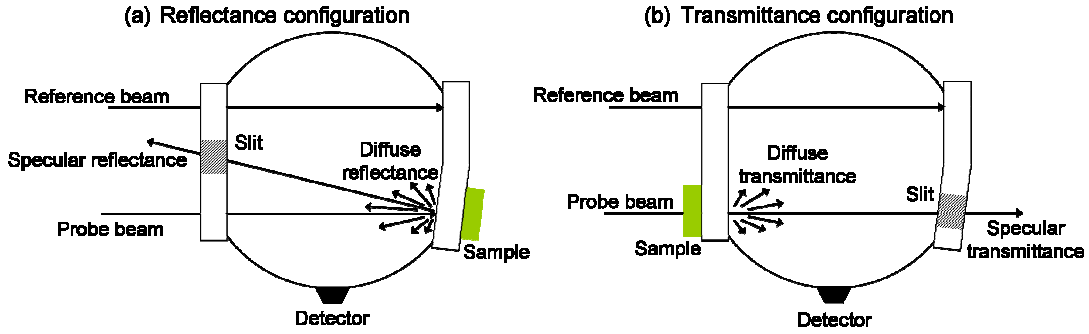

Figure 2.23: Scheme of the operation mode of the integrating sphere in (a) reflectance and (b) transmittance configurations.

Similarly, in the second case, total transmittance is measured only if the slit at the backside of the integrating sphere is closed, if not, the diffuse component is measured. Again, specular transmittance is obtained by subtracting the diffuse component to the total transmittance. It is worth noting that measuring the total reflectance (R_t) and transmittance (T_t) allows calculating the absorption (A) as:

$$A = 1 - R_t - T_t \qquad (2.12)$$

since the sum of the absorbed, reflected and transmitted light must be equal to unity.[68]

In this work, we used spectrophotometry for optical characterization of the fabricated nanostructured films containing metal nanoparticles. We used two spectrophotometers: a Varian Cary 5000 UV-Vis-NIR and a Shimadzu UV-3600 equipped with a 150 mm diameter integrating sphere. As previously mentioned, the optical behaviour of these nanostructures is

dominated by the absorption band associated to the excitation of the SPR, whose characteristics strongly depend on the nanoparticle morphology. Thus, we could use the optical response to qualitatively predict the morphology of nanostructured films. In addition, the integrating sphere allowed us to measure the optical properties, especially the diffuse reflectance, of the films grown on non-transparent substrates. The sensitivity of the optical measurements to morphology changes can be appreciated in Figure 2.24 that shows the extinction spectra, defined as E = 1 - T, where T is the specular transmittance, of three nanostructured films containing increasing amounts of Ag.

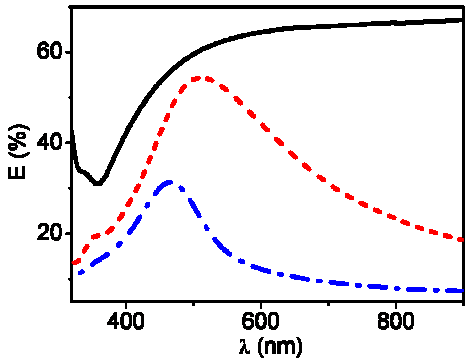

Figure 2.24: Extinction spectra of three nanostructured films containing increasing amounts of Ag. The spectra correspond to a nanostructure containing: (dash-dot blue curve) small Ag nanoparticle (5-10 nm) with almost circular shape, (dash red curve) coalesced Ag nanoparticle (10-30 nm) with circular and elongated shapes, and (solid curve) a percolated Ag film.

The spectra show an extinction band associated to the SPR for low amount of Ag, while for large amounts the optical response is almost flat in the whole range of considered wavelengths. As it will be discussed in detail in Chapter 4, this evolution of the optical response is consistent with the formation of nanoparticles whose size increases with increasing the amount of deposited Ag to lead finally to an almost continuous film.

References

(1) J. T. Cheung, In *Pulsed Laser Deposition of Thin Films*. Edited by D. B. Chrisey, G. K. Hubler (Wiley, New York 1994). Chapter 1

(2) C. N. Afonso and J. Gonzalo, In *Laminas Delagadas y Recubrimientos*. Edited by J. M. Albella (CSIC, Madrid, 2003). Chapter 8

(3) P. R. Willmott, J. R. Huber, Rev. Mod. Phys. **72**, 315-328 (2000)

(4) J. Schou, Applied Surface Science **255**, 5191–5198 (2009)

(5) L. Torrisi, A. Borrielli, D. Margarone, Nucl. Instr. and Meth. in Phys. Res. B **255,** 373–379 (2007)

(6) G. Koren, A. Gupta, R. J. Basemann, M. I. Lutwyche, R. Laibowitz, Appl. Phys. Lett. **55**, 2450 (1989)

(7) F. Claeyssens, S. J. Henley, M. N. R. Ashfold, J. Appl. Phys. **94**, 4 (2003)

(8) R. W. Dreyfus, J. Appl. Phys. **69**, 1721-1729 (1990)

(9) S. Amoruso, M. Armenante, V. Berardi, R. Bruzzese, N. Spinelli, Appl. Phys. A **65**, 265-271 (1997)

(10) A. L. Thomann, C. Boulmer-Leborgne, B. Dubreuil, Plasmas Sources Sci. Technol. **6**, 298-306 (1997)

(11) G. Baraldi, A. Perea, C.N. Afonso, J. Appl. Phys. **109**, 043302 (2011)

(12) K. L. Saenger, In *Pulsed Laser Deposition of Thin Films*. Edited by D. B. Chrisey, G. K. Hubler (Wiley, New York 1994). Chapter 7

(13) I. Weaver, C. L. S. Lewis, J. Appl. Phys. **79**, 7216-7222 (1996)

(14) R. del Coso, A. Perea, R. Serna, J. A. Chaos, J. Gonzalo, J. Solis, Appl. Phys. A **69**, 553-556 (1999)

(15) B. Toftmann, J. Schou, J. G. Lunney, Phys. Rev. B **67**, 104101 (2003)

(16) D. Dijkkamp, T. Venkatesan, X. D. Wu, S. A. Shaheen, N. Jisrawi, Y. H. Min-Lee, W. L. McLean, M. Croft, Appl. Phys. Lett. **51**, 619-621 (1987)

(17) J. Gottmann, E. W. Kreutz, Surface and Coatings Technology **116-119**, 1189-1194 (1999)

(18) Z. M. Ren, Y. F. Lu., H. Q. Ni, T. Y. F. Liew, B. A. Cheong, S. K. Chow, M. L. Ng, J. P. Wang, J. Appl. Phys. **88**, 7346-7350 (2000)

(19) A. Perrone, A. P. Caricato, A. Luches, M. Dinescu, C. Ghica. V. Sandu, A. Andrei, Applied Surface Science **133**, 239-242 (1998)

(20) H.-U. Krebs, O. Bremert, Y. Luo, S. Fähler, M. Störmer, This Solid Films **275**, 18-21 (1996)

(21) R. Dietsch, Th. Holz, D. Weißbach, R. Scholz, Applied Surface Science **197-198**, 169-174 (2002)

(22) D. H. A. Blank, M. Dekkers, G. Rijnders, J. Phys. D: Appl. Phys. **47**, 034006 (2014)

(23) R. Serna, M. Jiménez de Castro, J. A. Chaos, and C. N. Afonso, Appl. Phys. Lett. **75**, 4073 (1999)

(24) J.-P. Barnes, A. K. Petford-Long, R. C. Doole, R. Serna, J. Gonzalo, A. Suárez-García, C. N. Afonso, D. Hole, Nanotechnology **13**, 465-470 (2002)

(25) J. Margueritat, J. Gonzalo, C. N. Afonso, M. I. Ortiz, C. Ballesteros, Appl. Phys. Lett. **88**, 093107 (2006)

(26) J. Zúñiga-Pérez, A. Rahm, C. Czekalla, J. Lenzer, M. Lorenz, M. Grundmann, Nanotechnology **18**, 195303 (2007)

(27) A. Perea, J. Gonzalo, C. Budtz-Jørgensen, G. Epurescu, J. Siegel, C. N. Afonso, J. García-Lopez, J. Appl. Phys. **104**, 084912 (2008)

(28) R. Gupta, M. Weisheit, H.-U. Krebs, P. Schaaf, Phys. Rev. B **67**, 075402 (2003)

(29) K. Sturm, H.-U. Krebs, J. Appl. Phys. **90**, 1061 (2001)

(30) J. Gonzalo, A. Perea, D. Babonneau, C. N. Afonso, N. Beer, J. P. Barnes, A. K. Petford-Long, D. E. Hole, P. D. Townsend, Phys. Rev. B **71**, 125420 (2005)

(31) E. van de Riet, J. C. S. Kools, J. Dieleman, J. Appl. Phys. **73**, 8290 (1993)

(32) R. Jordan, D. Cole, J. G. Lunney, K. Mackay, and D. Givord, Appl. Surf. Phys. **86**, 24 (1995)

(33) V. Resta V, J. Gonzalo, C. N. Afonso, E. Piscopiello, J. Garcia-Lopez, J. Appl. Phys. 109, 094302 (2011)

(34) G. Baraldi, M. Carrada, J. Toudert, F. J. Ferrer, A. Arbouet, V. Paillard, J. Gonzalo, J. Phys. Chem. C **117**, 9431−9439 (2013)

(35) A. Gupta, In *Pulsed Laser Deposition of Thin Films*. Edited by D. B. Chrisey, G. K. Hubler (Wiley, New York 1994). Chapter 10

(36) W. J. Pan, J. Sun, H. Ling, N. Xu, Z. F. Ying, J. D. Wu, Applied Surface Science **218**, 297-304 (2003)

(37) J. F. M. Cillessen, M. J. M. de Jong, X. Croizé, Rev. Sci. Instrum. **67**, 3229-3237 (1996)

(38) E. Agostinelli, S. Kaciulis, M. Vittori-Anstisari, Applied Surface Science **156**, 143-148 (2000)

(39) B. Holzapfel, B. Roas, L. Schultz, P. Bauer, G. Saemann-Ischenko, Appl. Phys. Lett. **61**, 3178 (1992)

(40) C. K. Akkan, A. May, M. Hammadeh, H. Abdul-Khaliq, O. C. Aktas, Applied Surface Science **302**, 149-152 (2014) and reference therein

(41) S. M. Green, A. Piqué, K. S. Harshavardhan, J. S. Bernstein, In *Pulsed Laser Deposition of Thin Films*. Edited by D. B. Chrisey, G. K. Hubler (Wiley, New York 1994). Chapter 2

(42) H. Fujiwara, In *Spectroscopic Ellipsometry: Principles and Applications*. Edited by John Wiley & Sons (Chichester 2007)

(43) A. Vašíček, In *Optics of Thin Films*. North-Holland Publ. Co. (Amsterdam, 1960)

(44) R. Serna, J. C. G. De Sande, J. M. Ballesteros, C. N. Afonso, J. Appl. Phys. **84**, 4509-4516 (1998)

(45) J. S. Horwitz, J. A. Sprague, In *Pulsed Laser Deposition of Thin Films*. Edited by D. B. Chrisey, G. K. Hubler (Wiley, New York 1994). Chapter 8

(46) D. B. Geohegan, In *Pulsed Laser Deposition of Thin Films*. Edited by D. B. Chrisey, G. K. Hubler (Wiley, New York 1994). Chapter 5

(47) D. W. Koopman, Phys. Fluids **14**, 1707 (1971)

(48) J. Brčka, M. Alunovic, A. Voss, E. W. Kreutz, Plasma Sources Sci. Technol. **3**, 128 (1994)

(49) B. Doggett, J. G. Lunney, J. Appl. Phys. **105**, 033306 (2009)

(50) S. Amoruso, M. Armenante, V. Berardi, R. Bruzzese, R. Velotta, X. Wang, J, Phys. B: At. Mol. Opt. Phys. **32**, R131 (1999)

(51) C. V. Thompson, Annu. Rev. Mater. Res. **42**, 399-434 (2012)

(52) S. Morawiec, M. J. Mendes, S. Mirabella, F. Simone, F. Priolo, I. Crupi, Nanotechnology **24**, 265601 (2013)

(53) I. Tanyeli, H. Nasser, F. Es, A. Bek, R. Turan, Optics Express **21**, A798-A807 (2013)

(54) H. Tan, R. Santbergen, A. H. M. Smets, M. Zeman, Nano Lett. **12**, 4070-4076 (2012)

(55) E. Fort, C. Ricolleau, J. Sau-Peyo, Nano Lett. **3**, 65 (2003)

(56) A. N. Filippin, A. Borras, V. J. Rico, F. Frutos, A. R. Gonzalez-Elipe, Nanotechnology **24**, 045301(2013)

(57) M. Kaempfe, T. Rainer, K-J Berg, G. Seifert, H. Graener, Appl. Phys. Lett. **74**, 1200 (1999)

M. Kaempfe, T. Rainer, K-J Berg, G. Seifert, H. Graener, Appl. Phys. Lett. **77**, 459 (2000) (erratum)

(58) J. Doster, G. Baraldi, J. Gonzalo, J. Solis, J. Hernandez-Rueda, J. Siegel, Appl. Phys. Lett. **104**, 153106 (2014)

(59) J. M. Liu, Opt. Lett. **7**, 196 (1982)

(60) J. M. Campos Martín, In *Técnicas de análisis y caracterización de materiales*. Edited by M. Faraldos, C. Goberna (CSIC, Madrid, 2002). Chapter 12

(61) F. J. Grunthaner, MRS Bulletin **30**, 61 (1987)

(62) H.-J. Gossmann, L. C. Feldman, MRS Bulletin **12**, 26 (1987)

(63) http://home.rzg.mpg.de/~mam/

(64) R. F. Egerton, *Physical Principles of Electron Microscopy*. (Springer US, 2005)

(65) An introduction to Electron Microscopy, FEITM (2010)

(66) http://rsbweb.nih.gov/ij/

(67) E. Palik, *Handbook of Optical Constants of Solids*. Academic Press (New York, 1985)

(68) J. M. Palmer, In *Handbook of Optics.* Second Ed., Part II. Edited by M. Bass (McGraw-Hill, NY 1994).

Chapter 3
Dynamics of the Ceramic Aluminium Oxide and Silver Laser-generated Plasmas

Energetic species, mainly ions, present in the plasma produced by laser ablation can strongly influence the properties of the deposited films. For example, they can affect the structure of the deposited material or lead to material sputtering and implantation. In this chapter we study the dynamics of the plasmas generated upon ablation of silver and ceramic aluminium oxide targets that are the basic materials considered in this thesis for the fabrication of the nanostructures. We report and discuss the results concerning ion current density transient and yield, the ion kinetic energy distributions and, finally, the fraction of energetic species reaching the substrate.

3.1 ION YIELD AND ION KINETIC ENERGY DISTRIBUTION

In Chapter 2, we have already pointed out that one of the features that distinguishes PLD from other deposition techniques is the presence of species with a kinetic energy that can be as high as hundreds of eV in the laser-generated plasma. This actual value of the kinetic energy is determined by the laser parameters, such as laser fluence and wavelength, and the target thermal and electronic properties. The energetic species, mainly ions, play a key role in the properties of the deposited films. In the case of PLD of nanostructured films consisting of metal nanoparticles embedded in a dielectric matrix, both subsurface metal implantation and sputtering of metal atoms during their covering with a dielectric layer have been reported.[1,2] These effects were related to ions present in the laser-generated plasma having a kinetic energy higher than 200 eV.[3] As it will be discussed in detail in Chapter 4, we similarly observe in our experiments that a relevant fraction of the initial amount of deposited Ag is removed during deposition of the amorphous aluminium oxide covering layer, which is most likely related to sputtering of Ag promoted by the energetic species present in the Al_2O_3 laser-generated plasma. Thus, a complete understanding of the growth process and final properties of Ag nanoparticles requires the study of the dynamics of the plasma generated upon ablation of ceramic Al_2O_3 and Ag targets to determine the ion yields and kinetic energy distributions.

In the present work, these plasmas have been investigated using the LP setup described in section 2.2 of Chapter 2. The ion current density transient, J(t), was obtained from the Langmuir probe transient signal using equation (2.1), while the ion yield was calculated by time integrating J(t). Figure 3.1a shows representative ion current density transients obtained upon ablation of ceramic Al_2O_3 (from now on Al_2O_3) and Ag targets at 2.5 J cm^{-2}, which is the fluence typically used in our PLD experiments.

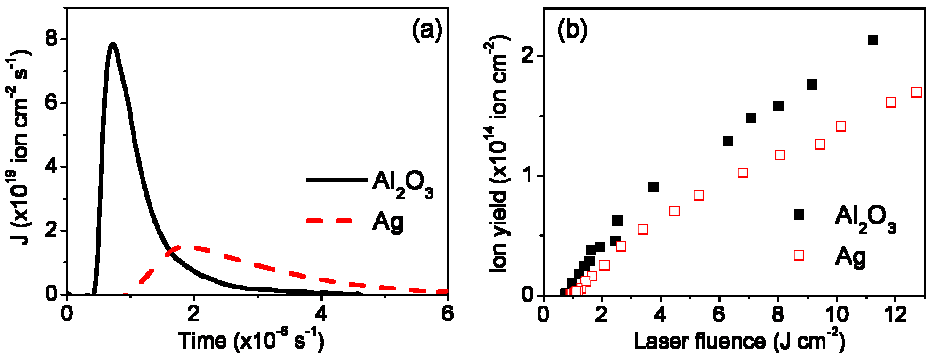

Figure 3.1: (a) Ion current density transients obtained upon ablation of Al_2O_3 and Ag targets at 2.5 J cm^{-2}. (b) Al_2O_3 and Ag ion yields as a function of laser fluence.

The transients show a fast increase followed by a slower decay that reaches zero after few microseconds (≈ 5-6 μs). In addition, in the case of Al_2O_3 the transient is narrower and shifted to shorter delay times with respect to the case of Ag. The transient maximum is observed at 0.7 and 1.8 μs for Al_2O_3 and Ag, respectively, while the corresponding full width at half maximum are 0.6 and 1.5 μs.

Figure 3.1b shows the Ag and Al_2O_3 ion yield (the total number of ions arriving to the probe per cm^2 per pulse) as a function of laser fluence. Ion yields are of the same order of magnitude (~ 10^{14} ion cm^{-2}) and their values increase with increasing laser fluence. In both cases, a change of slope is observed for fluences around 3 J cm^{-2}, the slope becoming lower for higher fluences.

In order to calculate the ion kinetic energy distribution N(E) from current transients such as those shown in Figure 3.1a, we followed the procedure described in section 2.2 of Chapter 2. In the case of Ag we used its atomic weight in the Jacobian of equation (2.4), since the species involved in the plasma are mainly Ag ions,[4,5] while in the case of Al_2O_3 some considerations have to be made before establishing the atomic weight to be considered. We know from literature that Al, O and AlO are the main species found in the plasma generated upon ablation of Al_2O_3 using ns pulses at 532 or 1064 nm.[6,7] Their proportion and positive charge degree depend on the experimental parameters. However, we have demonstrated that under our experimental conditions Al and Al_2O_3 plasmas have similar characteristics for low and intermediate laser fluences.[8] Figure 3.2 shows the ion current density transients obtained upon ablation of Al and Al_2O_3 at 2.5 J cm^{-2}. Apart from the difference in the signal intensity, the times at which the maximum of J(t) is observed and at which the signal becomes negligible are almost the same in the two cases, which supports that the ionic component of the Al_2O_3 plasma is most likely dominated by Al ions.

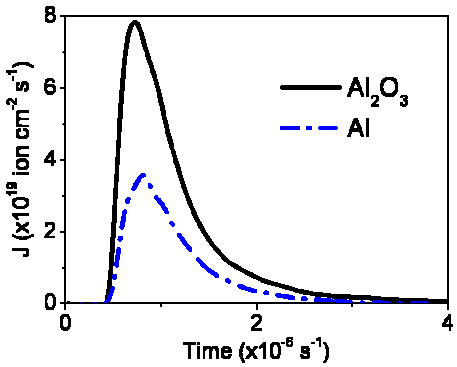

Figure 3.2: Ion current density transients obtained by ablating Al_2O_3 and Al targets at 2.5 J cm^{-2}.

Recently, the study of the ionic composition and excitation of plasmas generated upon ablation of a ceramic Al_2O_3 target at 193 and 248 nm has confirmed this conclusion.[9] Thus, we assume in this work that the ion population when ablating Al_2O_3 is dominated by single-ionized aluminium ions, and therefore the atomic weight of Al can be used in the Jacobian to obtain the N(E) corresponding to our Al_2O_3 plasma.

Figure 3.3a shows the calculated N(E) for Ag and Al_2O_3 at a laser fluence of 2.5 J cm^{-2}. The distribution trend is similar for both materials, showing a maximum at a relatively low kinetic energy followed by a long tail that extends up to kinetic energies of 1 keV. N(E) maxima are observed at 60 and 120 eV in the case of Ag and Al_2O_3, respectively, the maximum of Al_2O_3 being shifted towards higher energies. In addition, N(E) is broader in the case of Al_2O_3, which infers that an important fraction of ions in the Al_2O_3 plasma are expanding with kinetic energies higher than those of the Ag ions.

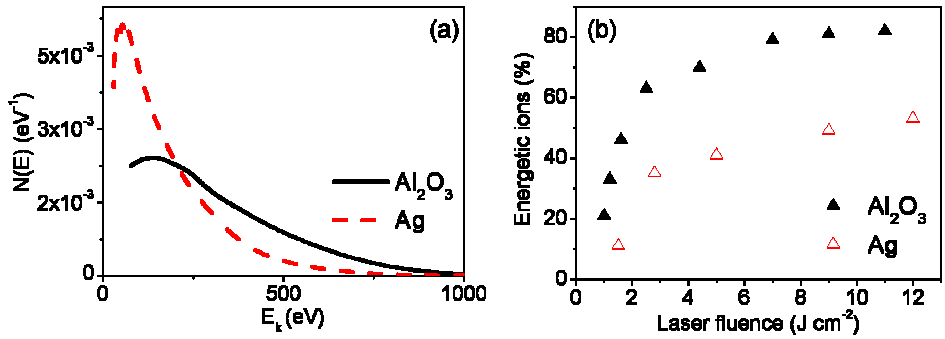

Figure 3.3: (a) Ion kinetic energy distribution calculated for Al_2O_3 and Ag plasmas generated at 2.5 J cm^{-2}. (b) Percentage of ions having kinetic energy higher than 200 eV as a function of laser fluence upon ablation of Al_2O_3 and Ag targets.

This is evidenced in Figure 3.2b that shows the percentage of ions with kinetic energy ≥ 200 eV as a function of laser fluence. This value was chosen since it represents the energy threshold for which sputtering and implantation processes at the substrate level start to be relevant during film growth.[1,3,10] The fraction of energetic ions increases with laser fluence for both materials and its dependence with fluence mirrors that of the ion yield shown in Figure 3.1b. We observe a change of slope around 3 J cm^{-2}, after which the fraction of energetic ions tends to saturate. Finally, the amount of energetic ions is at least twice for Al_2O_3 with respect to that of Ag irrespective of the laser fluence, and it is worth noting that 20% of ions present in the Al_2O_3 plasma are energetic already at fluences for which Ag shows negligible amount of energetic ions (≈ 1 J cm^{-2}).

The results presented in Figures 3.1a and 3.3a evidence that the ions involved in the plasma generated upon ablation of Al_2O_3, mainly Al ions, expand faster and they also have kinetic energies higher than those of Ag ions. In order to understand this behaviour we must bear in mind that the ion velocity is strongly related to the ion charge state through *Coulomb acceleration*. [5,11,12] This contribution to ion velocity arises from the charge imbalance that occurs in the plasma due to the fact that energetic electrons escape towards the leading edge of the plasma. This produces a high electrical field inside the plasma that contributes to make the distribution of ions forwardly peaked along the direction perpendicular to the target. In addition, the created field accelerates ions with an acceleration that scales with the ion charge. In the present case, the ionization potential of Al is 5.99 eV and that of Ag is 7.57 eV, while the laser photon energy is 6.4 eV, thus single-photoionization of Al atoms can take place.[8,9] This is likely to promote the formation of a plasma in the case of Al_2O_3 with very high degree of ionization which may experience a stronger Coulomb acceleration, resulting in a faster and more energetic plasma than in the case of Ag for which single-photoionization is not feasible. This effect is even more pronounced at low laser fluences for which the fraction of energetic ions in the case of Al_2O_3 is already 20%, while that for Ag is negligible.

The increase of the ion yield with fluence observed in Figure 3.1b is consistent with the fact that higher laser fluences result in a higher energy deposited on the target surface by the laser, which leads to an increase of the amount of material ablated and to more efficient collisional ionization processes.[5,6,11,13] However, the slope decrease observed at fluences close to 3 J cm^{-2} clearly suggests that the ablation process is less efficient. A similar behaviour has been reported in literature in the case of ns ablation of Al using laser wavelengths of 355 nm and 532 nm and in the case of Ag for 1064 nm. Ion yields saturate for fluences above 5-6 J cm^{-2} and 7-8 J cm^{-2}, respectively.[5,13] This has been associated to the plasma becoming opaque and starting to reflect the laser light, thus preventing the laser radiation from both ablating more material from the target and further heating of the plasma. In our case, the ion yield remains increasing with fluence, although at a lower rate, after the change of slope observed around 3 J cm^{-2}. This evidences that ionization processes are still active at high fluences values when using 6.4 eV photons. We have identified three different processes that might contribute to the observed increase. First, the energy of the laser photons is high enough to promote photoionization from first and second excited state of Al and Ag atoms.[14] Second, the production of multiple-charged ions for high laser fluences as reported for Ag[5] and Al,[9,13] would lead to an apparent increase of the ion yield, since LP does not allow distinguishing the

ion charge state. Finally, the ionization of neutral species generated upon dissociation of dimers that could be subsequently ionized, as observed in the case of Cu.[15]

Figure 3.1b also shows that in our experimental conditions, the ion yield of Al_2O_3 and Ag are of the same order of magnitude, that corresponding to Al_2O_3 being slightly higher. However, it is generally accepted, particularly for metals, that both the total[16] (the number of ablated atoms per pulse accounting for both neutrals and ions) and the ion[14] yields are strongly related to the melting temperature (T_m) of the material, i.e. the lower the T_m, the higher the total/ion yield. In the present case, the melting temperature of our Al_2O_3 target is 2273 K, a value that is almost twice the melting temperature of Ag (1234 K), which is in contrast with the expected trend. To explain this, one has to take into account that the yield does not only depend on T_m but also on thermal conductivity (TC) of materials. Figure 3.4 (left panel) shows the dependence of the ion yield to thermal conductivity ratio on melting temperature for Al_2O_3 and Ag together with data for other metals studied in our previous work[14] and for two selected fluences, namely 2 and 10 J cm^{-2}. The table in the right panel of Figure 3.4 reports T_m and TC values of the considered materials. It is seen that the ion yield of Al_2O_3 fits well to those of metals for both fluences, thus further supporting our assumption[14] that the ion yield scales with the thermal properties of the target.

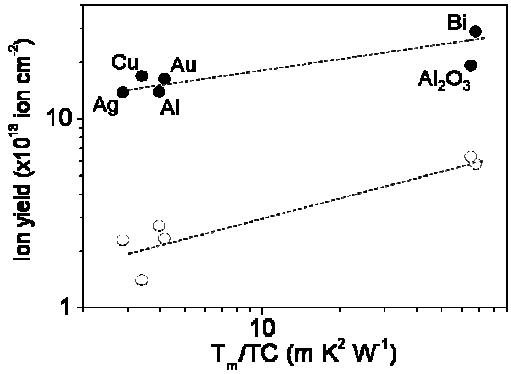

Material	T_m (K)	TC (W m^{-1} K^{-1})
Al	933	235
Cu	1357	400
Ag	1234	430
Au	1337	320
Bi	544	8
Al_2O_3	2273	35

Figure 3.4: (left panel) Log-log plot of the ion yield as a function of melting temperature (T_m) to thermal conductivity (TC) ratio of Al, Cu, Ag, Au and Bi together with those corresponding to Al_2O_3 at (open circles) 2 and (closed circle) 10 J cm^{-2}. The lines in the plot are guidelines to highlight the trend of ion yield with T_m/TC. (right panel) Melting temperatures (T_m) and thermal conductivity (TC) values of the investigated materials.

3.2 CONCLUSIONS

The results of this chapter allow us to reach two important conclusions. The first one concerns the relation between the laser photon energy and the degree of ionization of the plasma and, thus, its energetic nature. If the energy of the photon is high enough to promote

single-photoionization of atoms in the plasma the degree of ionization is high, which leads to a strong Coulomb acceleration. Thus, the plasma has a large fraction of energetic species having kinetic energy well above 200 eV. In the present case, this is observed in the case of Al_2O_3 for which the amount of energetic species involved in the plasma is as high as 20% for low laser fluence and the kinetic energy distribution of ions is shifted to higher energy values with respect to the case of Ag. The second conclusion concerns the relation between the ion yield and the thermal properties of the target. Our results show that the yield is not only determined by the melting temperature of the target, but also by its thermal conductivity. In the case of Al_2O_3, despite its melting temperature is higher than that of many metals (Ag included), the corresponding ion yield is comparable. This is most likely related to its thermal conductivity that is one order of magnitude lower than those of metals making the extraction of energy from the laser heated region less efficient.

As will be shown in next chapters, the results and conclusions obtained in the study of Al_2O_3 and Ag laser generated plasmas are very relevant for the growth of nanostructured films consisting of Ag nanoparticles embedded in amorphous aluminium oxide matrix. In our experiments, the laser fluence was maintained in the 2-2.5 J cm^{-2} range during film growth. For these values the percentage of energetic species is close to 60% and 30% for Al_2O_3 and Ag, respectively. Therefore, we should expect relevant implantation and sputtering effects during film growth.[1,2] However, we did not use lower fluence values because sputtering effects are not negligible even for fluences around ablation threshold of Al_2O_3 and they may lead to unpractical too low deposition rates.[17]

References

(1) V. Resta V, J. Gonzalo, C. N. Afonso, E. Piscopiello, J. Garcia-Lopez, J. Appl. Phys. **109**, 094302 (2011)

(2) J.-P. Barnes, A. K. Petford-Long, R. C. Doole, R. Serna, J. Gonzalo, A. Suárez-García, C. N. Afonso, D. Hole, Nanotechnology **13**, 465-470 (2002)

(3) A. Perea, J. Gonzalo, C. Budtz-Jørgensen, G. Epurescu, J. Siegel, C. N. Afonso, J. García-Lopez, J. Appl. Phys. **104**, 084912 (2008)

(4) M. E. Sherrill, R. C. Mancini, J. E. Baily, A. Filuk, B. Clark, P. Lake, J. Abdallah, Jr., Rev. Sci. Instrum. **72**, 1 (2001).

(5) D. Margarone, L. Torrisi, A Borrielli, F. Caridi, Plasma Sources Sci. Technol. **17,** 035019 (2008)

(6) F. Caridi, L. Torrisi, A. M. Mezzasalma, G. Mondio, A. Borrielli, Eur. Phys. J. D **54**, 467–472 (2009)

(7) L. Escobar-Alarcon, A. Arieta, E. Camps, S. Romero, M. Fernandez, E. Haro-Poniatowski, Appl. Phys. A **93**, 605–609 (2008)

(8) G. Baraldi, A. Perea, C. N. Afonso, Appl. Phys. A **105**, 75-79 (2011)

(9) R. J. Peláez, C. N. Afonso, M. Bator, T. Lippert, J. Appl. Phys. **113**, 223301 (2013)

(10) G. Baraldi, M. Carrada, J. Toudert, F. J. Ferrer, A. Arbouet, V. Paillard, J. Gonzalo, J. Phys. Chem. C **117**, 9431–9439 (2013)

(11) F. Claeyssens, S. J. Henley, M. N. R. Ashfold, J. Appl. Phys. **94**, 2203-2211 (2003)

(12) L. Torrisi, F. Caridi, A. Picciotto, D. Margarone, A. Borrielli, J. Appl. Phys. **100**, 093306 (2006)

(13) S. Amoruso, V. Berardi, R. Bruzzese, R. Capobianco, R. Velotta, M. Armenante, Appl. Phys. A **62**, 533 (1996).

(14) G. Baraldi, A. Perea, C. N. Afonso J. Appl. Phys. **109**, 043302 (2011)

(15) R. W. Dreyfus, J. Appl. Phys. **69**, 3 (1991)

(16) B. Thestrup, B. Toftmann, J. Schou, B. Doggett, and J. G. Lunney, Appl. Surf. Science **197–198**, 175 (2002)

(17) V. Resta, R. J. Peláez, C. N. Afonso, J. Appl. Phys. **115**, 124303 (2014).

Chapter 4
Characterization of Nanostructured Silver Films

In this chapter we first study the morphological and optical properties of nanostructured films in which Ag nanoparticles are exposed to air. Then, we discuss the film aging process related to nanoparticle tarnishing that progressively leads to the disappearance of the surface plasmon resonance. Finally, we report the results related to nanostructured films in which nanoparticles are covered with a thin layer of amorphous aluminium oxide. In this case, we show the effect the deposition of the covering layer has on films chemical mid-term stability, morphology and optical response.

4.1 FILM GROWTH MODES

The deposition of thin films through physical vapour deposition techniques can be described as the combination of kinetic adsorption and diffusion processes involving the atoms arriving on the substrate surface.[1,2] A deposited atom is adsorbed on the substrate surface and then it diffuses over the same surface before sticking to a stable position. The atom migrates on the surface according to its kinetic energy and to the concentration of surface defects (dislocation, vacancies, edges, ...).[1,2] During diffusion, the *adatom*‡ can bound to other film adatoms promoting cluster nucleation or attach to a pre-existing film cluster. If clusters are already formed on the substrate surface, atom adsorption and diffusion can also take place directly on the same cluster surface. Alternatively, the adatom can be re-evaporated either from the substrate or from a cluster, or leave the cluster and remain on the substrate surface.[2] All these processes that determine the morphology of the growing film strongly depend on the kinetic energy of arriving atoms and the deposition rate. This is particularly true in the case of PLD where the substrate is exposed to a large instantaneous flux of species and a large fraction of energetic ions.[2,3,4,5,6] In this sense, we want to remind the results reported in Chapter 3, where we observed that at a relatively low laser fluence (2.5 J cm^{-2}) and for a time shorter than 10 μs, the measured ion yield was as high as ~10^{14} ion cm^{-2} per pulse, with a fraction of measured energetic ions close to 30% and 60% for Ag and Al_2O_3, respectively.

Besides the properties of the arriving species, the formation of clusters and their growth is determined by the interaction energies of substrate atoms with film atoms. The initial stages of film growth are thus related to the strength of the bond of the adatom to the substrate compared to the bond strength to its surrounding neighbours.[1,2] Film growth modes are then usually classified in terms of the relation between the surface energy of the substrate and that of the growing film, given by the Young's equation:[1]

$$\gamma_s = \gamma_i + \gamma_f \cos\varphi \qquad (4.1)$$

where γ_s, γ_i and γ_f are respectively the surface energies of the substrate, film-substrate interface and film, and φ is the wetting angle of the cluster on the substrate (Figure 4.1).

‡contraction of *adsorbed atom*

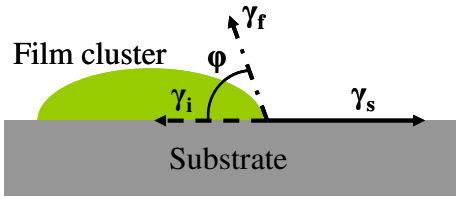

Figure 4.1: Schematic representation of the forces actuating on a film cluster formed on the substrate surface. γ_s, γ_i and γ_f represent, respectively, the surface energies of the substrate, the film-substrate interface and the film, while φ is the wetting angle.

Three different growth modes are thus identified:[1,2]

a) **Franck-van-der-Merwe.** (Figure 4.2a) It is also known as *Layer-by-Layer* growth mode. It occurs when $\varphi = 0$ and the inequality $\gamma_s > \gamma_i + \gamma_f$ is satisfied. In this case the interaction between substrate and film atoms is greater than between adjacent atoms. This leads to a rapid coalescence of the initially formed clusters to form a continuous film layer from the very first growth stages.

b) **Volmer-Weber**. (Figure 4.2b) It is also known as *Island* growth mode. It occurs when $\varphi > 0$ and the inequality $\gamma_s < \gamma_i + \gamma_f$ is satisfied. In this case the interaction between film atoms is greater than between adjacent film and substrate atoms. As a consequence, the atoms nucleate and form clusters of increasing size. Clusters form separated islands on the substrate surface that start to coalesce for increasing amount of material. As the amount of deposited material increases the lateral size of the islands increases until the percolation threshold is reached and an almost continuous network is formed. Then, the process ends with the formation of a continuous film.

c) **Stranski-Krastanov.** (Figure 4.2c) It is also known as *Layer-plus-Island* mode. It occurs when the film growth mode is Franck-van-der-Merwe followed by Volmer-Weber. In this case a few film complete monolayers, typically from 1 to 5, are formed; but then this is followed by the growth of separated islands due to a progressive increase of the interface energy with film thickness as a result of mismatched lattice spacing.

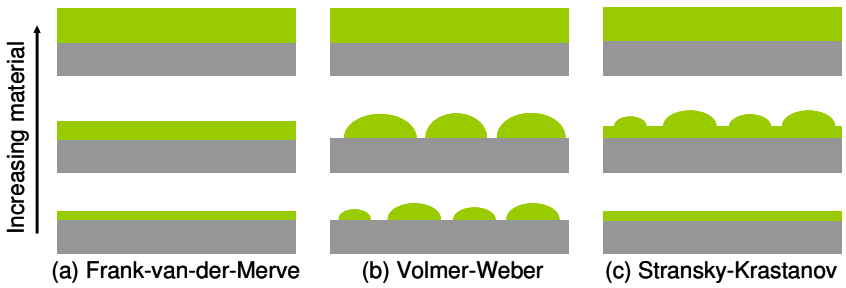

Figure 4.2: Types of film growth modes.

As described in Chapter 2, we use PLD to fabricate nanostructured films consisting of Ag nanoparticles lying on or embedded in an amorphous aluminium oxide (a-Al_2O_3) layer. Metals deposited using bottom-up techniques on oxide substrates typically follow the Volmer-Weber growth mode.[5,6,7] Thus, metal nanoparticles are spontaneously formed if the amount of deposited metal is below the percolation threshold. We can thus summarize the growth procedure for fabrication of our nanostructured films in three steps:

1. We grow first an a-Al_2O_3 buffer layer. Its thickness is adjusted to ensure the deposition of Ag and the subsequent nucleation of Ag nanoparticles to be independent on the substrate used.
2. Then, we deposit Ag. As previously discussed, Ag atoms diffuse on the substrate and form clusters, i.e. nanoparticles, which size and shape depend on the amount of deposited material.
3. Finally, we eventually grow a second a-Al_2O_3 layer on top of Ag nanoparticles. This covering layer constitutes a protective barrier to prevent Ag degradation, but its deposition also promotes Ag sputtering, as it will be discussed in detail in next sections.

The final result of the deposition process is schematically shown in Figure 4.3.

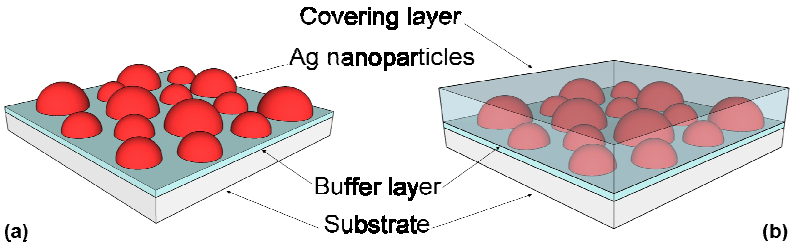

Figure 4.3: Sketch of (a) uncovered and (b) covered nanostructured films produced by a-PLD.

The amount of deposited Ag and the thickness of the a-Al_2O_3 layers are controlled by the number of pulses used to ablate each target which are determined from the deposition rate of the materials (section 2.3.1 Chapter 2).

The fact that Ag grows following the Volmer-Weber mode has a fundamental advantage in the case of the fabrication of nanostructured films containing metal nanoparticles with specific morphological and optical properties. The fact that nanoparticles are spontaneously formed and their properties can be simply modified by varying the amount of deposited Ag, without any other pre- or post-deposition processing, is a clear advantage. Nonetheless, due to the amorphous nature of the buffer layer, nanoparticles are "randomly" formed, it is hard to achieve with PLD a precise control over nanoparticle shape, orientation and distribution over the substrate surface. In addition, the size of the formed nanoparticles is naturally limited by the percolation threshold.

4.2 UNCOVERED NANOSTRUCTURED FILMS

The results reported and discussed in this section relate to nanostructured films that differ in the Ag content. We are interested in the analysis of the evolution of nanoparticles morphology as a function of the number of pulses used to ablate the Ag target and to study how the observed morphology affects the optical response of the nanostructures. In addition, we also evidence and discuss the chemical reactivity of the nanostructures when they are exposed to air.

4.2.1 Morphology

Figure 4.4 shows plan-view TEM images of three uncovered nanostructured films. The number of laser pulses on the Ag target was (a) 300, (b) 900 and (c) 4200[§] which, approximately, correspond to an Ag equivalent thickness[**] of 1.2, 3.6 and 12 nm, respectively. The dark contrast in the images corresponds to Ag, whereas lighter regions correspond to a-Al_2O_3. As it is shown in Figure 4.4a for 300 laser pulses, Ag nanoparticles can be either isolated, showing almost circular in-plane projected shape, or form apparently elongated chainlike structures that are composed of adjacent and/or overlapping nanoparticles.

[§] We will identify in the following sections and chapters of this thesis uncovered and covered nanostructured films with the acronyms UN-xxx and CN-xxx, respectively, where xxx stands for the number of laser pulses on the Ag target used to nucleate and grow the nanoparticles.

[**] Equivalent thickness refers to a thickness of a continuous layer of Ag produced with the same number of laser pulses on Ag target.

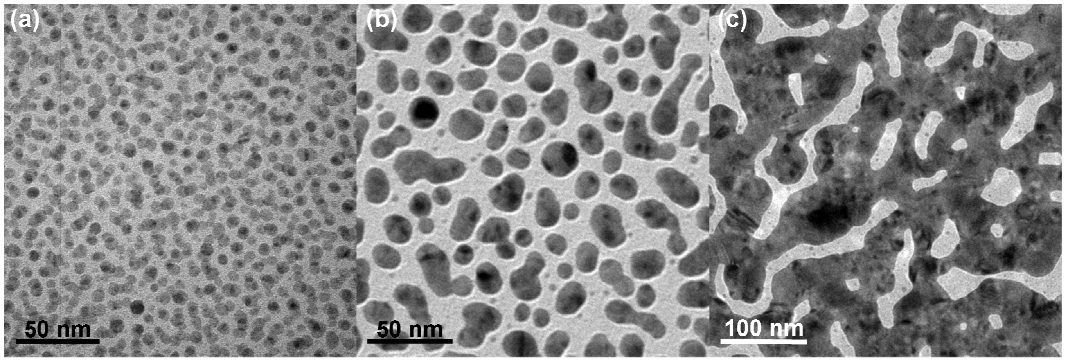

Figure 4.4: Plan-view TEM images of uncovered films obtained by ablating Ag with (a) 300, (b) 900 and (c) 4200 laser pulses. Note the different scale in (c).

This can be seen in most chainlike structures, appearing as a darker contrast area which corresponds to a higher amplitude contrast (Figure 4.5a), whereas the darker zones in the isolated Ag nanoparticles are due to diffraction contrast. Figure 4.5b is a high resolution TEM image showing a few Ag nanoparticles. We observe that the crystalline planes present different orientation which supports that nanoparticles are polycrystalline.

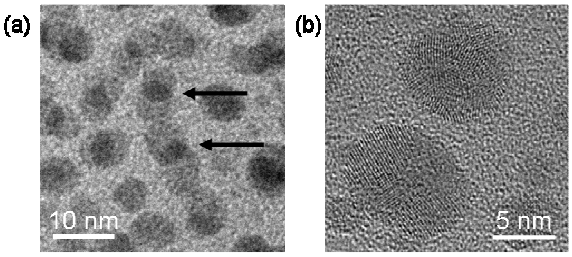

Figure 4.5: (a) Detail of Figure 4.4a. The arrows show the higher amplitude contrast in chainlike structures due to overlapping of nanoparticles. (b) High resolution TEM image of a few nanoparticles that shows the nanoparticles are crystalline.

The nanoparticle surface density of UN-300 is $\approx 1.3\times10^4$ NPs μm^{-2} and their surface coverage is 50%. Figure 4.6a shows the in-plane long axis length distribution (L) of thin film. Most nanoparticles, the isolated ones, have in-plane long axis values ranging from 2 to 8 nm (average value $<L_{UN\text{-}300}> = 5$ nm), while a small fraction, i.e. the aggregates of nanoparticles, shows a in-plane long axis length that can be as long as 22 nm.

Figure 4.4b shows the UN-900 film. It consists of a layer of randomly distributed and oriented Ag nanoparticles that show either circular or elongated in-plane projected shapes due to nanoparticle coalescence. The nanoparticle surface coverage as well as the nanoparticle

density are lower with respect to UN-300, their values being 44% and 1.8×10^3 NPs μm^{-2}, respectively.

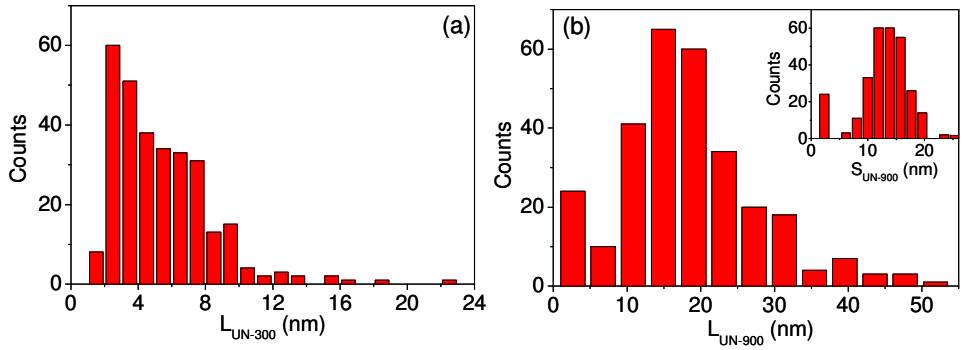

Figure 4.6: Nanoparticle in-plane long axis length (L) distribution of (a) UN-300 and (b) UN-900 films. The inset in (b) corresponds to the nanoparticles in-plane short axis length (S) distribution of UN-900 film.

Figure 4.6b shows the nanoparticle in-plane long and short (S) axes length distributions. Most nanoparticles have L_{UN-900} in the range from 10 to 30 nm, with an average value of $\langle L_{UN-900} \rangle$ = 20 nm. Only a very small fraction of the nanoparticles have smaller values, down to 2 nm, as well as larger values that can be as high as 50 nm. The in-plane short axis length distribution is much narrower, with almost 90% of the nanoparticles having S_{UN-900} in the 10-18 nm range, with an average value $\langle S_{UN-900} \rangle$ = 14 nm.

Finally, Figure 4.4c shows the UN-4200 film. In this case, Ag forms an almost continuous film that covers most surface and no more isolated nanoparticles are left behind.

The results shown in Figure 4.4 confirm that the nucleation and growth of Ag on a-Al_2O_3 follows the Volmer-Weber growth mode. The morphology observed in the case of UN-300 film (Figure 4.4a) relates to the initial stage of the growth when small clusters are formed upon adatoms nucleation on the substrate surface. The observed high nanoparticle density hints at the instantaneous and energetic deposition during PLD responsible to promote a high nucleation rate on the a-Al_2O_3 buffer layer,[5,6] while for UN-900 film (Figure 4.4b), nanoparticles become larger, elongated and their density decreases (about one order of magnitude) due to coalescence of smaller nanoparticles. Finally, the morphology observed for UN-4200 film corresponds to the last step of Volmer-Weber growth mode, when the percolation threshold has already been exceeded and no more isolated features are observed.[5]

4.2.2 Optical response

Figure 4.7 shows the extinction spectra measured for UN-300 and UN-900 films grown on fused silica and UN-4200 film grown on glass. The spectrum of UN-300 film shows a narrow extinction band. The band maximum (E = 30%) is reached close to 465 nm, while its Full Width at Half Maximum (FWHM) is approximately 110 nm. In the case of UN-900 film, the spectrum shows a main extinction band peaked at ≈ 515 nm and a FWHM around 220 nm. The band intensity at the maximum is 55%. UN-900 film spectrum also shows a very weak peak at 355 nm. Instead, the optical response of UN-4200 film differs, the extinction increase from 30% up to 60% in the 350-500 nm range, while for longer wavelengths it increases up to 66%.

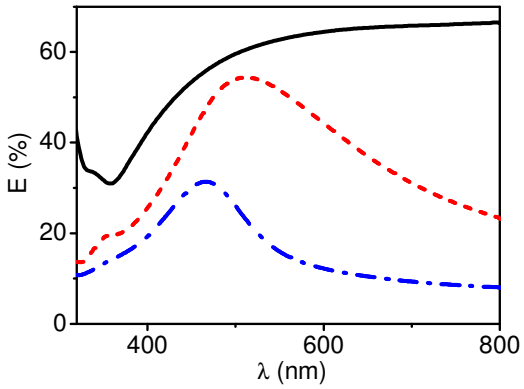

Figure 4.7: Extinction spectra of UN-300, UN-900 and UN-4200 films.

The extinction bands observed in the spectra corresponding to UN-300 and UN-900 films relate to the excitation of the surface plasmon resonance (SPR) of the nanoparticles.[8] The main extinction bands, i.e. those peaked at 465 nm and 515 nm, correspond to excitation of the dipolar mode, while the weak band, observed only in the case of UN-900 film at 355 nm, relates to the excitation of the quadrupolar mode.[8,9] The more intense SPR (the one corresponding to the dipolar mode) observed in the case of UN-900 film with respect to that of UN-300 film can be related to the different size of the nanoparticles characterizing the morphology of the two films. In Figure 4.4 we observed that nanoparticles in UN-900 film are bigger than those in UN-300 film. Since the Ag content in big nanoparticles is larger than in small ones, they are expected to absorb light more efficiently, which results in an enhancement of the resonance intensity. As reported in literature, the increased nanoparticle size is also responsible, together with interparticle coupling effects, for the observed 50 nm

peak-shift to the red of the extinction band corresponding to UN-900 film with respect to that of UN-300 film.[9,10,11] The increase of the FWHM of the extinction band in the case of UN-900 film can be associated to the fact that the measured optical response is an average of the optical properties of a nanoparticle assembly with broad size and shape distribution.[8,11] Finally, the extinction spectrum corresponding to UN-4200 is completely different. The optical response does not show any band associated to nanoparticle SPR but it resembles that of a continuous Ag film, which is consistent with the morphology shown in Figure 4.4c.

Figure 4.4a showed that the morphology of UN-300 film is quite complex since it is characterized by elongated chainlike structures that are composed of adjacent and/or overlapping particles. We have thus investigated if these structures contribute to the optical response either as unique elongated features or as isolated nanoparticles. To that purpose, we have modelled the optical response of the UN-300 film using an effective medium calculation based on the Yamaguchi theoretical approach.[12,13] We approximated the chain-like structures as ellipsoidal Ag nanoparticles with in-plane elongation, having random in-plane orientation and a isotropic in-plane organization. In order to take into account the fact that the nanoparticles were supported on the buffer layer and uncovered, they were assumed to be embedded in an average medium mixing the response of vacuum and a-Al_2O_3 (effective dielectric constant $\varepsilon_m = 1.82$). We consider a nanoparticle in-plane short axis length S = 4.5 nm, the height H = 3.6 nm and a center-to-center interparticle distance Λ = 25 nm. S and Λ values were chosen to resemble the morphology of nanoparticle layer observed in Figure 4.4a, while the value of H is determined from the cross-section TEM image that will be reported later (Figure 4.13a). Figure 4.8 shows the calculated evolution of the SPR parallel to the long axis of the nanoparticles as a function of the L. For the calculation we consider the nanoparticle in-plane short axis length S = 4.5 nm, the height H = 3.6 nm and the center-to-center interparticle distance Λ = 25 nm.

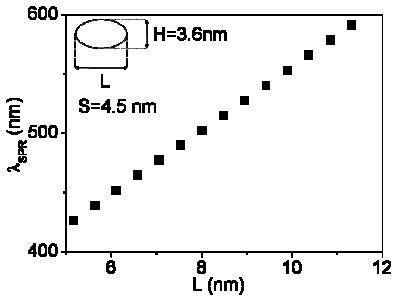

Figure 4.8: Calculated in-plane longitudinal SPR peak position as a function of L using effective medium modelling in which nanoparticles are supposed to be embedded in an average homogeneous medium mixing the dielectric function of vacuum and a-Al_2O_3.

The results of the effective medium calculations show that the SPR peak position shifts rapidly towards the near-infrared as the nanoparticle in-plane long axis length increases. This means that chainlike nanostructures behaving optically as strongly elongated nanoparticles would therefore lead to in-plane longitudinal surface plasmon resonance contributions peaking between 500 nm and the near-infrared. As a consequence, UN-300 film would show a broad extinction band peaking at $\lambda \geq 500$ nm. However, this is not the case, since it shows a quite narrow SPR peaking close to 465 nm (Figure 4.4a). Therefore, the optical measurements on UN-300 film likely probe independent nanoparticles with weakly anisotropic shapes rather than elongated coalesced nanostructures.

Besides the size and shape of the nanoparticles, the SPR is also strongly influenced by electromagnetic coupling that can occur among neighbouring nanoparticles.[9,10,14] In general, the SPR modes of densely packed nanoparticles can peak at wavelengths different from those of the same nanoparticles taken separately. For a given nanoparticle size, shape and embedding medium, the SPR wavelengths depend on the separation distance between nanoparticles. Thus, we have evaluated the consequences of interparticle coupling on the spectral position of the SPR in the case of a single layer of Ag nanoparticles similar in size to those observed in UN-300 (Figure 4.4a). To that purpose, we have calculated the absorbance spectra of densely packed assemblies of Ag nanoparticles using the Granfilm code.[12,15,16] This code allows determining the effective optical response of a single layer of monodisperse nanoparticles in the quasi-static size regime (nanoparticle size << wavelength of the incident light),[13] supported on a substrate and displaying a rotational shape with a vertical revolution axis. The Granfilm code allows taking into account the coupling between nanoparticles through the dipole and quadrupole contributions of their near-field, thus suggesting that it can be used in the case of densely packed nanoparticles.

Using this code, the absorbance was calculated at normal incidence for a simplified model system consisting of 6 nm-spherical Ag nanoparticles deposited on a-Al_2O_3 and organized on a square array. Calculations were performed as a function of the interparticle distance (array pitch, Λ). The results of the modelling are shown in Figure 4.9.

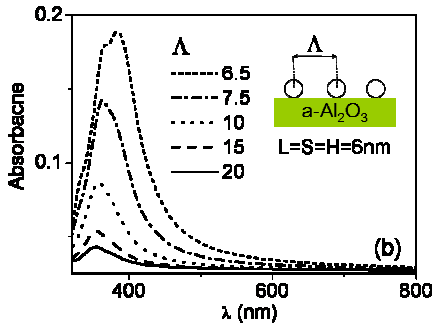

Figure 4.9: Granfilm simulation of the absorbance at normal incidence of 6 nm spherical Ag nanoparticles deposited on a-Al_2O_3 and organized on a square array as a function of center-to-center interparticle distance, Λ.

As we see in the figure, as we decrease Λ until the nanoparticles are almost in contact (0.5 nm gap) only a slight red-shift (approximately from 350 nm to 390 nm) of the dipolar in-plane SPR band is induced. Therefore, for the nanoparticle sizes involved in this work, near-contact coupling between nanoparticles might induce only a moderate in-plane SPR red-shift when compared to the same nanoparticles taken separately. The measured spectral position for the resonance (≈ 465 nm) is thus consistent with the excitation of individual nanoparticles separated by very small gaps and presenting a slightly non-spherical shape (weak in-plane elongation and/or flattened shape), which are most likely the building blocks of the chainlike structures. Indeed, the shape and interaction-induced red-shift with respect to the case of separated spherical Ag nanoparticles could sum and drive the in-plane SPR towards 465 nm. One has nevertheless to bear in mind that the simulations performed do not take into account exactly the complex nanostructure of UN-300 (Figure 4.4a) and thus, they only allow a qualitative interpretation of the SPR position.

4.2.3 Optical and chemical stability

The incorporation of plasmonic nanostructures in real devices requires the film properties to be stable once they are exposed to the environment. Unfortunately, bulk silver suffers from tarnishing upon exposure to atmosphere due to its reaction with atmospheric contaminants like hydrogen sulphide (H_2S) and carbonyl sulphide (OCS).[17,18] Therefore, the effect of tarnishing is expected to be more pronounced in the case of Ag nanoparticles due to their increased surface-to-volume ratio.[19,20] In fact, it has been reported that Ag nanoparticles exposed to atmosphere suffer from aging processes due to oxidation[21,22] or sulfidation.[23,24] The difference in the chemical reaction leading to tarnishing is generally ascribed to the fabrication process, the relative concentration of atmospheric reactants, the temperature and

humidity and to the environment surrounding or supporting nanoparticles.[12,20,25] The chemical reactivity of Ag strongly influences the optical properties of the nanostructured films containing Ag nanoparticles, unfortunately leading usually to SPR damping[21] and/or shifting.[23] In this scenario, the uncovered nanostructured films fabricated in this thesis do not represent an exception. In this section, we report the results concerning the effect the aging process has on UN-300 films.

The effect of exposure to air on the UN-300 film could be easily detected by eye. Figure 4.10a shows, on the left, an image that corresponds to the UN-300 film deposited on a 5 × 5 mm^2 fused silica substrate just after its growth (as-grown film). The whole area covered by the film is yellowish. The image on the right corresponds to the same UN-300 film but after 5 months of exposure to air. The film becomes almost transparent, the effect being more pronounced at the sample edges. Figure 4.10b shows the experimental evolution of the absorbance of the UN-300 film as a function of the exposure time to air.

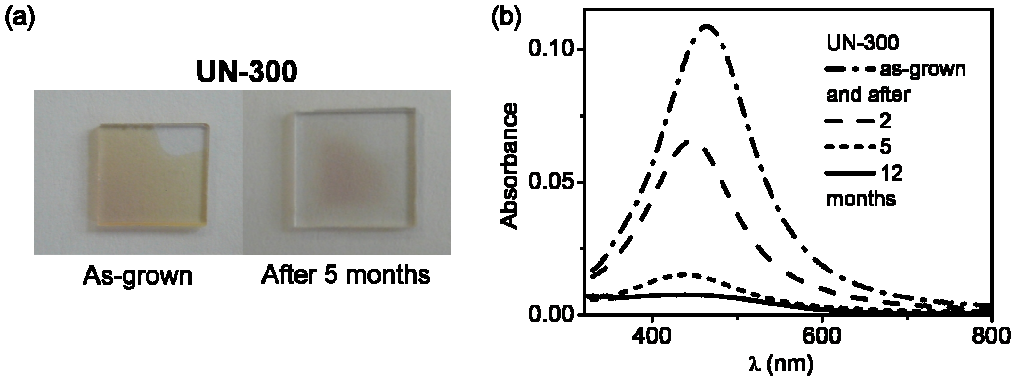

Figure 4.10: (a) UN-300 film just after growth (image on the left) and after 5 months of exposure to air (image on the right). (b) Experimental evolution of the absorbance of the UN-300 film as a function of the exposure time to air.

The intensity of the peak corresponding to the maximum of the SPR absorption band decreases, while its position slightly blue shifts during the months following deposition until, eventually, it almost disappears. The amplitude decreases by a factor of 14 and the resonance shifts from 465 to 435 nm after 12 months.

With the purpose to prevent the degradation of Ag nanoparticles, we produced a set of films in which Ag nanoparticles have been covered with a thin film of a-Al_2O_3. Each sample was produced separately in a single-step growth process in which we alternate the ablation of Al_2O_3 and Ag targets. For all films, we used 300 laser pulses on the Ag target to ensure a

similar nanoparticle morphology, while we varied the number of pulses on the Al_2O_3 target in the range from 160 to 5060 in order to deposit a-Al_2O_3 layers with increasing thickness. Figure 4.11 shows the experimental evolution of the absorbance of the CN-300 film, covered using 1270 laser pulses on Al_2O_3 target, just after its growth and twelve months later.

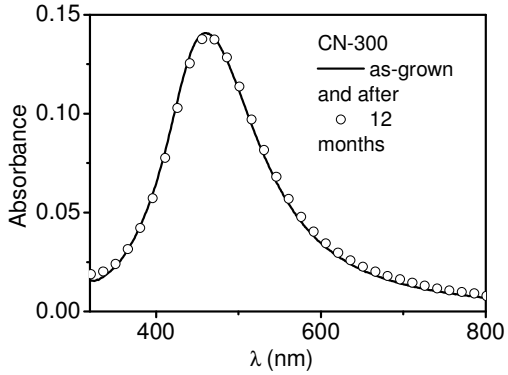

Figure 4.11: Evolution of the absorbance of the CN-300 film as a function of the exposure time to air. The number of laser pulses on the Al_2O_3 target is 1270.

Unlike the case of UN-300 film (Figure 4.10b), no changes either in amplitude or in position are observed, which demonstrates the excellent mid-term stability of the optical and chemical properties of the film. It is worth noting that, the lowest number of pulses on Al_2O_3 for which tarnishing of Ag nanoparticles was prevented was 1270, for all the fabricated films.

To shed more light on the nature of the contaminant responsible for sample aging we performed XPS measurements on UN-300 and CN-300 films. Figure 4.12 shows their XPS spectra 12 months after deposition at the (a) Al 2p, (b) O 1s, (c) Ag 3d, (d) S 2p and (e) N 1s levels. The corresponding peak energies are listed in the table included in Figure 4.12. The modified Auger parameter (α^*) has been calculated from the M_4VV and M_5VV Ag Auger signals in order to get information about the oxidation state of Ag.[26] The obtained values are 726.03 and 722.54 for CN-300 and UN-300 films, respectively.[12] The relative intensities of the Al, O and Ag signals are different for the two films due to their different in-depth distribution in the near-surface thin region from which photoelectrons escape. Peak positions for Al and O peak are similar both for UN-300 and CN-300 films. In contrast, the Ag peak of the CN-300 film is shifted to lower binding energies compared to that of the UN-300 film. Finally, we observe in this case a small peak related to S and a more pronounced one related to N.

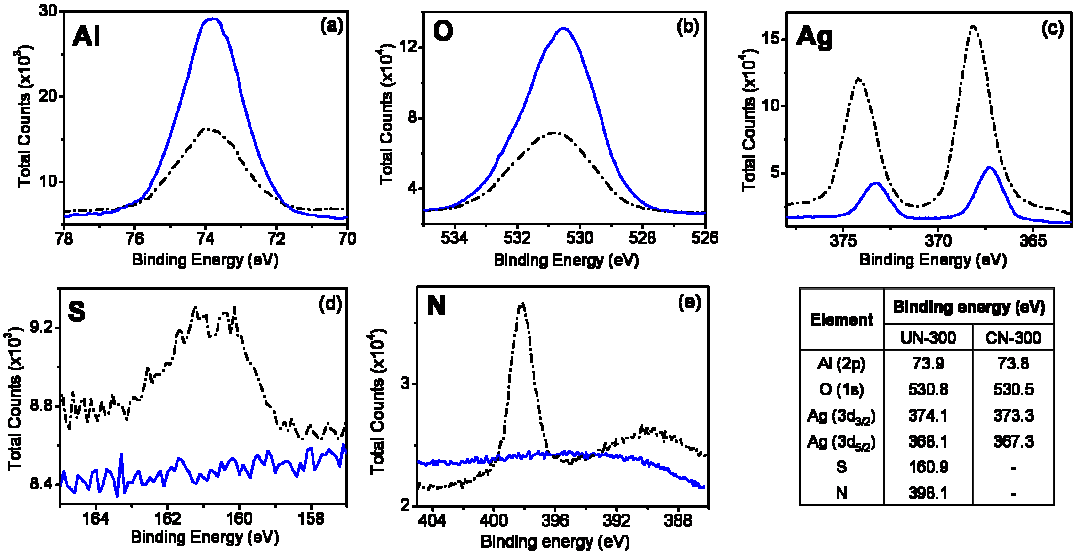

Element	Binding energy (eV)	
	UN-300	CN-300
Al (2p)	73.9	73.8
O (1s)	530.8	530.5
Ag ($3d_{3/2}$)	374.1	373.3
Ag ($3d_{5/2}$)	368.1	367.3
S	160.9	-
N	398.1	-

Figure 4.12: XPS spectra of UN-300 (dash-dot black curves) and CN-300 (solid blue curves) films corresponding to (a) Al 2p, (b) O 1s, (c) Ag 3d, (d) S 2p and (e) N 1s levels. The included table lists the binding energies (in eV) of the relevant elements found in the films.

These results allow us to point out three main facts. First, from Figures 4.12a and b we can conclude that the XPS signal coming from O is substantially related to the matrix. Indeed, in both cases, the measured binding energy for Al and O corresponds to the values measured for Al_2O_3.[27] Second, Figure 4.12c gives qualitative information about the oxidation state of Ag nanoparticles. In the case of the CN-300 film the binding energy of the Ag $3d_{5/2}$ level is 367.3 eV and the corresponding modified Auger parameter α* is 726.03, thus confirming that nanoparticles are made of metallic Ag.[27] However, in the case of the UN-300 film the Ag $3d_{5/2}$ peak is located at 368.1 eV and the corresponding α* is 722.54. These results are far from those typical of metallic Ag and are consistent with the tarnishing of Ag nanoparticles. The determination of the compound formed would require a more detailed chemical analysis. Nevertheless, the presence of S in the UN-300 film suggests the formation of compounds including this element such as silver sulphide,[23,24] whereas we can not rule out completely nanoparticle oxidation.[25] The role of N in Ag nanoparticle deterioration process is not clear at all,[25] since silver nitrates are usually not included in the possible product of Ag reaction with atmospheric contaminants.[24]

To conclude, we propose a microscopic interpretation to the trend observed in Figure 4.10b, which shows that the peak of the SPR weakens and blue-shifts with aging. The SPR evolution micht be interpreted in terms of the formation of a shell made of tarnished Ag

around metal nanoparticles whose thickness increases with time.[23] As the thickness of the shell increases, the nanoparticle metal core shrinks. Thus, a smaller Ag volume contributes to light absorption, which decreases the SPR peak intensity. In addition, due to the already initial reduced size of nanoparticles in UN-300 film, the additional shrinkage of the metal core related to the formation of the shell is likely to promote unconventional finite size effects,[8,28,29] which tend to blue-shift the surface plasmon resonance, in competition with the SPR red-shift usually reported in literature that is related to the increase in the refractive index of the medium surrounding nanoparticles.[23]

4.3 COVERED NANOSTRUCTURED FILMS

In this section we focus on two chemically stable nanostructured films, namely CN-300 and CN-900. As in the case of uncovered nanostructures, we first analyze the morphology and then we study the optical response of the films to figure out any possible change promoted by the deposition of the covering layer. In this sense, we also discuss and model the observed change in film morphology in the case of CN-300 with respect of UN-300 in terms of Ag sputtering promoted by the incoming Al ions.

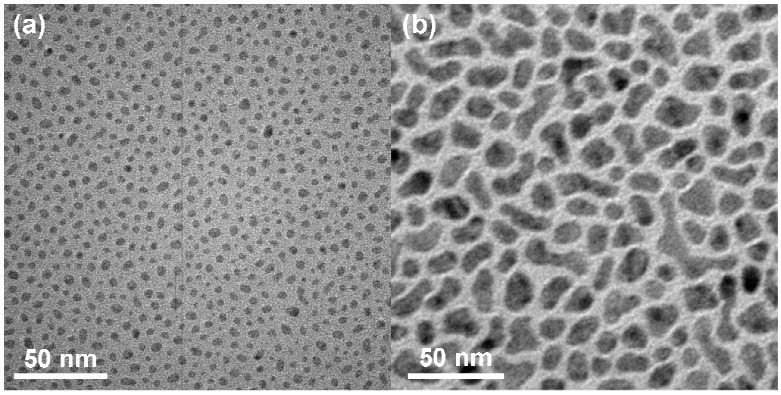

Figure 4.13: Plan-view TEM images of (a) CN-300 and (b) CN-900 films grown on C-mica.

4.3.1 Morphology

Figure 4.13 shows plan-view TEM images of (a) CN-300 and (b) CN-900 films grown on C-mica. CN-300 film consists of a single layer of isolated small nanoparticles whose in-plane projected shape is mainly circular or slightly elliptical, their in-plane long axis being randomly oriented. The nanoparticle density and surface coverage are 2.2×10^4 NPs μm^{-2} and 25%, respectively. The nanoparticles size distribution is quite homogeneous as shown by the

narrow histogram in Figure 4.14a. The in-plane long axis length value remains in the 3-12 nm range, the average value being $<L_{CN\text{-}300}> = 5$ nm.

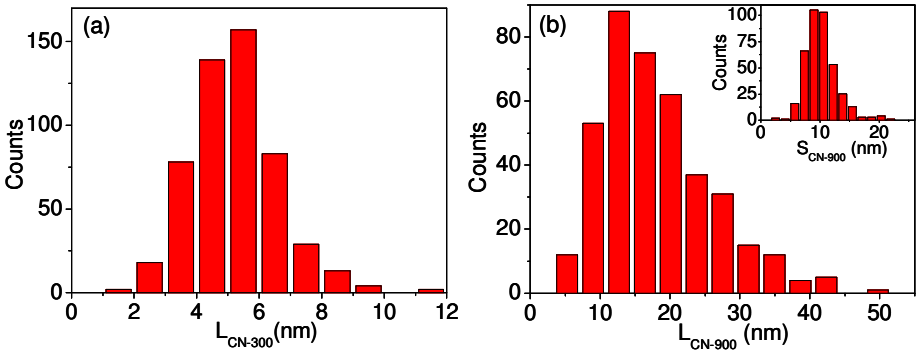

Figure 4.14: Nanoparticle in-plane long axis length distribution of (a) CN-300 and (b) CN-900 films. The inset in (b) corresponds to the nanoparticle in-plane short axis length distribution of UN-900.

The morphology of CN-900 (Figure 4.13b) is completely different. It mainly consists of a layer of randomly distributed and oriented partially coalesced Ag nanoparticles elongated in shape. The surface coverage is close to 43% and the nanoparticle density approximately 2.4×10^3 NPs μm^{-2}. The nanoparticle average in-plane long and short axis lengths (Figure 4.14b) are $<L_{CN\text{-}900}> = 20$ nm and $<S_{CN\text{-}900}> = 11$ nm.

If we compare the morphology of the covered films (Figure 4.13) with that of the corresponding uncovered films (Figure 4.4), we observe many differences, in particular in the case of CN-300 film (Figure 4.13a). The most evident change from the corresponding uncovered film, UN-300 (Figure 4.4a), is that no chainlike structures are seen. Simultaneously, the densely packed nanoparticle assembly characterizing the UN-300 film is lost and only well separated nanoparticles are observed in CN-300 film. This is further supported by the statistics performed on the images. We observed that $L_{CN\text{-}300} \leq 12$ nm while $L_{UN\text{-}300}$ could be as large as 22 nm, which is consistent with the disappearance of the chainlike structures. In addition, the nanoparticle surface coverage decreases from 50% in UN-300 to 25% in CN-300 film, whereas the nanoparticle density increases from 1.3×10^4 NPs μm^{-2} to 2.2×10^4 NPs μm^{-2}. In the case of CN-900 film (Figure 4.13b), the differences with respect to UN-900 film (Figure 4.5b) are smaller than in the case of CN- and UN-300 films. After deposition of the covering layer, the nanoparticle in-plane aspect ratio ($<L>/<S>$) slightly increases, from 1.4 to 2, the surface coverage keeps almost unchanged while the nanoparticle density increases from 1.8×10^3 NPs μm^{-2} to 2.4×10^3 NPs μm^{-2}. As a result nanoparticles come

closer. In addition, as evidenced from the histograms shown in Figures 4.13b and 4.6b, nanoparticles with L < 4 nm are not seen in CN-900 film.

Unlike the case of uncovered nanostructured films, we were able to perform TEM in cross-section mode. This was possible because the covering layer was robust enough to avoid film damaging during the preparation of TEM cross-section sample. Figure 4.15 shows cross-section TEM images corresponding to CN-300 (left panel) and CN-900 (right panel) films grown on Si. The number of laser pulses used to deposit the a-Al_2O_3 buffer layer was 1270 and 3000 in CN-300 and CN-900 films, respectively, while for the deposition of covering layer we used 1270 and 6560 pulses for CN-300 and CN-900 films, respectively. The sketches at the sides of the images help to distinguish the different layers constituting the films. The Si substrate and the glue used for TEM sample preparation are at the bottom and the top of the images, respectively. The a-Al_2O_3 buffer and covering layers, represented by blue areas in the sketches and characterized by light contrast in the images, are observed as an homogeneous layer between the Si substrate and the glue. The layer of Ag nanoparticles (red and orange areas in the sketches and dark contrast in the images) correspond to the elements embedded between of the buffer and covering layers. Finally, in both images a very thin bright layer of native SiO_2 (~2 nm thick) is also observed at the buffer layer/Si interface.

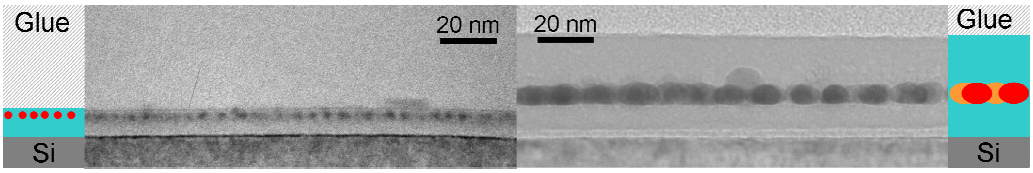

Figure 4.15: Cross section TEM images of (left panel) CN-300 and (right panel) CN-900 films. The sketches at the side of the TEM images help to distinguish the different layers constituting the films.

The images show that nanoparticles nicely lie on a single-plane with no evidence of implanted subsurface nanoparticle layer. The height (H) of nanoparticles is almost constant, being $H_{CN\text{-}300} \approx 3.6$ and $H_{CN\text{-}900} \approx 7$ nm. The nanoparticle height of CN-900 film is thus larger, as otherwise expected, due to the larger amount of deposited Ag in the nanostructure. We then estimated the nanoparticle height-to-average in-plane diameter ratio to be 0.7 and 0.5 for CN-300 and CN-900, respectively, where the average in-plane diameter was defined as $(\langle L_{CN}\rangle+\langle S_{CN}\rangle)/2$. The result obtained suggests that the ratio decreases for increasing amount of deposited Ag which is consistent with coalescence of the nanoparticles that favours the increase of their lateral size rather than of their height.[7,10]

Figure 4.15 also shows that the buffer layers are 5 and 10 nm thick in CN-300 and CN-900 films, respectively, and, thus, in good agreement with the estimated nominal thicknesses (number of pulses × deposition rate). This confirms the suitability of the optical characterization techniques (Chapter 2) to estimate the material deposition rates and it remarks the precise control we can achieve on the growth of the oxide layers and, as a consequence, on the in-depth distribution of Ag nanoparticles. The fact that nanoparticles lie on a single plane hints at the reduced roughness of the buffer layer surface. In particular, we found that the roughness of an a-Al_2O_3 calibration film measured using an Atomic Force Microscopy was better than 0.5 nm,[30] a result that is consistent with the fact that a-Al_2O_3 grows following the Frank-van-der-Merwe mode. The a-Al_2O_3 covering layers are flat, showing no corrugation due to the presence of the underlying nanoparticle layer. Their thickness, measured by neglecting the amount of material filling the space between nanoparticles, are 0.5 and 16 nm in CN-300 (Figure 4.15a) and CN-900 (Figure 4.15b) films, respectively. This result remarks the precise control achieved over nanoparticle layer positioning, not only with respect to the substrate, but also with respect to the surface exposed to external environment.

The comparison of the morphology shown in Figures 4.13 and 4.15 evidences two very interesting effects that can be associated to the deposition of the a-Al_2O_3 covering layer. First, the drastic morphology change observed in CN-300 compared to UN-300 film and second the disappearance of small nanoparticles in CN-900 film. As we introduced in Chapter 2, the properties of the films grown by PLD can be strongly determined by energetic ions and, in particular, we pointed out that ions having kinetic energies larger than 200 eV could promote material implantation and sputtering. In Chapter 3, we evidenced that the fraction of energetic ions in the Al_2O_3 plasma is 60% of the total at the laser fluence used for film growth, which points out that those effects can be relevant in our case. In the next section, we address this question by describing the covering layer effects as a result of Ag removal in terms of sputtering.

4.3.2 Silver removal and sputtering model

In order to reveal any effect on nanoparticle morphology due to Ag sputtering during the deposition of the a-Al_2O_3 covering layer, we limit our discussion to the case of the UN-300 and CN-300 films pair, since the observed changes are remarkably pronounced (Figures 4.4a and 4.13a). In order to measure the Ag loss during deposition of a-Al_2O_3 covering layer, we

measured the Ag content ([Ag], see section 2.4.2 of Chapter 2) of a set of films with similar characteristics to those described in section 4.2.3, i.e. films containing the same amount of Ag and covered with an a-Al_2O_3 layer of increasing thickness. Figure 4.16 shows the evolution of [Ag] with the number of pulses used to deposit the a-Al_2O_3 covering layer.

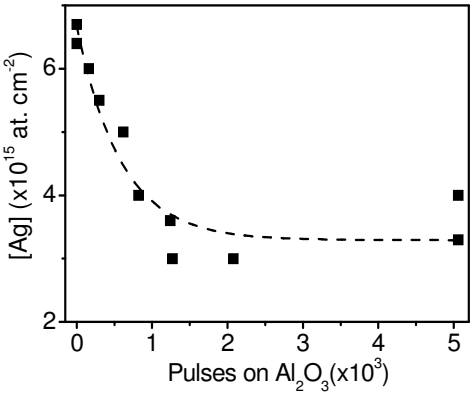

Figure 4.16: [Ag] content, as determined by RBS, in the films as a function of the number of pulses on Al_2O_3 used to deposit the a-Al_2O_3 covering layer.

[Ag] is close to 7×10^{15} atoms cm^{-2} for the UN-300 film and decreases almost exponentially as the number of pulses on the Al_2O_3 target increases, until it reaches a value of approximately 3.5×10^{15} atoms cm^{-2} for ≈1200 pulses on Al_2O_3, while for larger number of pulses, [Ag] remains almost constant.

The observed evolution of [Ag] in the films as a function of the number of laser pulses on the Al_2O_3 target confirms that the differences observed between the morphology of UN-300 (Figure 4.4a) and CN-300 (Figure 4.13a) films relate to the loss of Ag that takes place during deposition of the a-Al_2O_3 covering layer. In particular, we observe that the amount of Ag removed can be as high as ≈ 3.3×10^{15} atoms cm^{-2}, which corresponds to almost 50% of the initial amount of deposited Ag. The [Ag] evolution also suggests that the amount of Ag removed per pulse decreases as the thickness of the covering layer increases up to a thickness corresponding to ≈1200 laser pulses on Al_2O_3 target, after which the loss of Ag is negligible. In Figure 4.15a we observed that for a number of laser pulses equals to 1270, nanoparticles were buried under a continuous a-Al_2O_3 layer 0.5 nm thick. We can thus conclude that Ag removal stops as soon as nanoparticles are completely covered.

We ascribed these results to the sputtering of Ag atoms induced by the species arriving to the film during the deposition of the a-Al_2O_3 covering layer. To verify this assumption, we modelled the sputtering process using the approach we developed in a previous work that is

based on the SRIM 2008 software.[31,32] The main advantage of this method with respect to alternative standard analytical models[33,34] is that it allows taking into account the progressive growth of the covering layer on top of nanoparticles.[31] SRIM 2008 is a collection of software packages which allows calculating many features of the transport of ions in matter such as ion stopping and implantation and sputtering. In the latter case, SRIM 2008 allows estimating the sputtering yield (Y) that corresponds to the average number of atoms removed from the target surface (a bulk material or a film) per incident projectile (the impinging ion). Then, the amount of sputtered Ag per pulse on Al_2O_3 can be estimated as:[31]

$$[Ag]_{Sputt\,/\,pulse} = \int Q_{Al_2O_3} N_{Al_2O_3}(E) Y_{Ag}(E) dE \qquad (4.2)$$

where Q_{Al2O3} is the ion yield obtained upon ablation of Al_2O_3 target, $N_{Al2O3}(E)$ is the normalized Al_2O_3 ion kinetic energy distribution and $Y_{Ag}(E)$ is the kinetic energy dependent sputtering yield for Ag. In the present case, the value of $Q_{Al2O3} = 6.3\times10^{13}$ ions cm^{-2} and $N_{Al2O3}(E)$ are those experimentally obtained from Langmuir probe measurements at 2.5 J cm^{-2}, the laser fluence used for film growth, and reported in Chapter 3.

In order to calculate $Y_{Ag}(E)$, we consider Al ion as the projectile impinging on the target surface. This is consistent with the results reported in Chapter 3 showing that Al ions are the most abundant and energetic species in the Al_2O_3 laser-generated plasma. In addition, the target considered for estimating $Y_{Ag}(E)$ is a multilayered structure whose characteristics resemble those of CN-300 film (Figure 4.15a). The structure consists of an infinite silicon substrate that at its top has a 2.5 nm thick amorphous silica layer, the native oxide layer of Si substrates. On top of the amorphous silica we have an a-Al_2O_3 layer 5 nm thick (a-Al_2O_3 buffer layer) and finally a 3.6 nm thick Ag layer. The progressive growth of the a-Al_2O_3 covering layer is modeled by adding to the described structure an a-Al_2O_3 layer of selected thickness (0.1, 0.25, 0.5, 0.9 nm) on top of the Ag layer. In addition, since SRIM 2008 does not allow considering discontinuous layers like nanoparticles, the obtained Y_{Ag} are then weighted by the Ag surface coverage determined from TEM images: approximately 50% (Figure 4.4a) for a covering layer thickness < 0.2 nm and 25% (Figure 4.13a) for thicker covering layer. Figure 4.17 schematically shows the modeled multilayered structure. We consider Al ions to impinge on the film only at normal incidence.[31]

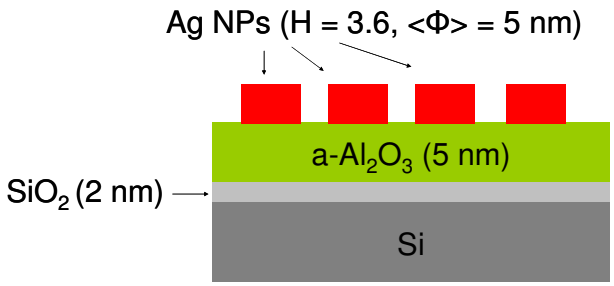

Figure 4.17: Schematic representation of the structure used for modeling Ag sputtering induced by Al ions using SRIM 2008.

Besides the thickness of the layers constituting the modeled structures and the energy of the ion bombarding the film surface, the additional parameters that determine the values of $Y_{Ag}(E)$ are the density of the material and its displacement, surface binding and lattice binding energies.[31] In sputtering, the surface binding energy plays a key role since it represents the energy that target atoms must overcome to leave the surface.[31] In our model, we used theAg bulk values for the density (ρ= 10.47 g cm^{-3}), lattice binding energy (3 eV) and displacement energy (25 eV), whereas we replaced the surface binding energy with the Ag cohesive energy (the energy needed to break the bond between metal atoms),[35] since it could be corrected for the finite size effects that reduce the stability of the Ag nanoparticles with respect to bulk Ag.[36,37] We estimate its value using the equation proposed in literature for freestanding spherical nanoparticles:[32,36]

$$E_{CC} = E_{CB}\left(1 - \frac{3}{4}\alpha\right) \tag{4.3}$$

where E_{CC} and E_{CB} are the corrected and bulk cohesive energies, respectively, and α the surface-to-volume atomic ratio:[32,36]

$$\alpha = \frac{3d}{4R} \tag{4.4}$$

where d is the atom diameter and R the nanoparticle radius. In the case of Ag, d = 0.288 nm,[38] while R is taken equal to $<L_{UN\text{-}300}>/2$ = 2.5 nm. In this way, we obtained $E_{CC\ UN\text{-}300}$ = 2.4 eV. In the case of amorphous SiO_2 and a-Al_2O_3 we have considered the bulk parameters except for the density of the latter for which we used the value ρ = 2.95 g cm^{-3} determined previously by the LPG for a-Al_2O_3 films fabricated under similar conditions.[39]

Figure 4.18a shows the calculated Ag sputtering yield as a function of the kinetic energy of incident Al ion and for increasing covering layer thickness.

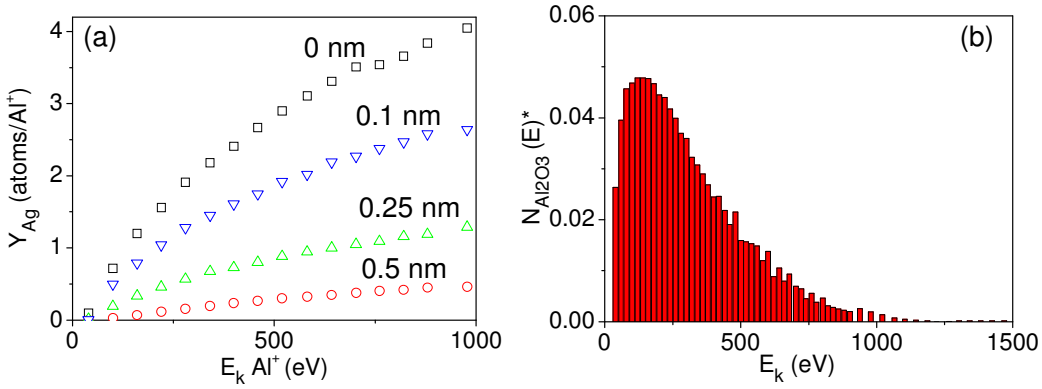

Figure 4.18: (a) Ag sputtering yield as a function of the kinetic energy of Al ions for films covered with a-Al_2O_3 layers having thickness in the 0-0.5 nm range. (b) Discretized Al_2O_3 ion kinetic energy distribution at a laser fluence of 2.5 J cm^{-2}.

In the case of uncovered nanoparticles, i.e. UN-300 film, the number of Ag atoms removed by a single Al ion is above 1 for incident kinetic energies higher than 160 eV, which is in good agreement with the assumption earlier reported in literature that the ions promoting sputtering are those with kinetic energy higher than 200 eV.[32,40] Y_{Ag} decreases when an a-Al_2O_3 layer is added on top of that of Ag in the modelled structure. The thicker the added layer the lower the Y_{Ag}. Using the Y_{Ag} values calculated from SRIM 2008 (Figure 4.18a) and the $N(E)_{Al2O3}$ discretized to the energy values considered in sputtering model that is shown in Figure 4.18b, we can obtain from equation (4.2) the total amount of sputtered atoms per cm^2 and pulse as a function of the thickness of the covering layer. The results obtained are shown in Figure 4.19.

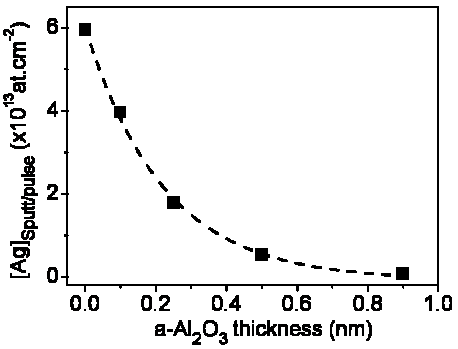

Figure 4.19: Calculated sputtered Ag atoms per laser pulse as a function of the thickness of the a-Al_2O_3 covering layer. The dashed line is an exponential decay fit to the calculated points.

The number of sputtered atoms per pulse is very high for uncovered nanostructures ($\approx 6\times10^{13}$ atoms cm^{-2}), but it decreases exponentially as the covering layer becomes thicker. Finally, we obtain the total amount of sputtered atoms, $[Ag]_{Sputt\text{-}SRIM}$, by integrating the curve in Figure 4.17c. The result is $[Ag]_{Sputt\text{-}SRIM} \approx (3.2 \pm 0.5)\times10^{15}$ atoms cm^{-2}, which is in very good agreement with the experimental value obtained from RBS, $[Ag]_{Sputt\text{-}RBS} \approx 3.3\times10^{15}$ atoms cm^{-2}.

The obtained result nicely confirms that the Ag removal occurring during covering layer deposition can be related mostly to Ag sputtering induced by Al ions in the Al_2O_3 laser-generated plasma. This effect is responsible for the removal of almost 50% of the initial amount of deposited Ag, which results in a drastic change of initial nanoparticle morphology and spatial arrangement. CN-300 only shows relatively small, well separated nanoparticles with almost circular in-plane projected shape contrary to the case of UN-300, which shows a densely packed layer of nanoparticle also including the nanoparticle chainlike structures. In addition, the better agreement between experimental and modelled data obtained in the present case with respect to earlier work,[32] support that the implementation of a proper ion kinetic energy distribution (Al_2O_3 instead of Al) can improve the accuracy of the model.

In the case of UN-900 films, we observed that after deposition of the covering layer (CN-900 films) nanoparticle morphology remains almost unchanged apart from small nanoparticles ($L < 4$ nm) that disappear. We already pointed out that the probability of an atom to be removed through sputtering is strongly related to the material cohesive energy which, in the case of nanoparticles, is strongly related to the nanoparticle size (equation (4.3)).[36,37] Taking this into account, we can deduce that during covering of UN-900 film small nanoparticles are removed via Ag sputtering, while large nanoparticles are only partially affected due to the increased stability. This reduced sputtering effect during covering of large nanoparticles will be discussed in next chapter.

Finally, the deposition of a flat a-Al_2O_3 covering layer surface (Figure 4.15) can be also ascribed to preferential sputtering of Ag. In the first stages of growth, while the space between Ag nanoparticles is being filled by the dielectric host, the energetic Al_2O_3 plasma species arriving on top of Ag nanoparticles are likely to contribute to its sputtering rather than to be deposited on them, which avoids the replication of the nanoparticle topography at the surface level.

4.3.3 Optical response

In previous sections, we have shown that the deposition of an a-Al_2O_3 covering layer on top of Ag nanoparticles guarantees the chemical and, subsequently, the optical stability of fabricated nanostructured films and, simultaneously, it promotes important changes in the nanoparticle morphology, mainly in the case of CN-300 films. Besides these effects, the deposition of the covering layer is also expected to influence the optical response of the films, since the SPR is sensitive to the change of the refractive index of the material surrounding nanoparticles.[41,42] We dedicate this section to investigate the optical response of the covered nanostructures. Figure 4.20 shows the optical extinction spectra of CN-300 and CN-900 films grown on fused silica.

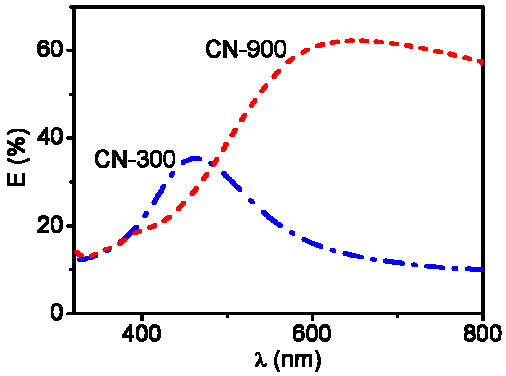

Figure 4.20: Extinction spectra of CN-300 and CN-900 films.

The spectrum corresponding to CN-300 film shows a narrow and relatively weak extinction band peaking at 465 nm with a FWHM ≈ 130 nm. The spectrum related to CN-900 film shows a much more intense (up to 60%) and broad (FWHM ≈ 680 nm) main extinction band peaking at approximately 640 nm. In the case of CN-900 an additional and very weak extinction band peaking at 395 nm is also observed.

The observed extinction bands are obviously related to the excitation of the SPR.[8,9] As already discussed in the case of uncovered nanostructured films, the differences between the optical response of the CN-300 and CN-900 films are mainly related to the different nanoparticle morphology (Figure 4.13). Larger nanoparticles lead to a more efficient light absorption resulting in a more intense extinction band, while the SPR broadening and red-shift observed for CN-900 is most likely related to interparticle coupling arising between

nanoparticles separated by very small gap and to the broader nanoparticle size and shape distributions (Figure 4.14).[9,10,11]

It is worth mentioning here that the extinction spectra of UN-300 and CN-300 films show very similar optical response. The position, width and intensity of the peak keep almost unchanged after deposition of the covering layer, irrespective of the changes underwent by nanoparticle morphology after covering and of the changed optical properties of the material surrounding nanoparticles (from air to a-Al_2O_3). On the contrary, spectra clearly differ in the case of UN-900 and CN-900 films. After deposition of the a-Al_2O_3 covering layer, the main and weak peaks are red-shifted (the main one from 515 to 640 nm), broadened (FWHM from 220 to 680 nm) and they are slightly more intense (the maximum of extinction increases from 54% to 62%).

The optical response of nanostructured films containing metal nanoparticles is known to shift toward longer wavelengths when the refractive index of the medium surrounding nanoparticles increases.[11,41,42] In our case, the refractive index increase from ≈ 1 to 1.67 when nanoparticles are exposed to air or embedded in the a-Al_2O_3 matrix, respectively. Thus, this can explain why the extinction band observed in the case of CN-900 film is red-shifted with respect to that of UN-900 film. However, the situation is different in the case of UN-300 and CN-300 films, since the SPR remains almost unchanged upon deposition of the covering layer. The morphology of CN-300 film is completely different from that of UN-300. After covering, the nanoparticle density increases whereas the surface coverage becomes half of the initial one, thus resulting in well separated nanoparticles. According to the results shown in Figure 4.8b, an increase of nanoparticle separation can lead to a SPR blue-shift. The similar optical response of UN-300 and CN-300 films is thus likely due to the increase of nanoparticle separation that leads to a SPR blue-shift that can compensate the red-shift induced by the increase of the refractive index related to the deposition of the covering layer. Moreover, the similar intensity of the extinction band for UN-300 and CN-300 films despite the different metal content, $[Ag]_{CN\text{-}300} \approx 0.5\ [Ag]_{UN\text{-}300}$ is consistent with the increased film reflectance after deposition of the covering layer.

4.4 CONCLUSIONS

In this chapter we first confirm that PLD is suitable for fabrication of nanostructured films containing Ag nanoparticles. The size of Ag nanoparticles strongly depends on the number of laser pulses used to ablate the target that determines the amount of deposited metal.

Nonetheless, when the percolation limit is reached, no more isolated features are observed and an almost continuous Ag film is formed.

In addition, we observed that Ag nanoparticles exposed to air suffer from tarnishing that leads to deterioration of the nanostructured films for long exposure times. The film becomes progressively transparent and the SPR damps with time. Several elements (O, S and N) can react with Ag which makes difficult identifying the chemical state of tarnished Ag with the performed experiments. We have demonstrated that Ag tarnishing can be prevented by deposition of an ultrathin (< 1 nm) a-Al_2O_3 film layer on top of nanoparticles. This result is most likely related to the low porosity of the a-Al_2O_3 layer which avoids contaminant diffusion.

Finally, we show that the deposition of the covering layer strongly influences the morphology of the nanostructured films, particularly in the case of films containing low amount of Ag (UN-300). We found that these changes can be related to Ag sputtering promoted by energetic Al ions during the deposition of the covering a-Al_2O_3 layer, which leads to removal of 50% of the initial amount of deposited Ag.

Uncovered nanostructured films show an optical response characterized by an extinction band related to the SPR of nanoparticles. Only in the case of percolated films, i.e. almost continuous Ag layer, the resonant behaviour is lost. The deposition of the covering layer influences the optical response of the nanostructured films. In the case of partially coalesced nanoparticles, i.e. CN-900 films, the SPR is red-shifted with respect to the case of uncovered films as a direct consequence of the increase of the refractive index of the material surrounding nanoparticles. Instead, in the case of small nanoparticles, i.e. CN-300 films, the SPR position is similar to that observed in the case of uncovered nanostructures, which can be related to the increased separation between nanoparticles and, hence, to a decrease of interparticle coupling effect (i.e., SPR red-shift).

References

(1) N. Kaiser, Applied Optics **41**, 3053-3060 (2002)

(2) J. S. Horwitz, J. A. Sprague In *Pulsed Laser Deposition of Thin Films*. Edited by D. B. Chrisey, G. K. Hubler (Wiley, New York 1994). Chapter 8

(3) A. Zenkevitch, J. Chevallier, I. Khabelashvili, Thin Solid Film **311**, 119-123 (1997)

(4) R. Dolbec, E. Irissou, M. Chaker, D. Guay, F. Rosey, M. A. El Khakani, Phys. Rev. B **70**, 201406(R) (2004)

(5) J. M. Warrender, M. J. Aziz, Phys. Rev. B **76**, 045414 (2007)

(6) V. Resta, C. N. Afonso, E. Piscopiello, G. Van Tendeloo, Phys. Rev. B **79**, 235409 (2009)

(7) J.-P. Barnes, A. K. Petford-Long, R. C. Doole, R. Serna, J. Gonzalo, A. Suárez-García, C. N. Afonso and D. Hole, Nanotechnology **13**, 465-470 (2002)

(8) U. Kreibig, M. Volmer In *Optical Properties of Metal Clusters*. Edited by Springer Verlag, Berlin 1995

(9) T. Jensen, L. Kelly, A. Lazarides, G. C. Schatz, J. Cluster Sci. **10**, 295-317 (1999)

(10) J. Gonzalo, R. Serna, J. Solís, D. Babonneau, C. N. Afonso, J. Phys.: Condens. Matter **15**, S3001-S3010 (2003)

(11) G. Xu, M. Tazawa, P. Jin, S. Nakao, Appl. Phys. A **80**, 1535-1540 (2005)

(12) G. Baraldi, M . Carrada, J. Toudert, F. J. Ferrer, A. Arbouet, V. Paillard, J. Gonzalo, J. Phys. Chem. C **117**, 9431-9439 (2013)

(13) J. Toudert In *UV-VIS and Photoluminescence Spectroscopy for Nanomaterials characterization*. Edited by Challa S. S. R. Kumar (Springer-Verlag Berlin Heidelberg 2013)

(14) B. Khlebtsov, A. Melnikov, V. Zharov, N. Khlebtsov, Nanotechnology **17**, 1437 (2006)

(15) R. Lazzari, I. Simonsen, Thin Solid Films **419**, 124-136 (2002)

(16) R. Lazzari, J. Jupille, Nanotechnology **22**, 445703 (2011)

(17) H. E. Bennett, R. L. Peck, D. K. Burge, J. M. Bennett, J. Appl. Phys. **40**, 3351 (1969)

(18) T. E. Graedel, J. P. Franey, G. J. Gualtieri, G. W. Kammlott, D. L. Malm, Corros. Sci. **25**, 1163-80 (1985)

(19) V. Antad, L. Simonot, D. Babonneau, S. Camelio, F. Pailloux, P. Guérin, J. Nanophoton. 6, 061502 (2012)

(20) T. W. H. Oates, M. Losurdo, S. Noda, K. Hinrichs, J. Phys D: Appl. Phys. **46**, 145308-145314 (2013)

(21) W. Cai, H. Zhong, L. Zhang, J. Appl. Phys. **83**, 1705-1710 (1998)

(22) H. Bi, W. Cai, C. Kan, L. Zhang, D. Martin, F. Träger, J. Appl. Phys. **92**, 7491-7497 (2002)

(23) M. D. Mcmahon, R. Lopez, H. M. Meyer, L. C. Feldman, R. F. Haglund, Appl. Phys. B : Laser Opt. **80**, 915-921 (2005)

(24) J. L. Elechiguerra, L. Larios-Lopez, C. Liu, D. Garcia-Gutierrez, A. Camacho-Bragad, M. J. Yacaman, Chem. Mater. **17**, 6042-6052 (2005)

(25) R. J. Peláez, A. Castelo, C. N. Afonso, A. Borrás, J. P. Espinós, S. Riedel, P. Leiderer, J. Boneberg, Nanotechnology **24**, 365702-365710 (2013)

(26) K. Luo, X. Lai, C.-W. Yi, K. A. Davis, K. K. Gath, D. W. Goodman, J. Phys. Chem. B **109**, 4064-4068 (2005)

(27) http://srdata.nist.gov/xps/Default.aspx

(28) W. Cai, H. Hofmeister, M. Dubiel, Eur. Phys. J. D **13**, 245-253 (2001)

(29) J. Lermé, B. Palpant, B. Prével, M. Pellarin, M. Treilleux, J. L. Vialle, A. Perez, M. Broyer, Phys. Rev. Lett. **80**, 5105-5108 (1998)

(30) G. Baraldi, E. Lopez-Tobar, K. Hara, S. Sanchez-Cortes, J. Gonzalo, J. Phys. Chem. C **118**, 4680-4686 (2014)

(31) J. F. Ziegler, http://www.srim.org/

(32) V. Resta, J. Gonzalo, C. N. Afonso, E. Piscopiello, J. Garcia-Lopez, J. Appl. Phys. **109**, 094302 (2011)

(33) P. C. Zalm, J. Vac. Sci. Technol. B **2, 151** (1984)

(34) Y. Yamamura, H. Tawara, At. Data Nucl. Data tables **62**, 149 (1996)

(35) C. Kittel In *Introduction to Solid State Physics*. 7th Edition. Edited by John & Sons Inc., New York, 1996

(36) D. Xie, M. P. Wang, W. H. Qi, J. Phys.: Condens. Matter **16**, L401-L405 (2004)

(37) W. H. Qi, B. Y. Huang, M. P. Wang, Z. Li, Z. M. Yu, Physics Letters A **370**, 494-498 (2007)

(38) http://www.knowledgedoor.com/

(39) R. Serna, J. C. G. de Sande, J. M. Ballesteros, C. N. Afonso, J. Appl. Phys. **84**, 4509-4516 (1998)

(40) A. Perea, J. Gonzalo, C. Budtz-Jørgensen, G. Epurescu, J. Siegel, C. N. Afonso, J. García-Lopez, J. Appl. Phys. **104**, 084912 (2008)

(41) G. Xu, M. Tazawa, P. Jin, S. Nakao, K. Yoshimura, Appl. Phys. Lett. **82**, 3811 (2003)

(42) J. Toudert, S. Camelio, D. Babonneau, M.-F. Denanot, T. Girardeau, J. P. Espinos, F. Yubero, A. R. Elipe, J. Appl. Phys. **98**, 114316 (2005)

Chapter 5
Post-growth Processing of Nanostructured Silver Films

In this chapter we apply two experimental approaches based on thermal annealing and laser irradiation to modify the morphology and shape and thus, the optical response of as-grown nanostructured Ag films. We first discuss the results obtained upon annealing of percolated Ag films in vacuum and air. We show the differences in nanoparticle morphology arising from the two different annealing environments, we study the optical response of the annealed films and the effects that the deposition of a covering layer has on nanoparticle assembly. In the second part of the chapter, we discuss the effects laser irradiation has on the shape and optical response of covered nanostructured films containing partially-coalesced Ag nanoparticles. In particular, we analyze the relation between nanoparticle reshaping and three main parameters: laser pulse duration, wavelength and fluence. We finally discuss the observed results in terms of thermal and non-thermal reshaping mechanisms.

5.1 THERMAL ANNEALING OF NANOSTRUCTURED FILMS: A SIMPLE WAY TO OVERCOME THE PERCOLATION LIMIT

Nanoparticles with size in the 100-200 nm range show enhanced far-field scattering at the SPR[1] which make them suitable for applications in optoelectronic devices such as photodetectors[2] and solar cells.[3] In section 4.2.1 we showed that above the percolation limit, Ag forms an almost continuous film, resulting from progressive nanoparticle coalescence. Qualitatively, we observed that the percolation threshold is almost reached when nanoparticles with typical size in the 50-60 nm range are formed. It is thus clear that percolation represents an intrinsic limit of the Volmer-Weber film growth mode to the spontaneous formation of nanoparticles that can scatter light efficiently. Many of the experimental approaches that have been developed to overcome this limitation are based on solid-state dewetting of thin-films.[4,5] This is a physical phenomenon that consists in the rupture of the thin film on an inert substrate when heated to sufficiently high temperatures, usually below the film melting point, leading to the formation of separated islands. It is caused by the thermodynamic instability characteristic of thin films and by the increase of atom mobility promoted by the temperature increase. The driving force during dewetting is the minimization of the total free surface energy of the film and substrate, and of the film/substrate interface.[4,5]

Qualitatively, dewetting takes place at preexisting holes or film edges, or requires the formation of new holes. The holes then grow to form dewetted regions that eventually overlap so that the entire film is dewetted.[4] As a result of surface energy minimization, dewetting ideally promotes the formation of spherical droplets. So far, dewetting of (metallic) thin films was considered only as an undesired effect in electronics since it can lead to degradation of electronic microdevices and systems, especially at high-temperatures operation.[4] However, recently, dewetting has received much more attention as a simple self-assembly method that allows the fabrication of metallic and alloyed nanoparticles at large-scale, with interesting characteristics for many applications.[4,5] The result of dewetting usually consists in an assembly of metallic nanoparticles whose characteristics depend on different parameters, like annealing temperature, initial film thickness and substrate properties (roughness, crystalline or amorphous structure).[6,7,8,9] Dewetting can be achieved, for example, by thermal[6,7,8,9] and laser annealing[10,11], or alternatively, by irradiating the film using ion and electron beams.[5] Nonetheless, thermal annealing is probably the simplest way to promote dewetting, particularly when working on large areas.

In this section, we first study the effect that thermal annealing performed in different environments has on the morphology and optical response of percolated Ag films fabricated by PLD. Then, we investigate the effect that the deposition of a covering layer has on the large nanoparticles formed upon annealing.

5.1.1 Morphology of dewetted Ag films

We annealed in vacuum and in air percolated films produced using 4200 pulses to ablate Ag target (i.e. UN-4200). In the first case we used the heater coupled to the substrate holder mechanism, while in the second we used the commercial oven. Both setups have been described in Chapter 2. Hereafter, we present the most representative results obtained varying both the annealing time and temperature.

Figure 5.1 shows plan-view TEM images of UN-4200 films grown on Si (a) just after deposition (as-grown film) and after 70 minutes of thermal annealing (b) in vacuum at 400º C and (c) in air at 300ºC. From now on, we will refer to the annealed films as UNv-4200 and UNa-4200, where the letters "v" and "a" stay for annealing in vacuum and air, respectively.

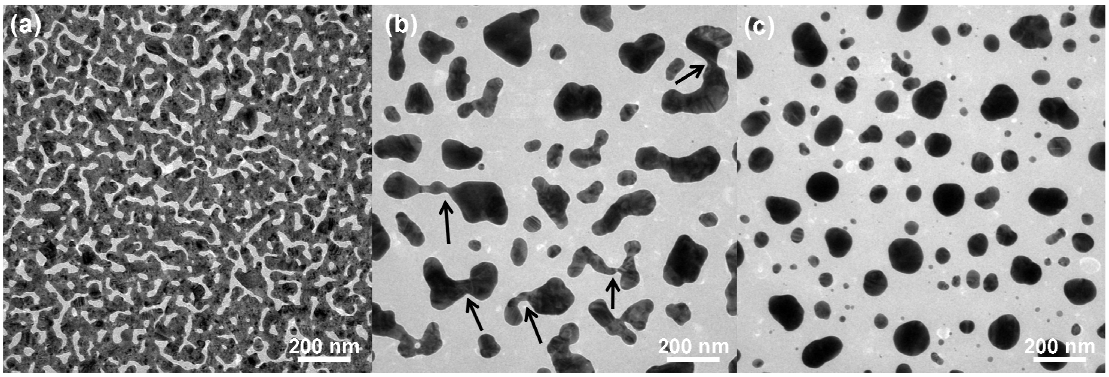

Figure 5.1: Plan-view TEM images of UN-4200 films: (a) as-grown and annealed for 70 minutes (b) in vacuum at 400ºC and (c) in air at 300ºC. The arrows in (b) show the points were nanoparticles may break upon effective annealing.

Figure 5.1a shows that Ag, the dark contrast regions in the image, forms a percolated in the as-grown film, while Figures 5.1b and c show that Ag forms nanoparticles after thermal annealing. The UNv-4200 film (Figure 5.1b) shows very large and elongated nanoparticles with irregular shape together with relatively small nanoparticles having circular or elliptical in-plane projected shapes. The density and surface coverage of large nanoparticles are 14 NPs μm^{-2} and 25%, respectively, while those of small nanoparticles are 7 NPs μm^{-2} and 2%.

Figure 5.2a show the in-plane long axis length distribution corresponding to UNv-4200. The histogram evidences a bimodal length distribution. Small nanoparticles have $<L_{UNv\text{-}4200}>$ ≈ 60 nm, while large ones have $<L_{UNv\text{-}4200}>$ ≈ 200 nm. L can be as long as ≈ 450 nm in the case of large nanoparticles.

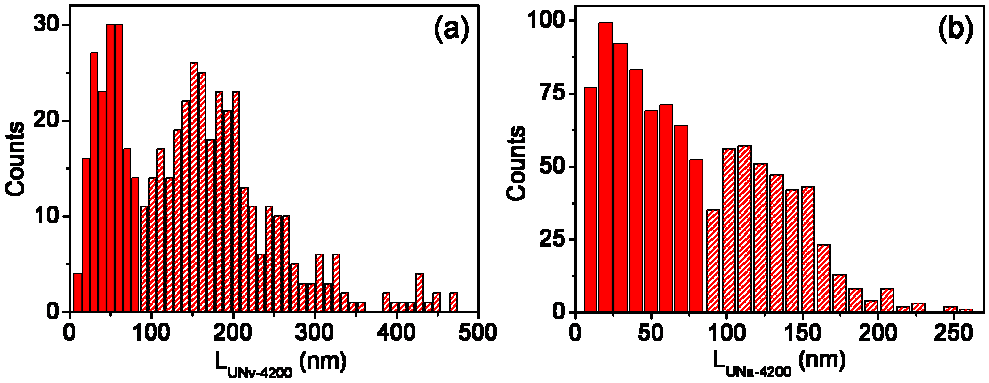

Figure 5.2: In-plane long axis length distribution of (a) UNv-4200 and (b) UNa-4200 films. We use two different colours to better distinguish the bimodal distribution.

The morphology of UNa-4200 film clearly differs from that of UNv-4200 film. We still observe large and small nanoparticles, but in this case all of them show almost circular in-plane projected shape. The density and surface coverage of large nanoparticles are 17 NPs μm^{-2} and 18%, respectively, while those of small ones are 28 NPs μm^{-2} and 4%. Figure 5.2b shows the in-plane long axis length distribution corresponding to UNa-4200 film. A bimodal length distribution is observed in this case, too. Small nanoparticles have $<L_{UNa\text{-}4200}>$ ≈ 50 nm, while large ones have $<L_{UNa\text{-}4200}>$ ≈ 135 nm. In this case the longest L is ≈ 250 nm.

Figure 5.3 shows a SEM cross-section image of the UNa-4200 film grown on Si. The sketch on the right side of the image helps to distinguish the different layers constituting the films, while the dashed line is a guideline to the Si/a-Al_2O_3 buffer layer interface.

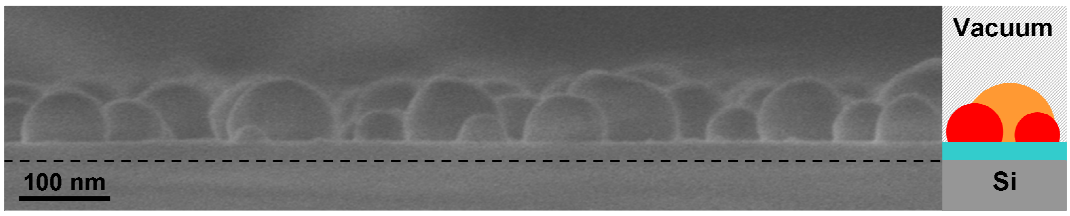

Figure 5.3: Cross-section SEM image of the UNa-4200 film. The sketch on the right side of the TEM image helps to distinguish the different layers constituting the films, while the dashed line is a guideline to the Si/a-Al_2O_3 buffer layer interface.

The Si substrate at the bottom of the image corresponds to the dark grey area. On top of the Si the a-Al_2O_3 buffer layer is hardly distinguished (blue colour in the sketch) due to the resulting contrast similar to that of Si. The buffer layer is ≈ 25 nm thick and its surface is very flat, which allows nanoparticles to be formed in a single plane. The height of the Ag nanoparticle layer (red and orange elements in the sketch) varies from 20 to 70 nm, the height being proportional to the in-plane size, and their shape resembles that of a truncated oblate spheroid.

The results shown in Figures 5.1b and c demonstrate that dewetting of percolated Ag film (Figure 5.1a) takes place both in vacuum and in air. The truncated spheroid shape of nanoparticles in the UNa-4200 film suggests that dewetting in air is more efficient than in vacuum that, instead, leads to the formation of elongated nanoparticles with very irregular shapes. Nanoparticle shape distributions similar those shown in Figure 5.1c have been observed in the case of thermal annealing in N_2 of Ag films with different thicknesses.[8] At moderate annealing temperatures, only thinner Ag films showed nanoparticles with in-plane circular shape, while thicker ones show nanoparticles with irregular shape. By increasing the temperature nanoparticles with in-plane circular shape were also formed in the latter case. This effect was related to the dewetting temperature threshold that increases with increasing film thickness.[8,12] However, in our case the initial amount of deposited Ag (equivalent thickness ≈ 12 nm) and the characteristics of the a-Al_2O_3 buffer layer are the same for both films. Finally, despite the different annealing temperature used in vacuum (400ºC) and air (300ºC), we want to remark that the effect of dewetting at 300ºC and 400ºC were found to be very similar in air. Thus, we can neglect any effect related to the Ag film thickness,[8] roughness or nature of buffer layer[6,9] and annealing temperature.[8,9]

We relate then the observed differences to the efficiency of the heat transfer process in the two environments. While in the oven the whole cavity reaches the selected annealing temperature and the film is homogeneously heated, in vacuum the film is heated indirectly from the rear side through the metallic substrate holder disk. The vacuum chamber cavity is expected to be at lower temperature due to the reduced convection heat transfer in vacuum. As a result, the Ag film in vacuum is surrounded by a "colder environment", which could be responsible for the observed "incomplete" dewetting process. This is further supported by the amount of small nanoparticles observed in the two cases, while the density of small nanoparticles is approximately 7 NPs μm^{-2} in UNv-4200, it is four times denser for UNa-4200. A fraction of the large nanoparticles observed in Figure 5.1b (UNv-4200), particularly

the more elongated ones, shows lateral sizes reduced to only few nm in certain areas (see arrows in the Figure 5.1b). We can thus suppose that at higher thermal annealing temperatures nanoparticles would break through these regions, resulting in a small and a relatively large nanoparticle pair. This would lead to a larger number of small nanoparticles and to large nanoparticles reduced in size with improved in-plane circular shape, as it is observed in the case of the UNa-4200 film (Figure 5.1c).

5.1.2 Effect of covering layer deposition

In section 4.2.3 of Chapter 4, we observed that Ag nanoparticles exposed to air suffer from tarnishing and that the deposition of an ultrathin a-Al_2O_3 covering layer was sufficient to improve their mid-term stability. The consequences of Ag chemical reactivity are expected to be less pronounced in large nanoparticles compared to the case of small ones due to the decreased surface-to-volume ratio.[13] Nonetheless, the degradation of large Ag nanoparticles cannot be neglected, as shown in the work of Yang and co-workers[14] in which they reported the detrimental effect that nanoparticles degradation has on solar cell lifetime and concluded that a protective barrier against Ag tarnishing was needed to guarantee a longer device lifetime. The drawback of depositing a protective layer by PLD was, as showed in Chapter 4, tha Ag sputtering from the film surface, leading to important changes of nanoparticle morphology. In this section we explore the effect of the deposition of an a-Al_2O_3 covering layer on the morphology of large nanoparticles formed upon annealing in air. To that purpose, we produced an UN-4200 film, we annealed it in the oven at 300ºC in air for 70 minutes and, finally, we deposited an a-Al_2O_3 covering layer by PLD, to lead to a covered nanostructured film referred as CNa-4200.

Figure 5.4 shows (a) plan-view, (b) cross-section and (c) tilted-view (15º with respect the normal to the sample surface) SEM images of a CNa-4200 film grown on Si. Ag nanoparticles correspond to the elements with light contrast in the images.

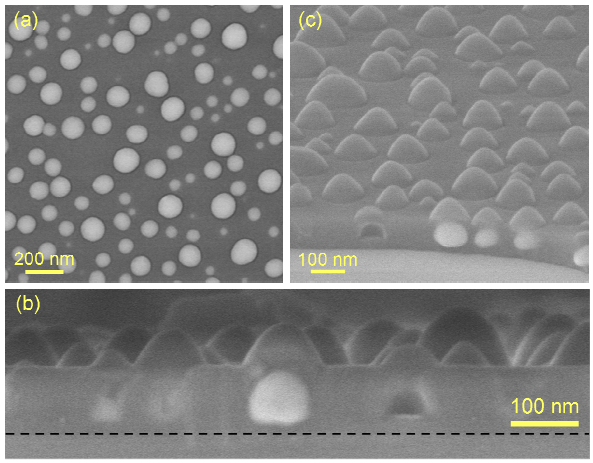

Figure 5.4: (a) Plan-view, (b) cross-section and (c) tilted-view SEM images of CNa-4200 film. The dashed line in (b) is a guideline to the Si/a-Al_2O_3 buffer layer interface.

Figure 5.4a shows that CNa-4200 consists of Ag nanoparticles with almost circular in-plane projected shape. Nanoparticle size distribution, density and surface coverage are very similar to those found in the case of UNa-4200 film (Figure 5.2b). In Figure 5.4b the Ag nanoparticle layer is hard to visualize since the insulating nature of the a-Al_2O_3 layers avoids collecting secondary electrons from the embedded nanoparticles. We can see a few bright elements and darker regions at the cut edge of the wafer that corresponds to Ag nanoparticles and to their footprints, respectively (see also Figure 5.4c). The thickness of the buffer and covering a-Al_2O_3 layers are approximately 25 and 70 nm, respectively. Moreover, the thickness of the covering layer is the same in between and on top of nanoparticles. As a result, the covered film shows a surface topography that is characterized by features that resemble nanodomes with tapered shape whose height and width are determined by the size and shape of the underlying nanoparticles.

Unlike the case of UN-300 and UN-900 films (Chapter 4), the deposition of the a-Al_2O_3 covering layer does not significantly affect nanoparticle morphology in the present case, as it is demonstrated by the similar nanoparticle size distribution, density and surface coverage of UNa-4200 and CNa-4200 films and by the conformal growth of a-Al_2O_3 over the nanoparticle layer. These results can be related to the large size of nanoparticles on which the cohesive energy depends. Large nanoparticles possess higher cohesive energy with respect to small ones,[15,16] which makes them more robust to the Al ion bombardment occurring during deposition of covering layer. As a result, Ag sputtering is most likely much smaller, while the nanoparticles are much larger. Thus, nanoparticle morphology keeps unchanged and the ions

arriving on top of nanoparticles basically contribute to the deposition of the covering layer, contrary to the cases of covering UN-300 and UN-900 films.

To confirm this point, we estimated Ag sputtering using the model described in Chapter 4. In particular, we estimated and compared the amount of sputtered Ag in UN-300 (from Chapter 4), UN-900 and UNa-4200 films after deposition of an a-Al_2O_3 covering layer with 1 nm thickness. We consider the variation of the cohesive energy with nanoparticle size according to equation (4.3) and adapt the modelled target to the buffer layer thickness, nanoparticle height and nanoparticle surface coverage obtained from TEM images for each film (Figures 5.1 and 5.3 for UNa-4200 films and Figures 4.11b and 4.13b for UN-900 film). The implemented values together with the obtained $[Ag]_{Sputt\text{-}SRIM}$ are listed in Table 5.1 for the three cases.

Table 5.1: List of the parameters used in the sputtering model and corresponding value of sputtered Ag after deposition of an a-Al_2O_3 covering layer 1 nm thick.

FILM	E_{CC} (eV)	Buffer layer (nm)	Ag layer (nm)	Surface coverage (%)	$[Ag]_{Sputt\text{-}SRIM}$ ($\times 10^{15}$ atoms cm^{-2})
UN-300	2.4	5	3.6	50	3.2
UN-900	2.7	10	7	44	2.5
UNa-4200	2.9	25	45	22	1.3

E_{CC} corresponds to the size-dependent cohesive energy of Ag nanoparticles.
The values in the 2º and 3º columns refer to the thickness and equivalent thickness of a-Al_2O_3 and Ag layers, expressed in nm.

The model gives $[Ag]_{Sputt\text{-}SRIM}$ of 1.3×10^{15} atoms cm^{-2} in the case of UNa-4200 film, that is approximately 50% and 40% the value predicted for UN-900 and UN-300 films, respectively. The model effectively predicts a lowering of Ag sputtering with increasing Ag nanoparticles size, which is consistent with the increased E_{CC} of nanoparticles in UNa-4200 films with respect to the case of UN-300 and UN-300 films. In addition, the reduced Ag sputtering can be also related to the reduced surface coverage of UNa-4200 film with respect to the other two considered cases, since a lower surface coverage implies to a lower amount of Ag exposed to the Al^+ bombardment. Finally, the fact that we do not observe any relevant morphological change in the case of covering UNa-4200 film despite a $[Ag]_{Sputt\text{-}SRIM}$ different from zero relates to the initial amount of deposited Ag. If we consider a linear increase of the amount of deposited Ag with the number of laser pulses on Ag target,[17] we can estimate $[Ag]_{UNa\text{-}4200} \approx 14\times[Ag]_{UN\text{-}300} = 98\times10^{15}$ atoms cm^{-2}. Thus, the percentage of sputtered Ag

corresponds to only 1% of the initial amount, which corresponds to a Ag fraction that makes almost impossible to detect any change in nanoparticle morphology.

5.1.3 Optical response

The formation of nanoparticles upon annealing must strongly influence the optical response of the films. Figure 5.5a shows the extinction spectra of UN-4200 and UNa-4200 films grown on glass, which differ considerably. The extinction of UN-4200 is almost constant, > 60%, for wavelengths longer than 520 nm, while the spectrum of UNa-4200 shows two clear extinction bands peaking at, approximately, 360 nm and 515 nm. The extinction band intensity at the maxima is 65% and 80%, while the corresponding FWHM is 65 nm and 180 nm, respectively.

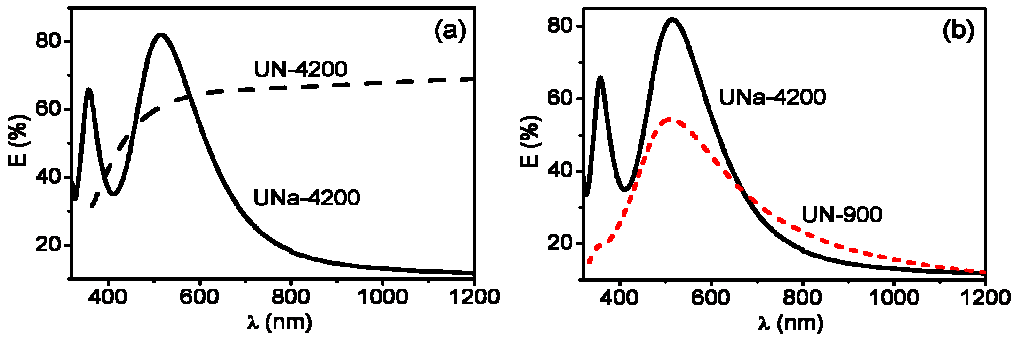

Figure 5.5: Extinction spectra of (a) UN-4200 and UNa-4200 films and (b) UNa-4200 and UN-900 films.

The evolution of the extinction spectrum of the percolated film (Figure 5.5a) is consistent with the evolution of film morphology observed before and after annealing (Figure 5.1). The optical response of the UN-4200 film is similar to that of a continuous Ag film in which no extinction bands related to the SPR of nanoparticles are observed, while that of UNa-4200 film shows two bands associated to the SPR of nanoparticles formed upon thermal annealing. The band at longer wavelengths relates to the dipolar modes of the SPR, while that at short wavelengths relates to the excitation of the quadrupolar mode.[8,18] The intensity of the bands, in particular that of the quadrupolar mode is considerably higher than those observed in the case of UN-900 film (Figure 5.5b), which suggests that large nanoparticles strongly contribute to the optical response of UNa-4200.[8,18]

If we compare the optical response of UN-900 and UNa-4200 films (Figure 5.5b), we observe that, apart from the different intensity, the extinction bands corresponding to the

dipolar mode are similar. The SPR maximum occurs at ≈ 515 nm and the FWHM is approximately 200 nm in both cases, in spite of their different morphology. We already pointed out that the spectral position and the width of the SPR are determined by the size and shape of nanoparticles and by their spatial arrangement, too.[18,19] Nanoparticles separated by small gaps (of the order of the nanoparticle radius, in the case of spherical nanoparticles) can interact, resulting in SPR shifted to longer wavelengths with respect to the case of isolated nanoparticles. Nanostructured films similar to UN-900 contain a dense layer of relatively large nanoparticles with broad shape distribution, while those similar to UNa-4200 contain well separated large nanoparticles with in-plane circular shape. Thus, the present results support that in the case of UN-900 the interparticle coupling effects may contribute to shift the SPR toward the red such that it peaks at a spectral position similar to that of UNa-4200 films, for which interparticle coupling can be neglected and the position of the SPR is mainly determined by the size of nanoparticles.

As earlier mentioned, metallic nanoparticles with size in the 100-200 nm range differ from smaller ones because they exhibit enhanced scattering to the far-field and reduced light absorption at the SPR wavelength.[1] These characteristic makes them suitable for application in optoelectronic devices, like solar cells.[3,20] In particular, one of the proposed approaches for increasing the path length of light inside the absorber layer in the case of thin-film solar cells is based on the incorporation of metallic nanoparticles that efficiently scatter light at angles different from that of specular direction.[21,22,23] In this sense, the suitability of a nanostructured film containing metal nanoparticle for this type of applications strongly relates to its capability to diffuse light. We have thus evidenced the dependence of scattering properties on nanoparticle size and having in mind the incorporation of fabricated nanostructured films in chalcopyrite-based solar cells, which will be discussed in the next chapter, we have investigated the optical response of covered nanostructured films in terms of total and diffuse reflectance spectra.

Figure 5.6 shows (a) total (R_t) and (b) diffuse (R_d) reflectance spectra of CN-300 and CN-900 films grown on fused silica and CNa-4200 film grown on glass. Figure 5.6a shows that the spectrum of CN-300 film is characterized by a very weak (≈ 12%) reflectance band peaking at ≈ 465 nm with a FWHM approximately of 130 nm. The spectrum corresponding to CN-900 film is different. It shows a very broad and relatively weak R_t band peaking at ≈ 640 nm. R_t decreases from 22% down to 18% in the 600-1200 nm wavelength range, while for shorter wavelengths R_t is as small as 6%.

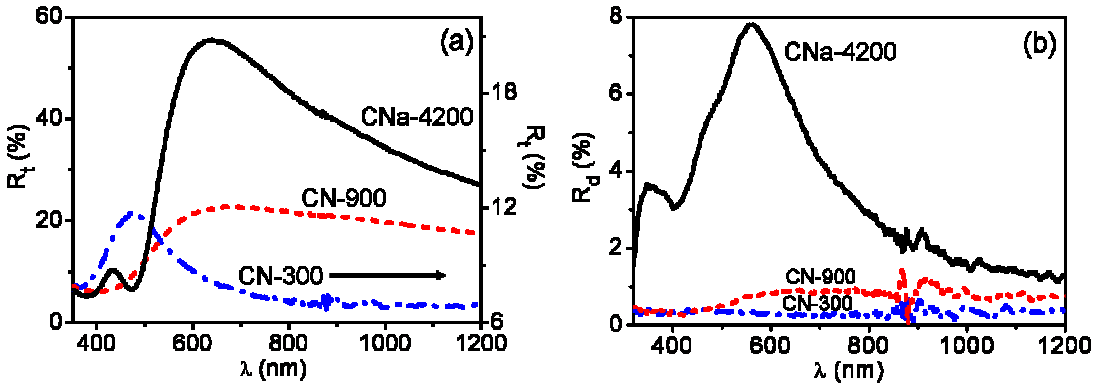

Figure 5.6: (a) Total and (b) diffuse reflectance spectra of CNa-4200, CN-900 and CN-300 films.

The spectrum corresponding to CNa-4200 film is clearly different. It shows a very intense and broad R_t band peaking at 640 nm, the intensity at the band maximum being close to 55%. R_t also shows a second very weak band peaking at 430 nm. Finally, Figure 5.6b shows that R_d is negligible for both CN-300 and CN-900 films, while for CN-4200 film the spectrum shows a weak ($R_{d\text{-}max} \approx 8\%$) and narrow (FWHM ≈ 245 nm) band peaking at 560 nm and a second very weak one at 360 nm.

These results show that nanoparticles smaller than 50 nm interact with light much less than the larger ones (Figure 5.6a). The value of $R_{t\text{-}max}$ for CNa-4200 film is more than twice and four times that of CN-900 and CN-300 films, respectively. These differences are even more pronounced in the case of diffuse reflectance. Only CNa-4200 film exhibits a significant diffuse reflectance. These results are consistent with the expected increase of light scattering with increasing nanoparticles size, but they also show that the fraction of light diffused away from specular direction, R_d, is small, below 10%, and that it occurs only in a tiny spectral window, in the range from 430 nm to 740 nm. This result is in contrast with those reported by Tan and co-workers[22] and, later, by Morawiec and co-workers[23] which showed very intense (up to 80%) and broad diffuse reflectance bands for a layer of Ag nanoparticles embedded in aluminum-doped zinc oxide matrix grown on a thick layer of Ag. The discrepancy between these results and ours can be ascribed to three main factors: the size of nanoparticles, the bimodal size distribution and their crystalline quality. Nanoparticles smaller than ≈ 200 nm scarcely contribute to light diffusion, while nanoparticles with low crystalline quality (i.e., polycrystalline) and with a size close to 50 nm favor light absorption rather than its diffusion.[8,22,23] In our case, we observed that nanoparticles formed upon annealing in air show

typical sizes close to 50 nm or 130 nm (Figure 5.4a). Thus, well below the size for which nanoparticles are expected to scatter light efficiently. In addition, the relatively short time and low temperature of annealing may be responsible for the poor crystalline quality. Therefore, according to literature, the performance of our nanostructured film could be improved by increasing both the initial amount of deposited Ag and the annealing temperature to promote the formation of larger nanoparticle with a narrower size distribution than the present case, while the increase of the annealing time would improve their crystalline quality.

5.2 LASER IRRADIATION OF NANOSTRUCTURED SILVER FILMS: REORGANIZATION AND SHAPING OF EMBEDDED SILVER NANOPARTICLES

The results reported in previous sections and chapters have shown the strong relation between nanoparticle shape and film optical response. The intensity, width and spectral position of the extinction band, i.e. the SPR, could be modified by varying the amount of deposited Ag and thus nanoparticle size, shape and spatial arrangement. The final nanoparticle shape, and therefore the optical response of the film, is exclusively determined by the physical processes responsible for nanoparticles formation (coalescence and dewetting), which represent the main limitation of bottom-up techniques (PLD included) for fabrication of nanostructured films with specific nanoparticle morphology. Therefore, many experimental approaches have been developed to overcome this limitation. The use of nanostructured substrates has been considered in order to achieve a controlled growth of regular arrays of silver nanoparticles, chains or stripes,[24,25] whereas a different approach, which is compatible with non-patterned substrates, is based on physical vapour deposition at glancing angle combined with post-treatment with a low power infrared nanosecond YAG laser.[26] The role of the laser is to heat, preferentially melt and merge certain nanoparticles. In all these cases, though, shaping is performed on nanoparticles at the substrate surface exposed to air, which, as already discussed in section 4.2.3 of Chapter 4, is especially problematic for Ag since it suffers from tarnishing.

An exciting alternative to overcome this problem is the possibility of shaping embedded nanoparticles using laser irradiation. Kaempfe and co-workers have demonstrated that irradiation with femtosecond (fs) laser pulses allows the modification of the shape of spherical Ag nanoparticles embedded in bulk glass.[27] The authors observed a fluence-

dependent broadening and a red-shift in the extinction spectrum together with dichroism, which they demonstrated to be related to an increase of the particle diameter and a nanoparticle shape change from spheres to spheroids. Despite being embedded in a matrix, the high peak intensities of ultrashort laser pulses enabled nanoparticle reshaping. Other studies based on this pioneering work reported about the shaping of spherical nanoparticles into prolate spheroids with high aspect ratios[28] or into nanodisks.[29] The dependence of the nanoparticle morphology change on the laser wavelength, fluence and polarization as well as on the irradiation mode, i.e. single- or multi-shot irradiation regime, was also reported.[28-30] Apart from these works dealing with Ag and Au nanoparticles embedded in bulk glass, Kiesow and co-workers[31] and Loeschner and co-workers[32] performed irradiation experiments on Ag films close to percolation limit embedded in thin polymer layers using ultrashort laser pulses. They showed that laser irradiation leads to the formation of periodic superstructures resembling line gratings with periodical changes in particle size and shape.

Despite the abundance of reports on irradiation with fs pulses, the case of irradiation with nanosecond (ns) pulses has been less explored, mainly because it is considered less efficient in promoting nanoparticle shaping,[33] especially when nanoparticles are embedded in a matrix. Usually, nanosecond irradiation leads to a reduction of metal nanoparticle size as a result of fragmentation, diffusion and evaporation in liquids and solid matrix or glass.[33,34,35,36] In the case of physically evaporated Au and Ag nanoparticles supported on solid substrates, Kawasaki and co-workers[37] and Resta and co-workers[38] have shown that irradiation with ns pulses leads to a sharpening of nanoparticles shape distribution due to melting and subsequent solidification of nanoparticles into more spherical ones, without evidence of nanoparticle fragmentation or evaporation. Recently, Fleming and co-workers,[39] using an approach similar to our,[40] reported about ns irradiation of a floating glass containing a 20 μm thick layer of Ag nanoparticles of ~ 15 nm in radius obtained by ion exchange and subsequent annealing. They showed that the irradiation with ns pulses led to the formation of a thin surface film containing Ag nanoparticles which size depended on the number of laser pulses and, thus, on the energy absorbed in the glass.

In view of these promising approaches for nanoparticle shaping and in order to overcome the limitations of PLD and thermal annealing to the control of nanoparticle morphology, we have exploited laser irradiation to modify the shape and tailor the optical response of the fabricated nanostructured films. In particular, we selected the nanostructured film containing a single layer of embedded coalesced nanoparticles, namely CN-900 film.

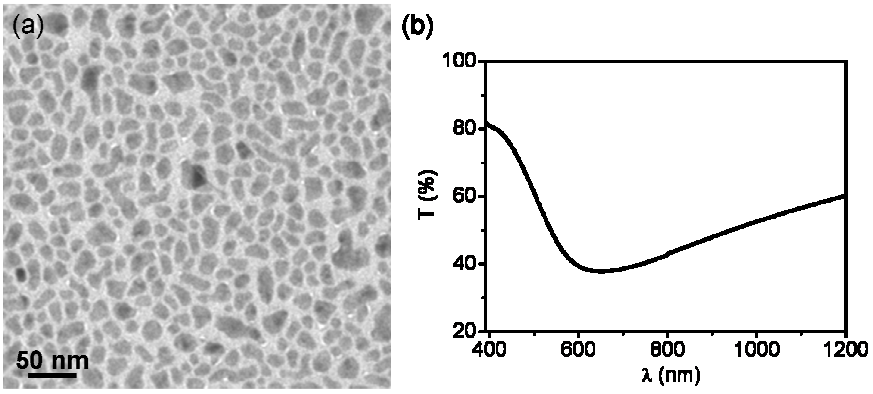

Figure 5.7: (a) Plan-view TEM image and (b) transmittance spectrum of CN-900 film.

As already discussed in section 4.3.1, this nanostructured film shows a very heterogeneous distribution of highly non-spherical and randomly oriented nanoparticles (Figure 5.7a), which leads to a broad SPR peaking at ≈ 640 nm (Figure 5.7b). This kind of nanostructure considerably differs from those of nanostructured films commonly used for irradiation experiments that are generally characterized by sparse nanoparticles with almost spherical shape obtained using ion implantation or ion exchange techniques[28-30,34,35,39] or by almost percolated Ag films embedded in polymer layers.[31,32]

We have investigated the effect that laser pulse duration has on nanoparticle morphology using nanosecond and femtosecond laser pulses. The interest in investigating different laser pulse durations relies in the processes leading to nanoparticle shaping that are expected to be driven by different mechanisms.[33] In addition, in the case of fs irradiation, we have also considered two different laser wavelengths (400 and 800 nm) to figure out any relevant feature related to the irradiation on- and off-resonance with respect the wavelength at which the SPR is observed.

5.2.1 Nanosecond irradiation

In the case of irradiation with ns laser pulses, the laser wavelength and pulse duration were 800 nm and 8 ns, respectively. We have performed different irradiation experiments changing either the laser fluence or the number of pulses used to irradiate the films. The results reported correspond only to the case of single pulse irradiation at a laser (peak) fluence of 740 mJ cm^{-2} since this value led to the strongest change. Changes were negligible for fluences below this value, while for higher fluences the ablation threshold was reached and

the film was damaged. In addition, multi-pulse irradiation did not lead to any relevant difference with respect to the case of single pulse irradiation. The laser polarization was chosen to be s-polarized in order to set the polarization vector (i.e., the electric field) to lie within the surface plane. For p-polarization or other polarization configurations, the polarization vector would have a component along the film depth, due to the 53º angle of incidence (see section 2.3.3 of Chapter 2), which would make the interpretation of transmission spectra much more complex. The small size of the white light probe spot allows us to record transmittance spectra at different positions of the laser-irradiated area (section 2.3.3 of Chapter 2). Since the spatial intensity distribution of the laser beam at the sample surface is Gaussian, this is equivalent to study the dependence of the shaping process on the local laser fluence.[41]

Figure 5.8 shows an optical micrograph corresponding to a region of the CN-900 film grown on fused silica irradiated with a single ns pulse at 740 mJ cm^{-2}. The image was recorded *ex-situ*, in transmission mode, with a commercial optical microscope using white light illumination and a colour digital camera to record the picture. The laser polarization is along the y axis. The symbols show the regions where we recorded the local transmittance spectra shown in Figure 5.9.

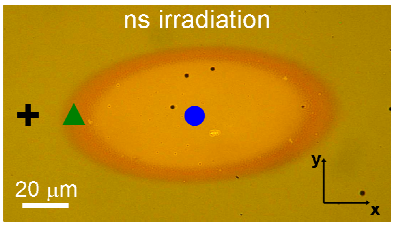

Figure 5.8: Color optical transmittance micrograph of the laser-irradiated area of a CN-900 film grown on fused silica. The film was irradiated with a single pulse of 8 ns at 800 nm with the laser polarization oriented along the y axis. The symbols schematically show the points where the transmittance spectra shown in Figure 5.9 have been recorded.

The laser-induced changes in the optical response of the film are clearly evidenced in Figure 5.8. A strong colour change is observed in the irradiated region, ranging from light brown for non-irradiated regions (as-grown CN-900 film) to dark orange at the edge of the irradiated region and light orange in the central part of the spot. Figure 5.9 shows the transmittance spectra of the film recoreded with the *in-situ* white light probe setup (a) outside the irradiated area (Figure 5.8, black cross) and at its edge (Figure 5.8, green triangle) and (c)

in the centre of the laser spot (Figure 5.8, blue circle). The local laser fluence was determined to be 125 and 740 mJ cm^{-2} at the ring and in the centre, respectively.

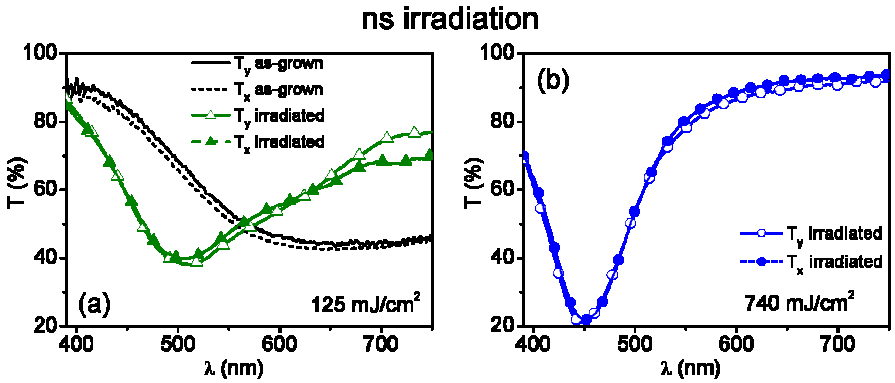

Figure 5.9: Transmittance spectra recorded (a) outside of the irradiated area (solid and dashed curves) and at its edge (△ and ▲) and (b) in the central part of the spot. T_x and T_y refer to the light probe polarized parallel (T_y) or perpendicular (T_x) to the laser polarization. The local fluence values at the spot positions considered are indicated in the plots.

In order to evidence any dependence of the optical response on the light probe polarization, the spectra have been recorded using the light probe polarized parallel (T_y) and perpendicular (T_x) to the laser polarization. The as-grown film, i.e. non-irradiated area, shows similar spectra for both polarizations (T_x and T_y). We observe a broad band of low transmittance peaking at 640 nm, similarly to the results obtained using the commercial spectrophotometer (Figure 5.7b). After laser irradiation, the optical response changes substantially. In correspondence of the dark orange ring (Figure 5.8), the bands are narrower and shifted to the blue with respect to non-irradiated region, with the minimum peaking at $\lambda_{SPR} \approx 500$ nm, while for the maximum laser fluence, i.e. in the centre of the light orange spot (Figure 5.8), the narrowing of the bands becomes more pronounced, as well as their intensity and shift to the blue ($\lambda_{SPR} \approx 450$ nm). For both laser fluences, T_x and T_y spectra overlap, which indicates that the spectra are not sensitive to the polarization of the light probe.

In order to relate the changes observed in the optical response to a modification of the nanoparticles morphology we performed SEM measurements of an equivalent CN-900 film on Si exposed to a single ns pulse. This substrate was chosen for SEM since fused silica leads to surface charging effects by the electron beam, whereas C-mica could not be used as it fractured already at low fluences when using ns laser pulses likely due to thermal effects.[38] Figure 5.10 shows plan-view SEM images of (a) the as-grown CN-900 film and (b) of an area of the same film irradiated with ns pulse at the maximum laser fluence, 740 mJ cm^{-2}.

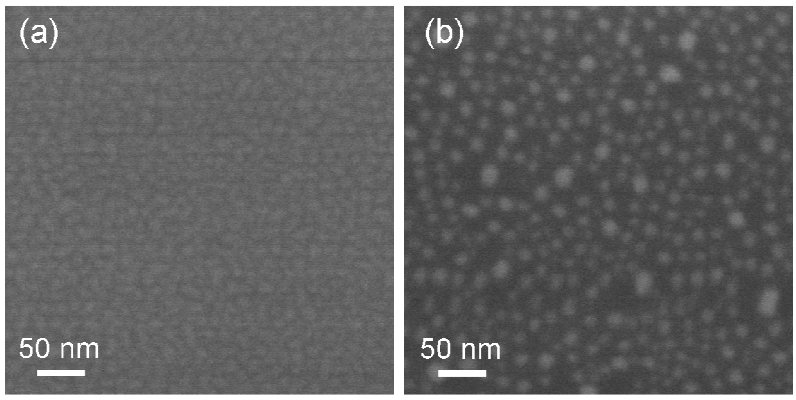

Figure 5.10: Plan-view SEM images of (a) the as-grown CN-900 film on Si substrate and (b) an area of the same film irradiated at the highest fluence (740 mJ cm^{-2}) with ns pulse.

Despite the low contrast achieved in SEM images due to the insulating nature of the a-Al_2O_3 covering layer, the effects of nanosecond irradiation are well evidenced. Compared to the case of as-grown film (Figure 5.10a), we observe well-separated nanoparticles with almost circular in-plane projected shape in the irradiated film (Figure 5.10b). The average diameter of nanoparticles is ≈ 15 nm, whereas the elongated features typical of the as-grown CN-900 film are barely seen. Finally, the nanoparticle density decreases from 2.4×10^3 NPs μm^{-2} down to 1.4×10^3 NPs μm^{-2}, which suggests that the spacing between nanoparticles increases.

The results present in Figure 5.10 confirm that ns irradiation efficiently reshape embedded Ag nanoparticles and they suggest that the main effect is to narrow both the nanoparticle size and shape distributions, which is consistent with the observed narrowing of the bands shown in Figure 5.9b. In addition, the strong blue shift experienced by the SPR band after irradiation is most likely related to the increased distance between nanoparticles, as this reduces the interparticle interaction responsible for SPR red-shift.[18,37] Moreover, the improved circular in-plane projected shape of nanoparticles leads to an overall and individual shape isotropy, which is consistent with the optical behaviour that does not depend on the probe light polarization as shown in Figure 5.9.

Finally, these changes on the nanoparticle morphology, namely the narrowing of the shape distribution, their circular in-plane projected shape and their larger interparticle distance support that the shaping process upon ns irradiation is mainly thermally driven, similarly to what observed by Kawasaki and co-workers[37] and Resta and co-workers[38] for Au and Ag nanoparticles supported on a substrate. Qualitatively,[37] nanostructured Ag films are likely to reach temperatures well above Ag melting point (1234 K) and close to Ag boiling point (2435

K), particularly at the highest laser fluence (740 mJ cm^{-2}). The diffusion of metal atoms through a solid matrix has already been observed in the case of thermal annealing of embedded Fe nanoparticles.[42] In addition, in the present case, Ag diffusion could be also favoured by transient melting of a-Al_2O_3 matrix (T_{Al2O3}=2273 K), which may occur in the vicinity of nanoparticles as a result of heat transfer process at the nanoparticle-matrix interface.[39] Then, surface energy minimization processes would tend to reshape melted Ag nanoparticles into more spherical ones, which would lead to a narrowing of the nanoparticle shape distribution,[37,38] due to the disappearance of elongated nanoparticles, as it is effectively observed in Figure 5.10b. The observed nanoparticle density decrease is most likely related to coalescence of neighbouring nanoparticles into larger ones.[30,31]

5.2.2 Femtosecond irradiation

Irradiation with laser pulses ≈ 100 fs long was performed either at 400 or 800 nm. As shown in Figure 5.7b, the spectrum corresponding to the as-grown CN-900 film on fused silica shows reduced transmittance values, i.e. large light absorption, in the vicinity of the SPR that peaks at ≈ 640 nm, while the transmittance is high for shorter wavelengths. For this reason, we will refer to these two fs irradiation conditions as off- and on-resonance in the case of 400 and 800 nm laser wavelengths, respectively. Contrary to the case of ns irradiation and accordingly to what has been reported in literature for fs laser irradiation, [28,43] we used low energy multiple pulse fs irradiation, since the effect observed for single pulse irradiation was very small. We set the number of laser pulses to 200 and the peak laser fluence was fixed to 66 mJ cm^{-2} (at 400 nm) or 82 mJ cm^{-2} (at 800 nm). These values were found to be those that led to the strongest change in the optical response without damaging the film. Finally, the laser polarization was chosen to be s-polarized in order to set the polarization vector to lie within the surface plane, as in the ns case.

Similar to the case of ns irradiation, we first investigate the effect of *on-resonant* (800 nm) fs irradiation on nanoparticle shape. Figure 5.11 shows the transmittance optical micrograph corresponding to the irradiated region of a CN-900 film grown on fused silica. The image was recorded in the same conditions as in the case of ns irradiation. The orientation of the laser polarization is directed along the y axis. The optical micrograph shows a strong colour change that ranges from light brown for the non-irradiated region (as-grown CN-900 film) over light orange at the edge of the irradiated region to orange in the central part of the spot.

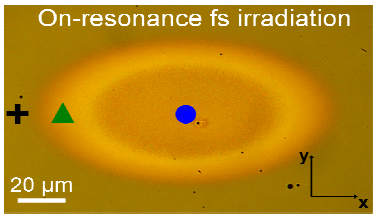

Figure 5.11: Colour optical transmittance micrograph of the irradiated area of the CN-900 film grown on fused silica. The film was irradiated with 200 pulses at 800 nm with the laser polarization oriented along the y axis. The symbols schematically show the points where the transmittance spectra shown in Figure 5.12 have been recorded.

The symbols illustrate the regions where we recorded the transmittance spectra shown in Figure 5.12 with the in-situ white light probe setup (a) at the edge of the light orange ring (Figure 5.11, green triangle) and (b) in the centre of the irradiated area (Figure 5.11, blue circle). The corresponding laser fluence was determined to be 15 mJ cm^{-2} and 82 mJ cm^{-2}, respectively. In (a) the T_y spectrum, corresponding to the non-irradiated region, is reported for reference (Figure 5.11, black cross). The spectra have been recorded with the probe light polarized parallel (T_y) and perpendicular (T_x) to the laser polarization.

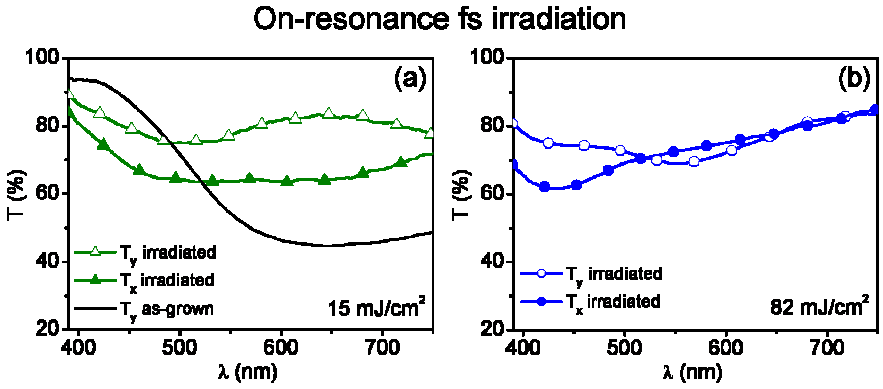

Figure 5.12: Transmittance spectra recorded (a) at the edge of the light orange ring (△ and ▲) and (b) in the centre of the irradiated area. In (a) T_y spectrum corresponding to the non-irradiated region is reported for reference. T_x and T_y refer to the light probe polarization that can be switched parallel (T_y) or perpendicular (T_x) to the laser polarization. In the lower part of the plots, the local fluence at the positions of (a) and (b) are given.

After on-resonance fs irradiation the optical response changes substantially compared to that of as-grown film. At low laser fluence (Figure 5.12a), spectra show no resonant behaviour and an overall increase of the transmittance in the whole spectral range (i.e. *spectral bleaching*), particularly for T_y, while at the highest fluence (Figure 5.12b) two weak and blue-shifted bands of low transmittance can be observed for T_x and T_y. The maximum of

the SPR for T_x is observed at ≈ 430 nm, whereas that of T_y is located at ≈ 560 nm. This results in a peak shift of 130 nm for the two light probe polarizations, resulting in a dichroic optical response.

In the case of *off-resonance* (400 nm) fs irradiation, the transmittance optical micrograph shown in Figure 5.13 of the irradiated region presents similar features as before.

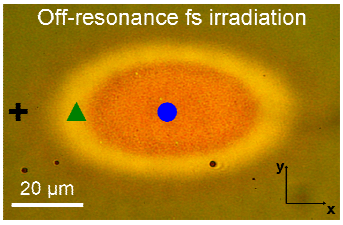

Figure 5.13: Colour optical transmittance micrograph of the irradiated area of the CN-900 film grown on fused silica. The film was irradiated using 200 pulses at 400 nm with the laser polarization oriented along the y axis. The symbols schematically show the points where the transmittance spectra shown in Figure 5.14 have been recorded.

We can observe a ring structure changing from light brown for the non-irradiated region to yellow at the edge of the irradiated region and orange in the central area of the spot. However, the effect of the fs irradiation on the optical properties is completely different. Figure 5.14a shows the transmittance spectra at the edge of the yellow ring (Figure 5.13, green triangle) and the spectrum recorded at the non-irradiated area (Figure 5.13, black cross) while Figure 5.14b shows the transmittance spectra recorded in the centre of the irradiated area (Figure 5.13, blue circle). The corresponding laser fluence was determined to be 31 mJ cm^{-2} and 66 mJ cm^{-2} in (a) and (b), respectively.

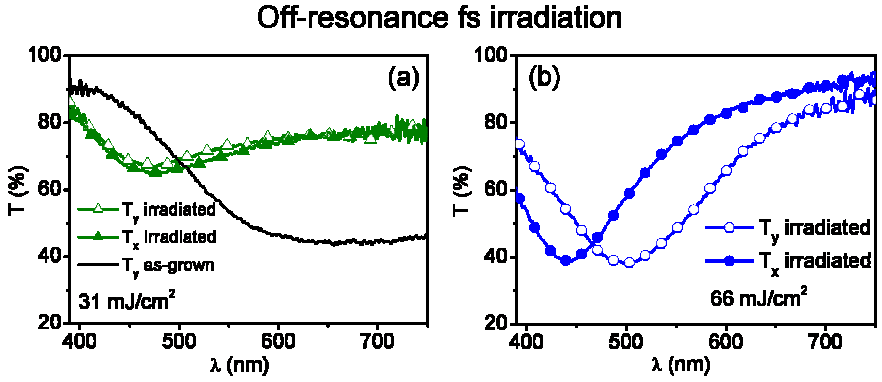

Figure 5.14: Transmittance spectra recorded (a) at the edge of the yellow ring (△ and ▲) and (b) in the centre of the irradiated area. In (a) T_y spectrum corresponding to the non-irradiated area is reported for reference. T_x and T_y refer to the light probe polarization that can be switched parallel (T_y) or perpendicular (T_x) to the laser polarization. In the lower part of the plots, the local fluence values at the positions of (a) and (b) are given.

We observe important changes in the optical response of the film depending on the local laser fluence of the laser-irradiated area. The spectra in Figure 5.14a shows no polarization dependence along with an overall spectral bleaching, in particular for $\lambda > 500$ nm, while only a weak band that can be related to the SPR is observed at $\lambda_{SPR} \approx 460$ nm. However, at the highest fluence, we clearly observe the splitting of the T_y and T_x spectra (Figure 5.14b). In addition, the intensity of the bands strongly increases and blue-shifts for both T_y and T_x with respect to the non-irradiated area. The minimum of T_x is observed at 440 nm compared to the peak of T_y, which is located at 500 nm, resulting in a peak shift of 60 nm. Thus, the nanostructured film develops a dichroic optical response after off-resonance fs irradiation, similarly to what observed in the case of on-resonance irradiation. These results clearly show that the shaping mechanism induced by fs pulses is considerably different from the case of ns irradiation. In addition, off-resonance fs irradiation (400 nm) leads to a more pronounced optical response modification than on-resonance fs irradiation (800 nm), especially at the highest fluence where off-resonance irradiation leads to narrower and more intense bands of low transmittance. In order to shed more light on the morphological transformation responsible for the enhanced optical response and dichroism in the case of off-resonance fs irradiation, we have performed TEM studies at different local positions of the irradiated region. Figure 5.15 shows plan-view TEM images corresponding to an equivalent CN-900 film on C-mica irradiated with, approximately, (a) 31 and (b) 52 mJ cm^{-2}. These values are slightly lower than those used on films grown on fused-silica. This relates to the fact that C-mica shows lower ablation threshold due to its different thermal properties.[38] However, the effects on optical properties are similar to those observed in the case of fused silica substrate, apart from a slightly less pronounced dichroism and SPR intensity (not shown).

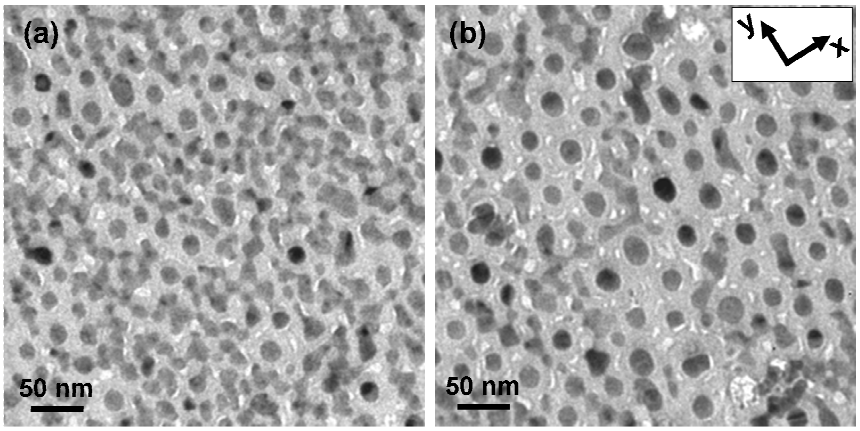

Figure 5.15: Plan-view TEM images of the CN-900 film areas irradiated with (a) intermediate (31 mJ cm^{-2}) and (b) the maximum (52 mJ cm^{-2}) local laser fluences upon off-resonance fs irradiation.

As it has been discussed, as-grown nanoparticles show irregular and elongated shape, their long axis being randomly oriented (Figure 5.7a). Upon irradiation the film morphology changes completely. At the intermediate laser fluence of 31 mJ cm^{-2} (Figure 5.15a), we observe that Ag, the dark contrast areas, forms isolated nanoparticles together with relatively large and irregular features, which are likely to arise from coalescence of neighbouring nanoparticles. We also observe the presence of white spots in the film close to the Ag nanoparticles, which suggest that a fraction of nanoparticles shrunk probably due to Ag diffusion into the matrix. We can thus, in a first attempt, relate the observed spectral bleaching observed in Figure 5.14a to the partial disintegration of nanoparticles and to the barely resonant response of the formed Ag nanoparticles.

At the highest fluence of 52 mJ cm^{-2} (Figure 5.15b), we observe that the film shows mainly isolated nanoparticles with circular or slightly elliptical in-plane projected shape. In the latter case, the short and long axes length average values are approximately 15 and 20 nm (aspect ratio, 1.33), respectively. In addition, elongated and irregular Ag features resembling those observed at intermediate fluences (Figure 5.15a) are still observed, too. The observed morphology is thus consistent with the optical response of Figure 5.14b which shows an intense resonant behaviour that can be attributed to the formed Ag nanoparticles. In addition, the dichroic optical response, with the SPR for T_y shifted to longer wavelengths compared to that of T_x, suggests that the long axis of elongated nanoparticles should be aligned in a direction parallel to that of the laser polarization.[28,29,43] The fact that this nanoparticle alignment is hardly seen in the TEM images (Figure 5.15b) can be related to the fact that irradiation on C-mica was performed at a 10% lower fluence with respect to the case of irradiation on fused silica (52 instead of 66 mJ cm^{-2}), leading to a less efficient reshaping process. As a result, optical measurements likely probe reshaped nanoparticle with higher aspect ratio than the one estimated for the elongated nanoparticles observed in TEM image.

Contrary to what reported in literatures,[28] we observed the spectral bleaching at laser fluence lower than the one needed for efficient nanoparticle reshaping. We propose an interpretation to this result by taking into account the *off-resonance* irradiation condition used in this work. *Off-resonance* irradiation prevents excitation of the collective oscillation of conduction electrons (i.e. the SPR), which is the main responsible for promoting Ag lattice heating through electron-phonon coupling,[30,34,44] Nonetheless, the interaction between laser and nanoparticles is expected to still induce a strong near-field enhancement in the vicinity of

the nanoparticle.[44] The induced near-field is likely to cause electron plasma formation in the dielectric matrix in contact with the nanoparticle, which can efficiently absorb laser energy.[44] After electron plasma relaxation through the transfer of the energy in form of heat to the matrix lattice, which may lead to an a-Al_2O_3 temperature increase above its melting temperature,[44] the nanoparticle/matrix interface region is most likely in the liquid phase. This would strongly favour diffusion of silver into the matrix. In the case of intermediate laser fluences, this situation leads to nanoparticle partial disintegration and it can also promote the closest nanoparticles to join together within the transient melting of the matrix[32] to form the observed Ag large and irregular features (Figure 5.15a).

However, the situation changes substantially at the high fluences. In this case, there is a larger heat transfer to the lattice, which can be high enough to promote Ag melting and subsequent formation of new nanoparticles,[31] different from those observed in the as-grown CN-900 film. In particular, newly formed nanoparticles should be rounder in shape as a result of surface energy minimization, similarly to the case of ns irradiation. This is supported by the almost circular in-plane projected shape of some of the nanoparticles in Figure 5.15b. The change in shape is accompanied by a change in the optical response of the nanoparticles. The SPR blue shifts towards the laser wavelength (400 nm), as a result of increased nanoparticle distance and of the narrowing of nanoparticle shape distribution.[18,37,38] Thus, the new nanoparticles formed after the firsts pulses start to absorb efficiently the laser energy of the following pulses at 400 nm. Under this new *on-resonance* conditions, the nanoparticle reshaping process is driven by the high transient electric field of the fs pulses,[28,43] as schematically represented in Figure 5.16.

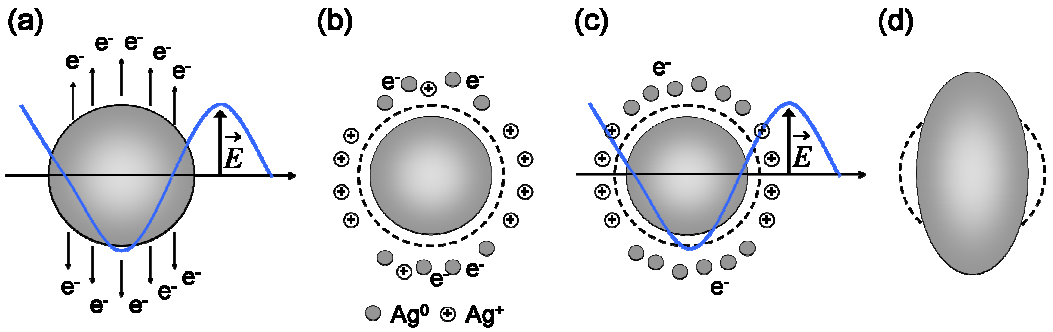

Figure 5.16: Scheme of the mechanism leading to nanoparticle shaping during multi-shot on-resonance fs irradiation. (a) Electrons are emitted at the poles of nanoparticles as a result of the high transient electric field . (b) The ionized nanoparticle emits Ag ions as a result of electrical instability, i.e. Coulomb explosion. (b) and (c) The ejected Ag ions recombine with the electrons trapped in the matrix to form Ag atoms. (d) The formed Ag atoms and clusters diffuse to the nanoparticle mainly through coarsening. Since they are formed at the poles, the nanoparticle is reshaped into a prolate spheroid. Adapted from Stalmashonak and co-workers.[28]

The high transient electric field induces strong oscillations of the electron distribution of the nanoparticles along the polarization direction of the laser. Since the excited SPR is mainly dipolar in nature for relatively small nanoparticles, electrons are ejected and trapped in the matrix mainly at the poles of the nanoparticles (Figure 5.16a).[30] Then, after electron thermalization and heat transfer to the Ag lattice, the electrically instable ionized nanoparticles are likely to emit Ag ions due to Coulomb explosion that can recombine with the electrons trapped in the matrix (Figures 5.16b-c).[28,30] Finally, Ag atoms and, eventually, the small Ag cluster formed at the poles diffuse back to the main nanoparticle through coarsening,[30] progressively leading to nanoparticles with pronounced prolate spheroidal shape, with the long axis oriented along the laser polarization (Figure 5.16d).[28,30] In this sense, the presence of the white spots, whose number increases from figure 5.15a to b, supports our interpretation, since they are likely to correspond to the voids left by the original nanoparticles that first shrank and then reshaped.

The picture of reshaping can be extended to the case of *on-resonance* fs irradiation. After irradiation at 800 nm at the highest fluence, we observed the splitting of T_y and T_x spectra that results in an optical shift between the two polarizations close to 130 nm (Figure 5.12b). The developed dichroism is the result of nanoparticles reshaping into prolate spheroid with higher aspect ratio than in the case of off-resonance irradiation. However, the bands are broad and show higher transmittance values compared to on-resonance irradiation. This is most likely related to an incomplete reshaping process that leads a fraction of Ag to remain dispersed in the a-Al_2O_3 matrix. As T_y progressively shifts to spectral values far from the irradiation wavelength, i.e. turning *off-resonance*, the interaction between nanoparticles and laser pulses is reduced, thus limiting the extent of nanoparticles reshaping,[28,45] that is exactly the opposite situation to what is observed in the case of *off-resonance* irradiation.

5.3 CONCLUSIONS

In this chapter we have investigated two approaches to overcome the limitations of bottom-up physical deposition techniques and Volmer-Weber growth mode for the fabrication of metal nanoparticles with controlled size and shape: thermal annealing and laser irradiation. The results obtained allow us to conclude that thermal annealing is an efficient approach for the fabrication of large nanoparticles (> 40-50 nm). We observed that annealing in air leads to nanoparticles with almost circular in-plane projected shape, contrary to the case of annealing

in vacuum that promotes the formation of very elongated nanoparticles with irregular shape. This difference was mainly related to the reduced convection heat transfer in the second case.

After the deposition of the covering layer we observed that sputtering is almost negligible in the case of large nanoparticles due to their increased cohesive energy and to the reduced surface coverage. As a result, the covering layer deposits over nanoparticle replicating their topography, resulting in a nanostructured film with enhanced surface roughness. Covered nanostructured films obtained by annealing, i.e. CNa-4200, show an optical response that differs from that of nanostructures containing smaller nanoparticles, i.e. CN-300 and CN-900 films, mainly because of the increased intensity of the SPR and of their scattering efficiency.

We also showed that laser irradiation is a powerful post-growth process for reshaping and reorganization of nanoparticles. The final morphology and the optical properties of irradiated films depend on laser pulse duration, wavelength and fluence. In particular we observed that the mechanism that leads to reshaping in the case of ns irradiation is driven by nanoparticle melting and subsequent formation of almost spherical nanoparticles with narrow size and shape distributions as a result of surface energy minimization. Instead, in the case of fs irradiations, we demonstrated that the reshaping mechanism is driven by the high transient electric field typical of fs pulses. We observed that *on-* and *off-resonance* fs irradiations of the nanostructures lead to a dichroic optical behavior that is consistent with the formation of elongated and aligned nanoparticles at the highest fluence. Although the shaping process is similar, the effect is much more pronounced for off-resonance irradiation. This difference is most likely related to the progressive formation of nanoparticles that resonantly absorb laser light in the case of off-resonance irradiation which, in turns, promotes the mechanism responsible for nanoparticle elongation.

References

(1) G. Mie, Ann. Phys. **330**, 377-455 (1908)

(2) H. R. Stuart, D. G. Hall, Appl. Phys. Lett. **69**, 2329-2329 (1996)

(3) H. A. Atwater, A. Polman, Nature Materials **9**, 205-213 (2010)

(4) C. V. Thompson, Annu. Rev. Mater. Res. **42**, 399-434 (2012)

(5) D. Wong, P. Schaaf, Phys. Status Solidi A 210, 1544-1551 (2013) and references therein

(6) C. M. Müller, F. C. F. Mornaghini and R. Spolenak, Nanotechnology **19**, 485306 (2008)

(7) T. W. H. Oates, H. Sugime, S. Noda, J. Phys. Chem. C **113**, 4820-4828 (2009)

(8) S. Morawiec, M. J. Mendes, S. Mirabella, F. Simone, F. Priolo, I. Crupi, Nanotechnology **24**, 265601 (2013)

(9) I. Tanyeli, H. Nasser, F. Es, A. Bek, R. Turan, Optic Express **21**, A798 (2013)

(10) S. J. Henley, J. D. Carey, S. R. P. Silva, Physical Review B **72**, 195408 (2005)

(11) C. E. Rodríguez, R. J. Peláez, C. N. Afonso, S. Riedel, P. Leiderer, D. Jimenez-Rey, A. Climent-Font, Applied Surface Science **302**, 32-36 (2014)

(12) H. C. Kim, T. L. Alford, D. R. Allee, Appl. Phys. Lett. **81**, 4287 (2002)

(13) H. Bi, W. Cai, C. Kan, L. Zhang, D. Martin, F. Träger, J. Appl. Phys. **92**, 7491 (2002)

(14) Y. Yang, S. Pillai, H. Mehrvarz, M. A. Green, Solar Energy Materials & Solar Cells **122**, 208-216 (2014)

(15) D. Xie, M. P. Wang, W. H. Qi, J. Phys.: Condens. Matter **16**, L401-L405 (2004)

(16) W. H. Qi, B. Y. Huang, M. P. Wang, Z. Li, Z. M. Yu, Physics Letters A **370**, 494-498 (2007)

(17) J. P. Barnes, A. K. Petford-Long, R. C. Doole, R. Serna, J. Gonzalo, A. Suárez-García, C. N. Afonso, D. Hole, Nanotechnology **13**, 465-470 (2002)

(18) T. Jensen, L. Kelly, A. Lazarides, G. C. Schatz, J. Cluster Sci. **10**, 295-317 (1999)

(19) G. Xu, M. Tazawa, P. Jin, S. Nakao, Appl. Phys. A **80**, 1535-1540 (2005)

(20) M. Schmid, R. Klenk, M. Ch. Lux-Steiner, M. Topič, J. Krč, Nanotechnology **22**, 025204 (2011)

(21) F. J. Beck, A. Polman, K. R. Catchpole, J. Appl. Phys. **105**, 114310 (2009)

(22) H. Tan, R. Santbergen, A. H. M. Smets, M. Zeman, Nano Lett. **12**, 4070-4076 (2012)

(23) S. Morawiec, M. J. Mendes, S. A. Filonovich, T. Mateus, S. Mirabella, H. Águas, I-Ferreira, F. Simone, E. Fortunato, R. Martins, F. Priolo, I. Crupi, Optics Express **22**, A1059 (2014)

(24) E. Fort, C.Ricolleau, J- Sau-Pueyo, Nano Letters **3**, 65-67 (2003)

(25) J. R. Sanchez-Valencia, J. Toudert, A. Borras, A. Barranco, R. Lahoz, G. F. de la Fuente, F. Frutos, A. R. Gonzalez-Elipe, Adv. Mater. **23**, 848 (2011)

(26) A. N. Filippin, A. Borras, V. J. Rico, F. Frutos, A. R. Gonzalez-Elipe, Nanotechnology **24**, 045301 (2013)

(27) M. Kaempfe, T. Rainer, K.-J. Berg, G. Seifert, H. Graener, Appl. Phys. Lett. **74**, 1200 (1999)

M. Kaempfe, T. Rainer, K.-J. Berg, G. Seifert, H. Graener, Appl. Phys. Lett. **77**, 459 (2000) Erratum

(28) A. Stalmashonak, A. Podlipensky, G. Seifert, H. Graener, Appl. Phys. B **94**, 459 (2009)

(29) A. Stalmashonak, H. Graener, G. Seifert, Appl. Phys. Lett. **94**, 193111 (2009)

(30) A. A. Unal, A. Stalamshonak, G. Seifert, H. Graener, Proc. SPIE **7032**, 703225 (2008)

(31) A. Kiesow, S. Strohkark, K. Löschner, A. Heilmann, A. Podlipensky, A. Abdolvand, G. Seifert, Appl. Phys. Lett. **86**, 153111 (2005)

(32) K. Loeschner, G. Seifert, A. Heilmann, J. Appl. Phys. **108**, 073114 (2010)

(33) S. Link, M. A. El-Sayed, In *Annual Review of Physical Chemistry* **54**, 331-366 (2000) and references therein

(34) R. A. Wood, P. D. Townsend, N. D. Skelland, D. E. Hole, J. Barton, C. N. Afonso, J. Appl. Phys **74**, 5754-5756 (1993)

(35) A. L. Stepanov, V. N. Popok, Surface and Coatings Technology **185**, 30-37 (2004) and references therein

(36) M. Sendova-Vassileva, M. Sendova and A. Troutt, Appl. Phys. A **81**, 871-875 (2005)

(37) M. Kawasaki, M. Hori, J. Phys. Chem. B **107**, 6760-6765 (2003)

(38) V. Resta, J. Siegel, J. Bonse, J. Gonzalo, C. N. Afonso, E. Piscopiello, G. Van Tenedeloo, J. Appl. Phys. **100**, 094302 (2006)

(39) L. A. H. Fleming, G. Tang, S. A. Zolotovskaya, A. Abdolvand, Optical Materials Express **4**, 969-975 (2014)

(40) J. Doster, G. Baraldi, J. Gonzalo, J. Solis, J. Hernandez-Rueda, J. Siegel, Appl. Phys. Lett. **104**, 153106 (2014)

(41) J. Bonse, G. Bachelier, J. Siegel, J. Solis, H. Sturm, J. Appl. Phys. **103**, 054910 (2008)

(42) G. T. Fei, J.-P. Barnes, A. K. Petford-Long, R. C. Doole, R. Serna, J. gonzalo, J. Phys. D: Appl. Phys. **35**, 916-922 (2002)

(43) A. Stalmashonak, G. Seifert, H. Graener, Opt. Lett. **32**, 3215 (2007)

(44) E. Boulais, R. Lachaine, M. Meunier, Nano Lett. **12**, 4763 (2012)

(45) A. Podlipensky, A. Abdolvand, G. Seifert, H. Graener, Appl. Phys. A **80**, 1647-1652 (2005)

Chapter 6
Applications of Nanostructured Silver Films

The unique optical properties of plasmonic nanostructures such as the generation of an enhanced near-field in the vicinity of the nanoparticle surface and the scattering of light to the far field make them suitable for different technological applications. In this chapter, we investigate the application of coalesced and thermally-formed nanoparticles as surface enhanced Raman scattering substrates and we present the first steps to improve the performance of chalcopyrite-based solar cells through the incorporation of nanostructured silver films.

6.1 SURFACE-ENHANCED RAMAN SPECTROSCOPY ACTIVITY OF NANOSTRUCTURED SILVER FILMS

Surface-Enhanced Raman Spectroscopy (SERS) is probably the most extended and powerful technique for chemical and structural characterization of molecules at very low concentrations.[1,2] Apart from molecular characterization, SERS is applied in detection of, for example, contaminants[3] and drugs[4] and in many other research field like biophysics and biomedicine,[5] due to its high sensitivity to the chemical substances adsorbed on the metal surface.

SERS is based on Raman spectroscopy, which, in turn, is based on inelastic scattering of light.[2,6] When a light beam interacts with the molecules of a material and photon absorption occurs, the molecules are excited to a higher energy level (virtual state, Figure 6.1). After excitation, molecules can relax back to their initial vibrational level or to a different one. In the first case, the interaction promotes the emission of a photon with the same energy of the incident one, a scattering process also known as elastic or Rayleigh scattering,[6] whereas in the second, the interaction leads to the emission of a photon with an energy different from that of the incident one. In this case the process is defined as inelastic or Raman scattering. The molecule can relax to a vibrational level at higher or lower energy than the initial one, which are known as Stokes or anti-Stokes Raman scattering, respectively. Figure 6.1 shows a schematic representation of the different light scattering processes.

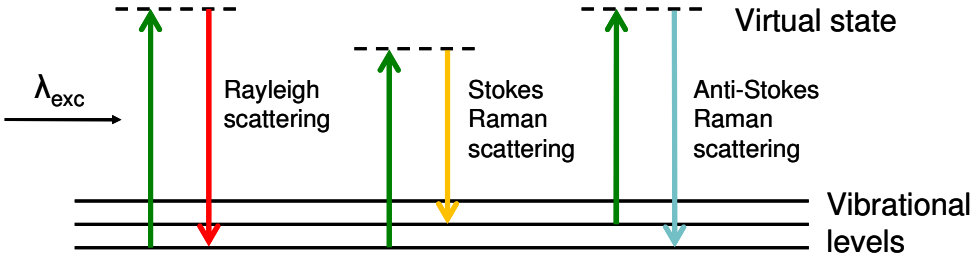

Figure 6.1: Schematic representation of Rayleigh and Raman scattering processes.

The vibrational levels are characteristic of each molecule, thus the vibrational spectrum can be considered as an actual fingerprint of the substance. Raman spectroscopy provides information about the molecular structure and the environment of molecules by measuring the shift between the energy of the incident light and that of the light that undergoes inelastic scattering after interacting with the sample.[6] The technique is based on a laser beam

irradiating a sample with a determined wavelength and power density and a spectrometer that collects the photons that undergo inelastic scattering. The resulting Raman spectrum consists of a series of frequency bands whose position is correlated to the vibrational levels of all molecules forming part of the investigated sample. The band position is independent on the excitation wavelength, while its intensity is proportional to the forth power of the excitation frequency.[2,6] At room temperature, Stokes transitions are more favourable and the corresponding signal intensity is larger with respect to the anti-Stokes ones. For this reason Raman spectroscopy is usually carried on in the Stokes frequency region.[6]

Raman spectroscopy is a very flexible technique used in many scientific and industrial research fields (from materials and chemical science to heritage and art studies) since it is non-destructive and it can be used for characterization of both organic and inorganic compounds without any specific limitations regarding their aggregation state. Indeed solids, liquids and gases can promote inelastic scattering. Despite its versatility, Raman spectroscopy suffers from the low intensity of the signal, since inelastic light scattering is a process millions of times less probable than elastic scattering, which mainly restricts its application to bulk materials.[2,6] However, the works carried on in the 70's first by Fleischman and co-workers[7] and later by Jeanmaire and Van Duyne[8] and, independently, by Albrecht and Creighton[9] represented a fundamental breakthrough for Raman spectroscopy since they demonstrated, for the first time, that the Raman signal of a molecule (Pyridine) adsorbed on a roughened metallic surface (Ag) could be drastically intensified compared to the case of non-supported molecules. This discovery led to the development of a much more sensitive technique, the Surface-Enhanced Raman Spectroscopy which allows reducing the detection sensitivity down to the single-molecule detection limit.[1,2] Qualitatively, the intensification of the Raman signal is strongly related to the near-field generated in the vicinity of a nanostructured metal surface (i.e., nanoparticles) at the SPR.[10,11] The near-field can contribute to the modification of the radiative properties of a molecule via two main multiplicative effects. The first one relates to the local enhancement of the incident field on the molecule, whereas the second is due to the intensification of the re-emitted Raman scattering from the same molecule.[2,12] Figure 6.2 schematically represents the different intensity of Raman signal of an analyte adsorbed on a (a) non-structured standard and (b) structured metallic substrate.

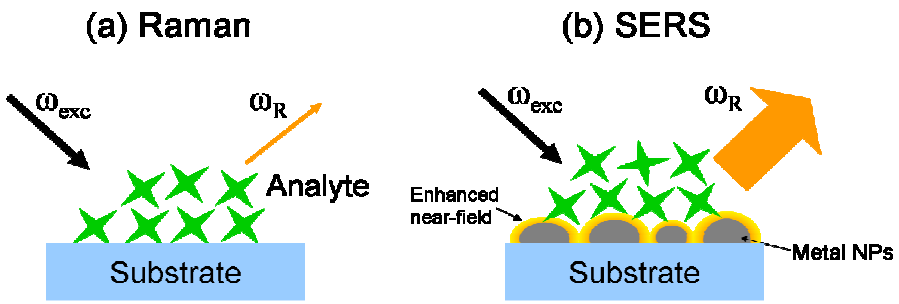

Figure 6.2: Schematic representation of the (a) Raman and (b) SERS processes in the case of a material in low concentration. ω_{exc} and ω_R represent the frequency of the laser beam used to illuminate the sample and the frequency of the inelastically scattered light (the Raman scattering frequency), respectively. Adapted from Guerrini and Graham.[2]

The SERS enhancement[1] (the ratio of the Raman-scattered intensity in the presence of the metal nanoparticle to its value in absence of the metal nanoparticle) lies in the range from 10^5 to 10^{11} depending on the configuration of the experiment.[2] The enhancement of the near-field and thus of Raman signal is maximum when the excitation wavelength is equal to the spectral position of the SPR maximum. In addition, the near-field intensity decreases rapidly with the distance from the metal surface.[10,11] As a consequence, SERS signal is larger when the distance between the metallic surface and the molecule is short. For this reason the molecule is usually adsorbed on the metallic surface in order to guarantee the highest Raman signal intensification in SERS experiment.

Apart from the dependence of SERS on electromagnetic factors, the intensification of the Raman signal can be also related to a chemical contribution. When a molecule is adsorbed on a metallic surface, new molecule-metal complexes are formed.[1,2] As a result, the electronic properties of the molecule are altered, resulting in new electronic transitions that, in some cases, can promote an increase of the Raman cross-section. These chemical effects scarcely contribute to the Raman intensification, such that it is generally accepted that SERS is mainly determined by electromagnetic factors.[1,2] Nonetheless, the charge-transfer effect can modify the spectral signal emitted by the adsorbed analyte.

This brief introduction evidences that SERS strongly depends on the optical response (i.e., the SPR) of the nanostructured metallic surface used to induce Raman scattering enhancement. In the case of metal nanoparticles, we have already shown that the SPR spectral position and intensity is determined by the material of which they are made, their size, shape and spatial arrangement and, in addition, by the refractive index of the surrounding or supporting material.[10,11] Thus, one can achieve the highest Raman scattering enhancement by

properly adjusting all these factors and by tuning the laser excitation wavelength to the SPR spectral position, which guarantees the highest intensification of the near-field in the vicinity of the metal surface.

Standard SERS-substrates do not exist since their optimum characteristics depend on the scope of the experiment and to the characteristics of the studied molecule. However, there are some concepts that generally lead to substrates with high SERS performance. Noble metals, in particular Au and Ag nanoparticles are usually considered the most suitable materials since they show intense SPR in the visible and near-infrared spectral regions, which are those of interest in SERS experiments.[2] Ag is generally preferred over Au since it shows higher absorption cross section in the visible range and because the SPR is not affected by the damping promoted by interband transitions, as it is in the case of Au.[1,13] Nonetheless, Au offers improved stability and non-toxicity compared to Ag.[2] In general, nanoparticles with typical dimension in the 10-80 nm range are more suitable for SERS.[1,2] Too small nanoparticles would support plasmon too weak to promote any Raman signal enhancement, whereas in large nanoparticles non-radiative multipolar resonances are excited, besides the dipolar mode, that do not significantly contribute to Raman intensification.[1,10,11] Besides the size, the nanoparticle shape is also important. Anisotropic nanoparticles characterized by corners or tips at the surface, like nanorods and triangles, can generate additional local huge near-field resonant enhancements in correspondence of those specific features.[2,10] Moreover, the nanoparticle spatial arrangement is fundamental. When two or more nanoparticles are separated by a gap of few nanometres, plasmon coupling can occur resulting in an additional enhancement of the local field at the interparticle junction, which is known as *hot spot*.[1,2,11] If a molecule is placed in the gap and the laser polarization is oriented along the inter-particle axis, the enhancement of its Raman signal can exceed up to 10^3-10^4 times that achieved with single nanoparticles.[2] Finally, the material embedding or supporting nanoparticles can promote a shifting of the SPR to longer wavelengths, thus providing a method to fit the SPR spectral position to the excitation laser wavelength and, hence achieving proper SERS excitation condition.[10]

Since SERS was first demonstrated, many efforts have been dedicated to the fabrication of high-performance SERS substrates. Nowadays, both chemical and physical techniques are successfully used to produce metallic nanostructures with optimized optical response to achieve the highest near-field intensification at the SPR. Usually, chemical routes are more flexible than physical approaches and they allow synthesizing nanoparticles with sizes in a

very broad range of values (10-100 nm) and with very different shapes.[2] Nanorods with different aspect ratios,[14] nanocubes[15] as well as nanostars[16] are only few examples that remark the suitability of chemical routes for synthesizing nanoparticles with unique characteristics. Nanoparticles are obtained in suspension, i.e. colloidal nanoparticles, and SERS can be performed directly in solution or on a solid substrate by immobilizing nanoparticles on a standard substrate (glass, silicon). In the first case, very high SERS performance is achieved but results suffer from low reliability since they can be molecule concentration dependent.[17] Instead the main problem in the second case is the irreproducibility of the results mainly due to the non-standard methods used to immobilize colloidal nanoparticles on a substrate.[2] In this sense, SERS substrates produced using physical techniques represent a valid alternative. Reliability is guaranteed by the fact that nanoparticle aggregation is strongly reduced since nanoparticle are fixed on a substrate, while reproducibility of results is improved since films with similar characteristics (nanoparticle morphology and spatial arrangement) can be fabricated by keeping the experimental parameters unchanged during the deposition process. Top-down and bottom-up approaches have been used to successfully produce either randomly or periodically organized metallic nanostructures. Top-down techniques, like lithography,[18,19] allow a precise control over nanoparticle size, shape and spatial arrangement, thus on interparticle distance, while bottom-up approaches offer only partial control over those parameters, but they are advantageous in terms of nanostructure fabrication process simplicity and low-cost and because they allow working on large areas. High performance SERS substrates have been successfully fabricated using electrodeposition[20], atomic layer deposition[21,22] and PLD.[23,24,25,26] In the latter case, SERS substrates made of Ag and Au nanoparticles were obtained in vacuum or in a gas background by depositing small amount of metal,[25,26] i.e. well below percolation limit, or by depositing thick metal films then followed by thermal or laser annealing.[23,24] In all these cases, only the substrates with proper nanoparticle morphology (size and shape) and interparticle distance to promote the formation of hot spots showed remarkable SERS activity.

In the previous chapters we have demonstrated that it is possible to produce nanostructured Ag films with specific morphology and optical response. Thus, we have finally investigated the SERS activity of our pulsed laser deposited nanostructures. In particular, we performed SERS experiments on two nanostructured films characterized by very different nanoparticle morphology and density using a non-commercial molecule, namely, 4,4”-terphenyl diisocyanide (TPDI) as test molecule. We investigate the dependence

of SERS signal on nanoparticle morphology, molecule concentration and molecule-to-nanoparticles surface distance. Finally, we show that our nanostructured films can act as a platform for nanoparticle superstructures, with the TPDI as linker between PLD and colloidal nanoparticles.

6.1.1 SERS substrates and test molecule

Figure 6.3 shows plan-view SEM images of nanostructured films grown on Si used as SERS substrates. They are fabricated using the same experimental conditions than for UN-900 (Figure 6.3a) and UNa-4200 (Figure 6.3b) films described in Chapters 4 and 5, respectively. The film in Figure 6.3a shows a completely similar morphology than of UN-900. It consists of a layer of coalesced nanoparticles with circular and elongated in-plane projected shapes. On the contrary, the film in Figure 6.3b slightly differs from UNa-4200. In addition of the large nanoparticles having almost circular in-plane projected shape and showing a bimodal size distribution, we observe the presence of elongated and irregular features that seem to be traces of the initial percolated film, which were not affected by annealing.

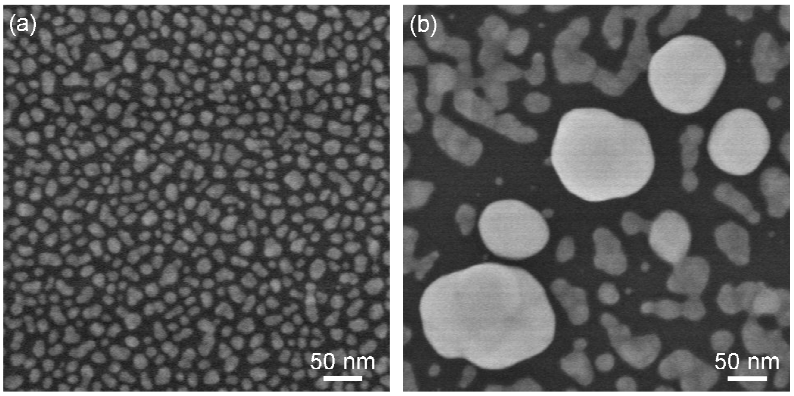

Figure 6.3: Plan-view SEM images of (a) S-NPs and (b) L-NPs substrates.

Similarly to UN-900 and UNa-4200 films, the average long axis length of nanoparticles is ≈ 20 nm in (a), while in (b) it is ≈ 50 nm and ≈ 135 nm for small and big nanoparticles, respectively. Besides the size, the two films show very different nanoparticle density. In (a) nanoparticles are dense (≈ 1.4×10^3 NPs μm^{-2}), while in (b) they are sparse (≈ 30 NPs μm^{-2}). Due to the obvious different size distributions, we have identified the films in Figures 6.3a and 6.3b as S-NPs (small nanoparticles) and L-NPs (large nanoparticles) substrates, respectively.

As mentioned previously, the molecule used to test the suitability of the S-NPs and L-NPs films as SERS substrates is the TPDI that is formed by three aromatic rings and by two isocyanide groups at its edges (Figure 6.4).

Figure 6.4: Structure of the TPDI.

This structure results in a very short (2-3 nm) and rigid molecule[27,28] that can strongly adsorb on metallic surfaces through the N≡C groups.[29] Diisocyanides have been widely studied in literature because they represent a promising candidate for stabilization of metal nanoparticles, functionalization of metal electrodes and for the creation of conducting-metal junctions in molecule-scale electronic devices.[28,30,31] Indeed, due to its stiffness, diisocyanides generally adsorbs on metallic continuous surfaces only through one N≡C group and keeps aligned perpendicular to the metallic surface,[27,32] with the second N≡C group that remains available for subsequent attachment of metal complexes, clusters or nanoparticles.[27] In addition, diisocyanides can interact with both N≡C groups linking two different nanoparticles in the case of adsorption on colloidal metal nanoparticles,[29,33,34] which hints at the possibility of using these types of molecules as molecular wires.[31,34] However, no SERS data of TPDI on substrates supporting metal nanoparticles fabricated using a physical technique have been reported yet. In this sense, our work provides new insight into the interaction and coordination mechanisms of TPDI when it adsorbs on a solid nanostructured SERS substrate.

The molecule was chemically synthesized at the *Catalysis Research Center group* of the *University of Hokkaido* (Sapporo, Japan) by Dr. K. Hara according to the method reported by Henderson and co-workers.[28] The molecule was dissolved in ethanol at different concentrations and then deposited on the S-NPs and L-NPs substrates by pouring a drop of solution on the same film surface. After evaporation of the solvent, the surface was rinsed with pure ethanol to eliminate any free TPDI molecule on the surface.

SERS spectra were collected on a Renishaw Raman InVia spectrometer equipped with an electrically cooled CCD camera. SERS spectra were recorded using the 532 nm laser line provided by a frequency-doubled Nd:YAG laser, the power at the sample surface being 50 μW. The spectral resolution was set to 2 cm^{-1}. Acquisition time for each SERS spectrum was

10 s and consisted of only one scan. The laser excitation wavelength was selected according to the fact that the position of the SPR of L-NPs and S-NPs substrates should resemble that of UN-900 and UNa-4200 films, respectively, which show an extinction band corresponding to the dipolar mode of the SPR supported by nanoparticles peaked at ≈ 515 nm (Figure 6.5). In addition, since high order poorly contribute to the enhancement of Raman signal,[1] the contribution to SERS of the quadrupolar mode (the extinction band peaking at shorter wavelength) observed in the case of UNa-4200 film could be neglected.

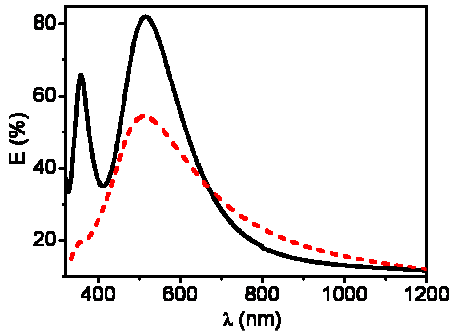

Figure 6.5: Extinction spectra of UNa-4200 and UN-900 films

Finally, we compared the obtained SERS spectra with those obtained performing FT-Raman spectroscopy. In this case, we used solid TPDI since its high insolubility avoids the preparation of TPDI solutions with sufficient high concentration to be detected using Raman spectroscopy. In the case of FT-Raman, we used a MultiRam Bruker spectrometer equipped with a high-sensitivity Ge diode detector. The 1064 nm line was provided by an air-cooled Nd:YAG laser. The laser power was 200 mW at the sample surface and the resolution was set to 4 cm^{-1}. The Raman spectra obtained were the result of 1000 accumulations. All the measurements were carried on at the *Instituto de Estructura de la Materia* (IEM) of the CSIC in collaboration with Dr. S. Sanchez-Cortes and E. Lopez-Tobar.

6.1.2 Dependence on film morphology

Figure 6.6 shows the SERS spectra of TPDI adsorbed on both S-NPs and L-NPs substrates grown on Si, compared to the Raman spectrum of solid TPDI. The molecule concentration was 10^{-6} M and 10^{-4} M for experiments performed on S-NPs and L-NPs substrates, respectively. The assignment of vibrational bands that is shown in Table 6.1 has

been made according to previously published SERS analysis of related isocyanides and diisocyanides.[27,29,35,36]

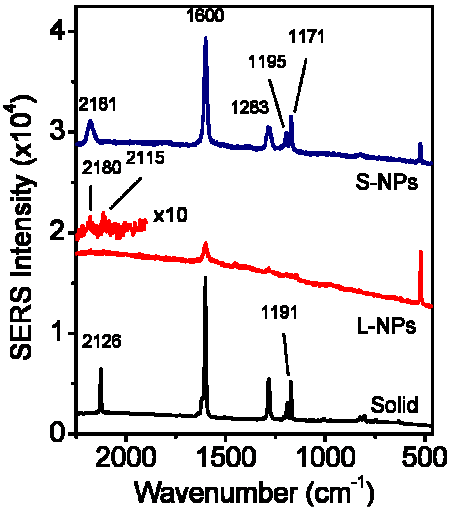

Figure 6.6: SERS spectra measured for TPDI solutions on S-NPs (10^{-6} M) and L-NPs (10^{-4} M) substrates. We also include the SERS spectrum, enlarged by a factor 10, in the range 1880-2300 cm^{-1} in the case of L-NPs substrate and the Raman spectrum corresponding to solid TPDI. The spectra have been shifted vertically to ease comparison. Excitation is at 532 nm (SERS) and 1064 (Raman).

Table 6.1. Vibrational assignments of Raman bands of solid TPDI and SERS spectra of TPDI on S-NPs substrate. Excitation at 1064 nm (Raman) and at 532 nm (SERS).

Raman of TPDI[c]	SERS of TPDI on S-NPs[c] (10^{-6} M)	Assignment[a,b]
	2181m	νN≡C (bounded)
2126m		νN≡C (free)
1620sh		
1602	1600	νC=C
1507vw		νC=C / δCH
1288sh		
1283m	1283m	νC-C (inter-ring)
1191w	1195w	ν(C-N≡C) / δCH
1172m	1171m	δCH
1007vw	1003vw	ν(Kekulé)
826w	822vw	γCH
804w	807vw	γCH
746vw		
631vw		Ring Skeletal Deformation

[a] Based on the assignments made in Refs 27,29,35,36.
[b] ν: stretching, δ: in-plane deformation; γ: out-of-plane deformation.
[c] m: medium, sh: shoulder, w: weak, vw: very weak.

The SERS spectrum of a 10^{-6} M solution of TPDI on S-NPs substrate resembles the Raman spectrum of the solid, although some differences can be found. The main change observed concerns the shift undergone by the band assigned to the ν(N≡C) vibration of the isocyanide group. It shifts from 2126 cm^{-1} in the solid toward higher wavenumbers (≈ 2181 cm^{-1}) in the S-NPs substrate. This large blue-shift indicates a strong interaction of this group with the Ag through the C lone pair of electrons.[37] This interaction with the Ag leads to a strengthening of the NC bond responsible for the observed blue-shift. Moreover, the absence of bands corresponding to free N≡C groups on Ag suggests that both isocyanide groups are interacting at the indicated concentration with two different nanoparticles through both terminal groups.

As it can be deduced from Figure 6.3a, the interparticle spacing in the case of S-NPs substrate is in many cases in the range from 2 to 3 nm, which suits the length of TPDI adsorbate and it makes possible that both TPDI isocyanide groups are attached to two Ag neighbouring nanoparticles.[33,31] Since TPDI molecules are uniformly linked to Ag nanoparticles, it is expected that only a small fraction of them are placed in the interparticle gaps below 3 nm. However, the fact that no vibration at 2126 cm^{-1}, corresponding to $\nu(N{\equiv}C)_{free}$, is observed suggests that only the small fraction of TPDI molecules placed in the nm-sized interparticle junctions are seen in the spectra. This is consistent with the formation of hot spots in correspondence of such nanogaps that lead to a huge intensification of the electromagnetic field and, consequently, to a large SERS signal.[1,2,11]

The other band related to the isocyanide group which undergoes a shift is that at 1191 cm^{-1}. This band shifts to 1195 cm^{-1} in S-NPs substrate and it can be attributed to the ν(C-NC) motion, which may be slightly affected by the interaction with the metal.[27] Finally, other strong bands observed in the SERS spectrum of TPDI on S-NPs substrate are those at 1600 and 1171 cm^{-1}. They are attributed to in-plane vibrations of the benzene ring that can be used as molecular orientation probes.[29,35,37] Their large intensification along with that of the ν(N≡C) bands and the absence of the out of plane band at 804 cm^{-1} indicate that the orientation of TPDI is predominantly perpendicular to the Ag nanoparticles surface, as it has been also reported for the related molecule phenyl diisocyanide.[34]

Figure 6.6 shows finally that the SERS intensity of TPDI is much lower in the case of L-NPs substrate, even for a 10^{-4} M solution of TPDI. Two very weak ν(N≡C) bands are observed at 2180 cm^{-1} and 2115 cm^{-1} corresponding to linked and free N≡C groups, respectively, together with the band at 1600 cm^{-1}. The different position of the free ν(N≡C)

band in relation to the solid sample can be attributed to the effect of the interaction with the metal.[27] In order to understand this response, we must bear in mind that the nanoparticle morphology of L-NPs substrate is completely different from that of S-NPs substrate. We observed very large nanoparticles, but their density is much smaller (Figure 6.3b). As a consequence the interparticle spacing is larger than 3 nm in most cases, which avoids TPDI to be linked to Ag nanoparticles through both isocyanide groups, while hot spots are much less likely to occur due to the larger interparticle spacing. Thus, the overall SERS intensity is much smaller than in the case of S-NPs substrate and TPDI molecules appearing in the corresponding SERS spectra are bounded to the surface through only one isocyanide group.

6.1.3 Dependence on molecule concentration

As previously discussed, SERS performed in solution on colloidal nanoparticles suffer from reduced reliability mainly due to the fact that the signal is generally adsorbate concentration and nanoparticle size dependent. For example, SERS spectra of biphenyl diisocyanides[29] and phenylene diisocyanides[33,34] in solution change with molecule concentration when measured on small (mean diameter < 60 nm) Au colloidal nanoparticles, while they keep almost unchanged if bigger (mean diameter > 60 nm) colloidal Au nanoparticles are used to induce the signal enhancement. Solid SERS substrates firmly immobilize nanoparticles on a surface which is expected to improve the reliability of SERS measurements since nanoparticle aggregation should be avoided. Thus, we have investigated the influence of TPDI concentration on SERS spectra obtained on S-NPs substrates.

Figure 6.7 shows three representative normalized SERS spectra at increasing concentrations of TPDI adsorbed on S-NPs films grown on Si.

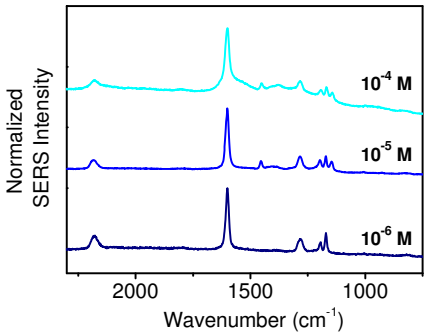

Figure 6.7: Normalized SERS spectra of TPDI on S-NPs substrate at different concentrations. Spectra have been shifted vertically to ease comparison. Excitation at 532 nm.

The vibration band at 2126 cm^{-1} related to free isocyanide groups is not observed in any of the cases, while bands at 2181 cm^{-1}, 1600 cm^{-1}, 1283 cm^{-1}, 1195 cm^{-1}, and 1171 cm^{-1} are clearly visible and their relative intensities remain similar. In addition, the peak position of these bands does not change with the TPDI concentration over the 10^{-6} M to 10^{-4} M concentration range. This result suggests that the adsorption scheme does not depend on the TPDI concentration, contrary to what is reported in literature.[29,33,34] Moreover, the fact that the band at 2126 cm^{-1} is not observed even for a concentration as low as 10^{-6} M suggests that the accessible hot spot sites at the S-NPs substrate are already occupied, which is likely related to the fixed interparticle spacing in SERS solid substrates.

The results presented here demonstrate that the performance of nanostructured films as SERS substrates strongly depends on the optimum choice of the interparticle spacing. In the case of S-NPs, this is small enough to favour the existence of hot spots among neighbouring nanoparticles. Moreover, in the case of TPDI the interparticle spacing is of the same order than the molecule length which allows both N≡C terminal groups to be attached to two Ag nanoparticles and leads to a strong SERS signal compared to that of L-NPs. This adsorption scheme of TPDI is similar to that observed in the case of diisocyanides adsorbed on colloidal nanoparticles but with a fundamental difference. In our case SERS is independent on molecule concentration. This is consistent with the fact that the position of nanoparticle in solid substrates is fixed which prevents nanoparticle aggregation.

6.1.4 Dependence on molecule-to-nanoparticle surface distance

As already discussed in Chapter 4, the main drawback of Ag for its application in real devices is its tarnishing when it is exposed to air. In the case of SERS, this degradation process drastically reduces the SERS activity since it damps considerably the nanoparticle SPR.[22,38,39] Zhang and co-workers[40] and John and co-workers[22] have shown that the stability of SERS substrates supporting Ag nanoparticles can be strongly improved by covering nanoparticles with a thin layer of Al_2O_3 deposited by atomic layer deposition. In addition, they also reported that the intensity of the SERS signal decreases almost exponentially with increasing the thickness of the covering layer due to the increase of the molecule-to-nanoparticle surface distance. We have demonstrated in Chapter 4 that PLD allows depositing very thin a-Al_2O_3 covering layer on top of nanoparticles which considerably improved the mid-term chemical and, consequently, optical stability of nanostructured films. Thus, we have

explored the SERS activity of S-NPs substrates covered with a layer of a-Al_2O_3 of increasing thickness produced by PLD.

Figure 6.8a shows SERS spectra of TPDI poured on a S-NPs substrate (Figure 6.3a) and on two S-NPs substrates having an a-Al_2O_3 covering layer with nominal thickness of 1 and 3 nm, while Figure 6.8b shows the evolution of the SERS intensity of the band at 2181 cm^{-1} with the thickness of the a-Al_2O_3 layer.

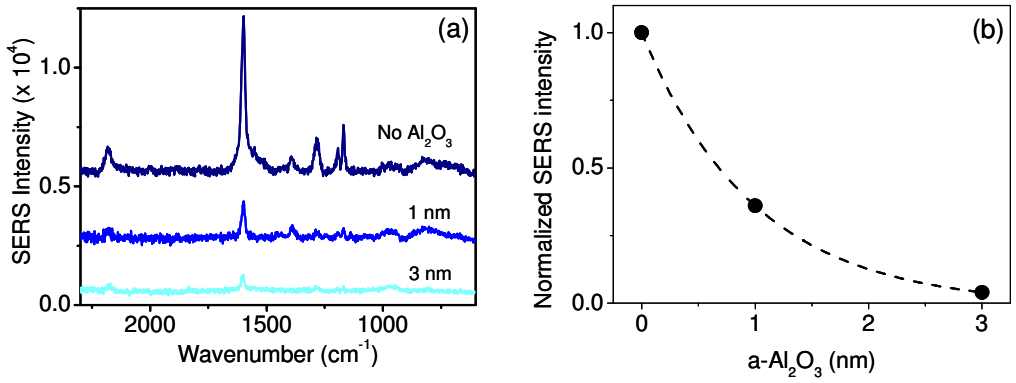

Figure 6.8: (a) SERS spectra of TPDI (10^{-5} M) on S-NPs substrate for increasing a-Al_2O_3 covering layer thickness. (b) SERS intensity as a function of the nominal a-Al_2O_3 thickness for 2181 cm^{-1} band. The curve is an exponential decay fit to experimental data.

The SERS intensity of TPDI markedly reduces for covered films. All bands are still observed for a covering layer with nominal thickness of 1 nm, whereas only the bands at 1600 cm^{-1} and at 2181 cm^{-1} are detectable for a thickness of 3 nm. Finally, they disappear for a thicker covering layer (not shown). It should be noted that the position of the bands does not shift in any of the cases reported which suggests that the adsorption scheme of the TPDI keeps unchanged.

According to the morphological results shown in Chapter 4, we do not expect a complete covering of the nanoparticles for any of the a-Al_2O_3 covering layers deposited on the S-NPs substrates. Thus, the fact that the band corresponding to N≡C is observed at 2181 cm^{-1} and not at 2126 cm^{-1} supports that both isocyanide groups are still bounded to metal atoms, i.e. to either Ag from the partially covered nanoparticles although we cannot rule out bounds to Al atoms from the covering Al_2O_3 layer. Similarly to the results reported in literature,[22,38,39] the decrease of the SERS intensity decay exponentially with the covering layer thickness (Figure 6.8b). This trend of the SERS signal with the thickness of the a-Al_2O_3 covering layer further supports that its intensification is mainly related to the electromagnetic

contribution provided by the near-field enhancement generated in the vicinity of the nanoparticle at the SPR. Upon increasing the a-Al_2O_3 thickness, a progressive filling of the interparticle space is likely to occur; thus the fraction of TPDI molecules directly attached to Ag nanoparticles decreases, whereas that of attached to the a-Al_2O_3 cover layer increases. The combination of these two factors together with the fact that the intensity of the near-field decrease rapidly with the distance from metal surface lead to a dramatic reduction of the electromagnetic intensification probed by the TPDI molecules and thus, to a decrease of the SERS signal.

The fact that the SERS signal disappears before the nanoparticles are completely covered supports that we could not improve the chemical and optical stability while maintaining the SERS activity of S-NPs substrates.

6.1.5 TPDI as nanoparticle linker for fabrication of nanoparticle superstructures

The adsorption scheme of diisocyanides when adsorbed on continuous or nanostructured metallic surfaces and the improved electron conductance of the formed metal-molecule junction have attracted an enormous research interest for several applications such as stabilization of metal nanoparticles, functionalization of metal electrodes or for the creation of conducting-metal junctions in molecule-scale electronic devices among others.[27-31,34]

The measured TPDI SERS spectra on S-NPs substrates revealed only the presence of those molecules linked to two Ag nanoparticles through both N≡C groups. Nonetheless, it is reasonable to assume that TPDI uniformly adsorbs on nanoparticles and thus molecules linked only through one N≡C group exist but they are not detected probably because they are outside of the hot-spot regions. If this were true, we should be able to elaborate nanoparticle superstructures by means of TPDI tethers. To verify this, we conclude our study of the application of nanostructured Ag films to SERS spectroscopy by exploring this possibility. To that purpose, we have conducted an experiment in which we combine S-NPs substrates with colloidal Ag nanoparticles (C-NPs) and look at the SERS response of TPDI molecules.

C-NPs were synthesized at the *IEM* of the *CSIC* by Dr. S. Sanchez-Cortes according to the method reported in literature:[41] Hydroxylamine Ag nanoparticles (AgH) are obtained by adding 10 mL of a 10^{-2} M silver nitrate solution to 90 mL of a 1.6×10^{-3} M solution of hydroxylamine hydrochloride adjusted to pH = 9 under vigorous stirring. Following this procedure, Ag nanoparticles having almost circular or elongated in-plane projected shape and

size in the 30-70 nm range were obtained (Figure 6.9). C-NPs were then deposited on the S-NPs / TPDI substrate by pouring a volume of 1 μL of the suspension and leaving the solvent (water) to evaporate.

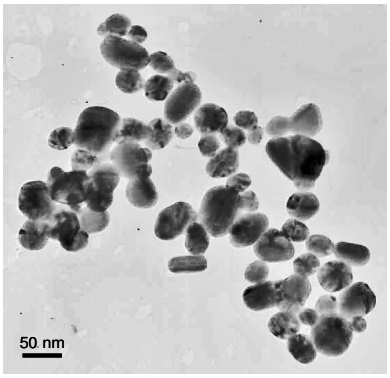

Figure 6.9: Plan-view TEM image of C-NPs deposited on a TEM Cu grid.

The immobilization of C-NPs on the S-NPs / TPDI substrate via molecule tethers may result in the formation of new hot spots between C-NPs and nanoparticles of S-NPs substrate and thus, to an increase of the overall SERS due to the signal of TPDI that are acting as tethers. Figure 6.10 shows a SERS map[††] obtained by recording the signal of $\nu(N\equiv C)_{bound}$ band at 2181 cm^{-1} over a 32 × 45 μm^2 area at the edge of the footprint left by the drop containing C-NPs.

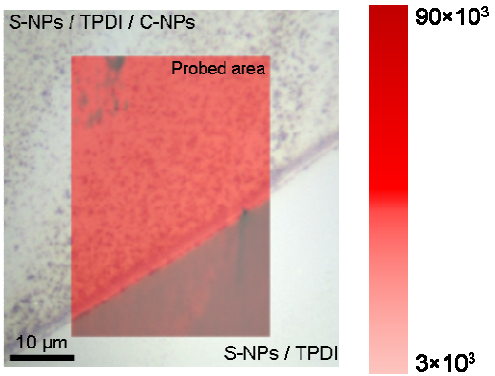

Figure 6.10: SERS map in the region between S-NPs / TPDI/ C-NPs superstructure and S-NPS / TPDI substrate regions. The signal recorded corresponds to the ν(N≡C) band at 2181 cm^{-1}. The color scale represents the intensity of the signal.

[††] SERS maps are obtained by scanning the laser probe over a selected region of the sample and only the signal coming from a specific Raman band is recorded in order to reveal any variation of its intensity.

The map shows that the signal recorded in a region of the S-NPs / TPDI / C-NPs superstructure can be up to thirty times more intense than in the case of S-NPs / TPDI substrate. This result would thus support the formation of new hot spots between C-NPs and those of the S-NPs substrate via TPDI tethers. To confirm this conclusion, we have investigated the morphology of the fabricated S-NPs / TPDI / C-NPs superstructure through SEM. The obtained plan-view image is shown in Figure 6.11.

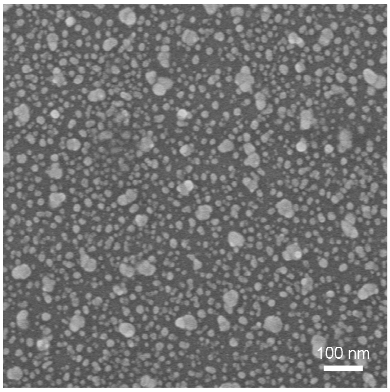

Figure 6.11: Plan-view SEM images of the S-NPs / TPDI / C-NPs superstructure on Si substrate.

We observe in the image two nanoparticle distributions with different characteristic size. The first one is characterized by a very dense layer of nanoparticles with size in the 15-25 nm range and almost circular or elongated in-plane projected shape, whereas the second shows larger and sparse nanoparticles ($\approx$ 40 NPs μm^{-2}) with a narrower size distribution, an average size approximately of 50 nm and an almost circular in-plane projected shape. The first nanoparticle distribution corresponds to that of the original S-NPs substrate (Figure 6.3a), whereas the second one corresponds to C-NPs. The image suggest that the C-NPs are immobilized on top the S-NPs substrate by the TPDI molecules and beautifully supports that the large SERS intensity observed in Figure 6.10 is related to TPDI molecules that would act as linkers between C-NPs and those of S-NPs substrate thus promoting the formation of new hot spots.

This simple experiment demonstrates that the S-NPs substrate produced by PLD is robust enough to allow the fabrication of nanoparticle superstructures where the adsorbed molecule acts as tether. Since TPDI molecules are able to adsorb on different types of metal surfaces this result opens new ways to fabricate more complex nanoparticle superstructures based on nanostructured metallic film produced by PLD.

6.2 INCORPORATION OF METAL NANOPARTICLES IN THIN FILM SOLAR CELLS

The working principle of solar cells is based on the photovoltaic effect, which is an opto-electronic physical process that allows converting light into electricity.[42,43] It takes place when a potential difference is generated in a material upon illumination. The photovoltaic effect is based on a three steps process that includes generation, separation and collection of photo-generated charge carriers. Semiconductors are the most suitable materials for the photovoltaic effect to take place due to their electronic band structure. Briefly, when a photon impinges on a semiconductor with an energy equal to or larger than the semiconductor bandgap, it can be absorbed, promoting the generation of an electron-hole pair (Figure 6.12a), that rapidly annihilates through recombination.

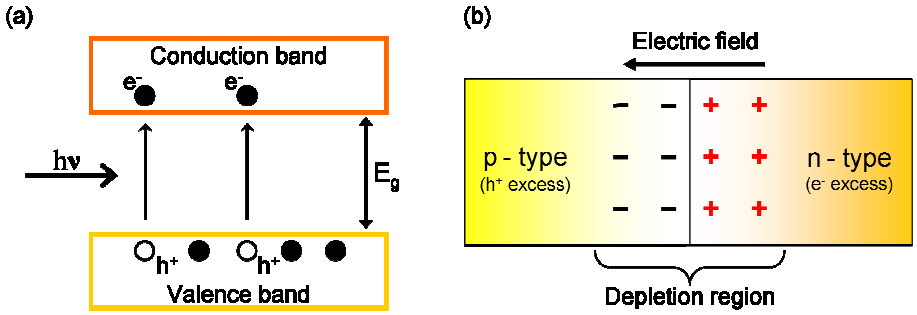

Figure 6.12: (a) Schematic view of the electronic band structure of a semiconductor, with the incoming photon with enough energy to generate an electron-hole (e^-, h^+) pair. E_g is the energy band gap. (b) Schematic representation of the depletion region formed in a p-n junction and of the associated electric field responsible for charge carriers' separation.

In order to allow the photovoltaic effect to take place, recombination must be avoided. The strategy consists in forming a junction between a semiconductor region doped with a controlled impurity level to produce electron excess (n-type semiconductor) and a second one doped with a controlled impurity level to produce hole excess (p-type semiconductor).[42,43,44] This p-n junction produces a depletion region at the contact area due to diffusion of charge carriers across the junction leaving space charges from ionized dopant ions, and a corresponding electric field gradient that is capable of separating photo-generated electron-hole pairs that diffuse to this junction (Figure 6.12b). Once the photo-generated charge carriers are separated, they can be collected and converted into electrical power through the application of a proper voltage to the terminal of the junction.

Solar cell operation is based on p-n junctions. For this reason most information about quality and performance of PV solar cells can be extrapolated from the current density-voltage (J-V) characteristic. Under dark conditions, a solar cell shows the rectifying behaviour typical of diodes, with the current density that increases exponentially upon application of a forward bias voltage and decreases to a very low and almost constant value upon application of reverse bias.[44] Under illumination, the J-V curve of the device is shifted in the fourth quadrant of the plot as a result of the contribution to the current coming from the photo-generated charge carriers. Figure 6.13 shows the characteristic J-V curve of a chalcopyrite-based solar cell measured under AM1.5‡‡ solar spectrum illumination.

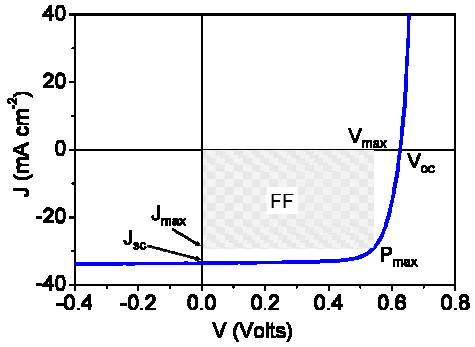

Figure 6.13: Characteristic J-V curve of a chalcopyrite-based solar cell under illumination. The photovoltaic parameters are included in the plot.

The main parameters defining the characteristics of the solar cell are (see Figure 6.13):[42,43,44]

- *Short circuit current density* (J_{sc}). It provides the maximum current density flowing through the solar cell when no voltage is applied. The light-generated current strongly relates to the amount of photons absorbed and electron-hole pairs generated and efficiently separated. This is why J_{sc} increases when lowering the bandgap of the material, since a larger amount of photons will be absorbed contributing to current generation.
- *Open-circuit voltage* (V_{oc}). It is the maximum voltage that can be measured across the two leads of the device when they are disconnected. It corresponds to the amount of forward bias of a p-n junction due to light generation current. At a voltage of V_{oc}, the

‡‡ AM stays for Air Mass. It refers to the air mass density of the atmosphere through which the sunlight has to go through before reaching earth. Thus, it relates to the spectral irradiance distribution that reaches the solar cell. The number refers to the angle at which the sunlight reaches the surface. The AM1.5 is the standard spectrum used to characterize solar cells and to compare the performance of different cells for earth applications.

light-generated (drift) current and the forward bias diffusion current of the p-n junction compensate. The maximum possible value for V_{oc} corresponds to that of the semiconductor bandgap. However, V_{oc} is usually smaller due to recombination processes and to the effect that solar cell contacts have on the energy levels of p-n junction.

- *Fill factor* (FF). It quantifies the "squareness" of the J-V curve under illumination. It is defined as:[42,43,44]

$$FF = \frac{J_{\max} V_{\max}}{J_{sc} V_{oc}} \tag{6.1}$$

where J_{max} and V_{max} are the values of the voltage and current density at the maximum power density (P_{max}) delivered by the cell. The FF represents the ratio of the area corresponding to the maximum power density ($P_{max} = J_{max} \times V_{max}$) to that associated to the values of J_{sc} and V_{oc}. The higher the FF, the higher the power density delivered.

- *Power conversion efficiency* (η). It is given by the equation:[42,43,44]

$$\eta = \frac{J_{sc} V_{oc} FF}{P} \tag{6.2}$$

where P represents the power density applied to the cell (i.e., 100 mW cm^{-2} in standard test conditions using a sun simulator resembling the AM1.5 light spectra).

Besides the parameters obtained from the J-V curve, the wavelength dependent quantum efficiency (QE) of a solar cell must be also taken into account for its characterization.[42,43,44] The quantum efficiency is related to the probability of an electron-hole pair generated upon absorption of a photon with a given wavelength to be collected by the solar cell for power generation. The QE can be external (EQE) or internal (IQE). The difference is that EQE includes the effect of optical losses such as transmission and reflection of the device. Figure 6.14 shows a typical EQE curve of a chalcopyrite-based solar cell compared to an ideal EQE curve.

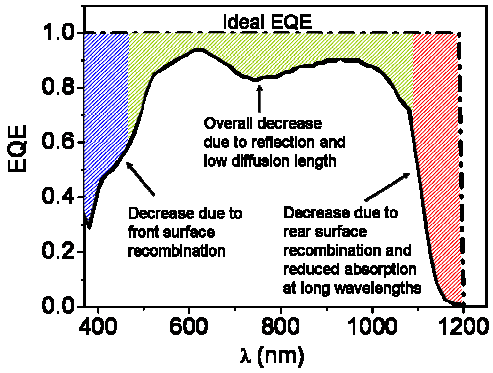

Figure 6.14: Typical EQE of a chalcopyrite-based solar cell. We also represent the ideal EQE in the plot and highlight the region where EQE is reduced due to recombination processes and low diffusion length of generated careers.

The ideal curve has a squared shape with EQE = 1 in the whole range of wavelengths, since in this case all photons of a given wavelength are absorbed and all the generated electron-hole pairs are efficiently collected by the device. However, the value differs from unity in the case of real solar cells mainly due to recombination effects. In particular, the quantum efficiency usually decreases at short (blue region in Figure 6.14) and long wavelengths (red region in Figure 6.14) because of recombination processes taking place at the front and at the rear surface of the solar cell, respectively.[42,43] Moreover, the EQE decreases as well as at wavelengths close to the material bandgap due to the reduced probability of photons absorption. Furthermore, photons with energy lower than the bandgap are not absorbed (EQE = 0).[43] Finally, the reduced EQE at intermediate wavelengths is mainly related to light reflection and to the low diffusion length of the photo-generated carriers, which prevents their collection.[42,43]

6.2.1 Solar cell technologies

The photovoltaic effect was discovered in 1839 by the French scientist E. Becquerel, but the first practical photovoltaic devices were fabricated only starting from the 1950s.[42,43] From that date, photovoltaic technology has experienced an increasing progress aiming to improve solar cell efficiency while reducing fabrication costs. In general, photovoltaic technologies can be classified into three generations, depending on power conversion efficiency and production cost of a solar cell module (Figure 6.15).[44]

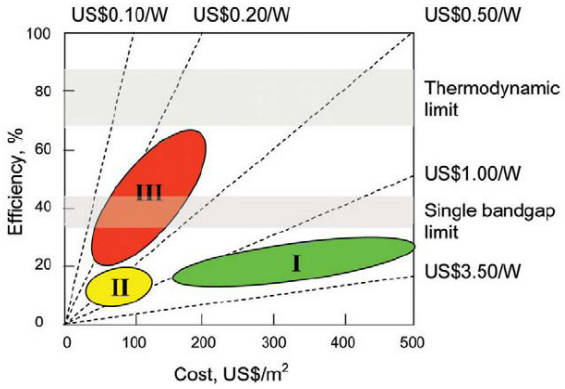

Figure 6.15: The three photovoltaic technologies generations scheme. The plot shows the module efficiency as a function of cost ($ m^{-2}). Adapted from Green.[45]

First generation mainly includes Si-based technologies.[44] These are characterized by relatively high production cost and moderate solar cell efficiency. Despite the high cost, crystalline Si-based solar cells have been the dominant cell type used in the last century. This is mainly related to the fact that Si is the second most abundant material in the earth's crust, which made it cheaper with respect to other materials. In addition, photovoltaic industry could take advantage of the large Si technological base developed by the electronic industry. However, Si is not the most suitable material for photovoltaics since it is an indirect bandgap semiconductor that absorbs light poorly. As a consequence, Si-based solar cells require thick absorber layers (~100-200 μm) to absorb > 90% of sunlight with energy above the bandgap (≈ 1.1 eV). Moreover, the increasing demand of Si for its incorporation in photovoltaic devices led recently to an increase of its cost.[44]

Second generation photovoltaics includes those technologies that aim at reducing production costs by using solar cells with thinner absorber layers (~1 μm thick) using physical and chemical deposition routes that allow working on low-cost substrates, such as glass or flexible polymers.[44] Some examples of second generation solar cells are those based on amorphous Si (a-Si), CdTe and chalcopyrite thin films.[44,46] These are direct bandgap semiconductors characterized by a higher absorption coefficient with respect to the case of conventional crystalline Si (c-Si).[44,46] As a consequence, they absorb light more efficiently than c-Si and hence a thinner absorbing layer is required to absorb the same amount of photons. Despite the reduced cost, second generation technologies suffer from low efficiency, that is usually equal or lower than the one obtained with first generation technologies.

Finally, third generation photovoltaics aims at maintaining low production costs, while increasing solar cell efficiency.[44] To that purpose, these technologies rely on the strategies

proposed for thin-film technologies and on the use of new approaches, mainly based on nanotechnology, aimed at improving cells efficiency by promoting the absorption of photons with energies lower than the bandgap, avoiding thermalization of "hot electrons" generated by absorption of photons with energy well above the bandgap or by increasing the optical pathlength of photons into the absorber layer.[44,45] Some examples of devices based on third generation approaches are: intermediate band, hot electrons, multijunction and plasmonic solar cells.[44,45]

6.2.2 Light trapping techniques

One of the main problems related to second generation technologies is the low absorption of photons with energy comparable to the material bandgap.[47] As a result of the large absorption length (the length required to a material to absorb photons of given energy/wavelength) and the reduced thickness of the absorber layer, low energy photons can pass through the solar cell without being absorbed, which also represents a physical limitation to the minimum thickness of the absorber layer that can be used in practice. Figure 6.16 schematically represents the absorption length of photons having different energies in (a) thick and (b) thin solar cells, highlighting that low energy photons can escape the cell without being absorbed.

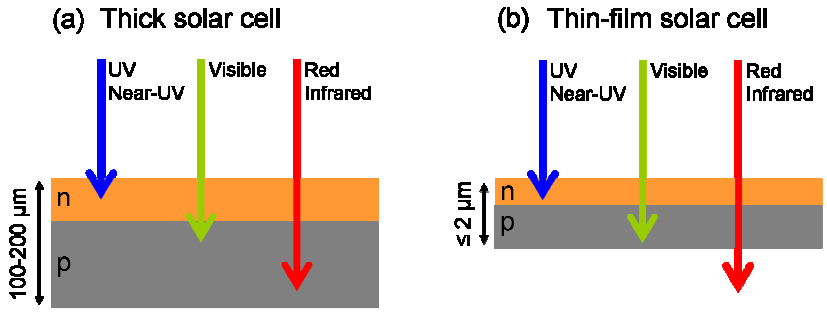

Figure 6.16: Scheme showing the absorption length of photons having different energies in the case of (a) thick and (b) thin film solar cells. In the second case, the reduced thickness of the absorber layer, comparable to the absorption length of impinging photons, leads lower photon absorption efficiency compared to the case of thick solar cells.

A strategy proposed to overcome this drawback is to increase the optical path length of radiation (distance that an unabsorbed photon may travel within the device before it escapes from it) in the absorber layer, as this would increase the probability of the incoming photon to be absorbed before leaving the cell.[42,43,48] This approach, known as *light trapping*, is a

technique commonly used both in thick and thin solar cells. It is based on deviate the rays of light away from the perpendicular direction with respect the solar cell surface and making them travel in the absorber layer at some angle (Figure 6.17a).

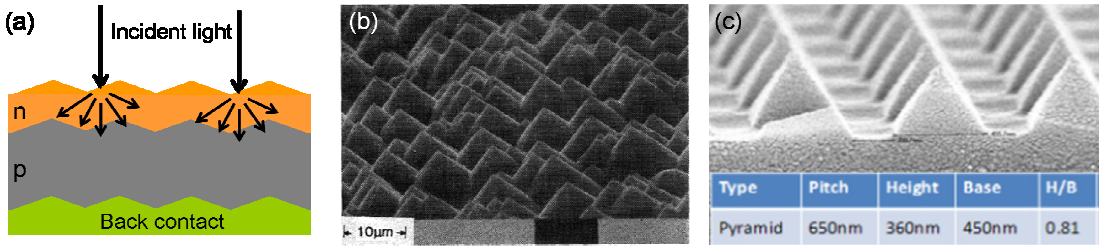

Figure 6.17: (a) Schematic representation of light trapping process. The light impinging on the device is deviated from its trajectory at wider angles. (b) Surface texturing of c-Si obtained via anisotropic chemical etching. Adapted from Campbell and Green.[49] (c) Surface nano-texturing of a glass substrate obtained using nano-imprint lithography. Adapted from Hilali and co-workers.[50]

If the angle at which a ray is deviated satisfies the total internal reflection condition, the light is completely trapped and can not escape from the cell, leading to the largest possible increase of the optical path length. In the case of a thin-film cell, the optical mode density decreases, thus light trapping only occurs when the light is coupled in the guided modes of the absorber layer.[42,48]

In conventional thick Si-based solar cells, light trapping is typically achieved by structuring the surface and, in most cases, the rear side of a solar cell. Uniform, typically pyramidal (Figure 6.17b), texturing of the surface can be achieved via different techniques, like preferential etching, photolithography or mechanical techniques. These processes are quite aggressive and texturing results from removing several microns of material from solar cell surface.[42] However, thin-film technologies require different approaches for surface texturing, since the surface roughness obtained using conventional techniques would exceed the absorber layer thickness (≤ 1-2 µm). One of the methods proposed is based on increasing the roughness of the supporting substrate, usually quartz glass, on which active layers are deposited.[50,51,52] In this way, the roughness of the substrate is transferred to the layers constituting the solar cell through conformal growth. Substrate texturing is obtained via chemical etching[51] or by using more sophisticated techniques based on nano-imprint[50] or nano-sphere[52] lithography. Templates with random or periodic texturing with different shape, from cones to pyramids (Figure 6.17c), can be obtained. The surface roughness is generally maintained in the 100-300 nm range, in order to allow proper deposition of solar cell. This

nano-texturing approach has been successfully applied to the case of a-Si thin-film solar cells, for which enhanced efficiency compared to the case of standard and flat cells was found.

Besides substrate nano-texturing, an alternative approach for promoting light-trapping in thin-film solar cells is based on incorporation of plasmonic nanostructured metallic films in the device.[47,53] These plasmonic nanostructures can offer at least three ways for improving light absorption in thin-film solar cells that are represented schematically in Figure 6.18.

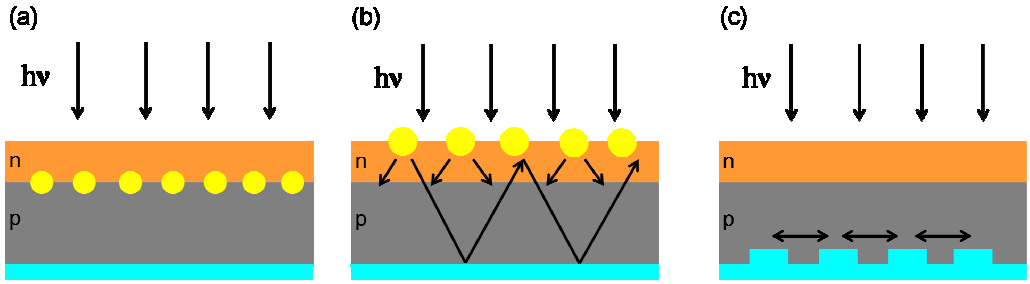

Figure 6.18: Schematic representation of light trapping approaches based on plasmonic properties of metallic nanostructures. (a) Small nanoparticles (diameter in the 5-20 nm range) are placed in the proximity of the junction and used to increase light absorption and creation of electron-hole pairs in the semiconductor in terms of the strong near-field enhancement occurring at the SPR of nanoparticles. (b) Large nanoparticles (diameter in the 100-200 nm range) works as scattering elements, increasing the path length of the radiation inside the absorber layer. (c) Structured metallic solar cell back contacts are implemented to promote light absorption in terms of surface plasmon polaritons at the metal-semiconductor interface and light scattering. Adapted from Atwater and Polman.[47]

First, nanoparticles can be used as nano-antennas in which the plasmonic near-field is coupled to the semiconductor, increasing its effective absorption cross-section (Figure 6.18a). The enhanced field is thus responsible for increasing optical transition rates, and consequently photon absorption and photocurrent generation.[53] The magnitude of the near-field enhancement is strongly related to the amount of absorbed light, which, in turns, depend on the nanoparticle size. From literature, it is known that the absorption cross-section is larger than scattering one for small nanoparticles.[47,53,54] As a consequence, in this light trapping scheme, nanoparticles with typical size in the 5-20 nm range should be used.

The second approach considers metallic nanoparticles that would act as scattering elements able to couple incident light into the guided modes of the absorber layer in a way similar to the nano-textured substrate case (Figure 6.18b). Since scattering cross-section becomes dominant over absorption cross-section for large nanoparticles,[47,53,54] nanoparticles with typical sizes larger than 100 nm but smaller than 300 nm are preferably incorporated in this light trapping scheme. Nanoparticles larger than 300 nm suffer from the presence of

multiple nearly degenerate modes that reduce the strength of the fundamental SPR and thus are not suitable.[53] Light scattering is more pronounced at the SPR wavelength, thus the optical response of the plasmonic nanostructure is usually tuned to match the SPR with the spectral position of the bandgap of the solar cell, where the photon absorption is expected to be reduced.

Third, a corrugated metallic film on the rear side of the device, i.e. the rear metallic contact of a solar cell, can promote light coupling into the thin-film guided modes and, additionally, couple light in surface plasmon polaritons (SPPs) supported at the metal-semiconductor interface, both effects leading to an increase of light absorption (Figure 6.18c).[47] Since the lateral dimension of a solar cell is orders of magnitude larger than the optical absorption length of the photons, the probability that the light trapped in terms of SPPs is absorbed by the semiconductor, and then converted into electron-hole pairs, increases.

The amount of works in literature demonstrating that the efficiency or the characteristics of solar cells can be improved through the incorporation of plasmonic nanostructures in their structure is really huge. Probably, the first experiments that show the capability of metal nanoparticle arrays to enhance the coupling of light into a semiconductor thin film are those reported by Stuart and Hall,[55,56] where they used Au nanoparticles to couple light into Si-on-insulator photodetector structure. The impact of this result on photovoltaics was recognized only later in the 2000s, when first Schaadt and co-workers[57] and then Derkacs and co-workers[58] reported improved light absorption and performance of a Si p-n junction diode and a-Si solar cell, respectively. From that moment on, the number of articles dealing with plasmonic for improving photovoltaics started to increase rapidly until nowadays. Ag and Au nanoparticles are incorporated in most cases, since they show intense SPR in the visible and near-infrared spectral regions where reduced photon absorption is expected.[47,53] Figure 6.19 shows the number of articles and reviews dealing with the incorporation of Ag and Au nanoparticles in thin film solar cells that have been published between 2006 and 2013. We obtained this result by searching articles related to “Solar cells and Silver nanoparticles” and “Solar cells and Gold nanoparticles”. As it can be seen, the number increases almost exponentially.

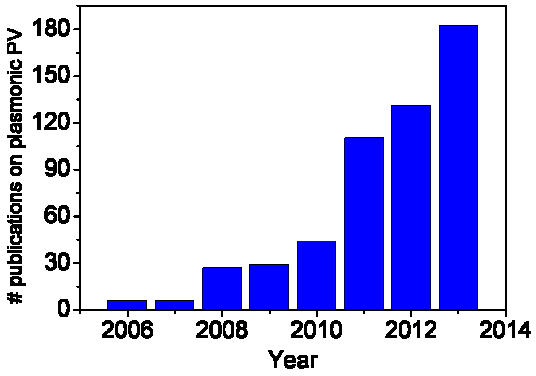

Figure 6.19: Plot representing the number of works (articles and reviews) dealing with the incorporation of Ag and Au nanoparticles in thin film solar cells published between 2006 and 2013.

The first light scattering approach (Figure 6.18a) has been successfully used in inorganic solar cells based on CdSe and Si,[47] even if it is considered to be more beneficial in the case of organic ones due to the short extension of the generated near-field at the SPR[10,11] that requires nanoparticles to be placed in the proximity of the collection junction area.[47,53] Ag is usually preferred when the second light trapping approach is used, due to its larger scattering cross-section with respect to the case of Au.[53] This approach (Figure 6.18b) has shown to be suitable for many types of inorganic solar cells, such as a-Si,[47,59,60] or those based on III-V compounds,[47,61,62] since scattering is a far field effect that allows working with nanoparticles placed far from the absorber layer.[53] Finally, the third approach (Figure 6.18c) has been mainly applied to the case of a-Si solar cells.[47,63,64]

6.2.3 Chalcopyrite solar cells

In this thesis, we have explored the feasibility of incorporating the nanostructured films fabricated using PLD in chalcopyrite-based thin film solar cells since. We want to remark that, unlike the case of Si or other compounds,[47] only very few works report on the application of plasmonic light trapping concepts to chalcopyrite solar cells[54,65] and here we show the results obtained with our firsts attempts. This is mainly related to the fact that chalcopyrite materials absorb light efficiently for absorber layer thicknesses down to 1 μm and because a further decrease of the thickness of the absorber would result in experimental difficulties.[66] However, we considered worth to explore this possibility in view of the tendency to reduce the amount of the material used and, hence, production costs. In particular, we consider two possibilities: nanostructured films containing very small nanoparticles and larger ones obtained through post-growth annealing of percolated Ag films to figure out any

plasmonic effect on the solar cells characteristics related to the first (light concentration) and second (light scattering) approaches described above (Figures 6.18a and b).

Chalcopyrite solar cells are based on the use of $Cu(In,Ga)(Se,S)_2$ compounds as absorber layer. However, the best solar cells are usually obtained with Se, hence in this thesis we work with $Cu(In,Ga)Se_2$ (CIGSe) and $CuInSe_2$ (CISe) absorber layers. Chalcopyrite materials are considered very attractive candidates for thin-film technologies since they are direct bandgap semiconductors with high optical absorption coefficient for photons with energies larger than the bandgap, such that only a few microns of material are needed to absorb most of the incident light. Generally, an absorber layer 2 μm thick is sufficient to promote efficient light absorption[65,66] and to achieve conversion efficiencies up to 20.9% in the laboratory.[67,68] Another advantage of these materials is that the bandgap can be tuned by varying the composition of the absorber layer and growth conditions, which makes them more flexible with respect to other materials with fixed bandgap. Typically, the bandgap can be varied in the 1.0-1.7 eV range[69] by varying, for example, the content of Ga[70] and Cu.[67]

The cells were fabricated in the *Helmholtz Zentrum Berlin* (HZB) by the group of C. Kaufmann using a multi-stage co-evaporation process at a temperature ≤ 500ºC.[67] They were grown on soda-lime glass substrates on which a Mo back contact ≈ 1 μm thick was deposited by sputtering. Then, CIGSe or CISe is deposited, depending if the Ga source is kept open or closed during growth, respectively. The device is then completed by the deposition of a thin layer (≈ 50 nm) of CdS by chemical bath, a RF sputtered ZnO/ZnO:Al bilayer and the Ni/Al contact grid that eases current collection. CdS is the buffer layer needed to form the p-n junction with the CIGSe or with the CISe layer and to prevent the absorber layer oxidation. It usually has large bandgap (> 2.3 eV) and reduced thickness to limit photon absorption. The ZnO/ZnO:Al bilayer, the window layer, is the transparent conductive oxide used as front contact. A sketch of the structure of a typical chalcopyrite-based solar cell used in this thesis is shown in Figure 6.20.

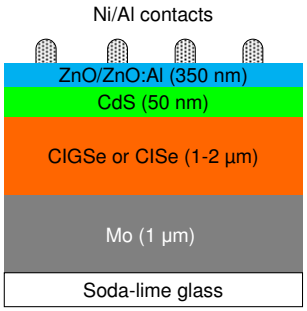

Figure 6.20: Structure of a typical chalcopyrite-based solar cell used in the present work.

6.2.4 Silver nanoparticles as light concentration centers

We first attempted to achieve light trapping trough the creation of electron-hole pairs boosted by the near-field enhancement generated around small nanoparticles at the SPR (6.18a). As previously mentioned, this approach requires nanoparticles to be placed in the vicinity of the p-n junction. However, since we had first to verify that incorporation of nanoparticles using PLD does not compromise the performance of solar cell, we deposited the layer of Ag nanoparticles on an almost complete device, between the ZnO/ZnO:Al bilayer and the grid of a CIGSe solar cell (Figure 6.21a).

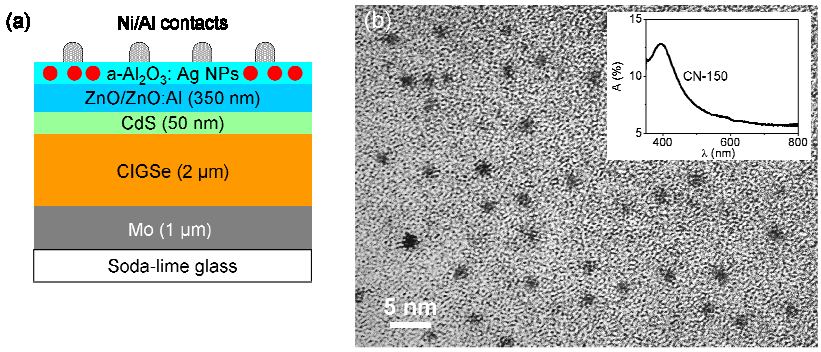

Figure 6.21: (a) Structure of the Ag NPs-CIGSe solar cell. (b) Plan-view high resolution TEM image of CN-150 film. The inset shows the optical absorption of the CN-150 film grown on fused silica.

Figure 6.21b shows a plan-view TEM image of a covered Ag nanostructured film grown on C-mica resembling the characteristics of those incorporated in solar cells. The number of pulses on the Ag target were 150 (i.e., CN-150 film), resulting in very small nanoparticles with circular in-plane projected shape and narrow size distribution. The nanoparticle average diameter is approximately 2 nm, while nanoparticle surface coverage and density are 5% and ≈ 2.3×10^4 NPs μm^{-2}. We embedded nanoparticles in between buffer and covering a-Al_2O_3 layers in order to prevent Ag tarnishing. The thickness of the whole nanostructured film was designed to be < 10 nm. The inset in Figure 6.21b shows the absorption of a CN-150 film grown on fused silica. We observe that Ag nanoparticles support a weak SPR resulting in a narrow (FWHM ≈ 80 nm) absorption band peaking close to 400 nm, according to their reduced size and narrow shape distribution.

Figure 6.22 shows compares (a) the J-V curves and (b) the EQE measurements of the best plasmonic, Ag NPs-CIGSe, solar cells with that of a reference CIGSe cell. The table in Figure 6.22 lists the associated photovoltaic parameters.

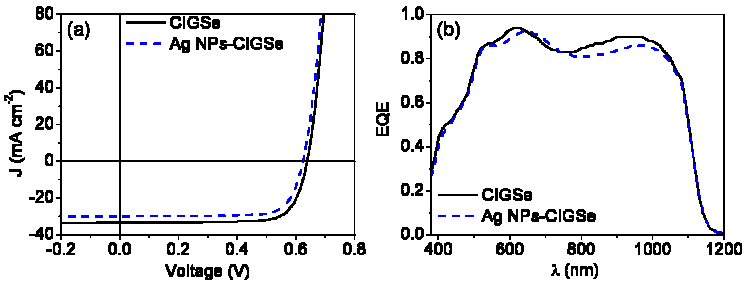

	CIGSe	Ag NPs-CIGSe
V_{oc} (V)	0.64	0.62
J_{sc} (mA cm^{-2})	34.0	33.1
FF (%)	76.4	76.9
η (%)	16.5	15.9

Figure 6.22: (a) J-V characteristic and (b) EQE of reference CIGSe and Ag NPs-CIGSe. The table on the right lists the solar cells parameters.

The results obtained evidence that the deposition of the nanoparticles does not lead to any significant enhancement or worsening of the device performance. The reference cell shows the expected behaviour with the EQE that decreases at short (< 540 nm) and long wavelengths (> 1000 nm) according to the recombination effects and reduced light absorption efficiency, as described previously (Figure 6.14). In the case of the plasmonic cell, only a lower J_{sc} is measured, which is consistent with the lower spectral response for wavelengths larger than 750 nm observed in the EQE (Figure 6.22b). From these results, we can extract three main conclusions. First, the deposition of the nanostructured film does not compromise the solar cell structure despite the high kinetic energy of the ions involved in the laser-generated Al_2O_3 and Ag plasmas (Chapter 3). Second, the a-Al_2O_3 layer embedding nanoparticles is thin enough to allow charges to be collected at the contact grid. Nonetheless, the slight decrease of J_{sc} can be associated to recombination processes promoted by the Ag nanoparticles or increased optical losses due to light reflection. Finally, the absence of improvement of the cell performance is most likely related to the reduced enhancement of the near-field owing to the low absorption of light by the nanoparticles (inset of Figure 6.21b). In addition, as mentioned previously, the near-field is expected to vanish within a few tens of nanometres from nanoparticle surface[10,11] in the case of small nanoparticles thus nanoparticles were placed too much far away (~ 400 nm) from the semiconductor junction to allow any coupling between the plasmonic near-field and the CIGSe. These results suggest that we could obtain better results by placing larger nanoparticles closer to the junction. However, since CIGSe rapidly reacts with the atmosphere and oxidize forming, for example, Ga_2O_3, this could be done safely in the case PLD of Ag nanostructures was performed in-situ during the fabrication of the solar cell which was not the case in the present experiments and thus we attempted a different approach based on light scattering.

6.2.5 Silver nanoparticles as scattering centers

The second experiment we performed was intended to improve the solar cell characteristics using the light trapping approach based on plasmonic light scattering (Figure 6.18b). To that purpose we incorporate a covered nanostructured film resembling CNa-4200 films (section 5.1.2 of Chapter 5) in the solar cell. These types of films contain nanoparticles formed upon annealing in air of percolated Ag films (Figure 6.23a) with almost circular in-plane projected shape and with average diameter of 50 nm (small nanoparticles) and 135 nm (large nanoparticles) and a diffuse reflectance close to 10% at ≈ 560 nm. In addition, as a result of conformal growth of the a-Al_2O_3 covering layer over nanoparticle layer, the surface of the nanostructured film showed an enhanced roughness characterized by vertical features with tapered shape (Figure 6.23b).

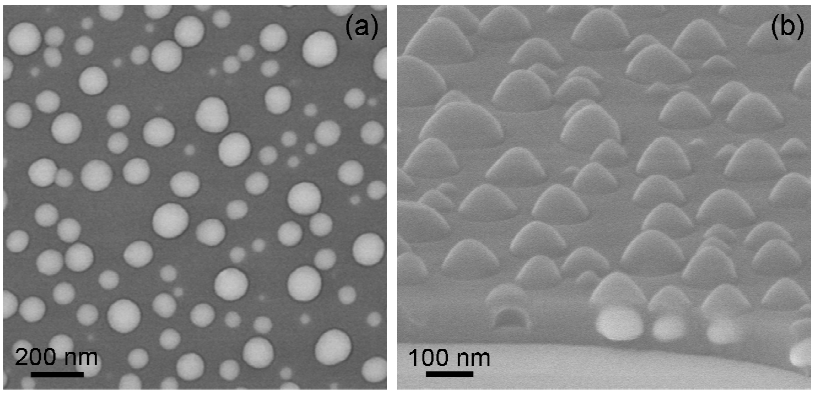

Figure 6.23: (a) Plan-view and (b) tilted-view SEM images of CNa-4200 film grown on Si.

In this case, we incorporated the nanostructured film in a CISe-based solar cell. The reason for this choice was that CISe technology allows obtaining operative solar cells using very thin absorber layers (≈ 1 μm) because of the simplification of the growth process control when Ga is not involved. In addition, the absence of Ga leads to a decrease of the V_{oc} in CISe solar cells,[70] resulting in a lower efficiency compared to the case of CIGSe (≈15% instead of ≈20%). However, the lowering of the solar cell efficiency was considered to be advantageous for our purpose, since any performance improvement related to plasmonic effects would be much easily observed. Within this type of light trapping approach two configurations are generally proposed in literature for placing metallic nanoparticles in the cell structure.[47,59,65,71] In the first configuration, nanoparticles are placed on top of the solar cell where they can act as scattering centers. However, nanoparticles placed on top may absorb light partially, thus

reducing the light that reaches the absorber layer. For this reason nanoparticles are preferred to be placed at the rear side of the cell. In this case, blue and green light is directly absorbed in the cell, whereas the longer wavelengths can be scattered and trapped. In addition, a properly designed plasmonic nanostructure may also act as back reflector reducing the fraction of transmitted light.[59,60] We thus deposited the nanostructured film on top of the Mo substrate, before the deposition of the CISE absorber layer. Moreover, in this case, the relatively thick a-Al_2O_3 buffer and covering layers were expected to be beneficial not only to prevent plasmonic degradation of the device,[72] but also to avoid additional surface recombination promoted by metal nanoparticles[71] and the diffusion of Ag into the absorber layer. However, such thick a-Al_2O_3 embedding layer could lead to Mo electrical insulation. To overcome this problem, one of the possible solutions should be to deposit the nanostructure trough a micro-sized stencil having holes with size comparable to the absorber layer thickness. In this way, the deposition of the nanostructured film on the Mo would occur only at the holes, while the rest of its surface would keep free from deposit and available for charge carrier collection. Unluckily, this type of stencil was not available at the time and we used an Al mask with holes of 1.2 mm diameter. We fixed it on top of Mo-coated soda-lime glass substrate (Figure 6.24a). After nanostructured film deposition, the mask was removed to allow the deposition of the other layers constituting the cell. Figure 6.24b shows a 2.54 × 2.54 cm^2 Mo substrate "decorated" with circles where the nanostructured film was successfully deposited, while Figure 6.24c shows a 2.54 × 2.54 cm^2 sample containing 6 solar cells of different area (0.5 and 1 cm^2). The circles corresponding to the region where the nanostructured film deposition occurred can be appreciated.

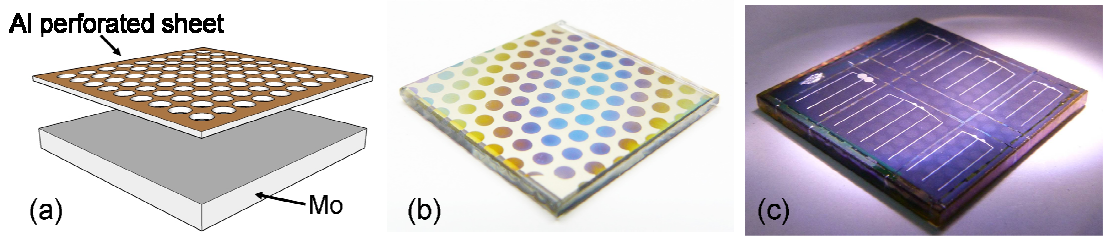

Figure 6.24: (a) Sketch of the Al perforated sheet applied to the Mo substrate to allow deposition of nanostructured film only at the holes. (b) Image of the Mo after deposition of the nanostructured film through the perforated sheet. (c) Image of the Ag NPs-CISe solar cells.

Once the cells were fabricated, we first investigated if the CISe was properly deposited on the the Ag NPs-decorated Mo layer. Figure 6.25 shows tilted SEM images of (a) CISe

reference and (b) Ag NPs-CISe cells. The structure of the cell is schematically represented in the sketches in between the images.

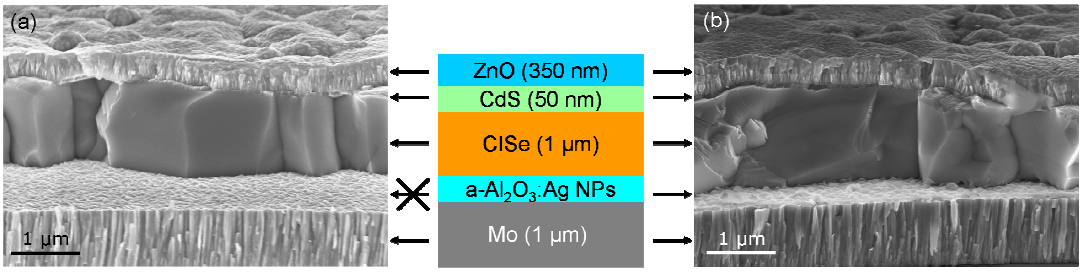

Figure 6.25: Tilted SEM images of (a) CISe reference and (b) plasmonic CNa-4200 / CISe solar cells.

Mo layer, at the bottom, shows a slightly rough surface, whereas the structure of the polycrystalline CISe layer is characterized by large grains with lateral size > 1 µm, typical of chalcopyrite materials.[67] On top of CISe, the thin CdS layer is observed, over coated by the ZnO/ZnO:Al bilayer (in the sketch referred as ZnO for simplicity). The latter shows a quite rough surface that is most likely related to granular structure of the CISe. The Ag NPs-CISe solar cell (Figure 6.25b) shows an almost identical structure to the reference one, apart from the additional layer observed in between Mo and CISe which corresponds to the nanostructured Ag film (Figure 6.26). In Figure 6.26, the a-Al_2O_3 layer shows a lighter contrast with respect to Mo, while nanoparticles cannot be seen due to the insulating character of the dielectric matrix.

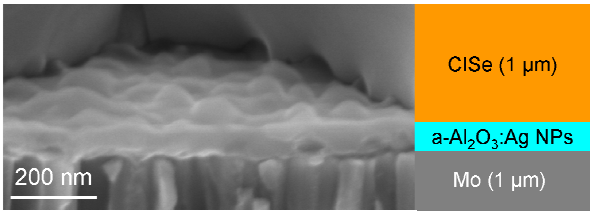

Figure 6.26: Detail of the Ag-CISe solar cell at the nanostructured film level.

Figure 6.27 shows plan-view SEM images of the rear side of (a) the CISe reference and (b) the Ag NPs-CISe cells. The layers on top of (a) Mo and (b) nanostructured Ag film were removed during SEM sample preparation. We observe a homogeneous dark contrast in Figure 6.27a, which corresponds to the Mo layer, while in Figure 6.27b brighter elements corresponding to Ag nanoparticles are seen.

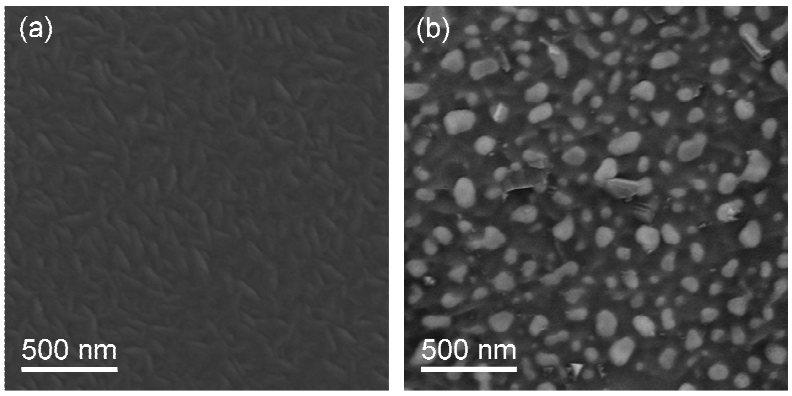

Figure 6.27: Plan-view SEM images of (a) CISe reference and (b) Ag NPs-CISe solar cells, where the layers over-coating (a) Mo and (b) nanostructured film were removed.

This confirms that the deposition of the nanostructured film took place successfully, without evidences of any effect related to the presence of the Al perforated sheet (i.e., shadow effect). We observe a homogeneous dark contrast in Figure 6.27a, which corresponds to the Mo layer, while in Figure 6.27b brighter elements corresponding to Ag nanoparticles are seen, which confirms that the deposition of the nanostructured film took place successfully, without evidences of any effect related to the presence of the Al perforated sheet (i.e., shadow effect). The nanoparticle size distribution, as well as nanoparticle density, is similar to that of the CNa-4200 film grown on Si (Figure 6.23a). However, nanoparticle shape changes significantly since they show elongated in-plane projected shape rather than circular one.

Once the cells were fabricated, we studied their photovoltaic response. Figure 6.28 shows the EQE corresponding to the CISe reference and Ag NPs-CISe solar cells. The photovoltaic parameters are listed in the table.

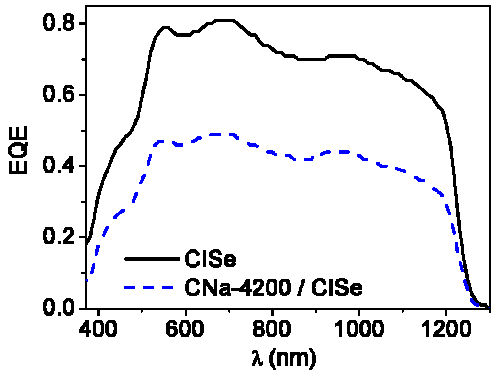

	CISe	Ag NPs-CISe
V_{oc} (V)	0.47	0.42
J_{sc} (mA cm^{-2})	36.5	18.6
FF (%)	72.8	43.8
η (%)	12.6	6.6

Figure 6.28: (Left) EQE of CISe reference Ag NPs-CISe solar cells. (Right) Photovoltaic parameters.

The comparison of the Ag-CISe cell with the CISe reference evidences that the former shows a worse EQE with values that are approximately half that of the reference cell. A similar relation is observed for the field factor, FF, and the power conversion efficiency, η, while J_{sc} and V_{oc} values are closer to those of CISe reference cell.

In order to understand these results, we must analyze first the morphology/structure of the cells. The cross-section SEM images (Figure 6.25) demonstrate that the incorporation of the nanostructured Ag film did not affect the deposition of CISe, as confirmed by the formation of large grains typical of chalcopyrite materials,[67] while it is also worth noting that the a-Al_2O_3 layer preserved its characteristics (Figure 6.25) after the deposition of CISe that takes places at relatively high temperature (450ºC) in a controlled atmosphere of Se, which is known to be aggressive. These facts support that our approach for incorporating nanoparticles is suitable for a proper growth of absorber layer and that a-Al_2O_3 is robust enough to guarantee nanoparticles encapsulation during solar cell deposition. Moreover, plan-view SEM images (Figure 6.26) show that nanoparticles are properly formed as a result of annealing, even if their in-plane projected shape is less circular than expected. This can be related to the roughness of the Mo layer that may promote the deposition of an a-Al_2O_3 buffer layer with enhanced roughness, which can decrease the efficiency of dewetting process with respect to the case of flat (Si) surfaces.[73] This is further supported by the fact that in Figure 6.26 the a-Al_2O_3 layer show an overall increased roughness, contrary to the case of CNa-4200 film in which well separated tapered features were observed (Figure 6.23b).

Thus, the solar cell containing the plasmonic nanostructured film (Figure 6.26) shows J_{sc} and V_{oc} values close to those of reference cell which supports that the quality of the p-n junction is preserved. However, FF and EQE are definitely smaller. Since FF corresponds to the power delivered by the cell, which is directly related to the photo-generated charge carriers collected at the cell contacts, we think the problem is most likely related to a lower collection efficiency of the photo-generated charge carriers, which could be related to the reduced free surface of Mo after deposition of the nanostructured film.

The experiments conducted so far and the results already obtained show that the solar cells in which we incorporated the nanostructured Ag films using PLD work properly, which confirm that PLD is in principle a compatible technique for fabrication of plasmonic solar cells similarly to other techniques commonly used, like thermal evaporation and magnetron sputtering.[47,59,60,71] However, the performance of the plasmonic cells produced so far is worse than that of CISe references, which clearly indicates that further studies are required to

optimize the cell configuration. According to the results reported in this work and those available in literature,[47,59,60,65] the following approaches may lead to more promising results:

- Deposit a larger initial amount of Ag and increase the annealing temperature to promote the formation of bigger nanoparticles with a better crystalline quality that would scatter light more efficiently.
- Tune the SPR of nanoparticles to wavelengths closer to the energy bandgap ($800 < \lambda < 1200$ nm) where the EQE starts to decrease (Figure 6.28) due to the reduced light absorption efficiency, for example by embedding nanoparticles in a dielectric matrix with higher refractive index, i.e. ITO.
- Use a micro-sized stencil to guarantee a better electric contact of the Mo.
- Change the a-Al_2O_3 matrix for a transparent conductive oxide material such as ITO, which would make the use of the mask unnecessary.
- Reduce the thickness of the absorber layer, while maintaining a reasonable device efficiency, to ease the detection of any effect related to the incorporation of nanostructured film.

6.3 CONCLUSIONS

In this Chapter we report the results obtained when applying the nanostructured Ag films produced by PLD to two technological applications based on near-field enhancement and light scattering, namely SERS and plasmonic photovoltaics.

We have demonstrated that nanostructured Ag films produced using PLD show strong SERS activity. In particular, the SERS substrates containing relatively small and partially coalesced nanoparticles show very high sensitivity and robustness. This was related to the nm-sized gap separating neighboring nanoparticles which leads to the formation of hot spots suiting the size of the TPDI test molecule. In addition, we verified that the SERS activity diminishes when a protective a-Al_2O_3 layer of increasing thickness is deposited on top of nanoparticles as a result of the increased molecule-to-nanoparticle surface distance. This result strongly relates to the short range of the near-field generated at the nanoparticle surface. Finally, we have showed that that the S-NPs / TPDI substrates can work properly as a platform for the creation of nanoparticle superstructures with the adsorbed molecule acting as tether.

The second part of this chapter was dedicated to a first exploration of the potential of PLD to incorporate metal nanoparticles in solar cells. We have demonstrated that the

incorporation of nanostructured Ag films in chalcopyrite solar cells without compromising the absorbing layer is feasible. We have explored two configurations based on light concentration and scattering and we concluded that the latter is the most promising approach. However, the results obtained so far do not show any improvement of the solar cells characteristics due to plasmonic effects, likely due to the lower efficiency of the plasmonic device with respect to reference one in light conversion and charge carrier collection. We have identified some of the problems related to the studied system and proposed different strategies that should improve the present results.

References

(1) M. Moskovits, J. Raman Spectrosc. **36**, 485-496 (2005)

(2) L. Guerrini, D. Graham, Chem. Soc. Rev. **41**, 7085-7107 (2012) and references therein

(3) L. Guerrini, A. E. Aliaga, J. Cárcamo, J. S. Gómez-Jeria, S. Sanchez-Cortes, M. M. Campos-Vallette, J. V. García-Ramos, Analytica Chimica Acta **624**, 286-293 (2008)

(4) I. Izquierdo-Lorenzo, J. V. García-Ramos, S. Sanchez-Cortes, J. Raman Spectrosc. **44**, 1422-1427 (2013)

(5) K. Kneipp, H. Kneipp, I. Itzkan, R. R. Dasari, M. S. Feld, J. Phys.: Condens. Matter **14**, R597-R624 (2002)

(6) M. A. Bañares-González, R. X. Valenzuela, In *Técnicas de análisis y caracterización de materiales*, edited by M. Faraldos, C. Goberna (CSIC, Madrid 2002)

(7) M. Fleischmann, P. J. Hendra, A. J. McQuillan, Chem. Phys. Lett **26**, 163-166 (1974)

(8) D. L. Jeanmaire and R. P. Van Duyne, J. Electroanal. Chem. **84**, 1-20 (1977)

(9) M. G. Albrecht and J. A. Creighton, J. Am. Chem. Soc. **99**, 5215-5217 (1977)

(10) K. L. Kelly, E. Coronado, L. L. Zhao, G. C. Schatz, J. Phys. Chem. B **107**, 668-677 (2003)

(11) N. J. Halas, S. Lal, W. S. Chang, S. Link, P. Nordlander, Chemical Reviews **111**, 3913-3961 (2011)

(12) E. C. Le Ru and P. G. Etchegoin, Chem. Phys. Lett. **423**, 63-66 (2006)

(13) J. Toudert, in *UV-VIS and Photoluminescence Spectroscopy for Nanomaterials characterization*, edited by S. S. R. K. Challa (Springer Verlag, Berlin, 2013)

(14) H. Guo, F. Ruan, L. Lu, J. Hu, J. Pan, Z. Yang, B. Ren, J. Phys. Chem. C **113**, 10459-10464 (2009)

(15) P. R. Edwards, D. Sleith, A. W. Wark and R. W. Martin, J. Phys. Chem. C **115**, 14031-14035 (2011)

(16) L. Rodríguez-Lorenzo, R. A. Álvarez-Puebla, F. J. G. De Abajo, L. M. Liz-Marzán, J. Phys. Chem. C **114**, 7336-7340 (2010).

(17) S. Mishra, A. K. Ojha, D. Singh, R. R. Prasad, S. K. Srivastava, R. K. Singh, J. Raman Spectrosc. **38**, 1454-1460 (2007)

(18) W. Gotschy, K. Vonmetz, A. Leitner, F. R. Aussenegg, App. Phys. B **63**, 381-384 (1996)

(19) M. J. Banholzer, J. E. Millstone, L. Qin, C. A. Mirkin, Chem. Soc. Rev. **37**, 885-897 (2008)

(20) C. Zhu, G. Meng, Q. Huang, Z. Zhang, Q. Xu, G. Liu, Z. Huang, Z. Chu, Chem. Commun. **47**, 2709-2711 (2011)

(21) J. D. Caldwell, O. J. Glembocki, F. J. Bezares, M. I. Kariniemi, J. T. Niinistö, T. T. Hatanpää, R. W. Rendell, M. Ukaegbu, M. K. Ritala, S. M. Prokes, C. M. Hosten, M. A. Leskelä, R. Kasica, Opt. Express **19**, 26056-26064 (2011)

(22) J. F. John, S. Mahurin, S. Dai, M. J. Sepaniak, J. Raman Spectrosc. **41**, 4-11 (2010)

(23) E. Vogel, W. Kiefer, V. Deckert, D. Zeisel, J. Raman Spectrosc. **29**, 693-702 (1998)

(24) S. J. Henley, J. D. Carey, S. R. P. Silva, Appl. Phys. Lett. **88,** 061904 (2006)

(25) C. Domingo, V. Resta, S. Sanchez-Cortes, J. V. García-Ramos, J. Gonzalo, J. Phys. Chem. C **111**, 8149-8152 (2007).

(26) C. D'Andrea, F. Neri, P. M. Ossi, N. Santo, S. Trusso, Nanotechnology **20,** 240656 (2009)

(27) S. A. Swanson, R. McClain, K. S. Lovejoy, N. B. Alamdari, J. S. Hamilton, J. C. Scott, Langmuir **21**, 5034-5039 (2005)

(28) J. I. Henderson, S. Feng, G. M. Ferrence, T. Bein, C. P. Kubiak, Inorganica Chimica Acta **242**, 115-124 (1996).

(29) S. W. Joo, W. J. Kim, W. S. Yoon, I. S. Choi, J. Raman Spectrosc. **34**, 271-275 (2003)

(30) R. J. Angelici, M. Lazar, Inorganic Chemistry **47**, 9155-9165 (2008)

(31) J. Kestell, R. Abuflaha, J. A. Boscoboinik, Y. Bai, D. W. Bennett, W. T. Tysoe, Chem. Commun. **49**, 1422-1424 (2013)

(32) J. I. Henderson, S. Feng, T. Bein, C. P. Kubiak, Langmuir **16**, 6183-6187 (2000)

(33) C. R. Lee, S. I. Kim, C. J. Yoon, M. S. Gong, B. K. Choi, K. Kim, S. W. Joo, J. Colloid Interface Sci. **271**, 41-46 (2004)

(34) H. S. Kim, S. J. Lee, N. H. Kim, J. K. Yoon, H. K. Park, K. Kim, Langmuir **19**, 6701-6710 (2003)

(35) S. J. Bae, C. R. Lee, I. S. Choi, C. S. Hwang, M. S. Gong, K. Kim, S. W. Joo, J. Phys. Chem. B **106**, 7076-7080 (2002)

(36) S. W. Joo, W. J. Kim, W. S. Yun, S. Hwang, I. S. Choi, Appl. Spectrosc. **58**, 218-223 (2004)

(37) G. Baraldi, E. Lopez-Tobar, K. Hara, S. Sanchez-Cortes, J. Gonzalo, J. Phys. Chem. C **118**, 4680-4686 (2014)

(38) J. P. Camden, J. A. Dieringer, J. Zhao, R. P. Van Duyne, Acc. Chem. Res. **41**, 1653-1661 (2008)

(39) Y. Han, R. Lupitskyy, T. M. Chou, C. M. Stafford, H. Du S. Sukhishvili, Anal. Chem. **83**, 5873-5880 (2011)

(40) X. Zhang, J. Zhao, A. V. Whitney, J. W. Elam, R. P. Van Duyne, J. Am. Chem. Soc. **128**, 10304-10309 (2006)

(41) M. V. Cañamares, J. V. Garcia-Ramos, J. D. Gómez-Varga, C. Domingo and S. Sanchez-Cortes, Langmuir **21** (18), 8546-8553 (2005)

(42) C. S. Solanki, *Solar Photovoltaics: Fundamentals, Technologies and Applications*. (Eastern Economy Edition, New Delhi, 2009)

(43) C. Honsberg, S. Bowden, http://pveducation.org/

(44) L. Tsakalakos, in *Nanotechnology for Photovoltaics*, edited by L. Tsakalakos (Taylor & Francis Group, Boca Raton, 2010)

(45) M. A. Green, Prog. Photovolt.: Res. App. **9**, 123-135 (2001)

(46) V. S. Arunachalam, E. L. Fleischer, MRS Bulletin **33**, 261 (2008)

(47) H. A. Atwater, A. Polman, Nature Materials **9**, 205-213 (2010) and references therein

(48) K. Catchpole, in *Nanotechnology for Photovoltaics*, edited by L. Tsakalakos (Taylor & Francis Group, Boca Raton, 2010)

(49) P. Campbell, M. A. Green, J. Appl. Phys. **62**, 243-249 (1987).

(50) M. M. Hilali, S. Yang, M. Miller, F. Xu, S. Banerjee, S. V. Sreenivasan, Nanotechnology **23** (2012)

(51) J. Zhu, C. M. Hsu, Z. Yu, S. Fan, Y. Cui, Nano Lett. **10**, 1979-1984 (2010)

(52) C. Battaglia, C. M. Hsu, K. Söderström, J. Escarré, F. J. Haug, M. Charrière, M. Boccard, M. Despeisse, D. T. L. Alexander, M. Cantoni, Y. Cui, C. Ballif, ACS Nano **6**, 2790-2797 (2012)

(53) E. T. Yu, in *Nanotechnology for Photovoltaics*, edited by L. Tsakalakos (Taylor & Francis Group, Boca Raton, 2010)

(54) M. Schmid, R. Klenk, M. Ch. Lux-Steiner, M. Topič, J. Krč, Nanotechnology **22**, 025204 (2011)

(55) H. R. Stuart, D. G. Hall, Applied Physics Letters **69**, 2327-2329 (1996)

(56) H. R. Stuart, D. G. Hall, Applied Physics Letters **73**, 3815-3817 (1998)

(57) D. M. Schaadt, B. Feng, E. T. Yu, Appl. Phys. Lett. **86**, 063106 (2005)

(58) D. Derkacs, S. H. Lim, P. Matheu, W. Mar, E. T. Yu, Appl. Phys. Lett. **89**, 093103 (2006)

(59) H. Tan, R. Santbergen, A. H. M. Smets, M. Zeman, Nano Lett. **12**, 4070-4076 (2012)

(60) S. Morawiec, M. J. Mendes, S. A. Filonovich, T. Mateus, S. Mirabella, H. Águas, I. Ferreira, F. Simone, E. Fortunato, R. Martins, F. Priolo, I. Crupi, Optics Express **22**, A1059-A1070 (2014)

(61) W. Liu, X. Wang, Y. Li, Z. Geng, F. Yang, J. Li, Solar Energy Materials and Solar Cells **95**, 693-698 (2011)

(62) J. Y. Wang, F. J. Tsai, J. J. Huang, C. Y. Chen, N. Li, Y. W. Kiang and C. C. Yang, Optics Express **18** (3), 2682-2694 (2010)

(63) V. E. Ferry, M. A. Verschuuren, H. B. T. Li, R. E. I. Schropp, H. A. Atwater, A. Polman, Appl. Phys. Lett. **95,** 183503 (2009)

(64) J. Bhattacharya, N. Chakravarty, S. Pattnaik, W. Dennis Slafer, R. Biswas, V. L. Dalal, Appl. Phys. Lett. **99,** 131114 (2011)

(65) M. Schmid, J. Klaer, R. Klenk, M. Topič, J. Krč, Thin Solid Films **527**, 308-313 (2013)

(66) O. Lundberg, M. Bodegård, J. Malmström, L. Stolt, Prog. Photovolt.: Res. Appl. **11**, 77-88 (2003)

(67) R. Caballero, V. Izquierdo-Roca, X. Fontané, C. A. Kaufmann, J. Álvarez-García, A. Eicke, L. Calvo-Barrio, A. Pérez-Rodríguez, H. W. Schock, J. R. Morante, Acta Materialia **58**, 3468-3476 (2010)

(68) http://www.solar-frontier.com/eng/index.html

(69) D. L. Young, J. Keane, A. Duda, J. A. M. AbuShama, C. L. Perkins, M. Romero, R. Noufi, Prog. Photovolt.: Res. Appl. **11**, 535-541 (2003)

(70) D. Abou-Ras, R. Caballero, C. A. Kaufmann, M. Nichterwitz, K. Sakurai, S. Schorr, T. Unold, H. W. Schock, Phys. Stat. Sol (RRL) **2**, 135-137 (2008)

(71) F. J. Beck, S. Mokkapati, A. Polman, K. R. Catchpole, Appl. Phys. Lett. **96**, 033113 (2010)

(72) Y. Yang, S. Pillai, H. Mehrvarz, M. A. Green, Solar Energy Materials and Solar Cells **122**, 208-216 (2014)

(73) C. M. Müller, F. C. F. Mornaghini, R. Spolenak, Nanotechnology **19**, 485306 (2008)

Chapter 7
Conclusions

In this thesis we have investigated first the potential of nanoparticle shaping methods, namely thermal annealing and laser irradiation to improve the control over size, shape and spatial organization of Ag nanoparticles in nanostructured films fabricated by PLD. Second, we have also explored the application of the fabricated Ag nanostructures as SERS substrates and as light trapping elements in solar cells.

We first studied how the nanoparticle morphology changes upon increasing the amount of deposited metal. Similarly to earlier reports, we observed that Ag forms separated nanoparticles below percolation threshold as a result of nucleation and coalescence processes. Their size increases and their in-plane shape changes from almost circular to elongated with increasing metal content. Above percolation, Ag forms an almost continuous film. The optical response of the fabricated nanostructured films containing Ag nanoparticles show a resonant behaviour due to the excitation of the SPR, while percolated films show a constant optical response resembling that of continuous films. The growth of these films remarked some drawbacks of pulsed laser deposited films: the low control over nanoparticle shape and spatial organization and the difficulty of obtaining nanoparticles with size > 50 nm in the as-grown configuration.

In general, SERS, as well as other techniques, requires nanoparticles to be exposed to the environment and thus nanostructure optical and chemical stability have to be guaranteed. We have shown that Ag nanoparticles exposed to air react with atmospheric oxygen, sulphur and nitrogen, which leads to nanoparticle tarnishing and to the progressive damping of the SPR. However, we were not able to determine precisely which compound was formed.

We thus investigated how to protect Ag nanoparticles from tarnishing and we demonstrated that an ultrathin (< 1 nm) a-Al_2O_3 covering layer was enough to prevent nanostructures deterioration. However, the deposition of the covering layer strongly modifies the morphology of the nanostructured films, particularly in the case of small nanoparticles. After the deposition of the covering layer, both nanoparticle size and shape distribution get narrower. We have related these changes to the sputtering of Ag promoted by the energetic Al ions produced during Al_2O_3 ablation. The study of the dynamics of the Al_2O_3 laser generated plasma has demonstrated that the fraction of energetic Al^+ ions (kinetic energy > 200 eV) is ≈ 50-60% for laser fluences similar to that used for film growth.

In order to obtain large nanoparticles (size > 50 nm), we have considered thermal annealing of the as-grown percolated Ag nanostructures. We have demonstrated that the

dewetting promoted by thermal annealing allows transforming percolated films in an assembly of elongated and irregular Ag nanoparticles with average long axis length of 60 nm and 200 nm (annealing in vacuum) or, alternatively, in an assembly of Ag nanoparticles with truncated oblate spheroidal shape with average long axis length of 50 nm and 135 nm (annealing in air). Contrary to small nanoparticles, the morphology of large nanoparticles is not significantly affected by the deposition of the a-Al_2O_3 covering layer. This was related to the increased cohesive energy of large nanoparticles that make them more resistant to the Al^+ bombardment. The deposition of the a-Al_2O_3 covering layer replicates the topography of the nanoparticle layer resulting in a surface characterized by features that resemble nanodomes with tapered shape. Moreover, we have demonstrated that large nanoparticles produced in this way diffused light at the SPR, contrary to the case of small nanoparticles, which is fundamental for the application of nanostructured films to solar cells.

Thermal annealing does not allow controlling at all the shape of the nanoparticles. For that purpose we have considered laser irradiation of covered nanostructures. Irradiations with ns single-pulse transform coalesced nanoparticles into a layer of well separated ones with circular in-plane projected shape, whereas multi-shot irradiations with hundreds of fs pulses reshaped coalesced nanoparticles into prolate spheroids with their long axis oriented parallel to the direction of laser polarization. This effect was more pronounced in the case of off-resonance irradiations. The reshaping mechanism is associated to thermal effects in the case of ns pulses, while in the case of fs pulses the observed elongated shape was associated to the high transient electric field, typical of ultrashort laser pulses, that is able to promote electron ejection at the poles of nanoparticles, and to the melting of nanoparticles that is the starting point for nanoparticle reshaping. The optical response of reshaped nanoparticles agrees with the morphology changes induced by laser irradiation. In the case of ns pulses, SPR shifts towards shorter wavelengths, its intensity increases and the FWHM decreases compared to the case of the as-grown film according to the narrowing of the nanoparticle shape distribution and the increased nanoparticle distance. While in the case of irradiation with fs pulses, the nanostructures developed a dichroic optical behavior that is consistent with the formation of elongated and aligned nanoparticles. The SPR is excited at longer or shorter wavelengths when the probe light polarization is parallel or perpendicular to the nanoparticle long axis, respectively.

We have explored the application of the produced nanostructures to SERS and solar cells. We have demonstrated that the enhancement of the signal strongly relates to the size and, particularly, spatial distribution of nanoparticle. The formation of hot spots in coalesced nanoparticles separated by very small gaps (≈ 2-3 nm) that nicely suit the length of the test molecule leads to an intense SERS activity due to the huge intensification of the near-field in between of neighbouring nanoparticles. The reproducibility of the molecule adsorption scheme as a function of molecule concentration confirmed the robustness of the fabricated SERS substrate, while the observed SERS signal decrease as a function of the molecule-to-nanoparticle surface distance evidenced the importance of electromagnetic contribution to the Raman signal enhancement and of its reduced extension.

Finally, the results related to the very first experiments, aimed at the application of plasmonic light trapping concepts to chalcopyrite solar cells, have demonstrated that the devices still work after incorporation of nanostructured films. In addition, we have found that the most promising approach should be the one based on light scattering, which basically consists in increasing the path length of light inside the absorber layer. This approach allows placing nanoparticles far from the p-n junction and hence to incorporate the nanostructure in a growth step independent from that of the absorber layer. We have shown that the absorber was properly deposited and the values of the J_{sc} and V_{oc} were similar to that of reference cells. However, the efficiency of plasmonic devices was reduced by a 50% with respect to the efficiency of the reference. We relate this behaviour to a lower collection efficiency of the photo-generated charge carriers. We thus propose several strategies to improve the obtained results, from increasing the scattering efficiency of Ag nanoparticles by increasing their size and crystalline quality, to the incorporation of micro-sized stencil to favour charge carriers collection.

Resumen en Español

CAPITULO 1 – Introducción y Objetivos

La Nanotecnologías y sus aplicaciones están cada vez más presentes en nuestras vidas cotidianas. Tejidos anti-manchas y anti-bacteriales, vidrios resistentes a los arañazos o pantallas táctiles son solo algunos ejemplos recientes en los cuales se aplican conceptos relacionados con la nanotecnología. No obstante, el interés de la comunidad científica en las nanotecnologías es muy anterior y tuvo su origen en el descubrimiento de que las propiedades de los materiales cambian cuando sus dimensiones están confinadas en la escala nanométrica.

Entre los resultados de las Nanotecnologías relacionadas con los materiales encontramos las láminas delgadas, los nanotubos, los nanohilos y las nanopartículas. En particular, las nanopartículas metálicas, que son el objeto de esta tesis, son de gran interés para aplicaciones en varios ámbitos tecnológicos como son sensores, catalizadores, células solares o en un campo tan importante como él de la medicina. Muchas de las aplicaciones basadas en nanopartículas metálicas aprovechan su respuesta óptica caracterizada por la Resonancia del Plasmon Superficial (SPR). La SPR corresponde a una oscilación colectiva de los electrones de conducción de un metal que es excitada por un campo electromagnético externo. A la longitud de onda a la que se produce dicha resonancia, las secciones eficaces de absorción y de dispersión de la luz de la nanopartícula aumentan y se produce una intensificación del campo electromagnético cercano en la proximidad de la nanopartícula. La posición espectral, la intensidad y la anchura espectral de la SPR dependen del tipo de metal, de la forma, tamaño y distribución espacial de las nanopartículas y del medio que las rodea. La posibilidad de modificar la respuesta óptica de una nanoestructura y, por tanto, la posibilidad de adaptarla a los requisitos de un determinado experimento es lo que hace posible que las nanopartículas puedan ser utilizadas en sectores tecnológicos tan distintos.

Ahora bien, por este mismo motivo, la fabricación, el estudio y la aplicación de nanoestructuras que contienen nanopartículas requieren técnicas de elaboración que permitan conseguir un control muy preciso sobre el tamaño, la forma y la distribución de las nanopartículas. Hoy en día, existen muchas técnicas de fabricación, cada una de las cuales presenta sus ventajas e inconvenientes. Por ejemplo, las reacciones de oxidorreducción permiten obtener nanopartículas de prácticamente cualquier forma en solución. Sin embargo, la inmovilización de las nanopartículas producidas en una superficie es problemática. Otro

ejemplo es la litografía por haz de electrones, que permite controlar con precisión la forma y la distribución de las nanopartículas sobre un sustrato sólido, pero requiere tiempos de procesado muy largos y está restringida a tamaños pequeños. Por último, las técnicas físicas de depósito como evaporación térmica, pulverización catódica y ablación láser también son de gran interés puesto que suelen ser mas sencillas que las anteriores y permiten fabricar capas de nanopartículas sobre superficies relativamente grandes con un buen control sobre el tamaño de las nanopartículas, aunque es difícil alcanzar un control similar sobre su morfología.

Teniendo en cuenta la importancia que el control de la morfología de las nanopartículas tiene para la fabricación de nanoestructuras con una respuesta óptica especifica, el **objetivo** de esta tesis ha sido la fabricación de nanoestructuras plasmónicas que contienen nanopartículas de Ag y que presenten propiedades adecuadas para su aplicación como sensores moleculares y como elementos que permitan mejorar la eficiencia de células solares convencionales. Para ello se ha utilizado la técnica de depósito por láser pulsado (PLD) para fabricar las nanoestructuras y se han desarrollado técnicas que permitan controlar la morfología y la orientación de las nanopartículas a través de procesos de recocido térmico e irradiación láser.

CAPITULO 2 - Técnicas Experimentales

En este capítulo describimos las características principales de los sistemas experimentales utilizados para la fabricación y caracterización de las nanoestructuras que contienen nanopartículas de Ag. Las nanoestructuras se han fabricado con la técnica de PLD. Se analizan sus principales características, sus ventajas y desventajas, así como las posibles estrategias para superar dichas limitaciones. A continuación de describe en detalle el sistema experimental utilizado. Posteriormente se describe la configuración experimental de la sonda de Langmuir (LP) utilizada en el estudio de la dinámica de los plasmas generados durante la ablación de blancos de Ag y Al_2O_3. Se presentan los fundamentos en los que se basa esta técnica y cómo hemos procesado los datos adquiridos.

Posteriormente se describen los sistemas utilizados en el desarrollo de técnicas de control de la forma de nanopartículas: los sistemas de recocido en atmósfera y en vacío y el sistema experimental utilizado para las irradiaciones con láser.

Por ultimo, se presentan las técnicas utilizadas en el análisis de la composición química (espectroscopia fotoeléctrica de rayos X, XPS, y espectrometría de retrodispersión Rutherford, RBS), de la morfología (microscopia electrónica de transmisión, TEM, y de barrido, SEM) y de la respuesta óptica (elipsometría y espectrofotometría) de las nanoestructuras.

CAPITULO 3 - Dinámica de los Plasmas Producidos por Ablación Láser de Oxido de Aluminio Cerámico y Plata

Este capítulo está dedicado al estudio de la dinámica de los plasmas generados por ablación láser de los blancos de oxido de aluminio cerámico (Al_2O_3) y de Ag utilizados para elaborar las nanoestructuras. Utilizando una LP hemos estudiado el flujo de iones, la distribución de la energía cinética de los iones en función de la fluencia láser y la fracción de iones energéticos que alcanzan el sustrato. Los resultados obtenidos han puesto de manifiesto la naturaleza energética de los iones presentes en los plasmas producidos durante la ablación de los blancos, ya que pueden alcanzar energías cinéticas de hasta 1000 eV. Este resultado es incluso más evidente en el caso de la ablación del Al_2O_3, ya que para fluencias láser cercanas al umbral de ablación, el porcentaje de iones energéticos llega a ser un 20-30%, mientras que para la plata el valor es casi despreciable. Esta diferencia ha sido relacionada con el hecho de que el potencial de ionización de los átomos de Al (IP = 2.99 eV) es menor que la energía del fotón (6.4 eV), lo que permite procesos de ionización a un solo fotón y favorece la generación de un plasma con un grado de ionización muy elevado que está sometido a una aceleración de Coulomb mucho mayor con respecto al caso de la Ag, por la cual la fotoionización a un fotón no puede suceder (IP = 7.57 eV).

CAPITULO 4 - Caracterización de las Nanoestructuras de Ag en lámina delgada

En este capítulo presentamos los resultados relacionados con la fabricación de nanoestructuras en las cuales hemos depositado Ag sobre una lámina delgada de a-Al_2O_3, dejándola por lo tanto expuesta al aire. Inicialmente optamos por esta configuración ya que es la más adecuada para la espectroscopia SERS. Analizamos tres casos representativos en los que la cantidad de plata se ha variado para formar nanoestructuras con diferente morfología: nanopartículas casi circulares de unos 5 nm de diámetro, nanopartículas alargadas con tamaño típico de unos 20 nm y, por último, láminas percoladas de Ag casi continuas. Junto con la morfología, hemos estudiado la respuesta óptica de las láminas lo cual nos permitió verificar como la SPR se mueve hacia el rojo y, por último, la intensidad aumenta al aumentar el tamaño de las nanopartículas y que el comportamiento resonante se pierde en el caso de láminas percoladas.

Estos experimentos pusieron de manifiesto que la intensidad de la SPR de las nanoestructuras disminuye con el tiempo, hasta casi desaparecer. Hemos relacionado este efecto de envejecimiento de las nanoestructuras con la reacción de la Ag superficial de la nanopartículas con el oxigeno, el azufre o incluso con el nitrógeno presentes en la atmósfera, lo que deteriora progresivamente las nanoestructuras. Hemos demostrado que su estabilidad química y óptica mejora al cubrir las nanopartículas con una capa de a-Al_2O_3 de un espesor inferior a 1 nm lo que permite evitar su envejecimiento. Finalmente, hemos observado que el depósito de la capa protectora provocaba una perdida de hasta el 50% de la Ag inicialmente depositada en particular en el caso de nanopartículas pequeñas. Hemos relacionado este efecto al arranque de Ag producido por los iones energéticos presentes en el plasma de Al_2O_3 observados en el estudio desarrollado en el capítulo 2. Para ello, hemos simulado los efectos de arranque con un modelo de *"sputtering"* basado en el software SRIM 2008, que ha demostrado estimar los resultados experimentales con muy buena precisión.

CAPITULO 5 - Procesado de las Nanoestructuras de Ag en lámina delgada

En este capítulo hemos estudiado la posibilidad de transformar la morfología de las nanoestructuras producidas mediante recocido térmico e irradiación con láser. En el primer caso el objetivo ha sido inducir la formación de nanopartículas de tamaño superior a las obtenidas mediante PLD, partiendo de láminas percoladas. En ambos casos hemos observado la formación de nanopartículas de tamaño medio entre 50-60 nm y 135-200 nm como resultado de los procesos de nucleación y coalescencia inducidos por los recocidos térmicos en aire y vacío, en un intervalo de temperaturas entre 200ºC y 400ºC. Ahora bien, las nanopartículas presentan características morfológicas diferenciadas. Se obtienen nanopartículas esferoidales en aire, mientras que en vacío las nanopartículas tienen una forma irregular y alargada. Hemos relacionado esta diferencia con la menor temperatura alcanzada durante el recocido en vacío, debido a la menor eficiencia de la transferencia de calor por convección. Además, hemos observado como la morfología de las nanopartículas no se ve afectada por el depósito de la capa protectora de a-Al_2O_3, lo que favorece que ésta se deposite replicando la topografía de las nanopartículas resultando en una superficie rugosa. Por último, hemos estudiado la fracción de luz dispersada por las nanopartículas. A diferencia de las nanopartículas más pequeñas, éstas presentan una contribución de la luz dispersada que no es despreciable, lo que es un resultado de interés para su aplicación en células solares.

El recocido permite formar nanopartículas de gran tamaño, pero no permite controlar la forma de las nanopartículas. Por este motivo hemos utilizado la irradiación láser para inducir cambios controlados en la forma y en la orientación de nanopartículas embebidas en a-Al_2O_3. En particular, hemos investigado los efectos sobre la morfología en función de la duración del pulso (8 ns o 1000 fs), de la longitud de onda (400 nm y 800 nm) y de la fluencia. La irradiación con pulsos de ns inducen la formación de nanopartículas con forma circular en el plano y de tamaño parecido, mientras que al utilizar pulsos de fs se observa primero la desintegración de las nanopartículas y, posteriormente, la formación de nanopartículas alargadas y orientadas en el plano, con el eje mayor paralelo a la dirección de polarización del haz incidente. Hemos identificado los posibles mecanismos de transformación de las nanopartículas en ambos casos: él de los pulsos de ns es principalmente térmico, mientras que para pulsos de fs éste está relacionado con los campos eléctricos ultraintensos, que son típicos de los pulsos ultracortos. En cuanto a la respuesta óptica, las nanoestructuras irradiadas con pulsos de ns presentan una SPR mucho mas estrecha y que aparece a longitudes de onda mucho menores que la de la nanoestructura sin irradiar de acuerdo con el estrechamiento de las distribuciones de la forma y tamaño de las nanopartículas, mientras que las nanoestructuras irradiadas con pulsos de fs presentan una respuesta dicroica como resultado de la forma alargada y de la alineación en el plano de las nanopartículas.

CAPITULO 6 - Aplicación de las Nanoestructuras de Ag en lámina delgada

La tesis concluye con el estudio de la aplicación de las nanoestructuras producidas en experimentos de detección molecular y como elementos para atrapar la luz en células fotovoltaicas. En el primer caso, hemos investigado su actividad mediante espectroscopía Raman amplificada por superficies metálicas (SERS) utilizando una molécula aromática, él *Terphenyl Diisocyanide*. Hemos analizado la respuesta en función del tamaño de las nanopartículas, la concentración de la molécula y la distancia entre la superficie de las nanopartículas y la molécula. Se han comparado dos tipos de nanoestructuras: Las nanoestructuras caracterizadas por una alta densidad de nanopartículas formada por procesos de coalescencia y las obtenidas tras un recocido térmico. Las primeras presentan una mayor actividad SERS debido a la formación de *hot spots* entre nanopartículas adyacentes. Además, hemos observado que las posiciones de las bandas en el espectro SERS eran independientes de la concentración de la molécula lo cual confirma que los sustratos fabricado son adecuados para garantizar una respuesta SERS fiable. Por último, hemos demostrado que la actividad SERS

disminuye al aumentar la distancia entre la superficie metálica y la molécula. Hemos relacionado este efecto al corto alcance del campo electromagnético cercano generado alrededor de la nanopartícula cuando se excita la SPR.

Por último hemos incorporado diferentes nanoestructuras en células de calcopirita para intentar mejorar la eficiencia de los dispositivos por medio de efectos plasmónicos. Hemos estudiado dos configuraciones. En la primera, hemos incorporado nanopartículas de 5-10 nm embebidas en a-Al_2O_3 en la parte superior del dispositivo con el objetivo de que la intensificación del campo cercano estimule la generación de pares electrón-hueco en la capa absorbente. En la segunda, hemos incorporado nanopartículas con tamaños entre 60 nm y 130 nm embebidas en a-Al_2O_3 en la parte posterior de las células para que actúen como elementos dispersivos, aumentado así el recorrido de los fotones dentro del material absorbente y, como consecuencia, su absorción. Ambos experimentos han puesto de manifiesto que el crecimiento de las células no se ve afectado por la presencia de la nanoestructura, pero tampoco hemos sido capaces de observar una mejora de sus características. Hemos relacionado este resultado a una menor eficiencia de colección de los portadores de cargas foto-generados en el caso de las células solares que incorporan nanopartículas.

CAPITULO 7 – Conclusiones y Aportaciones Fundamentales

En esta tesis hemos investigado cómo mejorar el control sobre el tamaño, la forma y la orientación de las nanopartículas producidas por PLD a través de procesos de recocido y de irradiación con pulsos láser ultracortos, así como la aplicación de las nanoestructuras de Ag producidas como sustratos SERS y como elementos para atrapar la luz en células solares con el objetivo de mejorar sus características.

La morfología de las nanopartículas cambia al aumentar el contenido de metal. Hemos observado que el tamaño de las nanopartículas aumenta y que su forma en el plano se hace más alargada con el contenido de Ag y que, una vez superado el umbral de percolación, la Ag forma una lámina casi continua. La respuesta óptica de las nanoestructuras (SPR) depende de la morfología del las nanopartículas, mientras que la respuesta de las láminas percoladas es prácticamente constante en todo el intervalo de longitudes de onda considerado. Estos primeros experimentos, nos han permitido observar algunas limitaciones del PLD, como la dificultad de fabricar nanopartículas de tamaño > 50 nm y el bajo control que se consigue sobre la forma y la orientación en el plano de las nanopartículas.

Las nanopartículas expuestas a la atmósfera se deterioran con el tiempo. Hemos relacionado esta falta de estabilidad con la reacción de la Ag de las nanopartículas con algunos elementos presentes en la atmósfera (oxígeno, azufre y nitrógeno), lo que provoca la progresiva desaparición del SPR. Es posible mejorar la estabilidad de las nanoestructuras cubriendo las nanopartículas con una capa de a-Al_2O_3. El resultado más sorprendente ha sido descubrir que la estabilidad mejoraba con el depósito de una lámina de tan solo 1 nm, o menos, de espesor.

No obstante, el proceso de recubrimiento provoca la perdida de Ag desde la superficie de las nanoestructuras que, en el caso de las nanopartículas más pequeñas, puede llegar al 50% del contenido inicial de Ag. Este efecto se atribuye al proceso de arranque de Ag inducido por los iones de Al más energéticos (energía cinética > 200 eV) presentes en el plasma del Al_2O_3.

Posteriormente, hemos investigado como producir nanopartículas de tamaño mayor que el alcanzable por PLD (i.e. >50 nm). Para ello hemos sometido las láminas percoladas a recocidos térmicos en vacío y aire. Hemos demostrado que en ambos casos las láminas casi continuas se transforman en una capa de nanopartículas cuyo tamaño puede alcanzar los 200 nm. El recocido en vacío induce la formación de nanopartículas con forma irregular y alargadas, mientras que el recocido en aire genera nanopartículas con forma esferoidal. A diferencia de las nanopartículas más pequeñas, éstas nos se ven afectadas por el depósito de la capa protectora ya que su tamaño las hace más resistentes al bombardeo iónico. La capa de a-Al_2O_3 se deposita replicando la topografía de las nanopartículas resultando en una superficie rugosa. Además hemos observado que estas nanopartículas de tamaño superior a 50 nm dispersan la luz de forma significativa, una propiedad necesaria para sus aplicaciones en células fotovoltaicas.

El recocido permite formar nanopartículas grandes, pero no permite controlar la forma. Para alcanzar dicho objetivo hemos utilizado la irradiación láser de nanopartículas embebidas en a-Al_2O_3. Las irradiaciones llevadas acabo con un solo pulso de ns transforman nanopartículas alargadas y densas en una capa de nanopartículas separadas y con forma circular en el plano, mientras que las irradiaciones con cientos de pulsos de fs inducen la formación de nanopartículas alargadas y orientadas paralelamente a la polarización del láser. El mecanismo de transformación es puramente térmico en el caso de pulsos de ns, mientras que en el caso de pulsos de fs los efectos asociados a los campos eléctricos extremadamente intensos típicos de los pulsos ultracortos son fundamentales en la formación de nanopartículas

ordenadas. La respuesta óptica de las nanopartículas transformadas es coherente con el cambio en la morfología inducida por la irradiación láser. En el caso de pulsos de ns, la SPR aparece a longitudes de onda menores, su intensidad aumenta y el ancho disminuye con respecto al caso de la nanoestructura sin irradiar, mientras que para pulsos de fs, las nanoestructuras desarrollan una respuesta óptica dicroica.

La aplicación de las nanoestructuras fabricadas como detectores moleculares ha permitido demostrar que la intensificación de la señal Raman es mayor en el caso de nanoestructuras que contienen nanopartículas de tamaño entre 20-30 nm separadas por distancias del mismo orden que la longitud de la molécula (2-3 nm). Este comportamiento lo hemos atribuido a la formación de *hot spots* entre nanopartículas vecinas al excitar la nanoestructuras con longitudes de onda próximas a su SPR característica. Además hemos demostrado que la señal no depende de la concentración de la molécula, mientras sí depende de la distancia entre la molécula y la superficie de una nanopartícula, i.e. la señal SERS disminuye al aumentar la distancia.

Se presentan los primeros resultados obtenidos al incorporar las nanoestructuras fabricadas en células solares de calcopirita. Hemos estudiado dos configuraciones para conseguir efectos de atrapamiento de luz y hemos demostrado que la más prometedora es aquélla que se basa en que las nanopartículas actúen como centros dispersores de luz. Hemos demostrado que la incorporación de la nanoestructuras no compromete el proceso de depósito de la capa absorbente y que la célula sigue funcionando. No obstante, no hemos evidenciado ninguna mejora en el dispositivo lo cual ha sido relacionado a una menor eficiencia de colección de los portadores de cargas fotogenerados en el caso de la célula donde se han incorporados las nanopartículas. Por último, hemos realizado un análisis crítico de los resultados obtenidos y se proponen posibles alternativas.

English Summary

CHAPTER 1 – Introduction and objectives

Nanotechnology and its applications are more and more present in our everyday life. Stain-resistant and anti-bacterial clothes, scratch-resistant glasses, faster-recharging batteries and electrically conductive displays are just a few examples of consumer goods making use of nanotechnologies. Nonetheless, it was only 40-50 years ago that nanotechnology attracted the interest of the scientific community because the properties of materials change substantially when their dimensions are confined at the nanoscale.

Thin films, nanowires, nanotubes and nanoparticles are some representative examples of nanotechnology products. In particular, metal nanoparticles that are the subject of this thesis, are of great interest because their properties can be beneficial for several applications, like sensors, catalysts, solar cells and they are expected to play an important role in the future of medicine. Many applications based on metal nanoparticles take advantage of their optical properties characterized by the Surface Plasmon Resonance (SPR). The SPR is a collective oscillation of the conduction electrons that can be excited by an external electromagnetic field. At the SPR, the absorption and scattering cross-sections of a nanoparticle increase and, simultaneously, an intense electromagnetic near-field is generated in the vicinity of the nanoparticle surface. The spectral position, intensity as well as the width of the absorption band at the SPR depend on the nature of the metal, the size, shape and spatial arrangement of nanoparticles and on the material surrounding nanoparticles. The capability of tuning the optical response by varying the morphology of the nanoparticles and thus, the possibility of adjusting the optical response to the specific requirements of an experiment is the reason why nanoparticles can be applied to very different technological fields.

It is thus evident that fabrication techniques that allow achieving a precise control over nanoparticle morphology are needed to design nanostructures with specific optical response. Nowadays, there is a wide range of techniques based on chemical and physical approaches that aim at controlling the largest number of parameters. However, none of them is able to control all parameters at the same time. For example, redox chemical reactions allow synthesizing nanoparticles with very different shape and size in solution. Unfortunately, a reliable immobilization method does not exist. Electron beam lithography allows precise control over nanoparticle shape and on their spatial arrangement on a solid substrate, but it is

a high time-expensive technique and it is limited to small sizes. Finally, physical techniques, like thermal evaporation, sputtering or pulsed laser deposition (PLD) allow producing layers of nanoparticles over relatively large areas with good control over nanoparticle size, but with a limited control over their morphology.

Taking into account the importance that the control over nanoparticle morphology has for the fabrication of nanostructures with a well-defined optical response, the **aim** of this thesis has been the fabrication of nanostructures containing Ag nanoparticles and having optical properties that make them of interest as molecular sensors and as light trapping elements in photovoltaics. In particular, we have used PLD to fabricate nanostructured films containing Ag nanoparticles and we considered methods to improve the control over nanoparticle morphology and spatial orientation using thermal annealing and laser irradiation.

CHAPTER 2 - Experimental Techniques

In this chapter, we briefly describe the basic principles of PLD and the setup used to produce the nanostructures. Then we introduce the fundamentals of Langmuir probe (LP) analysis and describe the setup used to study the kinetic energy distribution of the ions present in the Al_2O_3 and Ag laser generated plasmas. We also report the procedure followed for LP data analysis. In addition, we introduce the thermal annealing procedure and the laser irradiation setup. The chapter ends with a description of the operation mode of the techniques used for compositional (X-ray photoelectron spectroscopy, XPS, Rutherford basckscattering spectrometry, RBS), morphological (transmission, TEM, and scanning electron microscopy, SEM) and optical characterization (ellipsometry and espectrophotometry) of nanostructured Ag films.

CHAPTER 3 - Dynamics of the Ceramic Aluminium Oxide and Silver Laser-generated Plasmas

In this chapter, we analyze the results obtained in the LP study of the dynamics of the plasmas generated upon ablation of Ag and ceramic Al_2O_3 targets as a function of laser fluence. We report and discuss the results concerning ion current density transient and yield, the ion kinetic energy distributions and, finally, the fraction of energetic species reaching the substrate. The results evidence the energetic nature of the laser generated plasma, particularly in the case of Al_2O_3 ablation. Indeed, at laser fluences close to the ablation threshold the

amount of energetic ions (kinetic energy > 200 eV) is close to 20-30%, while the percentage is almost negligible in the case of Ag ablation. This was related to the fact that the ionization potential of Al atoms (IP = 2.99 eV), present in the Al_2O_3 plasma is lower than the laser photon energy (6.4 eV), which allows single photoionization to occur. As a result, the plasma obtained upon ablation of Al_2O_3 possesses a high degree of ionization which may result in a stronger Coulomb acceleration with respect to the case of Ag for which single-photoionization is not accessible since IP = 7.57 eV.

CHAPTER 4 - Characterization of Nanostructured Silver Films

This chapter is dedicated to the results concerning the fabrication and morphological and optical characterization of nanostructured Ag films. We have initially investigated the case of nanostructured films in which we deposit Ag on an a-Al_2O_3 buffer layer. This configuration was chosen since SERS requires the molecule to be adsorbed directly on the metal surface. We observe that nanoparticles with increasing size and more irregular shape are formed on the surface as a result of nucleation and coalescence processes as the amount of Ag increases. This nanoparticle size and shape evolution stops once the percolation limit is reached and, hence, an almost continuous Ag film is formed. The optical response of the films containing nanoparticles shows a SPR whose spectral position and intensity shift to the red with the nanoparticle size and with the broadening of nanoparticle shape distribution. No resonant response was observed in the case of percolated films.

The SPR of the Ag nanoparticles exposed to air damps with time, particularly in the case of small nanoparticles. We have investigated this aging process and we related it to the reaction of Ag with atmospheric oxygen, sulphur or nitrogen, which leads to a progressive deterioration of the nanostructured film. We thus have explored how to protect nanoparticle from tarnishing and we demonstrate that the deposition of an a-Al_2O_3 covering layer strongly improves the stability of the nanostructured films. In particular, we demonstrated that a layer of only 1 nm of thickness was enough to prevent deterioration.

Subsequently, we have analyzed the effect the deposition of the covering layer has on nanoparticle morphology and we observed that after its deposition part of the Ag was removed from the buffer layer surface (up to 50% of Ag initially deposited in the case of small nanoparticles) and, as a result, nanoparticle morphology was changed. This process was related to the sputtering of Ag promoted by the energetic species present in the Al_2O_3 plasma,

namely the Al ions, which were evidenced by LP analysis. This was confirmed using a model for sputtering based on SRIM 2008 software.

CHAPTER 5 - Post-growth Processing of Nanostructured Silver Films

We have explored the transformation of nanostructures morphology using thermal annealing and laser irradiation. In the first case we annealed percolated Ag films in different environments (air and vacuum). The dewetting process promoted by the temperature increase leads to the formation of Ag nanoparticles with characteristic size well above the one obtained spontaneously as a result of nanoparticle nucleation and coalescence. Annealing in vacuum led to the formation of elongated nanoparticles with average sizes of 60 and 200 nm and irregular shapes, while annealing in air led to the formation of spheroidal nanoparticles with average sizes of 50 nm and 135 nm. In addition, we also demonstrate that the morphology of large nanoparticles is not significantly affected by the deposition of an a-Al_2O_3 covering layer, contrary to the case of relatively small nanoparticles. This result relates to the increased cohesive energy of large nanoparticles. Thus the covering layer replicates the topography of the nanoparticle layer, which results in a surface characterized by nanodomes with tapered shape. Finally, we observe that large nanoparticles diffuse light at the SPR, which is relevant for their application in photovoltaics.

Thermal annealing does not allow improving the control over the shape of nucleated nanoparticles. To that purpose, we have studied the effect that laser irradiation has on covered nanostructured films containing coalesced nanoparticles (circular or elongated shapes, the long axis being randomly oriented). In particular, we have investigated the effect of ns irradiation at 800 nm and fs irradiation at 400 and 800 nm. Nanoparticles are efficiently reshaped in both cases. However, nanosecond pulses lead to the formation of nanoparticles with in-plane circular shape, while femtosecond pulses lead to in-plane elongated and aligned nanoparticles, which is attributed to the different mechanisms leading to morphology modification. In the case of ns reshaping is essentially thermally driven, while in the case of fs pulses, the high transient electric field characteristic of ultrashort laser pulses is responsible for promoting the formation of aligned elongated nanoparticles. The optical response of the nanoparticles reshaped with ns pulses shows a narrow SPR that is blue-shifted with respect to the case of as-grown film in good agreement with the observed morphological changes. In the case of irradiation with fs pulses, the nanostructures developed a dichroic optical behavior that is consistent with the formation of elongated and aligned nanoparticles.

CHAPTER 6 -Application of Nanostructured Silver Films

The thesis concludes with the study of the application of the fabricated nanostructures as SERS substrates and as elements to improve light trapping in chalcopyrite-based solar cells. In the first case, we have used an aromatic molecule, the *Terphenyl Diisocyanide* (TPDI), as test molecule to investigate the SERS activity of our nanostructured films as a function of nanoparticle morphology, molecule concentration and molecule-to-nanoparticle surface distance. We have compared two types of nanostructures: PLD as-grown nanostructures having a high density of nanoparticles and those obtained upon annealing of percolated Ag films.

SERS signal is much more intense in the case of uncovered coalesced nanoparticles separated by very small gap, i.e. of the same order of the molecule length (2-3 nm), mainly due to the formation of *hot-spots* where a huge near-field enhancement is expected to occur. In addition, we demonstrated that the measured signal is independent on the molecule concentration, which is important to guarantee SERS reproducibility and reliability. Finally, we observed that the signal decreases rapidly as the molecule-to-nanoparticle surface distance increases. This result is consistent with the role of the electromagnetic contribution to the SERS response and with the short range of the near electromagnetic field effects.

Finally, we report the initial results obtained by incorporating nanostructured films containing small and large nanoparticles in chalcopyrite solar cells. In the first case, nanoparticles should act as light concentrators that may promote the generation of electron-hole pair in the absorber layer through the near electromagnetic field arising at the SPR. In the second case nanoparticles should act as scattering centers and may increase the optical path length of light into the absorber layer, thus increasing the probability of light to be absorbed. In both cases, we have demonstrated that the incorporation of nanostructured films allows the proper deposition of devices, but without any significant improvement of their characteristics. This was related to the lower efficiency of plasmonic devices in charge carrier collection.

CHAPTER 7 – Conclusions and main contributions

In this thesis we investigated first the potential of nanoparticle shaping methods, namely thermal annealing and laser irradiation to improve the control over size, shape and spatial organization of Ag nanoparticles in nanostructured films fabricated by PLD. Second, we apply the fabricated Ag nanostructures as SERS substrates and as light trapping elements in solar cells.

Nanoparticle morphology changes upon increasing the amount of deposited metal. Ag forms isolated nanoparticles below percolation threshold as a result of nucleation and coalescence processes. Their size increases and their in-plane shape changes from almost circular to elongated when increasing the metal content until percolation starts to take place. Above percolation, Ag forms an almost continuous film. The optical response of the nanostructured films containing Ag nanoparticles show a resonant behaviour due to the excitation of the SPR, while percolated films show a constant optical response resembling that of continuous films. The growth of these films showed some of the drawbacks of pulsed laser deposited films: the low control over nanoparticle shape and spatial organization and the difficulty of obtaining nanoparticles with size > 50 nm in the as-grown configuration.

In general, SERS, as well as other techniques, requires nanoparticles exposed to the environment and thus, nanostructure optical and chemical stability have to be guaranteed. We have shown that Ag nanoparticles exposed to air react with atmospheric oxygen, sulphur or nitrogen, which leads to nanoparticle tarnishing and to the progressive damping of the SPR. We have demonstrated that an ultrathin (< 1 nm) a-Al_2O_3 covering layer is enough to prevent Ag tarnishing and thus, nanostructures deterioration. However, the deposition of the covering layer strongly modifies the morphology of the nanostructured films, particularly in the case of small nanoparticles. We have related these changes to the sputtering of Ag promoted by the energetic Al ions present in the plasma generated by laser ablation of Al_2O_3.

We have demonstrated that dewetting promoted by thermal annealing allows transforming Ag percolated films in an assembly of large Ag nanoparticles (size > 50 nm) having elongated and irregular shapes (annealing in vacuum) or, alternatively, in an assembly of Ag nanoparticles with truncated oblate spheroidal shape (annealing in air). Contrary to small nanoparticles, the morphology of large nanoparticles is not significantly affected by the deposition of the a-Al_2O_3 covering layer. This was related to the increased cohesive energy of large nanoparticles that make them more resistant to the Al^+ bombardment. The deposition of the a-Al_2O_3 covering layer replicates the topography of the nanoparticle layer resulting in a surface characterized by features that resemble nanodomes with tapered shape. Moreover, we have demonstrated that large nanoparticles produced in this way diffuse light at the SPR, which is fundamental for the application of nanostructured films to solar cells.

Thermal annealing does not allow controlling the shape of the nanoparticles. To that purpose we have considered laser irradiation of covered nanostructures. Single pulse ns-irradiation transform coalesced nanoparticles into a layer of well separated ones with circular

in-plane projected shape, whereas multi-shot irradiation with fs pulses reshape coalesced nanoparticles into prolate spheroids with their long axis oriented parallel to the direction of laser polarization. The reshaping mechanism is associated to thermal effects in the case of ns pulses, while in the case of fs pulses the high transient electric field, typical of ultrashort laser pulses, is considered to be responsible for the observed elongated shape. The optical response of reshaped nanoparticles agrees with the morphology changes induced by laser irradiation. In the case of ns pulses, SPR shifts towards shorter wavelengths, its intensity increases and the FWHM decreases with respect to the as-grown nanoparticles, while in the case of irradiation with fs pulses, the nanostructures developed a dichroic optical behavior.

The application of the produced nanostructures to SERS allowed us to demonstrate that the enhancement of the signal strongly relates to the size and, particularly, spatial distribution of nanoparticles. The formation of hot-spots in nanostructures containing nanoparticles separated by very small gaps (≈ 2-3 nm) that nicely suit the length of the test molecule leads to an intense SERS activity due to the huge intensification of the near-field in between of neighbouring nanoparticles. The reproducibility of the molecule adsorption scheme as a function of molecule concentration confirms the robustness of the fabricated SERS substrate, while the observed SERS signal decrease as a function of the molecule-to-nanoparticle surface distance evidenced the importance of electromagnetic contribution to the Raman signal enhancement and of its reduced extension.

Finally, we have presented the initial results on the application of the produced nanostructures as light traps in chalcopyrite solar cells. We have demonstrated that the devices still work after incorporation of nanostructured films. In addition, we have found that the most promising approach is based on light scattering to increase the path length of light inside the absorber layer. We have shown that the absorber was properly deposited and the values of the J_{sc} and V_{oc} were similar to that of reference cells. However, the efficiency of plasmonic devices was reduced by a 50% with respect to the efficiency of the reference. We relate this behaviour to a lower collection efficiency of the photo-generated charge carriers in the case of plasmonic device. We end this section with a critical analysis of the results obtained and we propose possible alternatives.

List of Publications, Communications and Awards

Publications

(8) *Tailoring the surface plasmon resonance of embedded silver nanoparticle by combining nano- and femtosecond laser pulses*
J. Doster, **G. Baraldi**, J. Gonzalo, J. Solis, J. Hernandez-Rueda, J. Siegel
Appl. Phys. Lett. 104, 153106 **(2014)**
DOI: 10.1063/1.4871507

(7) *Probing plasmonic effects on the Raman activity of Ag nanoparticle-based nanostructures through terphenyl diisocyanide adsorption*
G. Baraldi, E. Lopez-Tobar, K. Hara, S. Sanchez-Cortes, J. Gonzalo
J. Phys. Chem. C 118, 4680-4686 **(2014)**
DOI: 10.1021/jp410628m

(6) *Reorganizing and shaping of embedded near-coalescence silver nanoparticles with off-resonance femtosecond laser pulses*
G. Baraldi, J. Gonzalo, J. Solis, J. Siegel
Nanotechnology 24, 255301 (**2013**)
DOI: 10.1088/0957-4484/24/25/255301

(5) *Preventing the degradation of Ag nanoparticles using an ultrathin a-Al_2O_3 layer as protective barrier*
G. Baraldi, M. Carrada, J. Toudert, F. J. Ferrer, A. Arbouet, V. Paillard, J. Gonzalo
J. Phys. Chem. C 117, 9431-9439 (**2013**)
DOI: 10.1021/jp401421m

(4) *Selective gold nanoparticles formation by pulsed laser interference*
R. J. Peláez, **G. Baraldi**, C. N. Afonso, S. Riedel, J. Boneberg, P. Leiderer
Applied Surface Science 258, 9223-9227 (**2012**)
DOI: 10.1016/j.apsusc.2011.08.048

(3) *Application of PLD to the production of plasmonic structures containing Ag nanoparticles based on chalcopyrite solar cells*
G. Baraldi, R. Caballero, C. A. Kaufmann, J. Gonzalo
Energy Procedia 10, 38-42 (**2011**)
DOI: 10.1016/j.egypro.2011.10.149

(2) *Dynamics of ions produced by laser ablation of ceramic Al_2O_3 and Al at 193 nm*
G. Baraldi, A. Perea, C. N. Afonso
Appl. Phys. A 105, 75-79 (**2011**)
DOI: 10.1007/s00339-011-6523-9

(1) *Dynamics of ions produced by laser ablation of several metals at 193 nm*
G. Baraldi, A. Perea, C. N. Afonso
J. Appl. Phys. 109, 043302 (**2011**)
DOI: 10.1063/1.3549159

Contributions to Conferences

- *Laser based fabrication and modification of plasmonic nanostructures for optical applications*
  J. Gonzalo, **G. Baraldi**, J. Solis, J. Siegel
  6th ICOOPMA, Leeds (Reino Unido). July 27 - August 1, **2014**
  Invited
- *Tailoring the optical response of an embedded silver nanoparticle layer using nano- and femtosecond laser pulses*
  J. Siegel, J. Doster, **G. Baraldi**, J. Gonzalo, J. Hernandez-Rueda, J. Solís
  Nanospain 2014. 11th Nanospain workshop, Madrid. March 11-14, **2014**
  Oral
- *Plasmonically decorated Mo substrates for enhancing light trapping*
  J. Gonzalo, **G. Baraldi**, R. Caballero, C. A. Kaufmann
  COLA 2013, Ischia (Italy). October 6-11, **2013**
  Poster
- *Off-resonance fs-laser shaping of heterogeneous distributions of embedded Ag nanoparticle layers*
  G. Baraldi, J. Doster, J. Toudert, J. Gonzalo, J. Solis, J. Siegel
  EUROMAT 2013, Sevilla. September 8-13, **2013**
  Oral
- *In-situ characterization of fs-laser shaping of quasi-percolated Ag NP layers embedded in a-Al_2O_3*
  G. Baraldi, J. Gonzalo, J. Siegel
  CLEO 2013, Munich (Germany). June 21-25, 2013.
  Oral
- *Influence of Ag nanoparticle size and configuration on the SERS signal of Terphenyl Diisocyanide*
  G. Baraldi, E. Lopez Tobar, S. Sanchez-Cortes, J. Gonzalo
  E-MRS Spring Meeting 2013, Strasbourg (France). May 27-31, 2013
  Poster
- *Elaboration of noble metal nanoparticles by pulsed laser deposition and optical properties*
  J. Gonzalo, **G. Baraldi**, R. Morea, J. Solis
  GdR Or-Nano Plenary Meeting, Nantes (France). April 3-5, 2013
  Invited
- *Nanoestructuras plasmónicas producidas mediante depósito por laser pulsado*
  J. Gonzalo, **G. Baraldi**, M. Carrada, A. Arnaud, V. Paillard, Fco. Javier Ferrer, J. García López
  X Reunión Nacional de Óptica, Zaragoza. September 4-7, 2012
  Oral
- *Annealing effects on the absorption and scattering response of plasmonic structures for photovoltaic applications*
  G. Baraldi, R. Morea, J. Gonzalo
  E-MRS Spring Meeting 2012, Strasbourg (France). May 15-17, 2012
  Oral

- *Effect of dielectric covering layers on the morphology and optical response of plasmonic structures for photovoltaics*
  G. Baraldi, M. Carrada, J. Gonzalo, V. Paillard, A. Arbouet
  COLA 2011, Cancún (Mexico). November 13-19, 2011
  Poster
- *Application of PLD to the production of plasmonic structures containing Ag nanoparticles based on chalcopyrite solar cells*
  G. Baraldi, R. Caballero, C. A. Kaufmann, J. Gonzalo
  E-MRS Spring Meeting 2011, Nice (France). May 9-13, 2011
  Poster
- *Pulsed Laser Deposition for fabrication of plasmonic nanostructures*
  G. Baraldi, M. Carrada, J. Gonzalo, A. Arbouet, V. Paillard
  E-MRS Spring Meeting 2011, Nice (France). May 9-13, 2011
  Oral
- *Ion density and kinetic energies under laser ablation of metals: a comparison study*
  G. Baraldi, A. Perea, C.N. Afonso
  E-MRS Spring Meeting 2010, Strasbourg (France). June 8-10, 2010
  Poster
- *Limits to the nanoscale control during pulsed laser deposition*
  G. Baraldi, V. Resta, A. Perea, J. Gonzalo, C. N. Afonso
  Photonics West, Laser Applications in Microelectronic and Optoelectronic Manufacturing XV, San Francisco, California (USA). January, 2010
  Oral

Awards

- EMRS 2013 - Spring Meeting, Young Scientist Award, in recognition of the outstanding paper contributed to Symposium Q: “Bionanomaterials for Imaging, Sensing and Actuating”
- EMRS 2011 - Spring Meeting, Young Scientist Award, in recognition of the outstanding paper contributed to Symposium J: “Laser Materials Processing for Micro and Nano Applications”